POLISH ACADEMY OF SCIENCES

THERMODYNAMICS AND COMBUSTION COMMITTEE

archives of thermodynamics

Wydawnictwo IMP
Gdańsk

QUARTERLY
Vol. 38
2017
No. 4

Editorial Office

Archives of Thermodynamics
The Szewalski Institute of Fluid Flow Machinery, Fiszera 14, 80-231 Gdańsk, Poland,
Tel.: (+48) 58-341-12-71 int. 141, E-mail: redakcja@imp.gda.pl
http://www.imp.gda.pl/archives-of-thermodynamics/
http://at.czasopisma.pan.pl/

Publication funding of this journal is provided by resources of the Polish Academy of Sciences and the Szewalski Institute of Fluid-Flow Machinery PASci

Terms of subscription outside Poland
Annual subscription rate outside Poland (2017) is 120 EUR. Price of single issue is 30 EUR. Back of previously published volumes are available on request. Subscription orders should be sent directly to **IMP PAN Publishers, The Szewalski Institute of Fluid-Flow Machinery PASci, ul. Fiszera 14, 80-231 Gdansk, Poland**; fax: (+48) 58-341-61-44; e-mail: now@imp.gda.pl. Payments should be transferred to the bank account of IMP PAN: IBAN 28 1130 1121 0006 5498 9520 0011 at Bank Gospodarstwa Krajowego; Code SWIFT: GOSKPLPW

Warunki prenumeraty w Polsce
Roczna prenumerata (2017 r.) wynosi 168 PLN. Cena pojedynczego numeru wynosi 42 PLN. Osiągalne są również wydania archiwalne. Zamówienia z określeniem okresu prenumeraty, nazwiskiem i adresem odbiorcy należy kierować bezpośrednio do Wydawcy (Instytut Maszyn Przepływowych im. R. Szewalskiego PAN, ul. Fiszera 14, 80-231 Gdańsk, Aleksandra Nowaczewska, e-mail: now@imp.gda.pl). Wpłaty prosimy kierować na konto Instytutu Maszyn Przepływowych PAN nr 28 1130 1121 0006 5498 9520 0011 w Banku Gospodarstwa Krajowego

Articles in *Archives of Thermodynamics* are abstracted and indexed within:

Applied Mechanics Reviews • BazTech • Arianta • Baidu Scholar • Cabell's Directory • Celdes • Chemical Abstracts Service (CAS) - CAplus • CNKI Scholar (China National Knowledge Infrastucture) • CNPIEC • DOAJ • EBSCO (relevant databases) • EBSCO Discovery Service • Elsevier - SCOPUS • Genamics JournalSeek • Google Scholar • Inspec • Index Copernicus • J-Gate • Journal TOCs • Naviga (Softweco) • Paperbase • Pirabase • POL-index • Polymer Library • Primo Central (ExLibris) • ProQuest (relevant databases) • ReadCube • Referativnyi Zhurnal (VINITI) • SCImago (SJR) • Summon (Serials Solutions/ProQuest) • TDOne (TDNet) • TEMA Technik und Management • Ulrich's Periodicals Directory/ulrichsweb • WorldCat (OCLC)

Online ISSN 2083-6023
DE GRUYTER – http://www.degruyter.com/view/j/aoter

Typeset in LaTeX
Printed and bound by
Centrum Poligrafii Sp. z o.o., Łopuszańska 53, 02-232 Warszawa

archives
of thermodynamics
Vol. **38**(2017), No. 4, 3–13
DOI: 10.1515/aoter-2017-0021

Thermoelectric generation of current – theoretical and experimental analysis

ADAM RUCIŃSKI*
ARTUR RUSOWICZ

Division of Refrigeration and Energy in Buildings, Institute of Heat Engineering, Faculty of Power and Aeronautical Engineering, Nowowiejska 21/25, 00-665 Warsaw, Poland

Abstract This paper provides some information about thermoelectric technology. Some new materials with improved figures of merit are presented. These materials in Peltier modules make it possible to generate electric current thanks to a temperature difference. The paper indicates possible applications of thermoelectric modules as interesting tools for using various waste heat sources. Some zero-dimensional equations describing the conditions of electric power generation are given. Also, operating parameters of Peltier modules, such as voltage and electric current, are analyzed. The paper shows chosen characteristics of power generation parameters. Then, an experimental stand for ongoing research and experimental measurements are described. The authors consider the resistance of a receiver placed in the electric circuit with thermoelectric elements. Finally, both the analysis of experimental results and conclusions drawn from theoretical findings are presented. Voltage generation of about 1.5 to 2.5 V for the temperature difference from 65 to 85 K was observed when a bismuth telluride thermoelectric couple (traditionally used in cooling technology) was used.

Keywords: Thermoelectric generator; Waste heat sources; Efficiency; Thermoelectrics; Renewable heat sources

*Corresponding Author. Email adam.rucinski@itc.pw.edu.pl

Nomenclature

I	–	DC current, A
$\bar{T}$	–	mean temperature of thermo element
T_c	–	temperature of the lower heat source (surroundings), K
T_h	–	temperature of the upper heat source (waste or renewable source), K
Q_c	–	capacity of upper heat source, W
R	–	resistance of the thermoelement, Ω
R_L	–	load resistance, Ω
v	–	voltage, V
W	–	electrical power, W
$Z\overline{T}$	–	figure of merit

Greek symbols

α	–	Seebeck coefficient, V/K
λ	–	thermal conductivity, W/(m K)
ρ	–	resistivity, Ω m
$\eta_{\max\ t}$	–	thermodynamic efficiency

1 Introduction

Cost-effective methods of energy management are important and ways to improve energy efficiency of thermal processes are crucial in industrial and commercial applications [1]. Some ways of using waste heat sources are known, such as absorption and adsorption technologies [2,3]. Currently, thermoelectrics is one of the latest technologies recognized in many applications. Thermoelectric modules use the Seebeck effect, i.e., generation of electric current between two positive-type and negative-type semiconductor welds at various temperatures; this is a reverse effect to the Peltier cooling effect. Thermoelements can be considered an alternative source of electricity using waste exhaust heat produced in industrial (power plants, steel mills, heat sources in a variety of manufacturing industries) and commercial applications (car exhaust, gas furnaces for space heating). They could work in satellites where phase change materials (PCM) are a source of energy. What is more, renewable energy heat sources are currently considered as a driving force for thermoelectric generation. There are two main sources: geothermal and solar thermal energy. For solar applications, flat and concentrating solar thermal technologies, solar ponds, and evacuated tube heat pipe solar collectors are used. In aeronautical technology, thermoelectric modules are used to produce electricity by means of solar energy accumulated in PCMs [4]. It should be underlined that energy is widely used in heating, ventilation, air conditioning ans refrigeration (HVAC&R)

systems in buildings, too. There are problems to solve related to good and cost-effective energy flow [5,6]. Modern and wise use of fuels and renewable energy sources in buildings is where electricity generation based on a temperature difference could be taken into account as a future technology.

2 Thermoelectrics – properites and materials

The main advantages of electric current generation by thermoelements are the following [7]:

- The lack of refrigerant and lubricating oil, which puts thermoelectric devices in a series of future-oriented solutions for protection of the environment.
- The lack of moving parts contributes to operating cost savings related to time required for repair and maintenance (a broken thermocouple can be exchanged for a new one in short time).
- Possibility to maintain a constant operating temperature of thermocouples with a small deviation of ± 0.1 K.
- Possibility to adjust the range of cooling capacity between 0 and 100%.
- A simple, maintenance-free structure.
- Possible different shapes of thermocouples – they may take the form required for a particular application.
- Possibility of cooling only the selected area or component of a device or machine.
- Operation without noise emission.
- Possible operation in conditions of weightlessness and at high load, which is important in military and space applications.

Traditional bismuth telluride thermocouples have the following main disadvantages and limitations:

- Bismuth and tellurium form toxic alloys.
- Heat losses associated with the Joule effect (heating of a semiconductor, which is connected with conduction of electric current) are observed.

- A small figure of merit Z gives small thermal efficiency of electric power generation.

One definition of the figure of merit $Z\overline{T}$ is presented below, where $\bar{T}$ is mean temperature of a thermoelement (Lee 2010):

$$Z\overline{T} = \frac{\alpha^2}{\rho\lambda}\bar{T} \,. \tag{1}$$

A good thermoelectric material should have a high Seebeck coefficient to obtain high voltage. At the same time, high electrical conductivity and low thermal conductivity to limit heat loss at the joint are needed [8].

Traditional materials [9], such as bismuth telluride, Bi_2Te_3, have at ambient temperature (approx. 300 K) the $Z\overline{T}$ coefficient of approximately 1. Material engineering seeks to develop new materials with a better $Z\overline{T}$ coefficient, allowing to increase the area of application and improve the efficiency of electric current generation [10].

Modern thermoelectric materials are based on elements from the 4th group of the Mendeleev periodic table. Mainly, these are alloys composed of germanium and silicon ($Si_{0,8}Ge_{0,2}$ p-type and n-type). Their optimal temperature range of operation is from 870 K to 1300 K. The $Z\overline{T}$ coefficient is about 1.3. Other materials include magnesium silicide Mg_2Si, germanium magnesium Mg_2Ge, and magnesium stannate Mg_2Sn [11,12] with the $Z\overline{T}$ coefficient at a level of 0.8. In addition, materials based on lead telluride doped with lanthanum and chromium [13] are currently enjoying a growing interest. Their $Z\overline{T}$ coefficient is 2.2 in 550 K and 1.8 in 850 K.

There are other materials, such as polycrystalline glass PGEC (phonon-glass electron-crystal). They have a crystalline structure forming a network with doped metal atoms. Semiconductors $Sr_8Ga_{16}Ge_{30}$ with the $Z\overline{T}$ coefficient of 1.35 (at 900 K) are the examples. Other examples include $Ba_{0,08}Yb_{0,09}Co_4Sb_{12}$ and $Ba_{0,3}Ni_{0,05}Co_{3,95}Sb_{12}$ compounds with the $Z\overline{T}$ coefficient equal to about 1.7 at a temperature of around 850 K.

The latest materials have been developed by the use of modern material science techniques [14]. For instance, there are compounds such as $AgPb_{18}SbTe_{20}$(LAST) and $(GeTe)_{75}(AgSbTe_2)_{25}$(TAGS-75) with the $Z\overline{T}$ coefficient of 1.7 at the temperature range from 700 to 800 K.

3 Theory

A thermoelectric generator produces electric power that is obtained on the outside receiver of the electric resistance, R_L, [15], it is defined as in formula:

$$W = I^2 R_L \ . \tag{2}$$

The electric current generated depends on thermoelectric properties of the material, the temperature difference between the upper and lower sources, and the resistance of the receiver, as in formula

$$I = \frac{\alpha(T_h - T_c)}{R_L + R} \ . \tag{3}$$

The thermodynamic analysis of the efficiency of the conversion of thermal energy into electricity indicates that the maximum value of the efficiency depends on the temperature of the upper and lower heat sources and the $Z\overline{T}$ coefficient, as shown in formula:

$$\eta_{\max t} = \left(1 - \frac{T_c}{T_h}\right) \frac{(1 + Z\overline{T})^{\frac{1}{2}} - 1}{(1 + Z\overline{T})^{\frac{1}{2}} + \frac{T_c}{T_h}} \ , \tag{4}$$

where $\overline{T} = \frac{(T_h + T_c)}{2}$.

Table 1 lists some possible values of the maximum generation efficiency for fixed upper and lower source temperatures.

Table 1: Estimated thermodynamic efficiency of electric power generation.

T_c	T_h	Z	$Z\overline{T}$	$1 - \frac{T_c}{T_h}$	$\eta_{\max t}$
300	550	0.0015	0.64	0.45	0.15
300	550	0.0030	1.27	0.45	0.25
300	550	0.0064	2.72	0.45	0.37

The values presented in table confirm that high-quality thermoelectric materials with high temperatures of the upper source are capable of delivering electrical current generation with the efficiency from 20% to 30%, making it economically acceptable.

Further theoretical analysis can determine the current and voltage of

the electric current and the electric power generated that can be referenced to a possible maximum thermoelectric effect as a function of thermoelectric material properties and the receiver resistance in the electrical system:

$$\frac{\dot{W}}{\dot{W}_{\max}} = \frac{4\frac{R_L}{R}}{\left(\frac{R_L}{R}+1\right)^2}\,, \tag{5}$$

$$\frac{I}{I_{\max}} = \frac{1}{\frac{R_L}{R}+1}\,, \tag{6}$$

$$\frac{V}{V_{\max}} = \frac{\frac{R_L}{R}}{\frac{R_L}{R}+1}\,. \tag{7}$$

Graphs of these values as a function of the resistance of the receiver to the resistance of the thermoelectric material depending on the temperature of the upper and lower heat sources (given in Tab. 1) are provided below in Fig. 1.

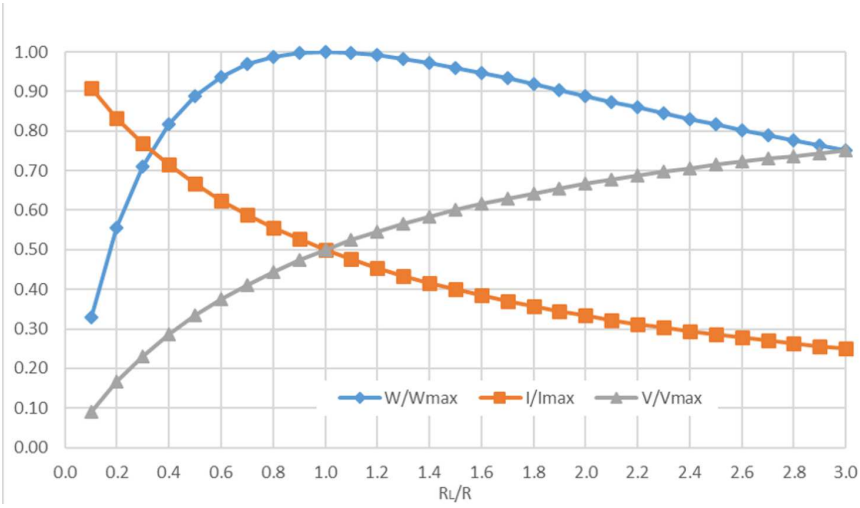

Figure 1: Dimensionless generation of electrical power (W/Wmax), current (I/Imax) and voltage (V/Vmax).

A simultaneous loss of power and current can be observed with an increasing ratio of the resistance of the receiver to the resistance of the thermoelectric material when the value of this ratio is significantly higher than 1. Thus, a thermoelectric generator with high efficiency is one that operates with

a receiver with comparable resistance in the range of 50 to 150% with respect to the resistance of the thermoelement generating electrical power. For a higher resistance of the receiver, electrical power decreases with a simultaneous voltage increase. Since the efficiency of the thermoelectric generator is lower in comparison with conventional devices, it is important to select materials properly to match the generator voltage and current. Otherwise, improper selection of these parameters significantly reduces the economic efficiency of the project.

4 Experimental setup

An experimental stand is used to examine generation of electrical power due to heat load. The main component of the experimental stand is a Peltier thermoelement mounted between two heat exchangers (the heat exchanger with hot water flowing simulates the waste (upper) heat source, while the heat exchanger with cooling water simulates the lower heat source). The Peltier element is insulated with mineral wool. Water is preheated in a buffer tank, then pumped through a band resistance heater to obtain a desirable temperature. Next, the hot water flows through hot-side heat exchanger and returns to the buffer tank. Cooling water is prepared in an ultrathermostat and flows through a cold-side heat exchanger (Fig. 2).

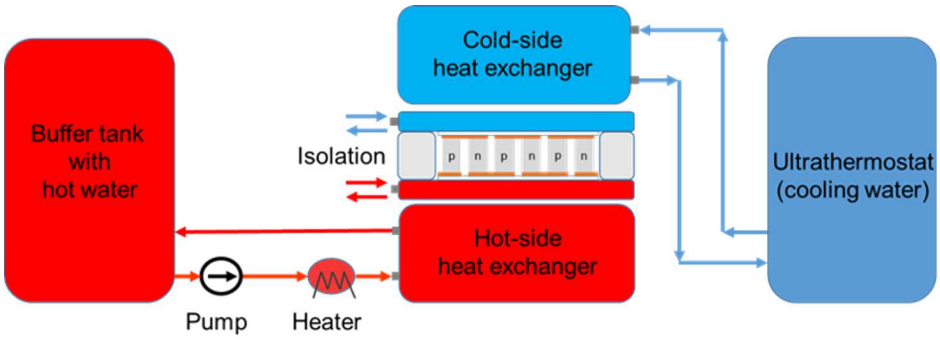

Figure 2: The scheme of experimental setup.

The study is conducted with three Peltier modules based on bismuth telluride, a traditional thermoelectric material. Tradenames of the modules are TEC1-12715, TEC1-12710, and TEC1-12708. Basic technical data are given below in Tab. 2.

Table 2: Technical data of thermoelectric modules.

Module	TEC1-12715	TEC1-12710	TEC1-12708
T_h [K]	323.0	323.0	323.0
ΔT_{max} [K]	79.0	79.0	75.0
U_{max} [V]	17.2	17.2	17.5
I_{max} [A]	15.0	10.1	8.4
Q_c [W]	164.2	110.5	79.0
R [Ω]	0.79–0.98	1.27–1.49	∼ 1.80

Measurements are performed via a measurement electronic card, and data are recorded in the personal computer memory. A series of measurements with the three thermoelements was performed. Basic measurement parameters were: temperature of the hot water inlet/outlet in/from the hot heat exchanger, temperature of the cooling water inlet/outlet in/from the cold heat exchanger, electric current, and voltage in the electric circuit (Fig. 3).

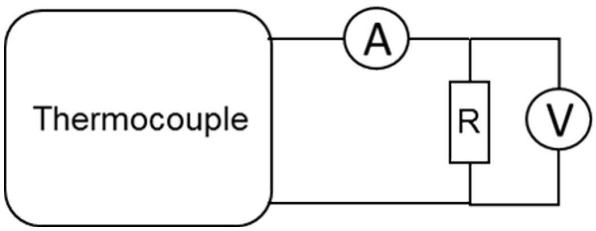

Figure 3: The scheme of measurement electric circuit.

During the experimental work, water temperature drops across both heat exchangers, thermal power supplied to the thermocouple, and electric power output on the receiver were also obtained. Table 3 shows selected measurement data and computing values gathered from the TEC1-12715 module examination. Based on the measurements, it was possible to draw voltage characteristics of thermomodules depending on the temperature difference between the upper and lower heat sources (Fig. 4).

Preliminary research results show that the level of voltage generated is similar to values obtained by other authors [16]. Getting a very small

Table 3: Selected results of the measurement and calculation for the TEC1-12715 module.

T_{hot} [K]	ΔT [K]	I [μA]	U [V]	W [mW]
335.06	69.07	333	1.55	0.516
335.25	69.35	334	1.56	0.521
335.44	69.57	342	1.60	0.547
335.69	69.88	339	1.58	0.536
336.38	70.50	340	1.59	0.541
336.50	70.69	340	1.59	0.541
336.69	70.95	342	1.60	0.547
336.88	71.17	343	1.60	0.549
337.12	71.44	345	1.61	0.555
337.31	71.69	348	1.63	0.567
337.56	71.94	356	1.67	0.595
338.37	72.75	360	1.69	0.608
339.12	73.50	363	1.70	0.617
339.81	74.22	366	1.72	0.630
340.50	74.91	370	1.73	0.640
341.19	75.56	373	1.75	0.653
341.81	76.22	376	1.77	0.666
342.50	76.94	380	1.78	0.676
343.12	77.56	374	1.75	0.655

value of electric current is an issue and it results in a minimum electric power generation. The reason for this is too high load resistance used. Hence, a very important conclusion can be drawn: to produce current from thermoelectric modules, a circuit with small resistance should be used or the energy should be stored properly. Otherwise, a low efficiency of power generation is observed. Besides, the operation with a small ΔT (from 60 to 80 K) near ambient temperature results in a low thermal conversion efficiency. That is why necessary modifications should be made to both the experimental setup and the way the experiments are carried out.

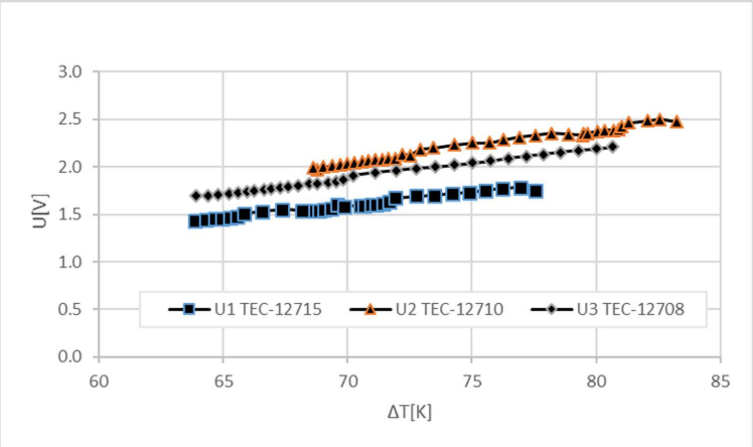

Figure 4: Voltage characteristics of Peltier modules as a function of the temperature difference.

5 Conclusions

The paper describes the application of Peltier thermomodules for electric current generation. For generating electric energy, either waste heat or renewable energy sources are used. Materials used at present and those of the future were listed. Basic mathematical relations were shown, and effectiveness of electric energy generation was analyzed. An experimental setup as well as the way of performing measurements and interpreting their results were described. The results of the experimental work indicate directions of future research, i.e., using materials with a better $Z\overline{T}$ coefficient and increasing the temperature difference between the 'hot' and the 'cold' sides of a thermoelement. What is more, new heat sources should be sought. It is possible to state that the issues mentioned in the paper are topical at the time and still in the research and development phase.

Received 1 October 2017

References

[1] Ziębik A., Gładysz P.: *System effects of primary energy reduction connected with operation of the CHP plants.* Arch. Thermodyn. **38**(2017), 2, 61–80. https://doi.org/10.1515/aoter-2017-0010

[2] Rusowicz A., Rucinski A.: *The mathematical modelling of the absorption refrigeration machines used in energy systems*. In: Proc. 8th Int. Conf. Environmental Engineering in Vilnius. Environ. Eng. **1-3**(2011), 802–806.

[3] Grzebielec A., Rusowicz A., Ruciński A.: *Analysis of the performance of the rotary heat exchanger in the real ventilation systems*. In: Proc. ICEE-2011 Int. Conf. on Environmental Engineering Selected Papers; DOI:10.3846/enviro.2014.259

[4] Jaworski M., Bednarczyk M., Czachor M.: *Experimental investigation of thermoelectric generator (TEG) with PCM module*. Appl. Therm. Eng. **96**(2016), 527–533. DOI: 10.1016/j.applthermaleng.2015.12.005.

[5] Rusowicz A., Grzebielec A., Ruciński A.: *Energy conservation in buildings using refrigeration units*. ICEE-2014 Int. Conf. on Environmental Engineering Selected Papers. http://doi.dx.org/10.3846/enviro.2014.281

[6] Jędrzejuk H., Dybiński O.: *The influence of a heating system control program and thermal mass of external walls on the internal comfort in the polish climate*. Energy Procedia **78**(2015), 1087–1092. http://doi.dx.org/10.1016/j.egypro.2015.11.058

[7] Rusowicz A., Ruciński A., Grzebielec A.: *Laboratory of Refrigeration*. Oficyna Wydawnicza PW, Warsaw 2011.

[8] Królicka A., Hruban A., Mirowska A.: *Advanced thermoelectric materials – literature review*. Materiały Elektroniczne **40**(2012), 4, 19–34 (in Polish).

[9] Goldsmid H. J.: *Bismuth telluride and its alloys as materials for thermoelectric generation*. Materials **7**(2014), 4, 2577–2592; DOI:10.3390/ma7042577

[10] Li L., Chen Z., Zhou M., Huang R.: *Developments in semiconductor thermoelectric materials*. Front. Energy **5**(2011), 2, 125–136.

[11] Sano S., Mizukami H., Kaibe H.: *Development of high-efficiency thermoelectric power generation system*. Komatsu Technical Rep. **49**(2003), 152, 1–7.

[12] Sales B. C.: *Critical overview of recent approaches to improved thermoelectric materials*. Int. J. Appl. Ceram. Technol. **4**(2007), 4, 291–296.

[13] Paul B., Rawat K., Banerji P.: *Dramatic enhancement of thermoelectric power factor in PbTe: Cr co-doped with iodine*. Appl. Phys. Lett. **98**(2011), 26, 262101.

[14] Hsu K. F. et al.: *Cubic AgPb(m)SbTe(2+m): Bulk thermoelectric materials with high figure of merit*. Science **303**(2004), 5659, 818–821.

[15] Lee H.S.: *Thermal Design: Heat Sinks, Thermoelectrics, Heat Pipes, Compact Heat Exchangers and Solar Cells*. Wiley and Sons, New Jersey 2010.

[16] Zhua N., Matsuurab T., Suzukib R., Tsuchiyaa T.: *Development of a small solar power generation system based on thermoelectric generator*. Energy Procedia **52**(2014), 651–658.

archives
of thermodynamics
Vol. **38**(2017), No. 4, 15–28
DOI: 10.1515/aoter-2017-0022

Modeling of pressure drop during refrigerant condensation in pipe minichannels

MAŁGORZATA SIKORA*
TADEUSZ BOHDAL

Koszalin University of Technology, Faculty of Mechanical Engineering,
Racławicka 15, 75-900 Koszalin

Abstract Investigations of refrigerant condensation in pipe minichannels are very challenging and complicated issue. Due to the multitude of influences very important is mathematical and computer modeling. Its allows for performing calculations for many different refrigerants under different flow conditions. A large number of experimental results published in the literature allows for experimental verification of correctness of the models. In this work is presented a mathematical model for calculation of flow resistance during condensation of refrigerants in the pipe minichannel. The model was developed in environment based on conservation equations. The results of calculations were verified by authors own experimental investigations results.

Keywords: Minichannels; Pressure drop; Refrigerant; Condensation

Nomenclature

A	–	heat transfer area, m^2
B	–	correction factor
C	–	wetted perimeter, m
c_p	–	specific heat, J/kg K
d	–	minichannel internal diameter, m
d_h	–	hydraulic diameter, m

*Corresponding Author. Email malgorzata.sikora@tu.koszalin.pl

f	–	Fanning coefficient
G	–	mass flux density, kg/m^{2}s
g	–	gravity acceleration, m/s^2
h	–	enthalpy, kJ/kg
L	–	length, m
$\dot{m}$	–	mass flow rate, kg/s
p	–	pressure, kPa, Pa
$\Delta p/L$	–	pressure drop per unit minichannel length, kPa/m
r	–	evaporating enthalpy, kJ/kg
s	–	slip
T	–	temperature, $^\circ$C
t	–	time, s
w	–	velocity, m/s
x	–	vapor quality
q_w	–	heat flux density, W/m^2
Pr	–	Prandl number, $\mathrm{Pr}_l = \frac{c_p \cdot \mu_l}{\lambda_l}$
Re	–	Reynolds number, $Re_l = \frac{G \cdot d}{\mu_l}$
z	–	lenght, m

Greek symbols

β	–	channel inclination angle
δ_H	–	thickness of the hydraulic boundary sublayer, m
φ	–	void fraction
λ	–	heat conductivity coefficient, W/m K
ρ	–	density, kg/m^3
μ	–	dynamic viscosity, kg/m s
τ_w	–	shear stress

Superscripts

H	–	hydraulic
h	–	at constant enthalpy
l	–	liquid
p	–	at constant pressure
s	–	saturation value
v	–	vapour
x	–	local value
TPF	–	two-phase flow

1 Introduction

Continuous technical progress demands the construction of highly efficient and low-energy machines and equipment. This applies to both high- and low-temperature processes. The analysis of global trends in the development of distributed energy indicates an increasing demand for miniaturized devices carrying large heat flux. There is a need for miniaturization in many

industries, including electronics, aerospace, telecommunications, medicine, microbiology, etc [11]. Ongoing work related to the improvement of existing devices and the development of new ones is underway in the power sector, as well as for refrigeration and air conditioning applications. There are high hopes associated with the creation and production of highly efficient cogeneration mini electric stations that can produce both electricity and thermal energy for the needs of small, individual customers [14,15]. Advanced work on the implementation of a high efficient mini refrigeration system that can be used to cool the processor for high performance computing is also underway [19]. Thermodynamic cycles, in accordance with the second law of thermodynamics, can be used to complimentary two thermal effects, i.e., the effect of heating or cooling. An important element of these installations is the presence of mini heat exchangers (evaporators and condensers). The use of the refrigerant phase transformations in these situations is essential. However, there is a need to intensify the heat exchange. One of the passive methods of convection heat transfer process intensification, from the side of the working fluid, is to reduce the diameter of the channels in which the refrigerant flows and performs the heat exchange process [16,21]. The measure of the intensification effectiveness is the increase of the heat transfer coefficient value. However, this is associated by an increase of flow resistance. In the case of minichannels, this raises a certain calculation problem in the design of mini heat exchangers [5,6]. It should be noted that, in the market, there are new types of refrigerants that have different physical and chemical properties, which complicate the calculation procedures.

In recent years, the interest as well as the number of published studies concerning the thermal and flow processes in mini heat exchangers, where the channels used have a smaller internal diameter than conventional channels ($d_h < 3$ mm) [4,7], have both increased. There are an increasing number of studies on heat transfer and flow resistance in small diameter channels devoted to the process of condensation. The authors use two methods to develop experimental studies. The first is to adapt the correlation verified for conventional channels and apply it to minichannels. The second method is to develop new correlation and computational models based on theoretical or experimental studies performed using minichannels. Correlations useful in the calculation of the heat transfer during condensation in the conventional channel, and applicable for minichannels, include: Akers *et al.* [1,2], Dobson and Chato [7], Shah [18], Cavallini and Zecchin [8], Tang *et al.* [21], Thome *et al.* [22,23], Tandon *et al.* [20], Moser *et al.*

[18], and Wilson *et al.* [25]. When using any correlation concerning condensation in minichannels, one must always refer to the source material of its origin and compare the parameters of the process and the scope of its verification.

For calculation of the frictional pressure drop, two calculation models, i.e., homogeneous and separated, are used in practice for both the conventional channels and minichannels. The separated model proposes the splitting of two calculation methods: a method of Lockhart-Martinelli [13] and a method due to Friedel [10]. In fact, modifications of these correlations describing the friction pressure drop and the results based on these methods embasked in two directions, i.e., to better define the constant C in the Lockhart-Martinelli equation or determination, usually through the experimental investigations of the real extent of a two-phase correction coefficient Φ_l^2 of resistance. With respect to the minichannels, the correlations due to Mikielewicz *et al.* [16], Mishima and Hibiki [17], Tran *et al.* [24], Lee and Lee, [12], Zhang and Webb [27] or Zhang *et al.* [26] should be acknowledged. Also deserving acknowledgement of confidence are the correlations of Cavallini and Garimella, which have been documented on a theoretical basis as well as tested experimentally.

There is a need for further experimental and theoretical research in the area of refrigerant transformations in minichannels. This study concerns the physical and mathematical modeling of ecological refrigerant condensation in pipe minichannels of compact heat exchangers. The model was developed in MATLAB environment based on conservation equations.

2 Numerical modeling

Mathematical modeling using numerical methods allows for calculation of a number of characteristic sizes, including thermal and flow parameters, heat transfer coefficients, and pressure drop along the channel where refrigerants condensate. For several years, researchers all over the world have conducted studies that aim to better understand the mechanism of this process and attempted to develop more accurate theoretical models. Currently, there are only a few proposed models for the condensation of refrigerants in minichannels that are based on reasonable theoretical rules. Moreover, none of them describe the process for a sufficiently large range of parameters. The below authors try to describe the process of refrigerants in a straight axial pipe minichannel. The two-phase system with

a single component (liquid or gas) is treated as a continuous medium, and the laws of energy, momentum and mass conservation are used to describe the phenomenon. The continuous medium is characterized by parameters describing the two-phase system, such as the two-phase mixture density, void fraction, and vapor quality. In accordance with industry practices, a one-dimensional model, in which the physical quantities are averaged over a cross section of the channel (for average speed, average pressure, average temperature, etc.), is used. The proposed homogeneous model (from non-slip class of models) allows for determination of the values of the basic condensation process parameters, the flow resistance and the heat transfer coefficient over the pipe minichannel length.

3 Assumptions of the model

In the proposed model, authors used the following assumptions:

1) straight axial channel is inclined at an angle β relative to the level of a two-phase mixture flows one component of the saturation temperature T_s, the speed of the two phases are equal (slip $s = 1$);
2) fluid flow is turbulent;
3) mass flux density is G;
4) mixture has a vapor quality, x, and void fraction, φ;
5) on the whole length of the channel, the constant heat flux is applied;
6) saturated vapor of the refrigerant is supplied to the minichannel;
7) refrigerant condensation process is conducted inside the minichannel. The process is thermally and hydraulically stable in time, that means $\frac{\partial T}{\partial t} = 0$;
8) longitudinal heat conduction is omitted $\frac{\partial^2 T}{\partial z^2} = 0$.

In the model were used conservation equations in the following forms:
– mass conservation equation:

$$\frac{\partial \rho}{\partial t} + w\frac{\partial \rho}{\partial z} + \rho\frac{\partial w}{\partial \rho} = -\rho w\frac{1}{A}\frac{\partial A}{\partial z}\,, \tag{1}$$

– energy conservation equation:

$$\rho\frac{\partial h}{\partial t} - \frac{\partial p}{\partial t} + \rho w\frac{\partial h}{\partial z} - w\frac{\partial p}{\partial z} = \frac{\tau_w w C}{A} + \frac{q_w C}{A}\,, \tag{2}$$

– momentum conservation equation:

$$\rho\frac{\partial w}{\partial t}+\rho w\frac{\partial w}{\partial z}=\rho g\cos\beta-\frac{\tau_w C}{A}-\frac{\partial p}{\partial z}\,. \tag{3}$$

The equation of state has the form of

$$\rho=\rho(h,p). \tag{4}$$

If the system is in steady state, the mass conservation equation (1) is in the 'integral of mass' form:

$$w\rho\,A=G\,A=\dot{m}=\text{const}\,. \tag{5}$$

After taking this into account the equation take the form:

$$-\frac{dp}{dz}+\rho\frac{dh}{dz}=\frac{\tau_w C}{A}+\frac{q_w\rho C}{\dot{m}}\,, \tag{6}$$

$$\left(1-\frac{\dot{m}D_1}{A^2\rho^2}\right)\frac{dP}{dz}-\frac{\dot{m}D_2}{A^2\rho^2}\frac{dh}{dz}=\frac{\dot{m}}{A^3\rho dz}+g\rho\cos\beta-\frac{\tau_w C}{A}\,, \tag{7}$$

where

$$D_1=\left(\frac{\partial\rho}{\partial p}\right)_h\,,\quad D_2=\left(\frac{\partial\rho}{\partial h}\right)_p\,. \tag{8}$$

It is a system of ordinary differential equations containing the equations of energy balance, momentum and mass transfer equation of state (7) and the closure equations describing the heat flux density, q_w, and shear stress, τ_w, on the inner wall of the channel.

3.1 The closing equations

Correlation describing the shear stress, τ_w, on the inner wall of the channel was assumed as the closure equation:

$$\tau_w=\frac{\mu_l\,w_l}{w_H}\,. \tag{9}$$

Equation (10) allows to calculate the frictional pressure drop which is balanced by shear stress on the wall of the channel:

$$\left[\frac{dp}{dz}\right]_{TPF}=\frac{C}{A}\,\tau_w\,, \tag{10}$$

where: C – wetted perimeter, $C = \pi d_h$, d_h – minichannel hydraulic diameter, A – cross sectional area, τ_{in} – shear stress.

The thickness of the hydraulic boundary sublayer, δ_H, defines the relationship

$$\delta_H = \frac{2\mu_l}{f\, w_l\, \rho_l} \,, \tag{11}$$

where f is the Fanning coefficient defined for transitional flow by the formula

$$f = \frac{0.316}{4}\,\mathrm{Re}^{-0.25} \,. \tag{12}$$

Velocity of the liquid phase can be calculated from the relationship

$$w_l = \frac{G}{\rho_l}\left(\frac{1-x}{1-\varphi}\right) \,, \tag{13}$$

where: G – mass flux density, ρ_l – density of the liquid phase, x – vapor quality, φ – void fraction.

After substitution of Eqs. (12) and (13) to formula (11) obtained

$$\left[\frac{dp}{dz}\right]_{TPF} = 0.16\,\frac{\mathrm{Re}^{-0.25}\,(w\rho)}{d_h\,\rho_l}\left(\frac{1-x}{1-\varphi}\right) \,. \tag{14}$$

The vapor quality x is determined from the following equation:

$$x_n = x_{n-1} - \frac{q_w}{G\,r} \,, \tag{15}$$

where r is the latent heat of the two-phase change process.

The homogeneous model assumes that the gas and liquid phases do not interact with each other in any way, which causes the divergence of the calculated results based on this model from the experimental results. In fact, there is a movement resulting from the turbulence of the gas phase. This causes the increase of shear stresses. For this reason, shear stresses were corrected by the correcting factor B:

$$\tau_w{}' = \tau_w\, B, \tag{16}$$

where

$$B = 2(1-x)^{0.8} + 0.008\,\mathrm{Re}^{0.75}\mathrm{Pr}^{-2.5} \,. \tag{17}$$

The value of coefficient B was determined by the method of matching the results of theoretical calculations to experimental results. After taking into account Eq. (16), the relationship for the friction pressure drop is obtained *via*

$$\left[\frac{dp}{dz}\right]_{TPF} = 0.16\,\frac{\mathrm{Re}^{-0.25} w\rho}{d_h\,\rho_l}\left(\frac{1-x}{1-\varphi}\right) B \,. \tag{18}$$

4 The modeling result

Based on the proposed model, describing the process of refrigerants condensation in pipe minichannels carried out were numerical calculations. It was possible to determine the flow resistance, $\Delta p/z$, change of pressure, p/z; refrigerant temperature, T, temperature of the minichannel wall, T_w, the vapor quality, x, and the void fraction, φ, in the refrigerant flow. Figures 1–6 show an example of the theoretically calculated results of the condensation parameters of the R134a refrigerant in channels with an internal diameter $d_h = 1.94$ mm and 0.64 mm. Calculations were performed for the following parameters: d_h= 1.94 mm, saturation temperature at the inlet to the channel $T_s = 42$ °C, heat flux $q = 30000$ W/m^2, mass flux $G = 451$; 376; 282, and 188 kg/m^{2}s, for $d_h = 0.64$ mm parameters were as follows: $T_s = 42.5$ °C, $q = 30000$ W/m^2 and $G = 950$; 691 and 431 kg/m^{2}s.

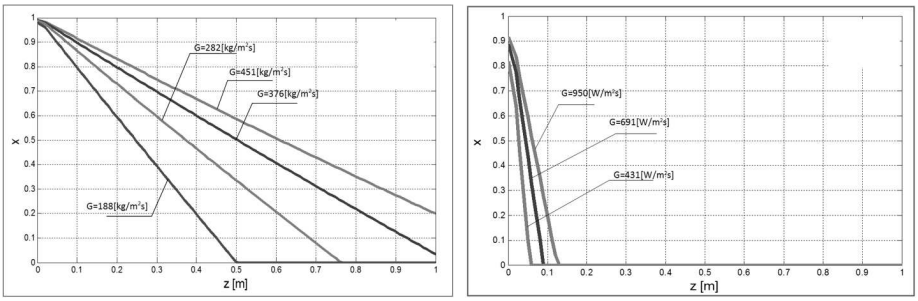

a) b)

Figure 1: The results of theoretical calculations of vapor quality, x, changes on the length of the channel, for selected mass fluxes G: a) $d_h = 1.94$ mm, b) $d_h = 0.64$ mm.

Conducted calculations show that, with the decrease of vapor quality, x, the void fraction, φ, temperature, T, and pressure, p, of the refrigerant all decrease. On the other hand the flow resistance increase, from the beginning of the condensation to the development of the process. When the content of the liquid phase in the flow increases, the flow resistance decreases rapidly to a value tens of times lower than the maximum.

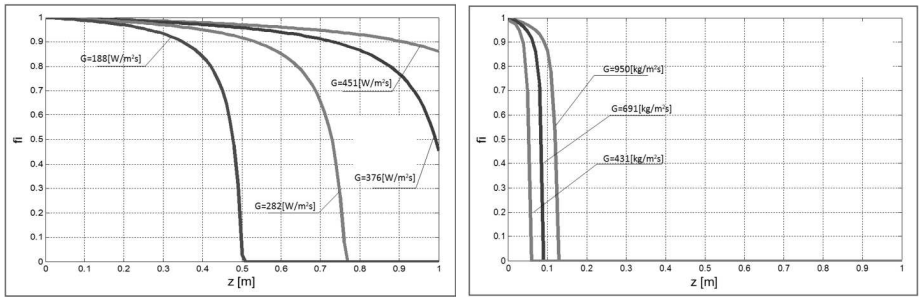

a) b)

Figure 2: Results of theoretical calculations of the void fraction, φ, changes on the channel length z, for few mass fluxes G: a) $d_h = 1.94$ mm, b) $d_h = 0.64$ mm.

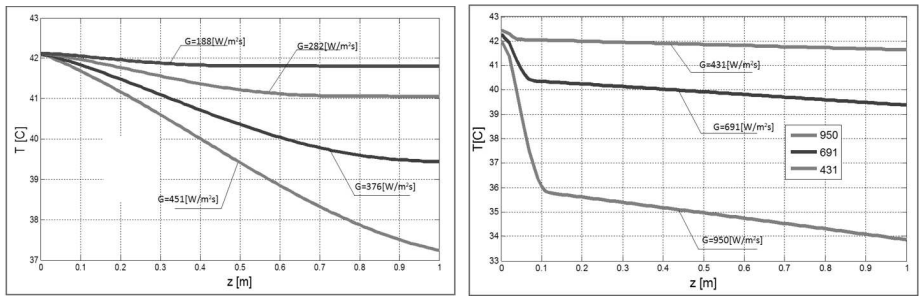

a) b)

Figure 3: Results of theoretical calculations of the refrigerant temperature, T, changes on the length of the channel z, for few mass fluxes G: a) $d_h = 1.94$ mm, b) $d_h = 0.64$ mm.

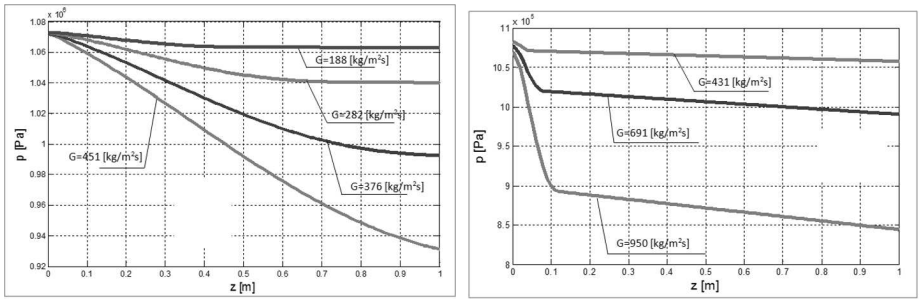

a) b)

Figure 4: Results of theoretical calculations of the refrigerant pressure, p, changes on the length of the channel z, for few mass fluxes G: a) $d_h = 1.94$ mm, b) $d_h = 0.64$ mm.

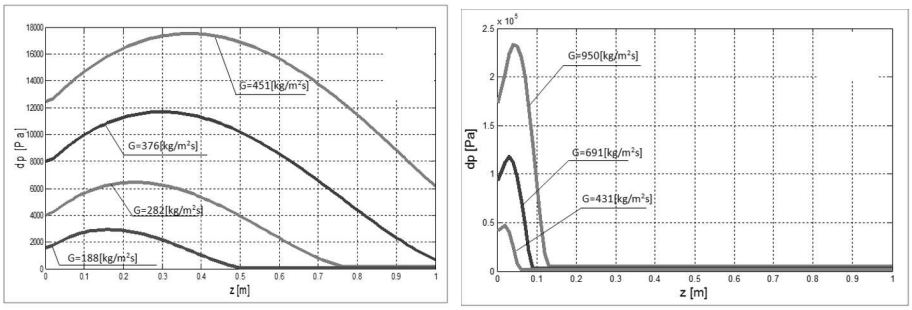

a) b)

Figure 5: Results of theoretical calculations of the refrigerant flow resistance, dp, changes on the length of the channel, z, for few mass fluxes G: a) $d_h = 1.94$ mm, b) $d_h = 0.64$ mm.

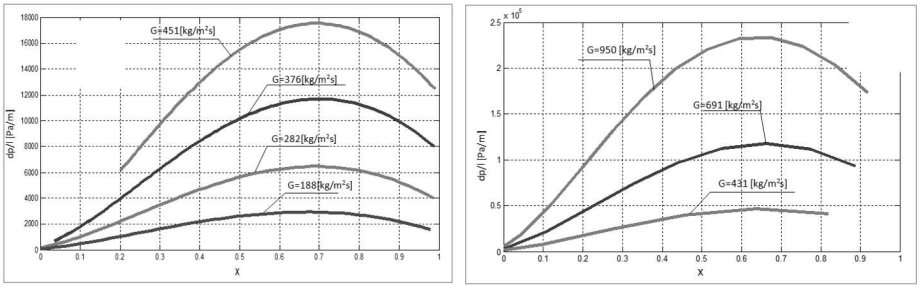

a) b)

Figure 6: Dependence of theoretical refrigerant flow resistance, dp/l, on the vapor quality, x, for few mass flux densities G; a) $d_h = 1.94$ mm, b) $d_h = 0.64$ mm.

5 Comparison of the results of model calculations with experimental results

Figure 7 presents a comparison between the computational model of the flow resistance, $\Delta p/L$, dependence on the vapor quality, x, and the experimental results. As observed, the results of calculations by the model satisfactorily describe the flow resistance during condensation of refrigerants, but, if vapor quality decreases below the value of 0.2, the discrepancy between the mathematical model and the experimental results increases. This is caused by the occurrence of a small amount of the gas phase and

a significant decrease in the interaction of the refrigerant phases. Figure 8 shows a comparison between the calculated results of the vapor quality on the length of the channel and the experimental results.

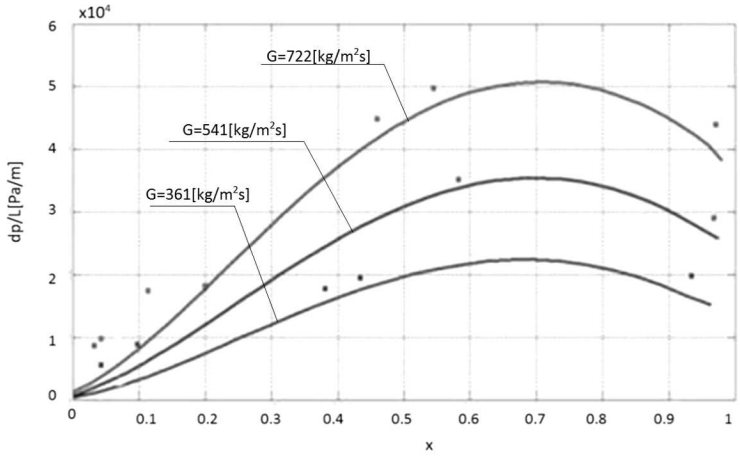

Figure 7: Comparison of calculated by the model flow resistance, dp/l, and values from experimental investigations, during condensation of R134a refrigerant in pipe minichannel with an internal diameter $d_h = 1.4$ mm, with changes of the vapor quality, x, in the whole range, for few mass fluxes, G.

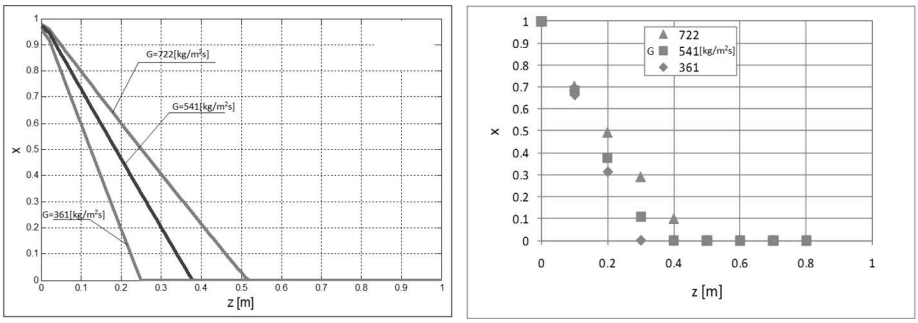

a) b)

Figure 8: Summary of the vapor quality x changes during condensation of R134a refrigerant in pipe minichannel with internal diameter $d_h = 1.4$ mm on the length of the channel, for few mass fluxes, G: a) according to theoretical calculations, b) according to the experimental tests.

Figure 9 shows a comparison between the modeling results and the experimental results for refrigerant R134a, R404A and R407C condensation.

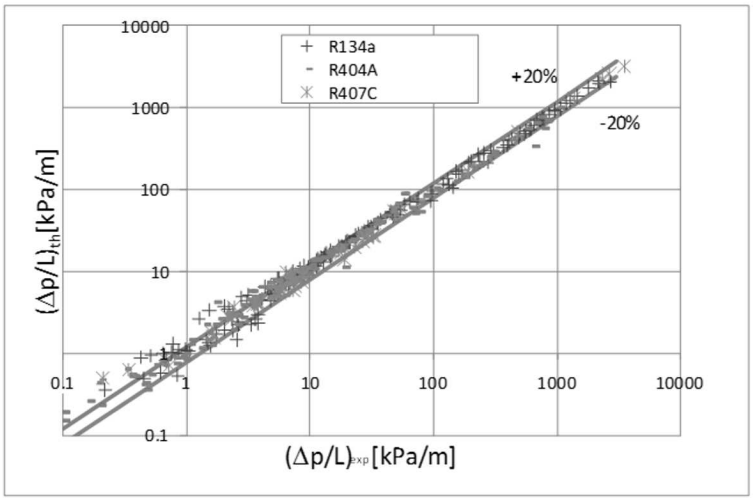

Figure 9: Comparison of modeling results with the experimental studies' results of condensation in the pipe minichannels for refrigerants: R134a, R404A and R407C in terms of flow resistance.

This comparison shows that 80% of the measuring points are in the range of ±20%. It can be concluded that the proposed model appropriately describes the experimental results with an accuracy of ±20% for condensing in a wide range of changes in process parameters. A model is used to determine the value of parameters describing the condensation process of the refrigerant in the pipe minichannel, including the flow resistance values. It can be used in engineering work to design compact heat exchangers.

6 Conclusions

1. Authors' own model describing the refrigerant condensation process in pipe minichannels was presented. In accordance with industry practices, a one-dimensional model, in which the physical quantities are averaged over a cross-section of the channel, was used. The proposed homogeneous model allows us to determine the values of the basic parameters of the condensation process, including the flow resistance over the length of the pipe minichannel. The proposed model recognizes the following important considerations: during the two-phase refrigerant flow in the pipe minichannels are flow resistances, the values of which are many times higher than those obtained in the

single-phase flow at the same flow rate, and the vapor phase, occurring during the condensation process, causes turbulence in this flow, which affects the growth of the flow resistance volume.

2. The model adequately describes the refrigerants condensation process in pipe minichannels. Obtained results of the flow resistance calculations from the model were compared with experimental results. Their compatibility was satisfactory in the range of ±20%.
3. It is proposed to use a developed model for the calculation of characteristic parameters of the condensation process of refrigerants R134a, R404A, R407C in pipe minichannels with an internal diameter of 0.64–3.3 mm. The value ranges of the process parameters should be: mass flux density 50–1000 kg/(m^2 s), saturation temperature 30–50 °C, the vapor quality 0–1.

Received 2 October 2017

References

[1] Akers W., Deans O.K., Crosser O.K.: *Condensation heat transfer within horizontal tubes*. Chem. Eng. Progr. **54**(1958), 89–90.

[2] Akers W., Deans O.K., Crosser O.K.: *Condensation heat transfer within horizontal tubes*. Chemical Engineering Progress Symp. **55**(1959), 171–176.

[3] Bohdal T., Charun H., Sikora M.: *Comparative investigations of the condensation of R134a and R404A refrigerants in pipe minichannels*. Int. J. Heat Mass Tran. 54(2011), 1963–1974.

[4] Bohdal T.: *Investigations of environmentally friendly refrigerants phase changes in minichannels*. Annual Set the Environment Protection **15**(2013), 107–126.

[5] Bohdal T., Charun H., Sikora M.: *Empirical study of heterogeneous refrigerant condensation in pipe minichannels*. Int. J. Refrig. **59**(2015), 210–223.

[6] Bohdal T., Widomska K., Sikora M.: *The analysis of thermal and flow characteristics of the condensation of refrigerant zeotropic mixtures in minichannels*. Arch. Thermodyn. **37**(2016), 2, 41–69.

[7] Cavallini A., Del Col D., Matkovic M., Rossetto L.: *Frictional pressure drop during vapour-liquid flow in minichannels: Modelling and experimental evaluation*. Int. J. Heat Fluid Fl. **30**(2009), 131–139.

[8] Cavallini A., Zecchin R.: *A dimensionless correlation for heat transfer in forced convection condensation*. In: Proc. 6th Int. Heat Transfer Conf., Tokyo, **3**(1974), 309–313.

[9] Dobson M.K., Chato J.C.: *Condensation in smooth horizontal tubes*. J. Heat Trans-T ASME **120**(1998), 1, 193–213.

[10] Friedel L.: *Improved friction pressure drop correlation for horizontal and vertical two-phase pipe flow*. European Two-Phase Flow Group Meeting, Ispra 1987, Paper 2.

[11] Kharangate C. R., Mudawar I.: *Review of computational studies on boiling and condensation*. Int. J. Heat Mass Tran. **108**(2017), 1164–1196.

[12] Lee H.J., Lee S.Y.: *Pressure drop correlations for two-phase flow within horizontal rectangular channels with small heights*. Int. J. Multiphas. Flow **27**(2001), 783–796.

[13] Lockhart R.W.: Martinelli R.C.: *Proposed correlation of data for isothermal two-phase, two-component flow in pipes*. Chem. Eng. Prog. **45**(1949), 1, 39–48.

[14] Mikielewicz J.: *Domestic combined micro heat and power plant*. Annual Set of the Environment Protection **11**(2009), 25–38.

[15] Mikielewicz J., Mikielewicz D.: *The dynamics of heat exchangers and instabilities in ORC circulation*. Annual Set of the Environment Protection **13**(2011), 425–440.

[16] Mikielewicz D., Wajs J., Andrzejczyk R., Klugmann M.:*Pressure drop of HFE7000 and HFE7100 during flow condensation in minichannels*. Int. J. Refrig. **68**(2016), 226–241.

[17] Mishima K., Hibiki T.: *Some characteristics af air-water flow in small diameter vertical tubes*. Int. J. Multiphas. Flow **22**(1996), 703–712.

[18] Moser K., Webb R.L., Na B.: *A new equivalent Reynolds number model for condensation in smooth tubes*. J. Heat Trans.-T ASME **120**(1998), 410–417.

[19] Shah M.M.: *A general correlation for heat transfer during film condensation inside pipes*. Int. J. Heat Mass Tran. **22**(1979), 547–556.

[20] Tandon T.N., Varrna H.K., Gupta C.P.: *New flow regimes map for condensation inside horizontal tubes*. J. Heat Trans.-T ASME **104**(1982), 4, 763–768.

[21] Tang L.: *Empirical Study of New Refrigerant Flow Condensation Inside Horizontal Smooth and Micro-Fin Tubes*. University of Maryland, College Park, 1997.

[22] Thome J.R., El Hajal J., Cavallini A.: Condensation in horizontal tubes, part 1: two – phase flow pattern map. Int. J. Heat Mass Tran. **46**(2003), 18, 3349–3363.

[23] Thome J.R., El Hajal J., Cavallini A.: *Condensation in horizontal tubes, part 2: new heat transfer model based on flow regimes*. Int. J. Heat Mass Tran. **46**(2003), 18, 3365–3387.

[24] Tran T.N., Chyu M.C., Wambsganss M.W., France D.M.: *Two-phase pressure drop of refrigerants during flow boiling in small channels*. Int. J. Multiphas. Flow **26**(2000), 11, 1739–1754.

[25] Wilson M.J., Newell T.A., Chato J.C., Ferreira C.A.: *Refrigerant charge, pressure drop and condensation heat transfer in flattened tubes*. Int. J. Refrig. **26**(2003), 4, 442–451.

[26] Zhang W., Hibiki T., Mishima K.: *Correlations of two-phase frictional pressure drop and void fraction in mini-channel*. Int. J. Heat Mass Tran. **53**(2010), 453–465.

[27] Zhang M., Webb R.L.: *Correlation of two-phase friction for refrigerants in small-diameter tubes*. Exp. Therm. Fluid Sci. **25**(2001), 3-4, 131-139.

archives
of thermodynamics
Vol. **38**(2017), No. 4, 29–51
DOI: 10.1515/aoter-2017-0023

Modeling of KERENA emergency condenser

RAFAŁ BRYK[a,b*]
HOLGER SCHMIDT[b]
THOMAS MULL[b]
THOMAS WAGNER[b]
INGO GANZMANN[b]
OLIVER HERBST[b]

[a] Warsaw University of Technology, Institute of Heat Engineering, Nowowiejska 21/25, 00-665 Warszawa, Poland

[b] AREVA GmbH, Paul-Gossen-Strasse 100, 91052 Erlangen, Germany

Abstract KERENA is an innovative boiling water reactor concept equipped with several passive safety systems. For the experimental verification of performance of the systems and for codes validation, the Integral Test Stand Karlstein (INKA) was built in Karlstein, Germany. The emergency condenser (EC) system transfers heat from the reactor pressure vessel (RPV) to the core flooding pool in case of water level decrease in the RPV. EC is composed of a large number of slightly inclined tubes. During accident conditions, steam enters into the tubes and condenses due to the contact of the tubes with cold water at the secondary side. The condensed water flows then back to the RPV due to gravity. In this paper two approaches for modeling of condensation in slightly inclined tubes are compared and verified against experiments. The first approach is based on the flow regime map. Depending on the regime, heat transfer coefficient is calculated according to specific semi-empirical correlation. The second approach uses a general, fully-empirical correlation. The models are developed with utilization of the object-oriented Modelica language and the open-source OpenModelica environment. The results are compared with data obtained during a large scale integral test, simulating loss of coolant accident performed at Integral Test Stand Karlstein (INKA). The comparison shows a good agreement.

*Corresponding Author. Email rafal.bryk@areva.com

Due to the modularity of models, both of them may be used in the future in systems incorporating condensation in horizontal or slightly inclined tubes. Depending on his preferences, the modeller may choose one-equation based approach or more sophisticated model composed of several exchangeable semi-empirical correlations.

Keywords: Condensation; Kerena; Emergency condenser; Modelica; OpenModelica

Nomenclature

A	–	cross section
D	–	internal diameter
e	–	Euler constant
h	–	specific enthalpy
j^*D	–	dimensionless steam velocity
l	–	length of a single volume
g	–	gravitational acceleration
G	–	mass flux
$\dot{m}$	–	mass flow
p	–	pressure
Pr	–	Prandtl number
$\dot{q}$	–	heat flux
Q	–	heat delivered to a volume
Ra	–	Rayleigh number
Re	–	Reynolds number
t	–	time
T^+	–	dimensionless temperature
v^*	–	steam velocity at the phases interface
w	–	averaged mass flow in a volume
x	–	steam quality
z	–	liquid water level

Greek symbols

α	–	heat transfer coefficient
δ^+	–	dimensionless condensate layer thickness
ε	–	void fraction
ζ	–	friction corrective coefficient
θ	–	inclination of the emergency condenser tubes
λ	–	thermal conductivity
Λ	–	friction coefficient
μ	–	dynamic viscosity
ν	–	kinematic viscosity
ρ	–	density
σ	–	surface tension

Subscripts

a	–	pressure drop due to acceleration
av	–	average value

Ann_lam	–	annular laminar flow
Ann_tur	–	annular turbulent flow
Ann_wave	–	Annular wavy flow
av	–	average value
BSP_lam	–	bubble, plug, slug flow laminar
BSP_tur	–	bubble, plug, slug flow turbulent
$crit$	–	critical value of Reynolds number
f	–	pressure drop due to friction
Fi	–	film
h	–	derivative with constant enthalpy
j	–	number of node
k	–	number of volume
L	–	liquid
Nu	–	according to Nusselt
mix	–	mixture
p	–	derivative with constant pressure
s	–	saturation
SPh	–	single phase
$Spray$	–	spray flow regime
$Strat$	–	stratified flow regime
TP	–	two phase
V	–	vapour
w	–	wall

1 Introduction

Currently, nuclear power plants provide over 11% of the world's electricity. In 30 countries all over the world, there is 448 operational reactors, 76 of which are boiling water reactors (BWR) [1]. A vast majority of the operational BWRs are generation II reactors. An important system for a proper reactor core protection is the emergency core-cooling system. Its purpose is to prevent the core from overheating either by maintaining the water level in the reactor pressure vessel (RPV) at an appropriate level or by flooding the core with coolant, when maintaining of the water level is not possible.

In general, BWRs under operation are equipped with two different types of emergency cooling systems. These are: high-pressure systems and low-pressure systems.

The purpose of high-pressure systems is to inject substantial quantities of water into the reactor when the water level decreases and the reactor is still at high pressure. The system is usually powered by steam from the reactor. Should the water level could not be maintained with the system, the next systems respond.

Low-pressure systems are activated after depressurization of the RPV.

These systems have larger capacity than the high-pressure systems and the coolant is supplied from several, redundant power sources. Thus, the low-pressure core spray system and low-pressure coolant injection system may be distinguished. The first one delivers water from the top of the RPV. The system collapses steam above the core, what – apart from cooling – has also an impact on RPV pressure reduction. The second low-pressure system consists of several pumps and it is designed as an emergency mode of the residual heat removal (RHR) system.

All the above systems are proven and verified during decades of operation of existing power plants. However, they need an external power supply. The most often, this power is delivered from a turbine, combustion engine or an electrical motor. The modern approach for nuclear reactors design is to avoid the necessity of external power supply and to equip reactors with passive safety systems. These systems are automatically triggered and they function according to basic laws of physics such as gravity and natural convection. By combining these passive systems with proven active systems, the advanced reactors of generation III/III+ are undoubtedly the safest ever developed.

In order to elaborate the BWR product line, AREVA in collaboration with German nuclear utilities and with support from European partners developed a new BWR design – KERENA – a medium-capacity boiling water reactor [2].

Figure 1 shows a cross section through the containment of KERENA. The reactor utilizes several innovative passive safety systems which ensure safe depressurization and heat removal in case of emergency or accidents, including loss of coolant accident (LOCA). The main components of KERENA passive safety features are containment cooling condenser (CCC), emergency condenser (EC), passive pressure pulse transmitters (PPPT) and passive core flooding system. These systems utilize basic physical laws such as gravity and free convection. Therefore, in order to operate them, there is no need for an external power supply and additional devices like pumps. This in turn leads to strong reduction of costs during construction of the plant.

In order to examine performance of the passive systems, a dedicated test facility was built at the Components Testing Department of AREVA in Karlstein, Germany. The Integral Test Facility Karlstein (INKA) represents the KERENA containment with a volume scaling of 1:24. Components heights and levels over the ground are kept in the full scale. The test

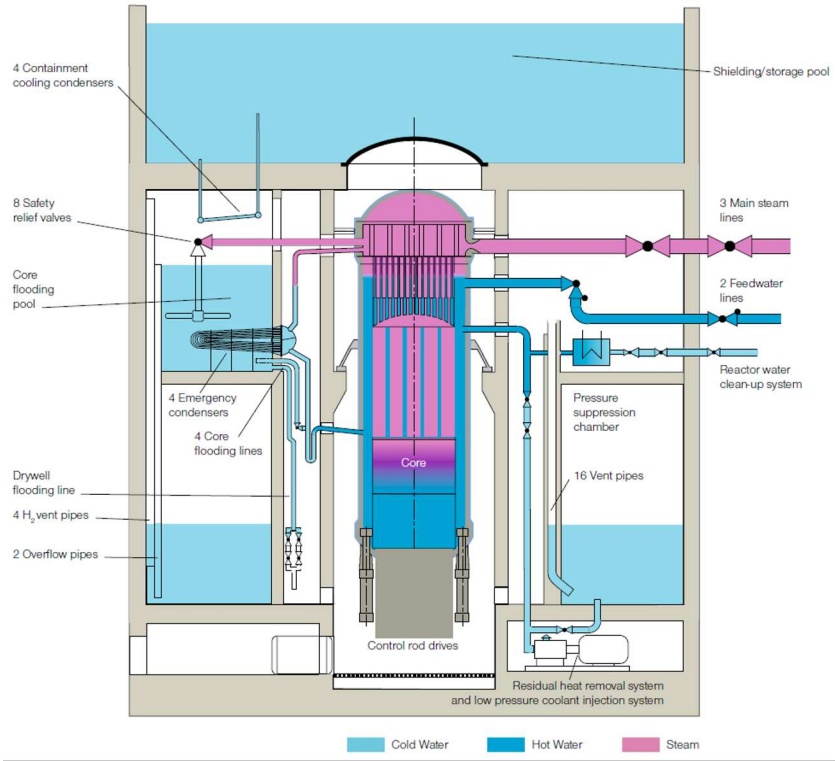

Figure 1: Cross section through the containment of KERENA.

rig setup allows to investigate both, each component individually and the whole system during integral tests. For the purpose of testing the integral system, INKA is equipped with several large vessels corresponding to individual pools and vessels of KERENA. The reactor pressure vessel (RPV) is represented by the steam accumulator of the Karlstein large valve test facility GAP (*Gross Armatures Prüfstand*). The vessel has a storage capacity of 1/6 of the KERENA RPV. In order to simulate the decay heat of the core, the vessel is fed with steam by Benson boiler with maximum power output of 22 MW. The vessel is designed for operation pressure up to 16 MPa. Compartments of the KERENA RPV are represented by separate vessels: flooding pool vessel, pressure suppression pool vessel and drywell vessel. An additional tank is used as a representation of shielding/storage pool vessel.

Due to the appropriate instrumentation concept and the density of sen-

sors, data obtained during experiments performed at the facility may be utilized for validation of thermal-hydraulic codes. Therefore, measurements collected during one of the tests performed in the framework of the integral experimental and analytical safety cases for design-basis accidents featuring passive systems were used to validate condensation models developed in open source OpenModelica Connection Editor environment utilizing the Modelica language.

Modelica is a non-proprietary, object-oriented, equation-based language to conveniently model complex physical systems [3]. There are several environments which utilize the language. Models described in this paper were developed with OpenModelica Connection Editor – an open-source environment developed by Open Source Modelica Consortium for industrial and academic usage [4]. Modelica is equipped with a large multi-domain, open-source library. Components encapsulated in the library may be developed, enhanced and their features may be inherited by other objects.

2 Operation of KERENA emergency condenser

The main purposes of the Emergency Condenser is heat removal and depressurization of the RPV in abnormal conditions. The principle of the EC operation is presented in Fig. 2.

The emergency condenser is composed of a large number of slightly inclined tubes. The tubes are submerged in the core flooding pool and they are filled with water during regular operation of the plant. Should the water level in the RPV decrease, the water drains from the tubes and the steam from the RPV enters the EC tubes. Due to the contact of tube walls with the cold water at the secondary side in the core flooding pool, heat transfer occurs leading to condensation of steam in tubes. Since the tubes of the emergency condenser are slightly inclined, the condensate flows back to the RPV due to gravity. The emergency condenser is connected to the RPV without any isolating elements and it comes into action automatically without any need for electric power. Thus, the device is operated according to the natural law of communicating vessels.

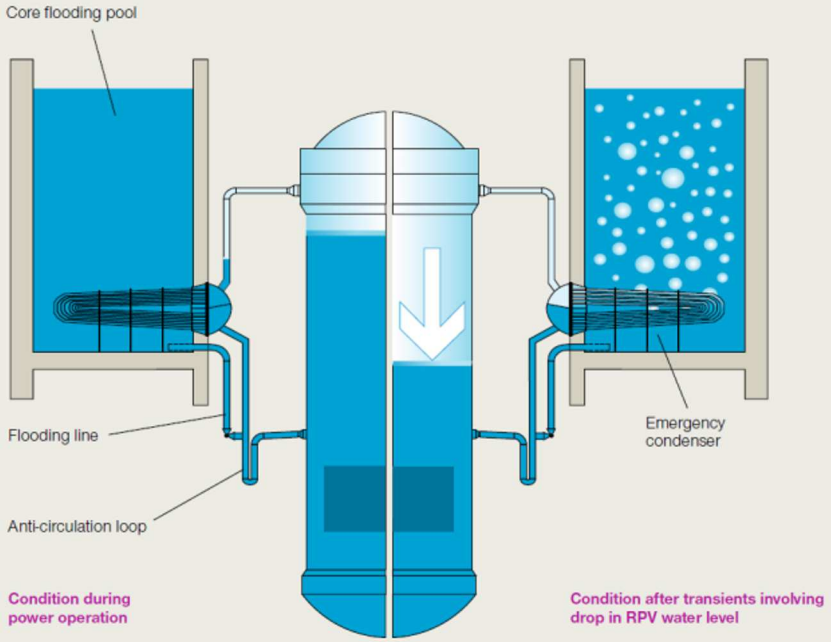

Figure 2: Operation scenarios of the emergency condenser.

3 Models development

3.1 System description and governing equations

The analysed system was a straight pipe slightly inclined to the horizontal orientation and a vessel filled with liquid water up to a certain level. The volume over the water surface was filled with the ideal gas.

The tube inclination was 1.3% and its length was 10.8 m. The inner diameter was 48.3×2.5 mm. The volume of the vessel was 210 m^3 and its diameter was 5 m. At the beginning, the water level in the vessel was 7.8 m.

The flow through the pipe is governed by the mass, energy and momentum conservation equations, as one-dimensional, partial differential equations. In the vessel the liquid water phase and ideal gas were distinguished. In the system the following assumptions were applied:

- uniform velocity is assumed on a cross section of the tube,
- longitudinal heat diffusion term in the tube is neglected,

- accumulation is considered in each control volume of the tube,
- influence of the angulation of the EC pipes is neglected,
- thermal-hydraulic properties of the fluid in the tube are calculated on the basis of pressure and enthalpy at each node,
- tube wall is assumed to have constant thermal conductivity,
- tube bundle influence is not taken into account,
- boundary conditions are assumed according to the measurements and initial conditions of the experiment,
- heat transfer coefficient at the secondary side is taken into account and calculated according to correlation for free convection in a pool of single-phase liquid water;
- liquid water in the vessel is modelled as an expandable medium so its volume increases with temperature,
- gas in the vessel is modelled as the ideal gas,
- heat transfer between liquid water and the gas is modelled as a linear function of the temperature difference between the mediums,
- there is no mass transfer between water and gas phases.

Figure 3 shows the diagram view of the object-oriented configuration of the model.

The pipe model was set up by adopting an extended version of the Flow1DFV2ph component of the Modelica ThermoPower library. The model was discretised and divided into 20 volumes. The component, in which the balance equations are discretized by means of the finite volume approach was modified by formulation of momentum balance equation for each volume instead of the whole component. This lead to more detailed description by enabling calculation of fluid properties and saturation conditions at each node taking into account pressure at a particular node. Before modification, fluid properties at each node were evaluated either with respect to inlet or outlet pressure.

The mass balance equation in each volume of the pipe is given by

$$\dot{m}_j - \dot{m}_{j+1} = Al\frac{d\rho_k}{dt} \,. \tag{1}$$

Taking pressure and specific enthalpy as state variables

$$\dot{m}_j - \dot{m}_{j+1} = Al\left[\left(\frac{\partial\rho_k}{\partial h_k}\right)_p \frac{dh_k}{dt} + \left(\frac{\partial\rho_k}{\partial p_j}\right)_h \frac{dp_j}{dt}\right] \,. \tag{2}$$

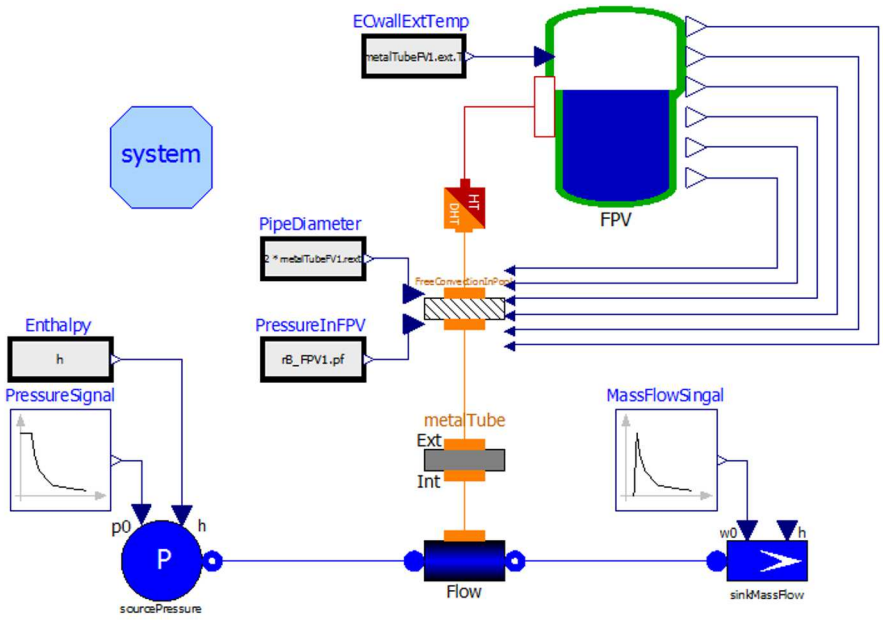

Figure 3: Diagram view of the model.

The energy balance equation in each volume of the pipe is given by

$$\dot{m}_j\, h_j - \dot{m}_{j+1}\, h_{j+1} + Q_k = Al\Big(\rho_k \frac{dh_k}{dt} - \frac{dp_k}{dt}\Big)\,. \tag{3}$$

The momentum balance equation for each volume of the pipe is given by

$$p_j - p_{j+1} = \frac{l}{A}\,\frac{dw_k}{dt} + \rho_k g l \sin\theta + \triangle p_{k,\ \ f} + \triangle p_{k,a}\,, \tag{4}$$

with acceleration and friction pressure losses for each volume given by

$$\triangle p_{k,\ a} = \frac{1}{A^2}\, {w_k}^2 \Big(\frac{1}{\rho_{j+1}} - \frac{1}{\rho_j}\Big)\,, \tag{5}$$

$$\triangle p_{k,f} = \zeta \frac{2\Lambda_k l}{DA^2\rho_k}\, w_k^2\,, \tag{6}$$

where Λ_k is calculated with Colebrook correlation:

$$\Lambda_k = \frac{0.332}{\ln\left(\frac{e}{3.7} + \frac{5.47}{\mathrm{Re}_k^{0.9}}\right)^2}\,. \tag{7}$$

In Eqs. (1)–(7) A and l stand respectively for tube cross section and length of a single volume. Subscript k denotes volume number while j stands for number of node. Subscripts p and h mean derivatives with constant pressure and enthalpy respectively.

In the flow model a replaceable module for heat transfer calculation was introduced. This allowed to call different models of heat transfer developed as separate objects.

In order to model the heat exchange, new heat transfer components were introduced so that to implement correlations expressing two approaches described in subsections 3.2 and 3.3. These models were then called in the flow model by redeclare model clause in the text view of the whole system model presented as diagrams in Fig. 3.

Additionally, a call of a function for calculation of void fraction was implemented into the standard Flow1DFV2ph component. The void fraction was calculated according to analytical heterogeneous momentum flux approach.

The Flooding Pool Vessel model was developed from basics. It takes into account expandability of water due to temperature increase and its influence on the pressure in the vessel. Properties of water in the FPV are delivered to the heat transfer component (placed between the pipe and the vessel in Fig. 3) which calculates the heat transfer coefficient at the secondary side.

In the FPV model there is no water mass flowing into or out from the vessel, so the mass conservation equation is given by

$$\rho_l A \frac{dz}{dt} + Az \frac{d\rho_l}{dt} = 0 \,, \tag{8}$$

where z is the water level. The energy balance equation for liquid in the FPV is given by

$$\rho_l V_l \frac{dh_l}{dt} - V_l \frac{dp}{dt} - p \frac{dV_l}{dt} = -Q_{surface} + Q_{EC} \,. \tag{9}$$

In the equation above, Q_{EC} is the power of EC and $Q_{surface}$ is the heat exchange between liquid water and gas given as a linear function of temperature difference.

The mass of gas is constant in the vessel and it is given by:

$$m_g = V_g \, \rho_g \,. \tag{10}$$

The energy balance for gas is given by

$$\rho_g V_g c_{pg} \frac{dT_g}{dt} = V_g \frac{dp_g}{dt} + Q_{surface} \ . \tag{11}$$

To the gas volume applies also the Clapeyron equation

$$p_g = \rho_g R T_g \ , \tag{12}$$

where R is the specific gas constant for air.

3.2 Flow regime map based model of condensation

The flow regime map based model was developed utilizing the map proposed by Tandon [9]. The model calculates the average at particular regime heat transfer coefficient by switching between several flow regime dependent semi-empirical correlations. Figure 4 illustrates different flow patterns in horizontal tube. The flow regime map, together with correlations applied in specific regime is shown in Fig. 5.

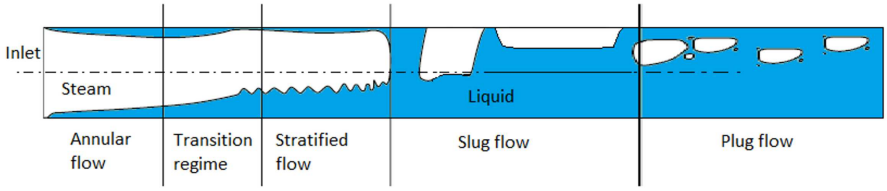

Figure 4: Flow patterns during condensation in horizontal tubes [5].

Tandon's flow regime map is based on the volume ratio of liquid and gas in a cross section area $(1 - \varepsilon)/\varepsilon$, where ε stands for the void fraction, and on the dimensionless steam velocity

$$j_D^* = \frac{xG}{[gD\rho_V (\rho_L - \rho_V)]^{0.5}} \ . \tag{13}$$

Since the EC pipes are initially filled with liquid water and due to possible single-phase condensate flow at the lower sections of the tube, an additional correlation for single phase liquid water flow was implemented into the model. Table 1 indicates all correlations and application ranges. In the table subscripts Fi and V indicate whether a variable refers to condensate film or vapour. Further details of different patterns formation development of the correlations can be found in [8–16].

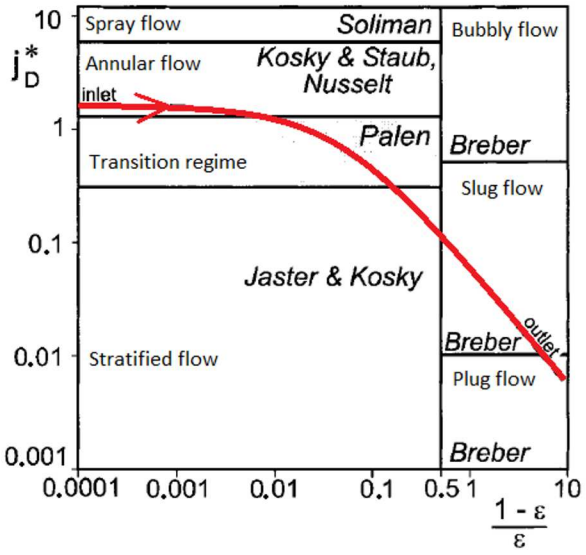

Figure 5: Tandon's flow regime map [5].

3.3 General correlation model of condensation

The implemented general correlation for condensation in horizontal tubes was developed by Shah [17]:

$$\alpha = \alpha_{SPh}\left[(1-x)^{0.8} + \frac{3.8\,x^{0.76}\,(1-x)^{0.04}}{p_r^{0.38}}\right], \tag{14}$$

$$\alpha_{SPh} = 0.023\mathrm{Re}_L^{0.8}\mathrm{Pr}_L^{0.4}\frac{\lambda}{D}\,. \tag{15}$$

The correlation was developed by analysis of a wide variety of experimental data. This includes different fluids and pipe orientations. Details of the correlation development may be found in [17].

3.4 Free convection modelling at the secondary side

In order to obtain a full picture of the performance of EC model, it is necessary to take into account the secondary side of the device. In the KERENA design, the EC tubes are submerged in the cold water of the flooding pool vessel. Thus, when the EC comes into action during accidental conditions,

Table 1: Heat transfer correlations with respect to flow regime.

Flow regime	Correlation	Range of application	Further details of calculations
Annular laminar [8]	$\alpha_{Ann\_lam} = 1.1025\,\lambda_{Fi}\mathrm{Re}_{Fi}^{-0.33}\left[\frac{\rho_{Fi}(\rho_{Fi}-\rho_V)g}{\mu_{Fi}^2}\right]^{0.33}$	$1 \le j_D^* \le 6$ and $\frac{1-\varepsilon}{\varepsilon} \le 0.5$ $\mathrm{Re}_{Fi} < \mathrm{Re}_{wave}$	$\mathrm{Re}_{Fi} = \frac{(1-x)GD}{\mu_{Fi}}$ $\mathrm{Re}_{wave} = 0.392\left[\left(\frac{\sigma}{\rho_{Fi}g}\right)^{0.5}\left(\frac{g}{\nu_{Fi}^2}\right)^{0.33}\right]^{0.75}$
Annular wavy [12]	$\alpha_{Ann\_wave} = 0.8\mathrm{Re}_{Fi}^{0.11} * \alpha_{\mathrm{Nu}}$	$1 \le j_D^* \le 6$ and $\frac{1-\varepsilon}{\varepsilon} \le 0.5$ $\mathrm{Re}_{wave} < \mathrm{Re}_{Fi} < \mathrm{Re}_{crit}$	$\mathrm{Re}_{crit} = \frac{100}{\mathrm{Pr}_{Fi}}$
Annular turbulent [13]	$\alpha_{Ann\_tur} = \frac{\rho_{Fi}v^*c_{p,Fi}}{T^+(\delta^+)}$	$1 \le j_D^* \le 6$ and $\frac{1-\varepsilon}{\varepsilon} \le 0.5$ $\mathrm{Re}_{crit} < \mathrm{Re}_{Fi}$	$\delta^+ = 0.0504(0.5\,\mathrm{Re}_{Fi})^{0.5}$ for $\mathrm{Re}_{Fi} < 1000$ $\delta^+ = 0.0504(\mathrm{Re}_{Fi})^{\frac{7}{8}}$ for $\mathrm{Re}_{Fi} \ge 1000$ $T^+(\delta^+) = \delta^+\mathrm{Pr}_{Fi}$ for $\delta^+ \le 5$ $T^+(\delta^+) = 5[\mathrm{Pr}_{Fi} + \ln(1+\mathrm{Pr}_{Fi}(0.2\,\delta^+ - 1))]$ for $5 < \delta^+ < 30$ $T^+(\delta^+) = 5\left[\mathrm{Pr}_{Fi} + \ln(1+5\mathrm{Pr}_{Fi}) + 0.495\ln(\frac{1}{30}\delta^+)\right]$ for $\delta^+ > 30$ $v^* = \sqrt{\frac{D}{4\rho_{Fi}}\left(\frac{dp}{dx}\right)_{fric,TP}}$
Stratified [8]	$\alpha_{Strat} = \varepsilon^{0.75} * \alpha_{Ann\_lam}$	$j_D^* < 1$ and $\frac{1-\varepsilon}{\varepsilon} \le 0.5$	
Bubble, slug, plug laminar [15, 16]	$\alpha_{BSP\_lam} = 1.86\frac{\lambda_{Fi}}{D}\left(\mathrm{Re}_{Fi}\mathrm{Pr}_{Fi}\frac{D}{l}\right)^{0.33}\left(\frac{\mu_{Fi}}{\mu_w}\right)^{0.14}$	$\frac{1-\varepsilon}{\varepsilon} > 0.5$ $\mathrm{Re} < 2000$	
Bubble, slug, plug turbulent [15, 16]	$\alpha_{BSP\_tur} = 0.024\frac{\lambda_{Fi}}{D}(\mathrm{Re}_{Fi}^{0.8}\mathrm{Pr}_{Fi}^{0.33})\left(\frac{\mu_{Fi}}{\mu_w}\right)^{0.14}$	$\frac{1-\varepsilon}{\varepsilon} > 0.5$ $\mathrm{Re} \ge 2000$	
Spray [10]	$\alpha_{spray} = 0.00345\,\mathrm{Re}_{av}^{0.9}\mathrm{Pr}^{0.33}\left(\frac{r}{c_{p,V}(T_S - T_W)}\right)^{-0.33}$	$j_D^* > 6$ and $\frac{1-\varepsilon}{\varepsilon} \le 0.5$	$\mathrm{Re}_{av} = \frac{GD}{\mu_{mix}}$ $\mu_{mix} = \frac{x}{\mu_V} + \frac{1-x}{\mu_L}$
Single phase	$\alpha_{SPh} = 0.023\frac{\lambda}{D}\mathrm{Re}^{0.8}Pr^{0.4}$	$\varepsilon = 0$	

heat is transferred to the FPV. Possible heat transfer mechanisms at the secondary side are single-phase free convection or pool boiling. The second mechanism occurs when either the water temperature in the FPV or the heat flux is high enough. Experiments at the INKA test facility show that the bubble formation does not occur in the FPV during simulation of large loss of coolant due to main steam line break. Therefore, in the model of the secondary side only the correlation for free convection was included. However, the model is equipped with variables informing the user, if the conditions in the FPV are close to evaporation state, and hence, the influence of bubbles formation on the heat transfer coefficient should be taken into account. Following the *VDI Heat Atlas* [7], the adopted condition for boiling occurrence is the empirical equation developed by Bergles [18]:

$$(T_w - T_{sat})_k = \frac{5}{9}\left[\left(\frac{\dot{q}}{1120}\right)^{0.463} p_k^{-0.535}\right]^{p^{0.0234}} . \tag{16}$$

In order to calculate the heat transfer coefficient at the secondary side, the correlation for external single-phase flow around horizontal cylinders was applied [19]:

$$\mathrm{Nu} = \left\{0.6 + 0.387\left[\mathrm{Ra} f\left(\mathrm{Pr}\right)\right]^{\frac{1}{6}}\right\}^2 . \tag{17}$$

The function $f(\mathrm{Pr})$ describes the effect of the Prandtl number over the entire range of Pr and is given by

$$f\left(\mathrm{Pr}\right) = \left[1 + \left(\frac{0.559}{\mathrm{Pr}}\right)^{\frac{9}{16}}\right]^{-\frac{16}{9}} . \tag{18}$$

4 Results

Experimental data for models validation were obtained during simulation of the main steam line break (MSLB) with taking into account the decay heat. The test was performed at the INKA test facility in the framework of the EASY (Integral Experimental and Analytical Safety Cases for Design-Basis Accidents Featuring Passive Systems) Project. Since the MSLB experiment was conducted in order to investigate performance of the integral system rather than a single component, it should be emphasised, that other components like reactor pressure vessel, drywell vessel, pressure suppression pool, shielding/storage pool and standpipe strongly influenced behaviour of the

emergency condenser. Furthermore, the test course assumed certain activities at certain time points, which lead to strong transients and backflows in the pipe in the volume occupied by steam and indisposed the comparison of results in steady states conditions.

As it may be concluded from Fig. 3, pressure applied to the system was given and at the inlet to the piping system. This pressure corresponds to the one measured in the RPV during the test which results from realising steam from RPV to the Dry Well. Figure 6 presents the pressure applied to the model which at the same time is the pressure measured in the RPV. The dashed and dotted lines illustrate measured and calculated pressure drops over the emergency condenser.

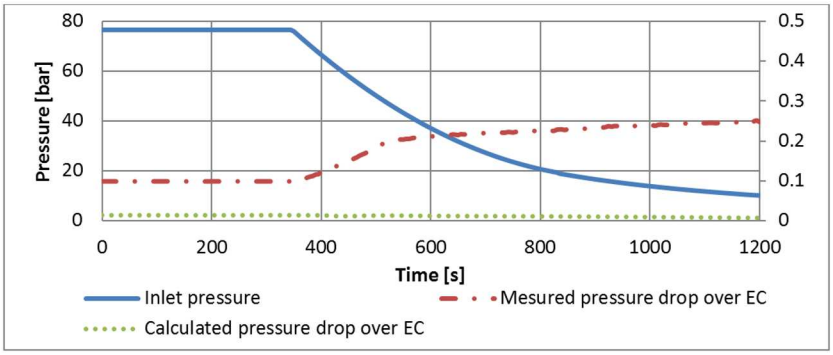

Figure 6: Inlet pressure and pressure drops over the EC.

The maximal value of the measured pressure drop over the EC is 0.025 MPa. The calculated value is lower. The discrepancy between the values of pressure drop comes from not taking into account the angulation of the EC tubes. The angulation introduces geodetic height of around 0.9 m which has an impact to the pressure difference between outlet and inlet of the tubes. Furthermore, insignificant value of the pressure drop comes from the fact, that some of the contributions of total pressure drop have positive and some negative values. This means that pressure drop due to friction is compensated by the pressure build-up due to negative acceleration of the fluid and inclination of the tubes.

Strong decrease of pressure in the RPV impacts mass flows at the inlet and outlet of the EC tubes. The outlet liquid water flow is mainly governed by the water level in the RPV, since EC and RPV operate as communicating vessels. The inlet flow is influenced by depressurisation of the RPV and consequent depressurization of the EC. This results in the steam mass

flowing upward out of the EC at beginning of the pressure drop which results in turn in measurement of zero value. Measured and calculated mass flows are presented in Fig. 7.

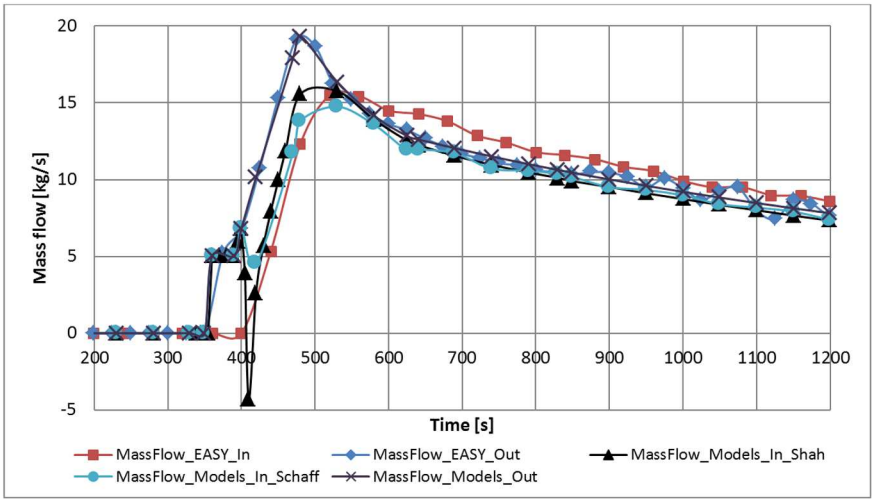

Figure 7: Measured and calculated mass flows.

Figure 7 shows that both models predicted the inlet mass flow peak with a good accuracy. The inlet mass flow according to flow regime based model is slightly lower. After 600 seconds both models calculate around 8% lower value of the inlet flow than the measured one. The measured water level in the RPV with reference to the middle of the EC is presented in Fig. 8.

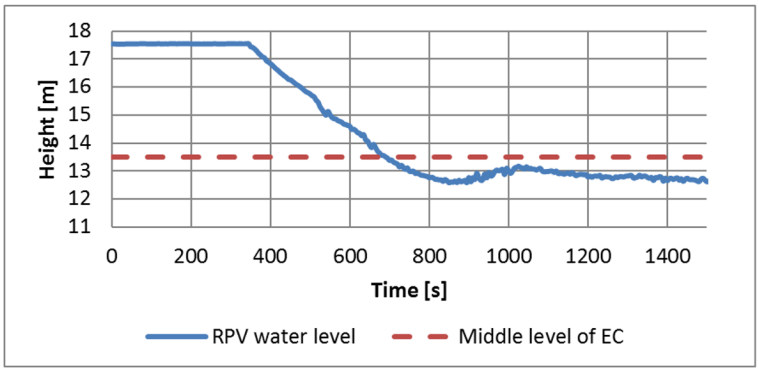

Figure 8: RPV water level and the middle level of the EC.

The water level drop in the RPV enabled the steam to enter the EC tubes (as depicted on the right side of Fig. 2). The contact of saturated steam with cold tubes walls leads to heat exchange and condensation of steam. The power of the EC calculated on the basis of measurements is presented in the figure below together with these computed by the models. The dashed lines indicate ±15% deviations from the measurement curve.

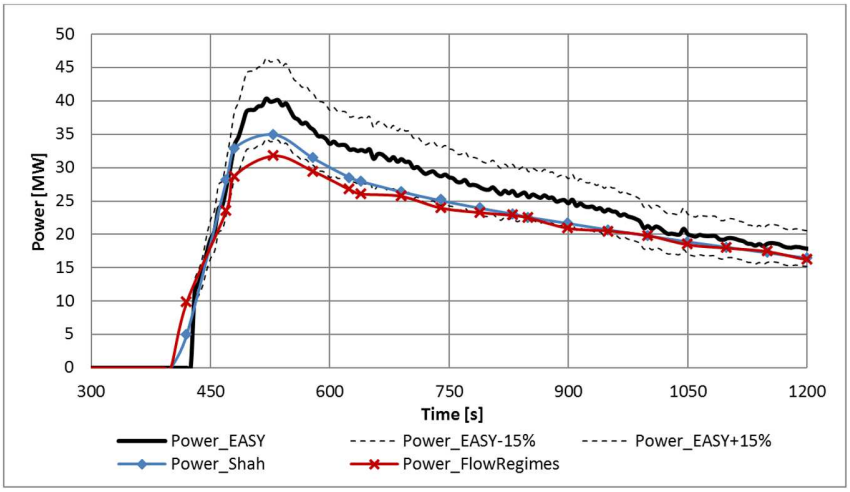

Figure 9: EC Power.

Figure 9 shows that the model on the basis of Shah correlation does not exceed 15% error during the whole simulation. The flow regimes based model shows larger discrepancy at the beginning of the transients. Both models show better accuracy with decreasing pressure variation.

Regarding the fluid temperature, two points were chosen to compare measurements with calculations. The first measurement point was situated ahead of the angulation of the EC pipes, i.e., at the $x = 4.423$ m, where x is the longitudinal coordinate of the pipe. Corresponding calculation point was $x = 4.32$ m. The discrepancy of around 10 cm is caused by location of thermocouple during the test and nodalization of the models. In order to decrease this discrepancy, 4 times denser nodalization would have to be applied which would strongly influence calculation time, but would not lead to improvement of comparison quality. The second measurement point was located at $x = 5.756$ m, i.e., at the bottom part of angulation of the pipe. Figure 10 shows positions of thermocouples arrangement at EC tube at INKA.

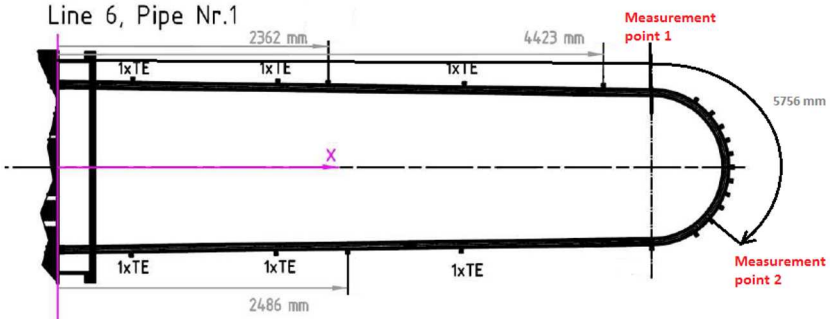

Figure 10: Positions of thermocouples chosen for comparison.

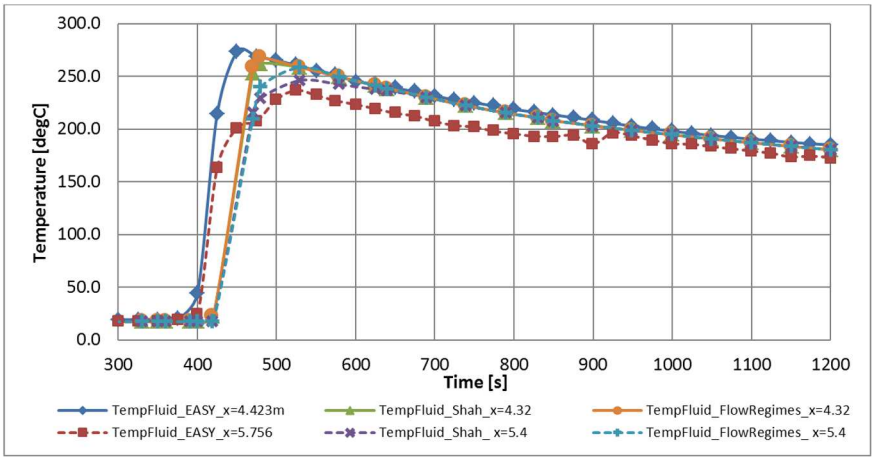

Figure 11: Fluid temperatures.

Figure 11 shows temperatures measured at both locations and calculated values at corresponding positions. It indicates that around 4.3 meters from the EC inlet, the flow is still a two-phase mixture at the saturation temperature. This is both, in the case of calculation and measurements. Temperature calculated at the second point is in both models larger than the measured value. This comes obviously from the discrepancy of calculated and measured heat transfer and partly due to relatively large distance of 0.35 m between measurement and calculation points. Figure 11 shows also that measured temperature at the second position reaches saturation temperature at around 900 s. This is caused by significant depressurization and corresponding saturation temperature drop.

Considering the wall temperature, due to the falling water film and stratification, significantly different values were measured at the upper and bottom wall of the tube. Therefore, two measurements are presented in the picture below. Both come from the part of EC ahead of the angulation, but one represents the upper part of the wall, and the second the bottom part. Since the water film at the bottom part of the tube is thicker, the heat transfer at this part of the tube is lower, and so is the temperature. Figure 12 shows measured and calculated values.

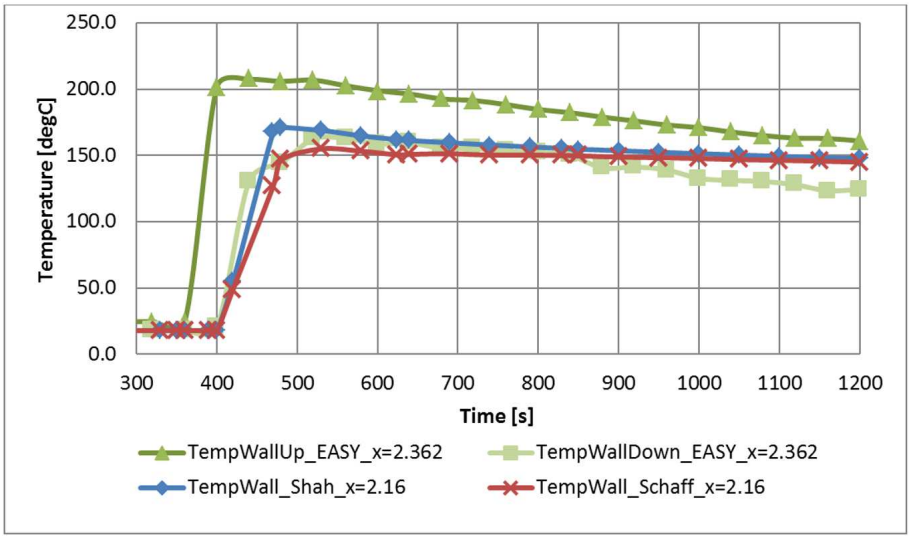

Figure 12: Inner wall temperatures.

Since the wall temperature in both models was calculated without distinction of the top and bottom side, there is a significant discrepancy between measured and calculated values. At the beginning of the transient, calculated values are close to temperature of the bottom part of the tube. With proceeding depressurization of the system, the calculated temperature becomes closer to the upper part of the tube. The issue of modelling of condensation in horizontal tubes with distinction between upper and bottom parts of the tube will be the subject of the future work.

An important factor in modelling of the EC is the FPV, i.e., water temperature in the vessel and the heat transfer coefficient at the secondary side. Figure 13 shows measured and calculated temperatures of the water at the secondary side.

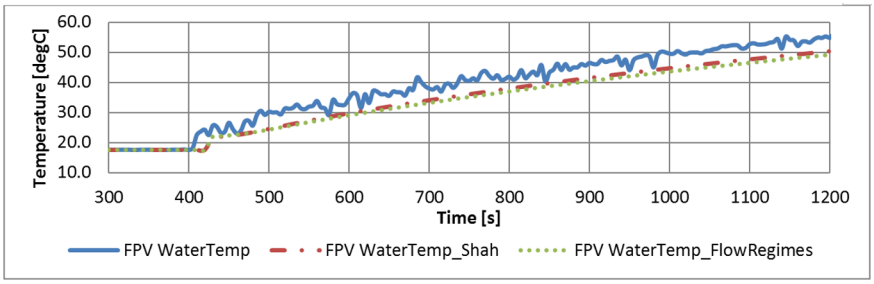

Figure 13: FPV water temperatures.

As it was assumed, the water temperature stays below the evaporation point, particularly if we consider the fact of pressure increase in the dry well due to the steam release during LOCA.

Although the proper measurements are not available, it is worth to have a look at some other values obtained from simulations. These values are void fraction and heat flow rates in particular volumes. Figure 14 shows the void fraction distribution along the pipe in a function of time.

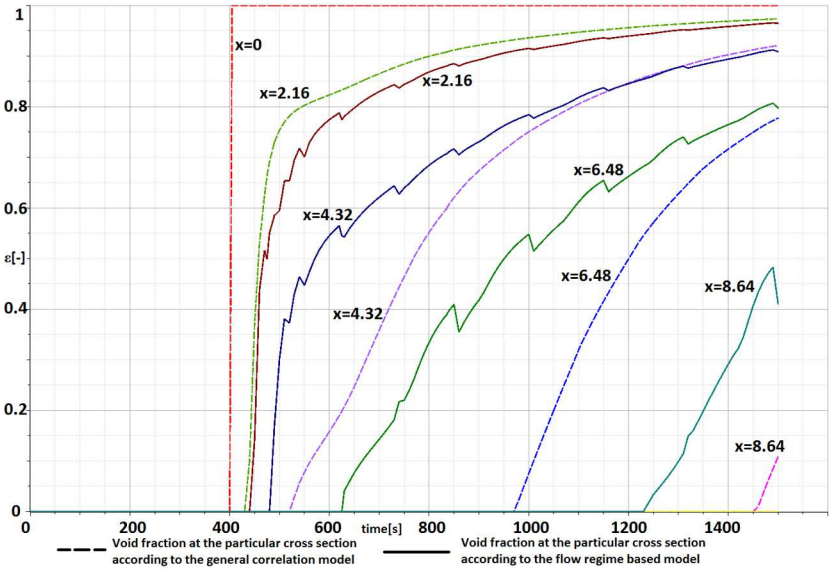

Figure 14: Void fraction distributions.

In Fig. 14, dashed lines depict void fractions at particular cross sections calculated with the general correlation model. The solid lines show void

fractions at the same points according to the flow regime based model. The differences between model become large as the void fractions have small values. They reach, however, very close values as the pressure change with time becomes lower.

The values of heat flow rates presented in Fig. 15 are negative because the heat transfer proceeds from the fluid to the outside – to the FPV in this case. Heat flow rates distribution along the tube shows clearly different origins of the models. The curves calculated with flow regime based model have much more jerky course. This comes from switching between correlations. As it could have been predicted from previous analysis the values calculated according to general correlation are larger, and more stable.

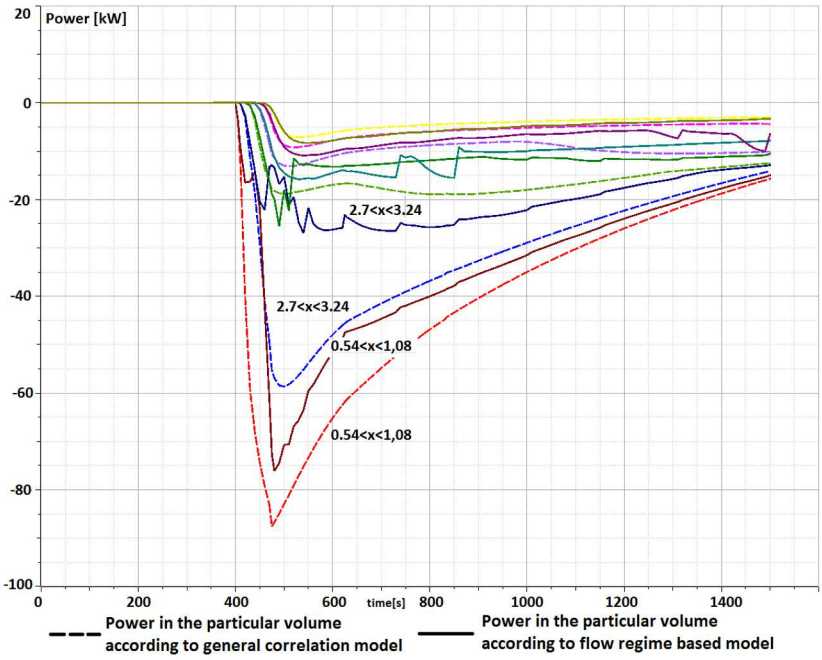

Figure 15: Heat flow rates in volumes.

5 Conclusions and outlook

Two different approaches for modelling of condensation in horizontal tubes have been investigated and implemented with utilization of object-oriented

Modelica language and OpenModelica environment. The aim of this work was investigation, verification and comparison of performance of models applied with usage of open-source OpenModelica environment in order to draw conclusions considering their reliability in modelling of passive safety systems. The main conclusions are:

- both models calculate correctly the mass flow rates at the inlet to the tubes,
- since the flow regime based model switches between different heat transfer coefficient correlations, significant peaks of heat flow rates and void fractions were observed,
- these peaks may lead to discrepancies of parameters values and instabilities of simulations,
- general correlation based model is more stable, requires less computation time and gives better results;
- due to thinner film layer at the upper wall part of the tube, the wall temperature is significantly higher in this region which is not taken into account in the models,
- further work on EC modelling will be performed with consideration of distinction between upper and bottom parts of the tubes.

Received 29 September 2017

References

[1] IAEA, *Power Reactor Information System,* https://www.iaea.org/PRIS/home.aspx

[2] Drescher R., Wagner T. and Leyer S.: *Passive BWR integral LOCA testing at Karlstein test facility INKA*. VGB PowerTech, 5 (2014), 33–37.

[3] Modelica website www.modelica.org

[4] OpenModelica website www.openmodelica.org

[5] Schaffrath A., Hicken E.F., Jaegers H. and Prasser H-M.: *Operation conditions of the emergency condenser of the SWR1000*. Nucl. Eng. Des. **188**(1999), 3, 303–318.

[6] Schaffrath A., Krüssenberg A., Fjodorow A., Gocht U., Lischke W.: *Modeling of condensation in horizontal tubes*. Nucl. Eng. Des. **204**(2001), 1-3, 251–265.

[7] *VDI Heat Atlas*, Second Edition. Springer-Verlag Berlin Heidelberg 2010.

[8] Nusselt W.: *Oberflächenkondensation des Wasserdampfes*. Zeitschr. Vereins Deutscher Ingenieure **27**(1916), 541–546, 569–575.

[9] Tandon T.N., Varma H.K., Grupta C.P.: *A new flow regimes map for condensation inside horizontal tubes*. J. Heat Transfer **104**(1982), 4, 763–768.

[10] Soliman E.N.: *The mist-annular transition during condensation and its influence on the heat transfer mechanism*. Int. J. Mutiphas. Flow **12**(1986), 2, 277–288.

[11] Grimley S.S.: *Liquid flow conditions in packed towers*. Trans. Inst. Chem. Eng. **23**(1945), 228–235.

[12] Kutateladse S.S.: *Fundamentals of Heat Transfer*. Edward Arnold, 1963.

[13] Kosky P.G., Staub W.F.: *Local condensing heat transfer coefficient in the annular flow regime*. AICHE J. **17**(1971), 5, 1037–1043.

[14] Jaster H., Kosky P.G.: *Condensation heat transfer in a mixed flow regime*. Int. J. Heat Mass Tran. **19**(1976), 1, 95–99.

[15] Breber G.W., Palen J.W., Taborek J.: *Prediction of horizontal tubeside condensation of pure components*. Trans. ASME J. Heat Transfer **102**(1980), 3, 471–476.

[16] Sieder E.N., Tate G.E.: *Heat transfer and pressure drop of liquids in tubes*. Ind. Eng. Chem. **28**(1936), 12, 1429–1435.

[17] Shah M.M.: *A general correlation for heat transfer during film condensation inside pipes*. Int. J. Heat Mass Tran. **22**(1979), 4, 547–556.

[18] Bergles A.E.: *The determination of forced-convection surface boiling heat transfer*. J. Heat Transfer **86**(1964) 3, 365–372.

[19] Churchill W., Chu H.H.S.: *Correlation equations for laminar and turbulent free convection from a horizontal cylinder*. Int. J. Heat Mass Tran. **18**(1975), 1049–1053.

[20] Mikielewicz D., Andrzejczyk R.: *Comparative study of flow condensation in conventional and small diameter tubes*. Arch. Thermodyn. **33**(2012), 2, 67–83 DOI: 10.2478/v10173-012-0011-2

archives
of thermodynamics
Vol. **38**(2017), No. 4, 53–63
DOI: 10.1515/aoter-2017-0024

Preliminary electrochemical characterization of anode supported solid oxide cell (AS-SOC) produced in the Institute of Power Engineering operated in electrolysis mode (SOEC)

JAKUB KUPECKI*
KONRAD MOTYLIŃSKI
MAREK SKRZYPKIEWICZ
MICHAŁ WIERZBICKI
YEVGENIY NAUMOVICH

Department of High Temperature Electrochemical Processes, Institute of Power Engineering, Augustowka 36, 02-981 Warsaw, Poland

Abstract The article discusses the operation of solid oxide electrochemical cells (SOC) developed in the Institute of Power Engineering as prospective key components of power-to-gas systems. The fundamentals of the solid oxide cells operated as fuel cells (SOFC – solid oxide fuel cells) and electrolysers (SOEC – solid oxide fuel cells) are given. The experimental technique used for electrochemical characterization of cells is presented. The results obtained for planar cell with anodic support are given and discussed. Based on the results, the applicability of the cells in power-to-gas systems (P2G) is evaluated.

Keywords: SOFC; SOEC; Electrolysis; Power-to-gas

1 Introduction

High temperature fuel cells become increasingly attractive technologies for highly efficient power generation. Both the molten carbonate (MCFC) and solid oxide fuel cell (SOFC) are applied in various demonstration systems.

*Corresponding Author. Email jakub.kupecki@ien.com.pl

While several commercial plants based on MCFC can be found worldwide, the market penetration of SOFC is not as reconisable. The features of both types of cells enable their use in novel applications. The earlier is considered as a strong candidate for CO_2 separation, which can compete with such technologies as MEA-based CCS (carbon capture and storage) units [1]. The latter can operate in regenerative mode as the solid oxide electrolyser (SOEC). Solid oxide electrolysis is believed to be the most attractive solution for power-to-gas (P2G) and power-to-liquid (P2L) systems [2]. Moreover, electrolysis can find good application in biomass-to-liquid (BTL) systems for enhancing the conversion of the feeding gas by combining the gasification and solid oxide electrolyser [3].

The solid oxide cell can operate in interchangeable mode on condition that the material compatibility is assured. The most typical mechanism of the degradation of SOC during the change between the SOFC and SOEC mode is caused by the electrode delamination [4]. Certain ceramic oxides, including the lanthanum strontium cobaltite ferrite (LSCF), exhibit good stability in the electrolyser mode and the rapid degradation is therefore prevented. Once the stability issues are resolved and the ability for long-term operation is demonstrated, the SOEC unit can be the key component of the energy storage systems, which realize the power-to-gas concept. The high temperature electrochemical processes occurring in solid oxide cells (SOC) can proceed both ways depending on the operational mode: current generation from fuel gas (e.g., hydrogen, CO) or steam electrolysis powered from outside (e.g., from grid).

2 Solid oxide electrolysis – theoretical background

The chemical energy of fuel can be converted into electricity or the electricity can be used for steam electrolysis. The former concept has been known for years as solid oxide fuel cell, while the latter known as solid oxide electrolysis cell has gained a lot of attention in the last decade. Ability of the SOC to operate interchangeably between the modes allows in one system to either deliver electricity or produce the synthetic fuel which can be a new vector in power generator sector and serve as a storage medium. The integration of renewable energy sources such as wind and photovoltaics causes several issues to the electrical grid. Mostly, due to the intermittent character of these sources, the grid experiences imbalances which destabilize the energy system. Use of SOEC enable utilization of the excess electricity

and production of the gas which can be stored for direct use during the peak hours or can be further processed to produce synthetic natural gas (SNG). The generated fuel can be injected into gas grids or used for various applications, including transportation. Reversion of the fuel cell operation mode can be done in a dynamic mode during operation within minutes. Such system can be easily modulated and is able to frequently interchange between power-to-gas and gas-to-power modes. SOC allows therefore the coupling of two sectors: electrical and the gas. This increases the flexibility of the combined electrical-gas grids, provides extensive storage capacities and allows way higher modulation than two separate standalone systems.

The advantages of solid oxide electrolysis over the conventional electrolysers should be noted:

- SOEC offers an outstanding efficiency, exceeding 70–80% [5],
- noble metals are not required due to sufficient catalytic activity of the ceramic materials of electrodes at elevated temperatures,
- SOEC mode can be switched to SOFC and the interchange supports the unique self-healing of the cells [6],
- modular design makes it easy to scale-up the system based on SOC stack,
- absence of liquid electrolyte which has to be replaced on regular basis due to evaporation, hydration or contamination.

The solid oxide electrolysis overcomes therefore the drawbacks of low temperature electrolysis which include: (i) higher terminal voltage by 150–300 mV, (ii) accumulation of impurities in the liquid electrolyte which has to be replaced, (iii) highly expensive catalysts based on noble metals, (iv) inability to operate reversibly.

The interchangeable operation of solid oxide cells relies on reversing the directions of occurring electrochemical processes. In such a case, the roles of electrodes change and the SOFC anode (electrode on which oxidation of species occurs) becomes the cathode (electrode on which reduction of species occurs) in SOEC mode. The working conditions in the anodic and cathodic compartments change as well. The basic comparison of the parameters in fuel cell and electrolyser modes is shown in Fig. 1.

Modifications, which are needed for obtaining stable operation as the reversible solid oxide cell (ReSOC) in a stack, include adaptation of the cell electrodes, interconnectors and the sealings due to the fact that the working

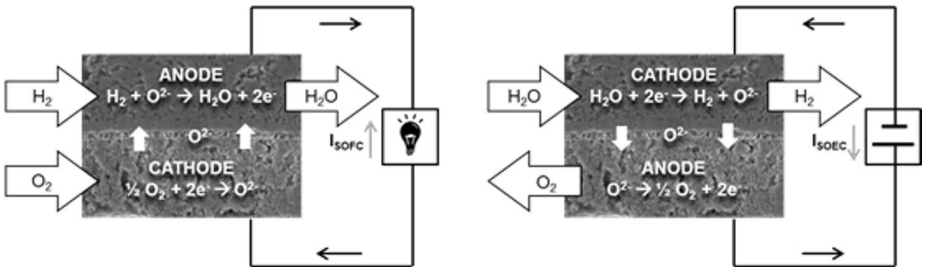

Figure 1: Comparison of the fuel cell (SOFC) and electrolysis (SOEC) operation.

conditions inside the anodic and cathodic compartments of the solid oxide cells operated as electrolysers and as fuel cells alter. The interchangeable SOEC/SOFC operation exposes the cell to both sets of conditions.

3 Experimental evaluation of SOEC

The purpose of the recent study presented in the article was to assess the performance of existing cell in order to verify its operation as the electrolyser and to verify that the current composition of the cells qualifies them for the reversible operation. The study was aimed at identification of improvements which are needed for optimization of the cell to operate as ReSOC with a special focus on the SOEC mode.

The cells with external dimensions of 50 mm x 50 mm and the thickness about 1 mm were manufactured in the Ceramic Department (CEREL) of the Institute of Power Engineering (IEN) and experimentally characterized in the laboratories of the Department of High Temperature Electrochemical Processes (HiTEP) of IEN. Cross-section of the cell is shown in Fig. 2 and the main parameters of the cell are summarized in Tab. 1.

The LSCF electrodes, which were fabricated as SOFC cathodes„ already confirmed to be sufficient as anodes (oxygen electrode) in SOEC [7,8], however the adaptation of porosity and barrier interlayers is needed to assure the long-term stability, reversibility of current and the reduction of the fuel cell degradation. Experimental characterization of the SOFC and SOEC was done in a ceramic housing which accommodates a single 50 mm x 50 mm cell. The active area of the currently analysed cell was 16 cm^2. For all electrochemical measurements, electrochemical workstation Zahner Im6ex coupled with PP240 4-quadrant power potentiostat were used. The exper-

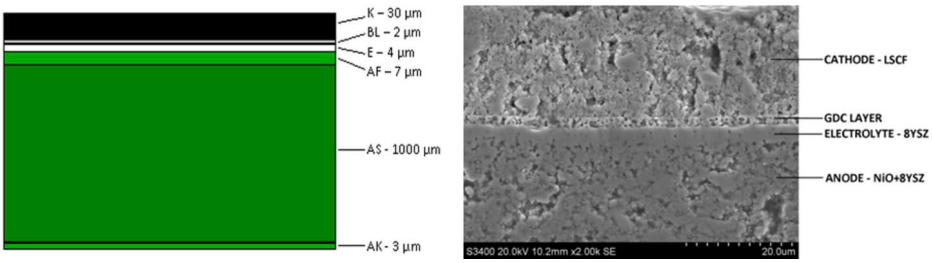

Figure 2: The cross-section of the cell with dimensions of interlayers (left) and their microstructure (right).

Table 1: Basic specification of the cell which was characterized in the SOFC and SOEC modes.

Layer	Material	Thickness	Porosity
Cathode layer (K)	$La_{0.6}Sr_{0.4}Fe_{0,8}Co_{0.2}O_{3--\delta}$	30 μm	25 vol.%.
Barrier layer (BL)	$Gd_{0,1}Ce_{0,9}O_2$	1.5 μm	–
Electrolyte (E)	8YSZ	4 μm	–
Anode functional layer (AF)	NiO/8YSZ 50/50 wt.%	7 μm	–
Anode support (AS)	NiO/8YSZ 66/34 wt.%,	1.0 mm	25 vol.%
*A*node contact layer (AK)	NiO	3 μm	–

imental setup used for the preliminary electrochemical characterization of the cell is shown in Fig. 3.

The electrochemical performance of solid oxide cells is dependent on several operation parameters, for the fuel cell mode including: (i) temperature, (ii) fuel flow, (iii) oxidant flow, (iv) composition of the fuel. Under these conditions, the current is varied in order to observe the voltage of the cell.

The experimental setup relies on Bronkhorst mass-flow controllers, K/N-type thermocouples, Kikusui power electronics. This assures that the measurements are done with high accuracy with error lower than 1%. In-house software was used for acquisition and processing of the process data.

The key parameters which can be determined, include the fuel utilization, the oxidant utilization, efficiency and power obtained from a single cell. In the electrolysis mode, the methodology is analogical with the differences related to the composition of the incoming gases. Once the SOEC is

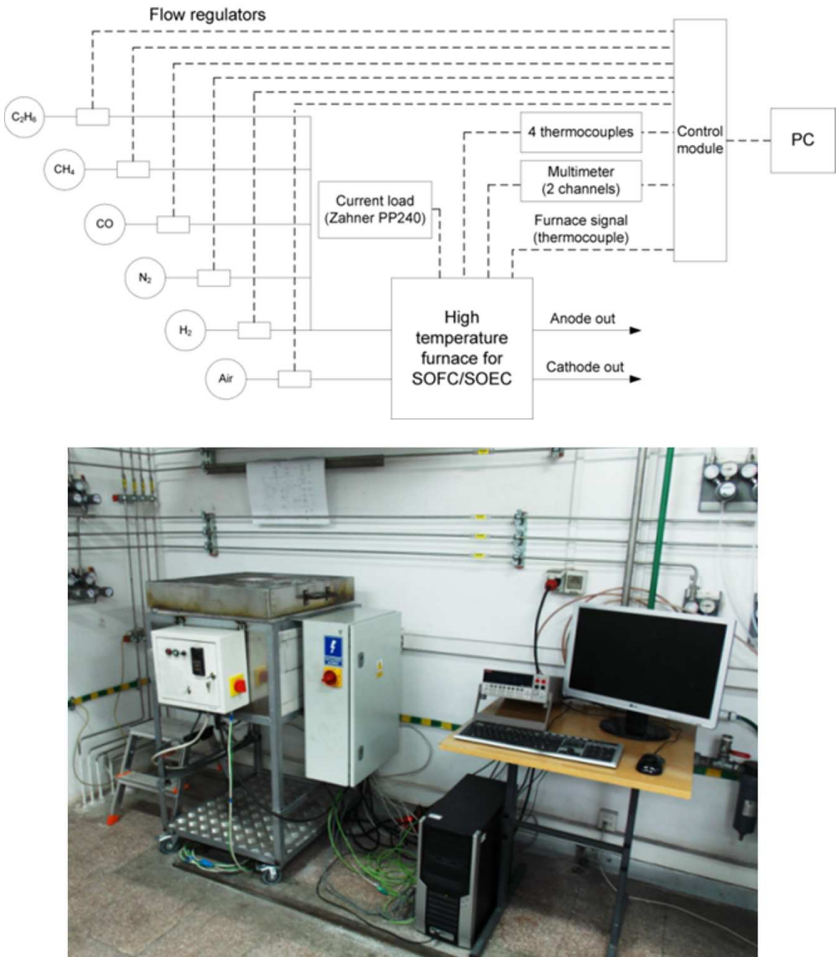

Figure 3: Experimental setup used for characterization of the 50 mm x 50 mm SOC operated as SOEC: test stand scheme (upper) and the actual photo (lower).

considered, the cathode is supplied with steam, while the exiting gases are the oxygen and hydrogen for the anode and cathode, respectively. Steam delivery in the experimental setup is organized using a precise steam generator (not shown in Fig. 3) which allows humidification of the incoming fuel to the set level. In the electrolysis mode the steam from the generator is premixed with the fuel.

The measurements were performed at the temperature of 850 °C. Over the entire duration of the experiments, the variation of temperature of the

cell in range 849–855 °C was observed. The fluctuations were caused by transition from the exothermic conditions to the endothermic conditions and backwards, also passing the cell thermoneutral point (∼1290 mV). The temperature variations equal to the maximum of 0.58% from the set point (5°C/850°C), therefore relatively high stability of the temperature was achieved during the measurements. Constant volumetric flow of reagents was supplied to the anodic and cathodic compartments (defined for fuel cell mode) equal to 200 ml_N/min and 400 ml_N/min, respectively. The mixture of H_2 and H_2O 50%/50% was supplied continuously to the anode to allow the ease of transition between SOFC/SOEC operation modes and air was constantly supplied to the oxygen electrode.

4 Results

In order to observe the performance of the cell operated in reversible SOFC/SOEC modes, the experimental methodology included transition from fuel cell to electrolysis mode and backwards. With such an approach it was possible to measure the current while gradually increasing the voltage in potentiostat mode. In the performed experiment, the maximum current achieved in the fuel cell mode was 25 A and in electrolysis mode – 40 A. The reported values represent the maximum current which was drawn and applied in the fuel cell and electrolysis modes, respectively. The values indicate the ability of the cell to operate at high current densities, but such conditions lead to rapid degradation of the electrochemical performance. The values should be considered as a possible maximum values observed for a short duration. Long term operation and characterization of SOC is done at moderate current densities which will be described in the next section.

It should be noted that neither the solid oxide cell, nor the experimental methodology were optimized for either the fuel cell or the electrolyser mode of operation. Additionally, the existing ceramic housing which was optimized only for investigation of the fuel cell mode was used. This explained the moderate performance of the cell.

Based on the experimental data, the current density-voltage curve was generated. Fuel cell mode corresponds to the positive value of the current density, while negative current density range defines the electrolysis mode. The results can be seen in Fig. 4. The reversible voltage of 869 mV was observed at open circuit voltage (OCV). Such low value of OCV is a result of

(1) an "open" cell setup (no sealing) applied and (2) relatively low stream of fuel supplied to the fuel cell compartment – clearly observable in concentration polarization region (Fig. 4 at current densities >300 mW/cm^2). As can be seen in Fig. 4 the polarization of the cell was reversed twice by adapting the current density in order to start the characterization from OCV (869 mV), achieve 400 mV is SOFC mode, achieve 1500 mV in SOEC and finalize the measurements at OCV. The development of hysteresis can be noted.

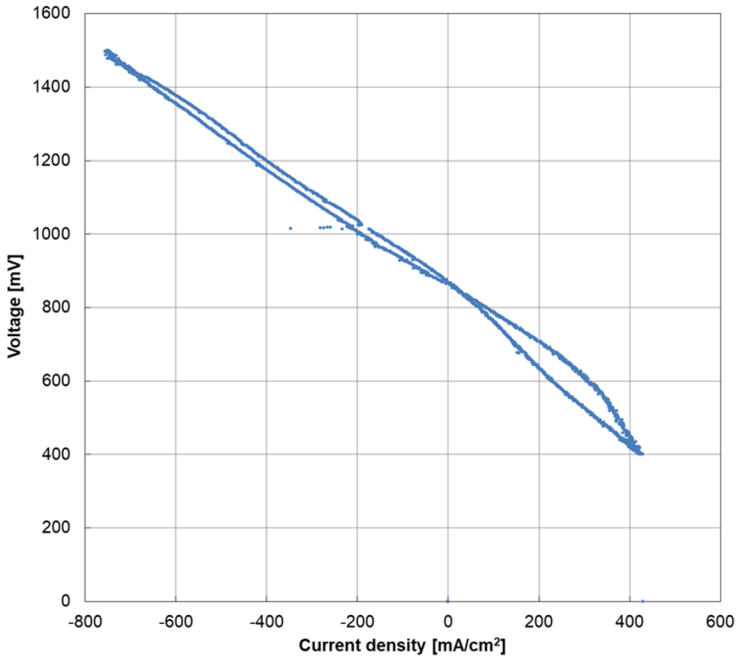

Figure 4: Characterization of the cell during reversion of the polarization between the modes.

The current-voltage characteristics measured in the fuel cell mode was below the typical working conditions of the SOFC cell what was caused by the (1) relatively low stream of fuel supplied to the fuel cell and (2) dilution of fuel with high steam content in the fuel gas both clearly observable in the concentration polarization region. Moreover, the test rig was an 'open – type' cell housing (no sealing), therefore the level of leakages could not be addressed in the current study.

The SOEC mode curve, measured up to 1500 mV (to avoid the reduction of yttria stabilized zirconia – YSZ) was rather linear, of an area specific resistance (ASR) equal 0.8 Ωcm^2 calculated from the current-voltage curve angle at 1050 mV.

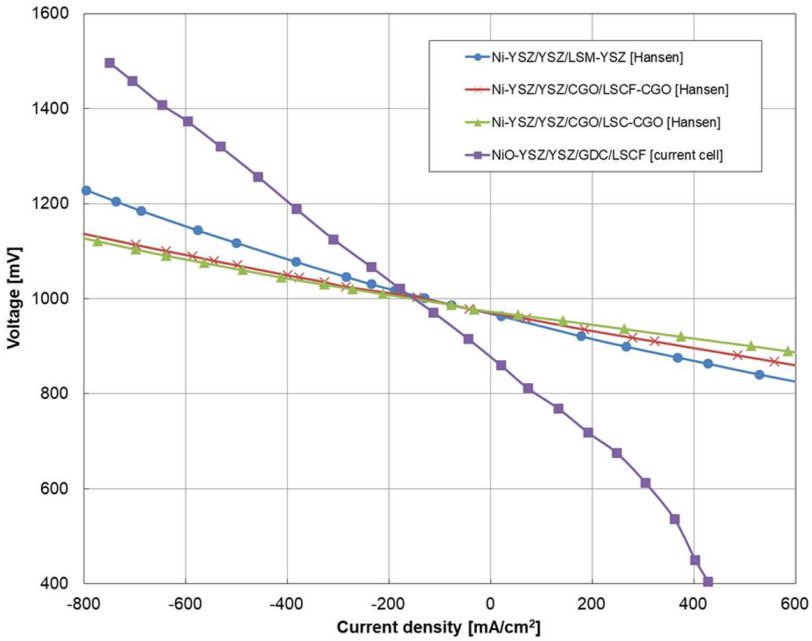

Figure 5: Comparison on the performance of reference cells [9] and the current version of cell at IEN.

Among previous experimental studies related to the operation of the same SOC as a fuel cell and as an electrolyser, the evaluation of Ni-YSZ/YSZ/LSM-YSZ, Ni-YSZ/YSZ/CGO/LSCF-CGO and Ni-YSZ/YSZ/ /CGO/LSC-CGO cells was done by [9]. For the purpose of comparative analysis, the currently obtained results were plotted against the literature data reported previously. The comparison can be seen in Fig. 5. It should be noted that while the current cell was analyzed at temperature of 850 °C, data reported by Technical University of Denmark [9] were obtained for 800 °C.

5 Conclusions

The preliminary experimental studies confirmed applicability of the solid oxide cells developed and fabricated in the Institute of Power Engineering in short-term operation for operation in electrolysis mode. The moderate performance during the experiment could be explained by the fact that neither the cell itself nor the experimental methodology and setup were optimized for investigation of the reversible operation. The interpretation of the experimental data provide a starting point to elaborate the required modifications of the cell in order to increase the performance in SOEC mode and to reduce long term degradation which can be due to several factors including the delamination of oxygen electrode.

The results of the current study can be combined with outcomes of conceptual studies related to utilization of electrochemical processes for generation of synthetic fuels in hybrid systems [10] or support the carbon capture technologies when the SOEC handles the carbon dioxide operating in co-electrolysis [11].

Finally, the further work needs to be performed that will address the modifications of the experimental methodology and setup, as well as studies of the steam utilization for different H_2/H_2O compositions involving the electrochemical impedance spectroscopy (EIS) measurements needed to determine the particular losses within the processes.

Acknowledgment Authors would like to acknowledge the valuable comments on the work from Dr. Mariusz Krauz and Dr. Ryszard Kluczowski from the Ceramic Department (CEREL) of the Institute of Power Engineering to whom they express the gratitude. This work was financially supported by the Ministry of Science and Higher Education of the Republic of Poland through the Statutory Grant CPE/1/STAT/2017 in the Institute of Power Engineering.

Received 4 October 2017

References

[1] Milewski J., Wołowicz M., Lewandowski J.: *Optimization of the working conditions of a laboratory size (100 cm2) molten carbonate fuel cell.* ECS Transactions **51**(2013), 1, 37–45.

[2] Schwarze K., Posdziech O., Kroop S. *et al.*: *Green industrial hydrogen via reversible high-temperature electrolysis*. ECS Transactions **78**(2017), 1, 2943–2952.

[3] Pozzo M., Lanzini A., Santarelli M.: *Enhanced biomass-to-liquid (BTL) conversion process through high temperature co-electrolysis in a solid oxide electrolysis cell (SOEC)*. Fuel **145**(2015), 39–49.

[4] Virkar A.V.: *Mechanism of oxygen electrode delamination in solid oxide electrolyzer cells*. Int. J. Hydrogen Energ. **35**(2010), 18, 9527–9543.

[5] Sun X., Chen M., Jensen S.H., *et al.*: *Thermodynamic analysis of synthetic hydrocarbon fuel production in pressurized solid oxide electrolysis cells*. Int. J. Hydrogen Energ. **37**(2012), 22, 17101–17110.

[6] Graves C., Ebbesen S.D., Jensen S.H., *et al.*: *Eliminating degradation in solid oxide electrochemical cells by reversible operation*. Nat. Mater. **14**(2015), 239–244.

[7] Jae S., Gyeong K., Choi M.: *Stability of LSCF electrode with GDC interlayer in YSZ-based solid oxide electrolysis cell*. Solid State Ionics **262**(2014), 303–306.

[8] Kim S.J., Kim K.J., Dayaghi A.M., *et al.*: *Polarization and stability of La2NiO4+δ in comparison with La0.6Sr0.4Co0.2Fe0.8O3-δ as air electrode of solid oxide electrolysis cell*. Int. J. Hydrogen Energ. **41**(2016), 33, 14498–14506.

[9] Hansen J.B.: *Solid oxide electrolysis – a key enabling technology for sustainable energy scenarios*. Faraday Discuss. **182**(2015), 9–48.

[10] Milewski J.: *Solid oxide electrolysis cell co–methanation supported by molten carbonate fuel cell – a concept*. J. Power Technologies **96**(2016), 1, 8–14.

[11] Bartela L., Skorek-Osikowska A., Kotowicz J.: *Integration of a supercritical coal-fired heat and power plant with carbon capture installation and gas turbine*. Rynek Energii **100**(2012), 3, 56–62.

archives
of thermodynamics
Vol. **38**(2017), No. 4, 65–87
DOI: 10.1515/aoter-2017-0025

Analysis of energy storage system with distributed hydrogen production and gas turbine

JANUSZ KOTOWICZ
ŁUKASZ BARTELA
KLAUDIA DUBIEL-JURGAŚ*

Silesian University of Technology, Institute of Power Engineering and Turbomachinery Konarskiego 18, 44-100 Gliwice, Poland

Abstract Paper presents the concept of energy storage system based on power-to-gas-to-power (P2G2P) technology. The system consists of a gas turbine co-firing hydrogen, which is supplied from a distributed electrolysis installations, powered by the wind farms located a short distance from the potential construction site of the gas turbine. In the paper the location of this type of investment was selected. As part of the analyses, the area of wind farms covered by the storage system and the share of the electricity production which is subjected storage has been changed. The dependence of the changed quantities on the potential of the hydrogen production and the operating time of the gas turbine was analyzed. Additionally, preliminary economic analyses of the proposed energy storage system were carried out.

Keywords: Power-to-Gas-to-Power; Hydrogen; Gas turbine; Electrolysis

1 Introduction

The increase in the share of renewable energy sources, observed in recent years, which are characterized by variable in time production potential, contributes to the intensification of research into energy storage systems. This is primarily due to the variability of electricity production by solar and wind power plants. At present in Poland, the installed power in wind power plants amounts to 5813 MW [1], whereas in power plants generating

*Corresponding Author. Email: klaudia.dubiel-jurgas@polsl.pl

electricity from solar radiation it is 100 MW. For comparison, in 2011 it was 1616 MW and 1.1 MW, respectively [1]. Thus, within 5 years, more than 3 times increase in installed power in wind power and almost 90 times in solar power was recorded. The increase in the share of this type of source in the power system increases the disproportion between production and consumption of electricity by final consumers. One way of storing energy and thus bridging the gap between electricity demand and electricity supply, analyzed in this paper, is hydrogen production in the electrolysis process, using excess electricity (power-to-gas). Then, hydrogen can be directly used for energy purposes during periods of increased demand for electricity in the system, e.g., in gas piston engines, gas turbines, fuel cells, or as a substrate for chemical reactions such as methanisation.

2 Description of the energy storage system with selection of the location of gas turbine

The article presents a concept of energy storage system using a gas turbine (GT) co-firing hydrogen with natural gas. Hydrogen, which is a product of electrolysis of water, is produced in several separate electrolysis installations (EI), each of which cooperates with a single wind farm. Distributed sources of hydrogen production are located in a short distance from the proposed construction site of the gas turbine. The transport of hydrogen is carried out by tube trailers, each with a capacity of 20 m^3, at a pressure of 20 MPa. Analyses were conducted for a specific investment location. The main criteria for selecting locations for this type of investment are: the significant installed power of nearby wind farms and the availability of the power grid and gas network, due to the proper functioning of the gas turbine. A schematic diagram of the system was presented in Fig. 1.

The intensity and force of the wind are highly relevant to the planning of wind farms. The Institute of Meteorology and Water Management draws wind maps with the division into 5 zones of the wind energy, from the most favourable to the least favourable conditions for the construction of a wind power plant [3]. In Poland, the most favourable conditions (zone I) have the Baltic coastline, the area of the Gulf of Gdansk and the Suwalszczyzna region. The windiness is often dependent on local conditions, so investments are preceded by a few years of measurements at the site of the planned wind farm. In Poland, the highest density of large wind farms (> 5 MW) is observed in the Slupsk and Koszalin regions, as illustrated in Fig. 2. Within

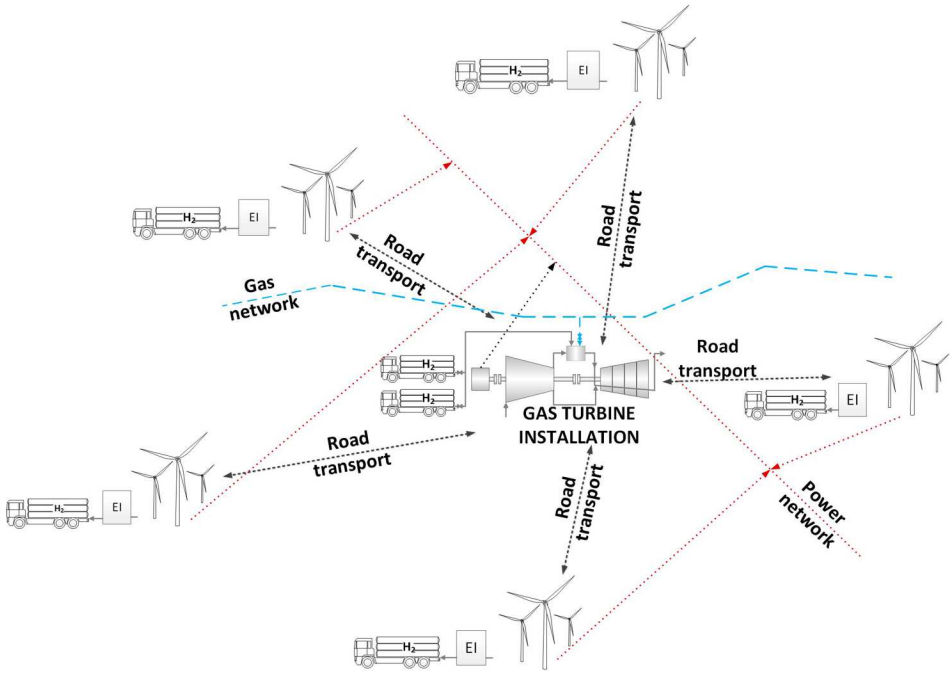

Figure 1: Scheme of energy storage system with gas turbine and distributed hydrogen production.

the analyses, the location of the installation of gas turbine between the towns of Tychowo and Noskowo in the Western Pomeranian voivodship in the Slawno district was selected. This location is justified because of a short road distance not exceeding 40 km from at least 19 wind farms, each with installed power of at least 5 MW. The total installed power of the analyzed 19 wind farms is 623.9 MW. In the discussed concept of the system, these farms are also the places of hydrogen generation. In addition, within close proximity there is the existing natural gas transmission pipeline, which is the nominal GT fuel, and the 110 kV power transmission line, allowing evacuation of power from GT.

The location of large wind farms (> 5 MW) in Poland with the marked analyzed area are presented in Fig. 2. Details are shown in Fig. 3.

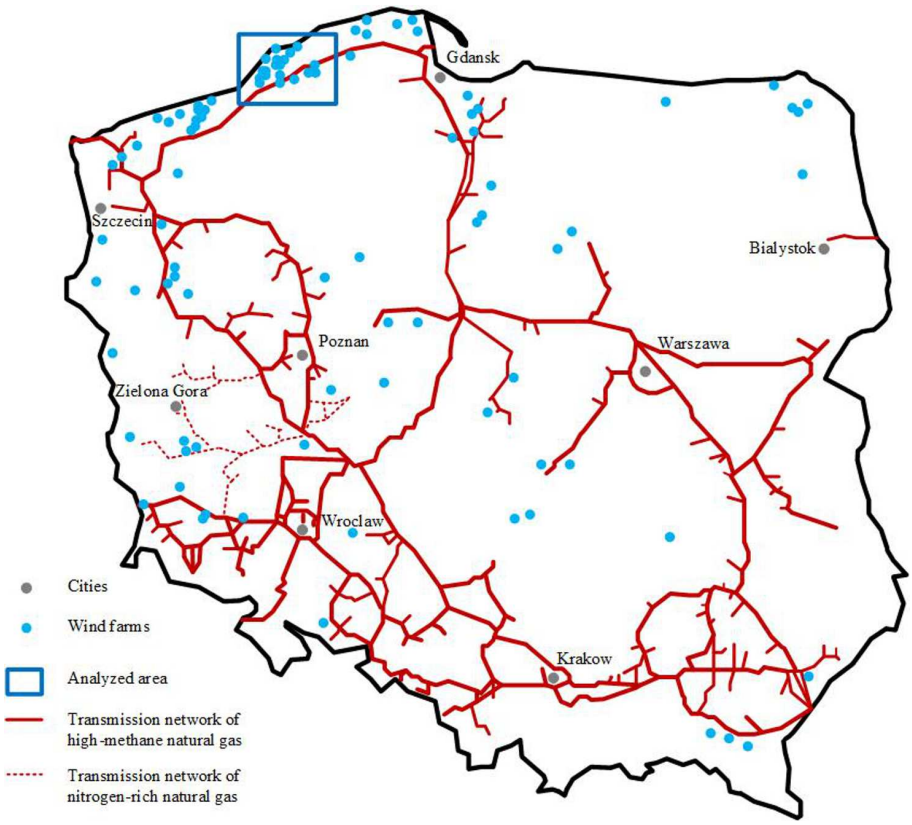

Figure 2: The location of wind farms with installed power over 5 MW, with the natural gas transmission network.

3 Methodology and assumptions

The input data, required for system analyses, were the hourly characteristics of power for the annual operating cycle of the wind farms. The analyses used one wind farm power characteristic, scaled depending on the installed power of individual farms. An example basic power characteristic for 100 MW installed power wind farm is shown in Fig. 4.

The influence of the distance of the wind farms included in the storage system to the gas turbine on the hydrogen production potential was also analyzed. Details of the installed power of individual wind farms and the road distances between the planned plant and farms are shown in Tab. 1.

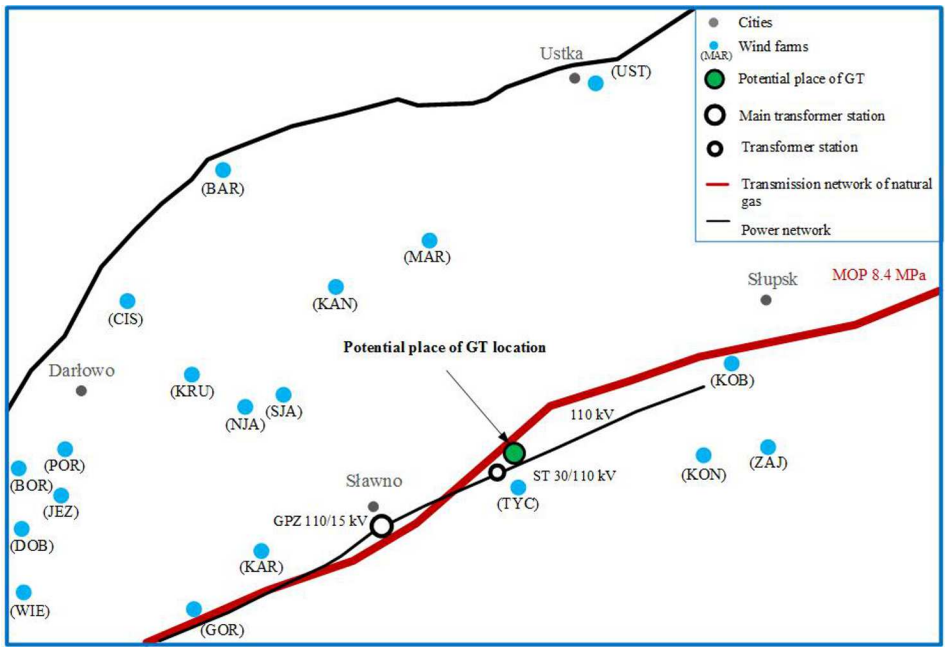

Figure 3: Analyzed area with the marked wind farms, natural gas transmission network and high voltage power grid.

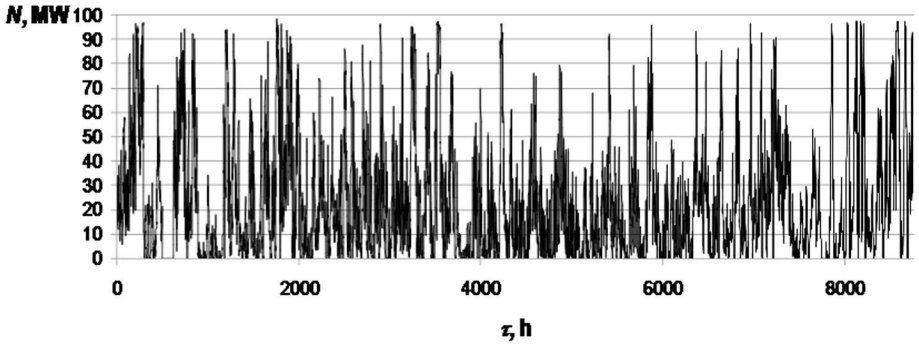

Figure 4: An example of power characteristics of wind farm with installed power of 100 MW for the annual operating cycle.

As the road distance to the GT increases, the installed power of wind farms, included in the storage system is increasing. The analyses considered the variants included in Tab. 2.

Table 1: The installed power of the analyzed wind farms and the road distance to the GT installation.

No.	Wind farm	Installed power, MW	Road distance to the GT, km
1	BAR	22.5	29
2	BOR	32.5	35
3	CIS	20.0	38
4	DOB	27.5	36
5	GOR	37.5	25
6	JEZ	27.5	35
7	KAN	20.0	25
8	KAR	40.0	19
9	KOB	41.4	20
10	KON	42.0	23
11	KRU	17.5	24
12	MAR	80.0	24
13	NJA	25.0	22
14	POR	24.0	38
15	SJA	22.5	20
16	TYC	50.0	1
17	UST	21.0	37
18	WIE	25.0	35
19	ZAJ	48.0	21

An assumption has been made that the particular installations of electrolysis operate in daily cycle and are supplied by electricity from a wind farm cooperating with it in the period of low demand (night valley), i.e., between 10 pm and 6 am. It was assumed that the efficiency of installation is equal to 67%. This quantity is defined as

$$\eta_{EI}=\frac{\dot{m}_{\mathrm{H2}}\,\mathrm{HHV}}{N_{\mathrm{EI}}}\ , \tag{1}$$

where: $\dot{m}_{\mathrm{H2}}$ – stream of produced hydrogen, HHV – Higher Heating Value, N_{EI} – electrical power supply of electrolysis installation.

A decisive factor for the amount of electricity to be stored is the so-called degree of storage, γ_s, defined as the ratio of the amount of electricity directed to electrolysis process, E_{el_EI}, to the total amount of electricity

Table 2: List of analyzed scenarios of a distributed storage system.

Variant	The total installed power of wind farms covered by the system, MW	Road distance to the GT, km
A	50	1
B	90	19
C	153.9	20
D	201.9	21
E	226.9	22
F	268.9	23
G	366.4	24
H	423.9	25
I	446.4	29
J	531.4	35
K	558.9	36
L	579.9	37
M	623.9	38

generated by wind farm during the year, E_{el_a}[4]:

$$\gamma_{\mathrm{s}} = \frac{E_{\mathrm{el\_EI}}}{E_{\mathrm{el\_a}}} \ . \tag{2}$$

The power supply of the electrolysis installation is limited by its nominal power determined at assumed value of γ_s or by instantaneous potential of the wind farm. In the period of low demand, the part of wind farm's power that does not supply the electrolysis installation is directed to the power grid. In the situation of low potential of wind farms, electrolysis installations operate with power supply lower than nominal.

An example of the daily characteristic of the installation operation with assumed the power characteristic of wind farm shown in Fig. 4 and $\gamma_s = 0.2$ was presented in Fig. 5. In order to obtain the assumed degree of storage, the required nominal power of the electrolysis installation cooperating with such a farm is 22.7 MW. In addition, in Fig. 5 the night valley period and the production of a wind farm directed at that time to the electrolysis installation were marked.

The surplus of electricity, occurring in the periods of night valleys and the production outside the night valleys which are directed to the power grid were also marked.

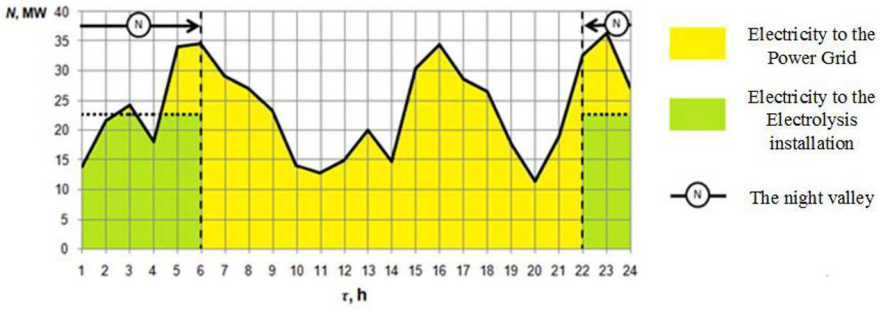

Figure 5: Randomly selected power characteristics of wind farm with installed power of 100 MW for daily operation cycle, with assumed degree of storage of 0.2 and determined nominal power of electrolysis installation (22.7 MW).

4 Gas turbine

It was assumed that the gas turbine, which is to be applied in the system, it is the GE LMS100 construction. The basic data of the turbine are summarized in Tab. 3.

To perform analyses, the own computational code which allows to simulate the change in operating parameters of a gas turbine unit in the case of load changes, ambient conditions and supply gas parameters other than those specified in the nominal operating point of the analyzed unit, were used [2]. The computation code of the gas turbine, which is presented in details in [2], allows simulations of gas turbines of various configurations, including units with inter-stage cooling of compressed air, as occurs in the analyzed GE LMS100PB gas turbine. A diagram of the gas turbine with marked characteristic points is presented in Fig. 6.

An important issue in the case of performing analyses for the commercially available turbines is to develop assumptions for calculations that will allow for the most accurate representation of the structural features of the unit. The model validation for nominal operating conditions of the gas turbine was made. For this purpose, the data, which are made available by manufacturers and literature [5–8] were used. In this case, the power of the gas turbine, the electrical efficiency, the compression ratio, the flue gas temperature behind the combustion chamber and the temperature of flue gas leaving the expander, are known. The basic input quantities in the computational algorithm are the compression ratio and the flue gas temperature behind the combustion chamber. Other sizes, among those

Table 3: Characteristic quantities for LMS100PB turbine.

Component	Characteristic quantity	Turbine model	GE LMS100PB	Unit
Inlet	Ambient temperature	15	15	°C
	Ambient pressure	101.325	101.325	kPa
	Relative humidity	60	60	%
	Pressure drop	1.0	NA	%
Compressors	Total compression ratio	42	42	-
	Air flow	225,4	NA	kg/s
	Pressure behind low-pressure compressor	390	390	kPa
	Pressure behind inter stages cooler	380	380	kPa
	Temperature behind cooler	35	35	°C
	Isentropic efficiency C (L)	88.0	NA	%
	Isentropic efficiency C(H)	88.0	NA	%
	Mechanical efficiency	99.5	NA	%
Combustion	Fuel	Natural gas	Natural gas	
	LHV (lower heating value)	50.0	NA	MJ/kg
	Stream of fuel	4.92	NA	kg/s
	Pressure drop	4.4	NA	%
Turbine	Outlet temperature of flue gas	1380	1380	°C
	Outlet temperature of flue gas	420.8	421.0	°C
	Isentropic efficiency of stage	89.0	NA	%
	Ratio of amount of cooling air	17.5	NA	%
	Cooling air distribution indicator	50/35/15/0	NA	%
	Outlet pressure of turbine	102.5	NA	kPa
	Stream of flue gas	230.3	NA	kg/s
	Mechanical efficiency	99.0	NA	%
Generator	Efficiency	98.5	NA	%
General	Power	108.0	108,0	MW
	Efficiency of electricity generation	43.92	43,90	%

mentioned above, are obtained as the results of calculations and are used for selection of other input quantities, which are present in the algorithm. The quantities taken from the literature, remaining assumptions and results from the calculations of the developed LMS100PB turbine model are presented in Tab. 3. As a nominal fuel, natural gas with 100% CH_4 was assumed.

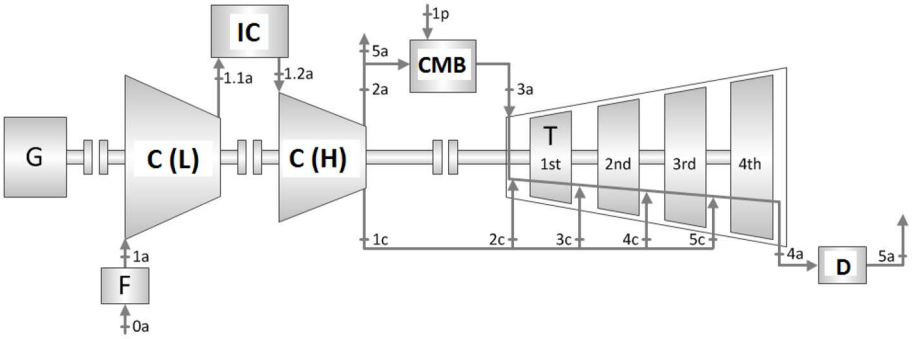

Figure 6: Diagram of gas turbine, where F – air filter, S – compressors (C(L) – low pressure section, C(H) – high pressure section), IC – inter stages cooler, CMB – combustion chamber, T – expander of turbine, G – electricity generator, D – dampler, a-air/exhaust, c – cooling air, p – fuel.

It was assumed that the gas turbine operates in a daily cycle, during the period of peak demand for electricity. In each case, a fuel is a mixture of hydrogen and natural gas, taken from the transmission network. During the analyses, the hydrogen volume content of the mixture was changed between 20% and 70%. The nominal power of the gas turbine (with natural gas) is 108 MW. In the framework of the present analyses, the impact of hydrogen content in the mixture with natural gas was also examined taking into account basic quantities of the gas turbine: efficiency and power. The characteristics of the effects of hydrogen volume fraction in the mixture with natural gas, on the efficiency of the gas turbine and its power is presented in Fig. 7.

5 Analyses results

The production potential of hydrogen depends on the total power of wind farms covered by the energy storage system, which for the indicated location is determined by the maximum distance determining the activity area, the

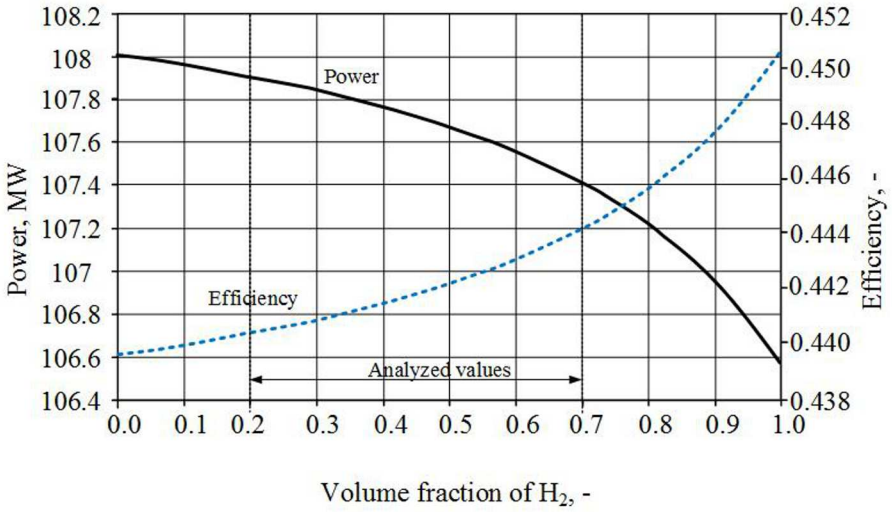

Figure 7: Power and efficiency of the gas turbine, as a function of the volume fraction of hydrogen in the gas mixture.

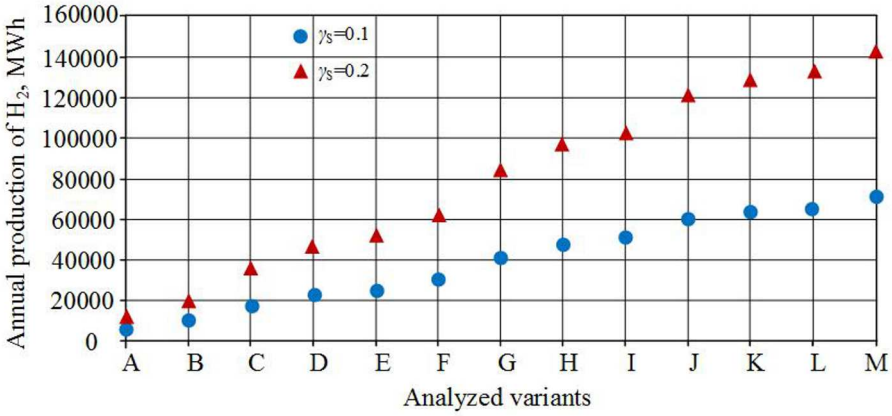

Figure 8: The amount of hydrogen produced in the year for the analyzed variants in case of two values of the degree of storage.

wind farm's production potential and the selected value of the degree of storage. The amount of produced hydrogen per year for different variants, differentiated by installed power of the wind farms is shown in Fig. 8. The presented results were obtained for two values of the degree of storage: 0.1 and 0.2.

In the case of the energy storage system, that is the subject of this analyses, the loading and unloading of the storage take place within the daily operation cycle. It should be noted that the GE LMS100 turbine is characterized by favourable start-up characteristics, mainly a short start-up time of approximately 10 min, from a cold condition. In the case of a gas turbine designed to work as a peak source of energy, the start-up time is important – the lower is operation time of the gas turbine, the more important it is. This is mainly due to relatively high fuel consumption in relation to electricity production. The start-up characteristics, showing the relative change in electrical power and relative change in the chemical energy flux of fuel (referenced to the nominal values), which was assumed for starting the turbine are shown in Fig. 9.

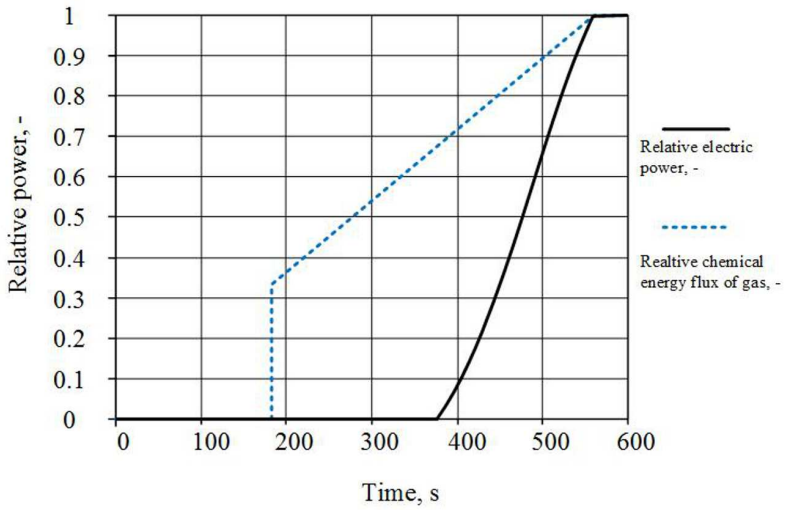

Figure 9: Relative electrical power and chemical energy flux during start-up of the analyzed turbine.

With the natural gas supply, the average efficiency of the GE LMS100 gas turbine at its start-up is only 19.07%. For the first hour of operation of this turbine, the average efficiency is 41.69%, which represented less than 95% of the nominal efficiency (43.9%). The start-up period, due to low efficiency, will affect the average efficiency of the turbine during its daily operation. The shorter operation time, the stronger impact of start-up period. The characteristics of the average efficiency, relative to nominal efficiency, as a function of operating time of gas turbine are shown in Fig. 10.

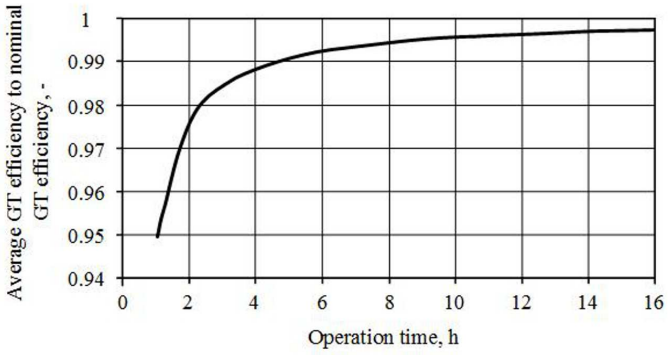

Figure 10: Average efficiency of gas turbine, relative to nominal efficiency, as a function of operating time.

As part of the analysis, the road distance from the gas turbine and thus the total installed power of the wind farms covered by the storage system, was changed. As shown in Fig. 8, the higher the distance, the greater the amount of stored hydrogen. The analyses were carried out for two different values of the degree of storage: 0.1 and 0.2. The maximum operation times of the gas turbine that would be required in the daily cycle of its operation for the energy use of the maximum amount of stored hydrogen with $\gamma_s = 0.1$ were presented in Fig. 11. Results for $\gamma_s = 0.2$ were summarised in Fig. 12. The work of the gas turbine for the analyzed energy storage system, should be planned in the period of peak daily demand for electricity. Such a period in the national power system occurs generally between hours 12 am and 8 pm. Assuming that the operating time of gas turbine in the daily cycle would be 8 hours, it could be seen that many of the analyzed options would not allow to use the total amount of stored hydrogen. For the degree of storage 0.1, this relates to selected cases, where the hydrogen content of the fuel mixture would be 20% and 30%. Accordingly, for a hydrogen fraction of 20% and 30%, the distance from the gas turbine should not be higher than 22 km (variant E, which corresponds to the power of 226.9 MW) and 25 km (variant H – 423.9 MW), respectively. In the case when the degree of storage is 0.2, with 20% hydrogen in the gas mixture, even a 24-hour gas turbine operation will not allow us to use all hydrogen production, if the road distance from gas turbine will be higher than 24 km (variant G – 366.4 MW).

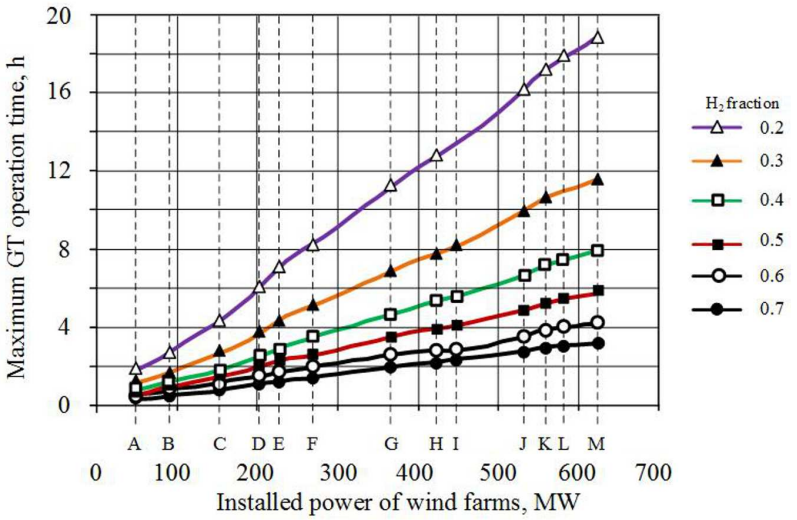

Figure 11: Influence of the amount of hydrogen in the mixture and the installed power of wind farms on the maximum daily operation time of the gas turbine for the degree of storage of 0.1.

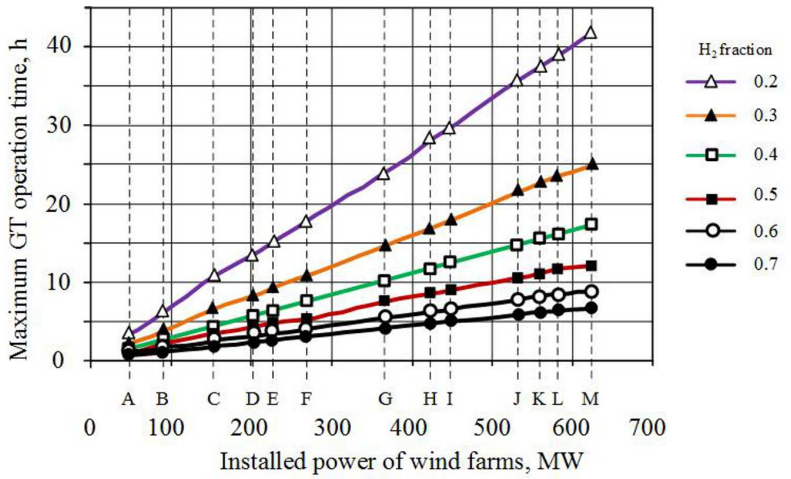

Figure 12: Influence of the amount of hydrogen in the mixture and the installed power of wind farms on the maximum daily operation time of the gas turbine for the degree of storage of 0.2.

A similar situation will occur with hydrogen content at 30% and the distance higher than 37 km (variant L – 579.9 MW). It was considered that

these cases may not take place and therefore no further analyses for these cases were carried out. With the operation time of eight hours, the distance limitation for hydrogen production will not occur at the hydrogen fraction of 0.7. For fractions of 0.6, 0.5, 0.4, 0.3, and 0.2, it will not be possible to utilize fully the stored hydrogen, if it is generated at a road distance from the gas turbine, higher than 35 km (variant J – installed power of wind farms 531.4 MW), 24 km (variant G – 366.4 MW), 23 km (variant F – 268.9 MW), 20 km (variant C – 153.9 MW) and 19 km (variant B – 90 MW) respectively.

The maximum turbine operation time is the one that will be required for the disposal of hydrogen which was stored during the maximum generation potential of hydrogen generators co-operating with wind farms. Due to the diverse potential of hydrogen production, the average daily operation time of the gas turbine in the year will be lower, as shown for the two different values of degree of storage in Figs. 13 and 14.

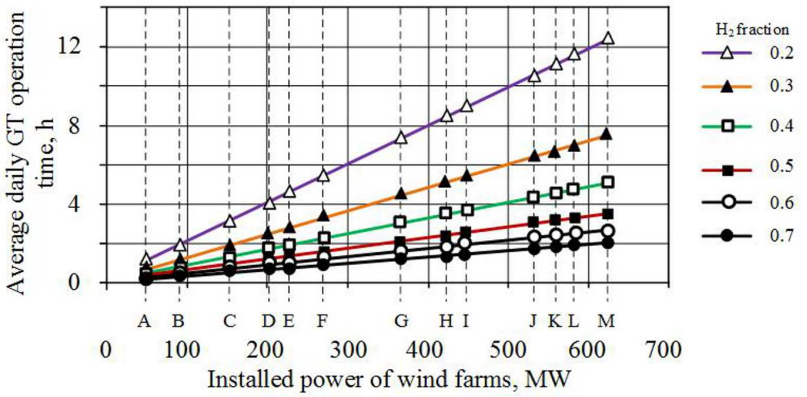

Figure 13: Influence of the amount of hydrogen in the mixture and the installed power of wind farms on the average daily operation time of the gas turbine for the degree of storage of 0.1.

As shown in Figs. 13 and 14, with the lower power of the wind farms covered by the system, the average daily operation time of the gas turbine is often less than 1 hour. For the degree of 0.1, at road distances of up to 22 km (variant E – 226.9 MW), regardless of the hydrogen content of the fuel mixture, the average daily working hours do not exceed in any case 5 hours. As shown in Fig. 9, the lower the operation time of the gas turbine, the lower the efficiency. In Figs. 15 and 16 respectively for the degrees of

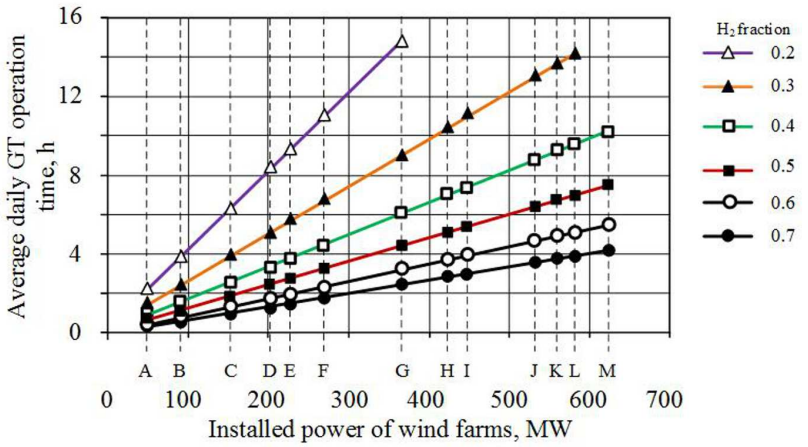

Figure 14: Influence of the amount of hydrogen in the mixture and the installed power of wind farms on the average daily operation time of the gas turbine for the degree of storage of 0.2.

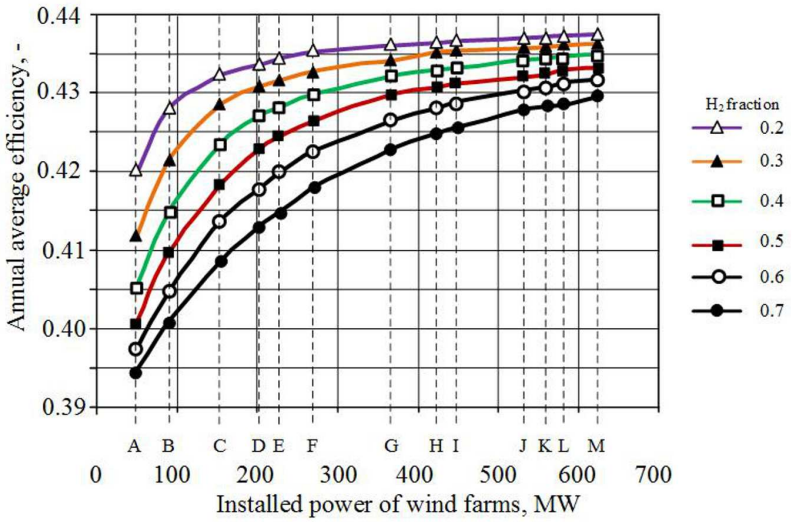

Figure 15: Influence of the amount of hydrogen in the mixture and the installed power of wind farms on the annual average efficiency of the gas turbine for the degree of storage of 0.1.

storage of 0.1 and 0.2 for various wind farms power and different hydrogen content in the fuel mixture, the annual average efficiency of the gas turbine is presented.

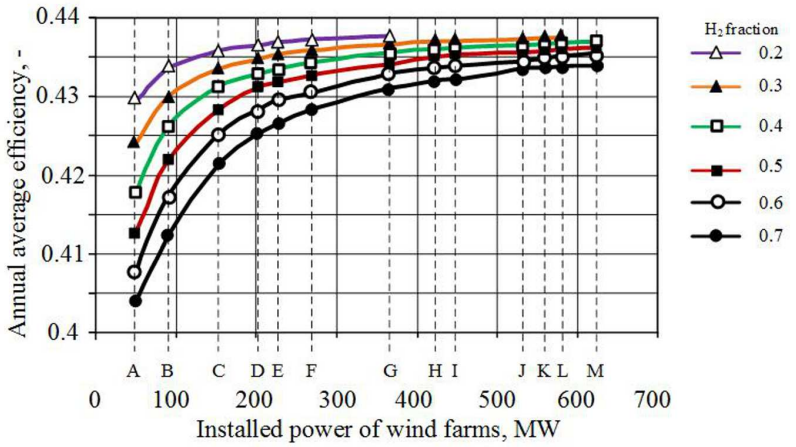

Figure 16: Influence of the amount of hydrogen in the mixture and the installed power of wind farms on the annual average efficiency of the gas turbine for the degree of storage of 0.2.

6 Economic analysis

The P2G2P technologies may in the future be an important mechanism to compensate for the disparities between the demand for electricity and its production within wind and solar power plants. Currently, there is an increased interest in energy storage systems [9,10]. The development of such an important energy industry as energy storage, which may decide, in the reasonably near future about energy security conditions, may require the development of various types of support mechanisms. Such support will be less required, when the storage systems are more efficient and cheaper. The analysis presented in this chapter shows the current economic potential of the energy storage system in question.

As part of the economic analysis, the break-even sales price of electricity was calculated from the condition

$$\mathrm{NPV} = 0\ . \tag{3}$$

NPV is a net present value that for the investment and operating period (for N years) is determined by the relation:

$$\mathrm{NPV} = \sum_{\mathrm{t}=0}^{\mathrm{t}=\mathrm{N}} \frac{CF_{\mathrm{t}}}{(1+r)^{\mathrm{t}}}\ , \tag{4}$$

where: CF_{t} – cash flows for the year t, r – the discount rate.

Cash flows CF_t are determined by the general relationship [2,11,12]

$$CF_{\mathrm{t}} = \left[-J + S - (K_{\mathrm{op}} + P_{\mathrm{d}}) + A + L\right]_{\mathrm{t}} \ , \tag{5}$$

where: J – total investment cost, S – net revenue, K_{op} – operating costs, P_{d} – income tax, A – depreciation, L – liquidation value. Therefore, the value of break-even sales price of electricity can be expressed as

$$C_{\mathrm{en.el.}}^{\mathrm{b-e}} = \frac{\sum\limits_{\mathrm{t=0}}^{\mathrm{t=N}} \dfrac{J + K_{\mathrm{op}} + T - A - L}{(1+r)^{\mathrm{t}}}}{\sum\limits_{\mathrm{t=0}}^{\mathrm{t=N}} \dfrac{E_{\mathrm{en.el}}}{(1+r)^{\mathrm{t}}}} \ , \tag{6}$$

where: T – taxes (the income and the property tax), $E_{\mathrm{en.el}}$ – electricity production, t – another year of analyses from $t = 0$ (start of construction) to $t = N$ (last year of analyses).

The investment cost of an energy storage system consisting of a number of electrolysis installations, resulting from the amount of wind farms included in the system and the installation of the gas turbine was estimated on the basis of the dependence

$$J = B\left(j_{\mathrm{GT}}\, N_{\mathrm{elGT,nom}} + j_{\mathrm{EI}} \sum N_{\mathrm{EI}}\right) , \tag{7}$$

where: B – a coefficient taking account of the cost of construction (it was assumed $B = 2$), j_{GT} – unit purchase cost of gas turbine, $N_{\mathrm{elGT,nom}}$ – nominal power of gas turbine, j_{EI} – unit purchase cost of electrolysis installation, N_{EI} – power of specific electrolysis installations. The unit purchase cost of gas turbine can be determined from a formula [2]

$$j_{\mathrm{GT}} = 21346\left(N_{\mathrm{elGT,nom}}\right)^{-0.271} . \tag{8}$$

The most important assumptions for the analysis are presented in Tab. 4 [2, 11-16]. On the basis of the adopted assumptions, the break-even sale price of electricity in accordance with Eq. (6) was determined. Within the analysis, it was assumed that the electricity directed to the storage is free. The results of the analysis for the two values of the degree of storage γ_s are shown in Figs. 17 and 18.

In analysing the results it can be noted that as the amount of hydrogen in the mixture increases, the break-even sales price of electricity increases.

Table 4: Basic assumptions for economic analysis.

Quantity		Value	Unit
Exploitation time		20	years
Construction time		2	years
Depreciation rate		6.67	%
Income tax rate		19	%
Discount rate, r		4.86	%
Unit cost of repair (% of the investment cost)	Year 1 2–3 4–7 8–11 12–15 16–20	1 1.5 2 2.5 3 3.5	%
Number of employees	Electrolysis installation GT installation	4 0.2	Person/installation Person/MW
Monthly salary including related costs		1163	EUR/per./month
Unit cost of transport H_2		1.67	EUR/kg
Unit price of CO_2 emission		6	EUR/Mg
Unit price of natural gas		7.75	EUR/GJ
Unit price of demineralised water		70	EUR/m^3
Unit price of electrolysis installation		1000	EUR/kW

Furthermore, it seems reasonable to consider larger storage systems with road distance from GT over 24 km (366 MW), that cooperate with electrolysis installations at the higher degrees of storage ($\gamma_s = 0.2$).

The lowest break-even sale price of electricity of 380 PLN/MWh was obtained for variant G, where the transport distance was 24 km, the installed power of the wind farms was 366.4 MW, the hydrogen fraction in mixture 0.2 and the degree of storage $\gamma_s = 0.2$. For this case, the impact of the unit price of the electrolysis installation and the unit price of deminer-

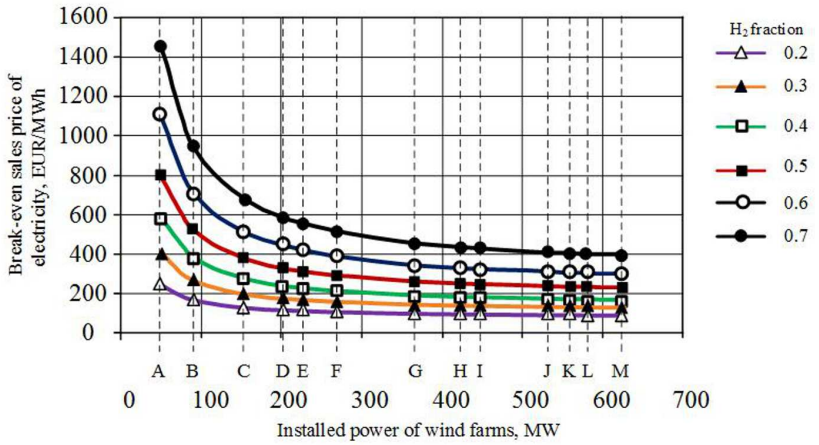

Figure 17: The break-even sale price of electricity depending on the amound of hydrogen in the mixture and the installed power of wind farms covered by the investment for the degree of storage of 0.1.

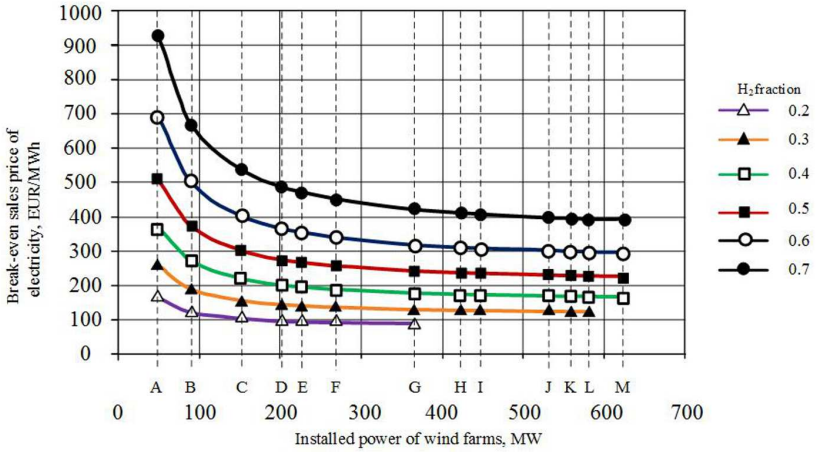

Figure 18: The break-even sale price of electricity depending on the amound of hydrogen in the mixture and the installed power of wind farms covered by the investment for the degree of storage of 0.2.

alised water on the value of break-even price of electricity were analyzed. The results are shown in Figs. 19 and 20.

When analyzing the impact of unit costs of an electrolysis installation, it can be assumed that, with the development of electrolysis technology and hydrogen generators, and thus falling unit prices, the investments in

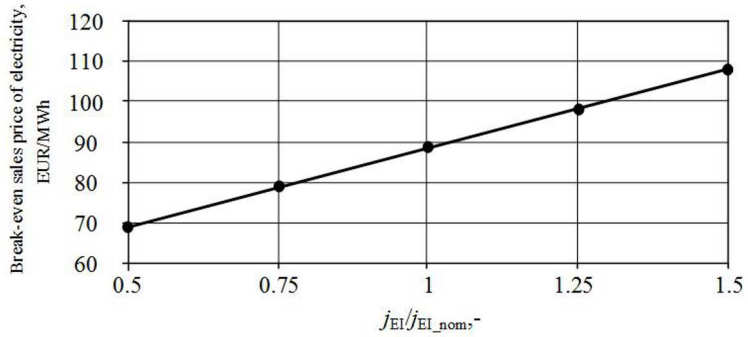

Figure 19: The break-even sale price of electricity for the most favourable case (variant G, the degree of storage of 0.2), depending on the unit price of the electrolysis installation.

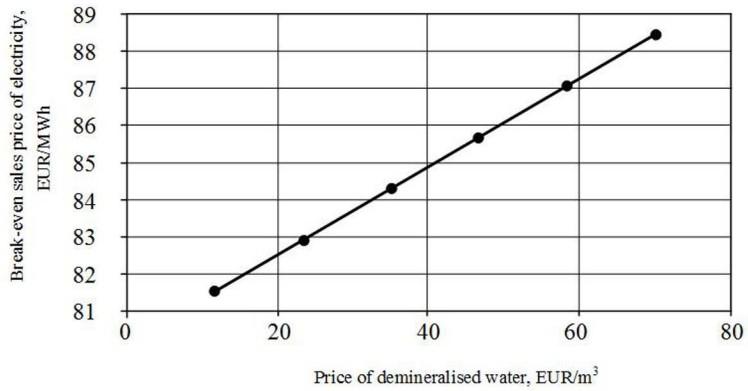

Figure 20: The break-even sale price of electricity for the most favourable case (variant G, the degree of storage of 0.2), depending on the unit price of demineralised water.

such technologies may become more attractive to potential investors. In addition, the installation of individual water purification modules should be considered to reduce the operating costs of the electrolysis installation.

7 Summary

An analysis of the energy storage system using water electrolysis as a one of the processes was performed. The variant assumed the use of a gas turbine powered by a mixture of hydrogen and natural gas taken from the gas transmission grid. The analyses allowed us to determine the basic energy

flows within the system and the selection of basic quantities, which can decide on the selection of machines and equipment. It was assumed that there is a gas turbine in the system with the characteristics of a turbine GE LMS100 available on the market. The calculations to demonstrate the effect of changing the fuel supplying the turbine on its operating characteristics were made using an own algorithm. The turbine calculations took into account the effects resulting from changes in energy and mass balances and did not consider the issue of kinetics of hydrogen combustion.

The analyzed case is the concept of large-scale energy storage, which is based on the use of wind farms with a total power of 623.9 MW. Such a large installation requires the use of very extensive infrastructure.

The analyzes were carried out for real location assumptions, determining regional potential for obtaining electricity for the hydrogen generation process. During the analyses, the road distance from the gas turbine site, thus the installed power of wind farms covered by the storage system was changed.

The results obtained indicated the significance of selection of the right value for the degree of storage γ_s. For specific gas turbine, this indicator decides about the daily time, in which the turbine is operated to ensure full utilization of the fuel. Economic analyses pointed to the advantage of systems with higher value of the degree of storage. No less important is the composition of the fuel mixture. The profitability analysis showed the advantage of lower hydrogen shares in the mixture with natural gas. It should be borne in mind that the possibility of construction of such a storage system depends on the functioning of the power system in the years to come, the interests of potential investors and companies responsible for the hydrogen infrastructure and on the development of support mechanisms for storage system.

Acknowledgements The research conducted within statutory research funds.

Received 2 October 2017

References

[1] www.ure.gov.pl (accessed 12.06.2017).

[2] Kotowicz J., Bartela Ł., Skorek-Osikowska A., Janusz-Szymańska K., Chmielniak T., Remiorz L., Iluk T.: *Thermodynamic and economic analysis*

of combined gas-steam cycle integrated with coal gasification and membrane separation of carbon diocide. Silesian University of technology Publishers, Gliwice 2012 (in Polish).

[3] http://www.imgw.pl (accessed [1.07.2017]).

[4] Kotowicz J., Bartela Ł., Węcel D., Dubiel K.: *Hydrogen generator characteristics for storage of renewably-generated*. Energy **118**(2017), 156–171.

[5] *GE Energy. LMS100: Flexible Power.*

[6] *GE Energy. New High Efficiency Simple Cycle Gas Turbine – GE's LMS100^{TM}.*

[7] Chmielniak T., Rusin A., Czwiertnia K,: *Gas Turbines*. Ossolineum, Wrocław 2001.

[8] Tabari A., Khaledi H., Benisi A.H.: *Comperative evaluation of advanced gas turbine cycles with modified blade cooling models*. In: Proc. GT2006, ASME turbo Expo 2006: Power for Land, Sea and Air, May 8-11, 2006, Barcelona.

[9] Bussar C, Stocker P, Cai Z, *et al.*: *Large-scale integration of renewable energies and impact on storage demand in a European renewable power system of 2050 – sensitivity study*. J. Energy Storage **6**(2016), 1–10.

[10] Milewski J, Szczęśniak A, Lewandowski J.: *Dynamic characteristics of auxiliary equipment of SOFC/SOEC hydrogen peak power plant*. IERI Procedia **9**(2014), 82-87.

[11] Kotowicz J., Bartela Ł.: *The influence of economic parameters on the optimal values of the design variables of a combined cycle plant*. Energy **35**(2010), 911–919.

[12] Kotowicz J, Bartela Ł.: *The influence of the legal and economical environment and the profile of activities on the optimal design features of a natural-gas-fired combined heat and power plant*. Energy **36**(2011), 1, 328–338.

[13] Singh, S., Jain, S., Ps, V., Tiwari, A.K., Nouni, M.R., Pandey, J.K., *et al.*: *Hydrogen: A Sustainable Fuel for Future of the Transport Sector*. Renew. Sust. Energ. Rev. **51**(2015), 623–633.

[14] Bartela Ł., Kotowicz J., Dubiel K.: *Technical – economic comparative analysis of the energy storage systems equipped with the hydrogen generation installation*. J. Power Technologies **96** (2016), 2, 92–100.

[15] http://vertis.com (accessed 18.09.2017).

[16] Weinert J.X., Shaojun L., Ogden J.M., Jianxin M.: *Hydrogen refueling station costs in Shanghai*. Int. J. Hydrogen Energ.**32**(2007), 4089–4100.

archives
of thermodynamics
Vol. **38**(2017), No. 4, 89–107
DOI: 10.1515/aoter-2017-0026

The influence of stack position and acoustic frequency on the performance of thermoacoustic refrigerator with the standing wave

JAKUB KAJUREK*
ARTUR RUSOWICZ
ANDRZEJ GRZEBIELEC

Warsaw University of Technology, Institute of Heat Engineering, Nowowiejska 21/25, 00-665 Warszawa, Poland

Abstract Thermoacoustic refrigerator uses acoustic power to transport heat from a low-temperature source to a high-temperature source. The increasing interest in thermoacoustic technology is caused due to its simplicity, reliability as well as application of environmentally friendly working fluids. A typical thermoacoustic refrigerator consists of a resonator, a stack of parallel plates, two heat exchangers and a source of acoustic wave. The article presents the influence of the stack position in the resonance tube and the acoustic frequency on the performance of thermoacoustic refrigerator with a standing wave driven by a loudspeaker, which is measured in terms of the temperature difference between the stack edges. The results from experiments, conducted for the stack with the plate spacing 0.3 mm and the length 50 mm, acoustic frequencies varying between 100 and 400 Hz and air as a working fluid are consistent with the theory presented in this paper. The experiments confirmed that the temperature difference for the stack with determined plate spacing depends on the acoustic frequency and the stack position. The maximum values were achieved for resonance frequencies and the stack position between the pressure and velocity node.

Keywords: Thermoacoustic; Thermoacoustic refrigerator; Stack position; Acoustic frequency

*Corresponding Author. Email: jakub.kajurek@itc.pw.edu.pl

Nomenclature

a	–	speed of sound, m/s
A	–	cross-sectional area, m^2
BR	–	blockage ratio
c_p	–	isobaric heat capacity, J/(kg K)
c_s	–	heat capacity of the stack plates, J/(kg K)
DR	–	drive ratio
f	–	frequency, Hz
i	–	imaginary unit
$\dot{H}$	–	energy flux, W
k	–	wave number, 1/m
K	–	thermal conductivity, W/(m K)
l	–	half of the plate thickness, m
L	–	length, m
p	–	pressure, Pa
Pr	–	Prandtl number
$\dot{Q}$	–	heat flux, W
s	–	entropy, J/(kg K)
t	–	time, s
T	–	temperature, K
u	–	velocity in x direction, m/s
w	–	velocity in y direction, m/s
$\dot{W}$	–	acoustic power, W
y_0	–	half of the plate spacing, m
x	–	longitudinal coordinate to acoustic wave propagation direction, m
y	–	perpendicular coordinate to acoustic wave propagation direction, m

Greek symbols

β	–	thermal expansion coefficient, 1/K
δ_k	–	thermal penetration depth, m
δ_v	–	viscous penetration depth, m
ϵ_s	–	plate heat capacity ratio
Γ	–	normalized temperature gradient
κ	–	ratio, isobaric to isochoric specific heats
λ	–	wavelength, m
π	–	perimeter, m
ρ	–	density, kg/m^3
ω	–	angular frequency, rad/s

Superscripts

A	–	amplitude
c	–	center
$crit$	–	critical
m	–	mean
n	–	normalized
s	–	solid or standing
1	–	fluctuating part

1 Introduction

In recent years the environmental aspects of refrigeration systems have become more important. Hence, the current interests of researchers focus on the development of alternative technologies, which will be able to replace solutions based on hazardous refrigerants. One of the most promising approach in the field of the alternative cooling systems is the thermoacoustic refrigeration [1]. Other solutions include adsorption and the absorption devices [2,3].

The theory of thermoacoustic includes all the effects in which heat and acoustic energy are transported together or mutually transformed [4]. The devices that convert heat to acoustic energy are called thermoacoustic engines, and the devices that use acoustic energy to transport heat from a low-temperature source to a high-temperature source are called thermoacoustic refrigerators [5]. The increasing interest in the thermoacoustic technology is not only due to its environmentally friendly working fluids, but also because of its simplicity and reliability – the thermoacoustic devices have no moving components and sliding seals [6]. Despite many advantages of the thermoacoustic technology, it has still not reached technical maturity. The thermoacoustic refrigerators, as a result of lower efficiency than the commercial refrigerators, are not yet competitive. They achieve 10 to 20% of Carnot efficiency as opposed to 33 to 50% for conventional solutions [7]. Thus, many efforts are taken to improve and optimize the design and the performance of the thermoacoustic devices.

The paper investigates the influence of stack position in the resonance tube and the acoustic frequency on the performance of standing wave thermoacoustic refrigerator. Nine different stack positions at four frequencies were examined in terms of temperature difference across the stack ends at a prototype device driven by a loudspeaker and air as a working fluid, assembled for experimental setup. Besides the results and conclusions presented in last paragraphs, the basis of the thermoacoustic theory and construction of the thermoacoustic refrigerators are also discussed in this paper.

2 Thermoacoustic theory

The thermoacoustic devices include two thermodynamic media: an oscillating fluid and a solid, such as a thin plate [8]. The plate introduced into the oscillating fluid, because of the heat transfer with the fluid, modifies the

original temperature oscillations caused by the acoustic wave, both in magnitude and in phase, about a thermal penetration depth $\delta_k = \sqrt{K/(\rho_m c_p \omega)}$ away from the plate. Therefore, in the fluid the heat can be transported in parallel to the plate and acoustic power can be absorbed or produced [5].

2.1 Thermodynamic cycle

The thermodynamic cycle of thermoacoustic devices can be explained by considering a solid plate aligned in the direction of acoustic standing wave, with imposed mean-temperature gradient ∇T_m along the plate. Because of the acoustic wave the gas parcel near the plate experiences changes in pressure, velocity and temperature. On the one hand the temperature changes of gas parcel comes from its adiabatic compression and expansion by acoustic wave, on the other, it is a result of heat transfer between the plate and the fluid. The heat flow between these two media creates a time delay in temperature oscillation, which is needed to realize a thermodynamic cycle by the fluid parcels [5]. But not every parcel is driven through the thermodynamic cycle. Those, which are far from the plate have no thermal contact and are simply compressed and expanded adiabatically by acoustic wave, while the parcels that are too close the plate have a very good thermal contact and are simply compressed and expanded isothermally. The elements of fluid, at about a distance of a thermal penetration depth from the plate, have enough of good thermal contact (imperfect thermal contact) to exchange some heat, and thus create a time delay between heat transfer and the motion [9].

Whether the plate works as a refrigerator or as an engine depends on the magnitude of the mean temperature gradient imposed on the plate relative to a critical temperature gradient, defined as [5]

$$\nabla T_{crit} = T_m \frac{\beta \omega p_1}{\rho_m c_p u_1^s} \,. \tag{1}$$

The critical temperature gradient is a value for which the temperature change due to adiabatic compression and expansion matches the temperature change due to parcel's motion along the plate with given mean temperature gradient ∇T_m. For $\nabla T_m < \nabla T_{crit}$ the acoustic energy is absorbed, and the heat is transported in the mean temperature gradient direction (refrigerator cycle). For $\nabla T_m > \nabla T_{crit}$ the acoustic energy is generated by utilizing heat flowing against the mean temperature gradient (engine cycle) [10].

The refrigeration cycle of a fluid parcel in the thermoacoustic refrigerator is shown in Fig. 1. To keep things simple, the acoustic wave is considered as a square wave. In the first step, under the influence of standing wave, the fluid parcel is compressed adiabatically, moves towards the pressure antinode and increases in temperature by an amount $2T_1$. After the displacement, the fluid parcel is warmer than the plate, so in the second step heat flows irreversibly at constant pressure from the parcel to the plate. In the third step, the fluid parcel moves back to its initial position, expands and cools down adiabatically. After the displacement in opposite direction the fluid parcel is colder than the plate, and in the fourth step irreversible constant pressure heat transfer from the plate towards the fluid parcel takes place. The fluid parcel after this process reached its initial parameters, so also completed the thermodynamic cycle.

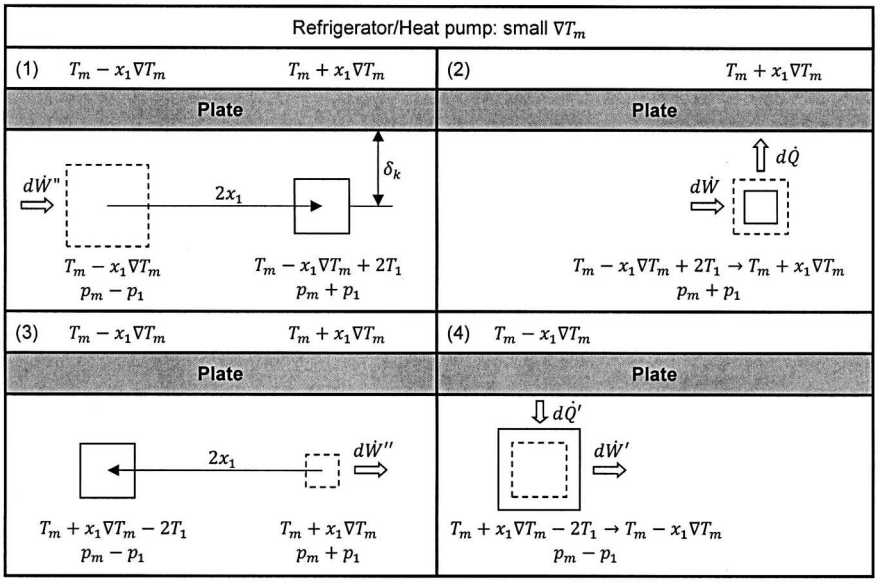

Figure 1: Thermodynamic cycle of the fluid parcel in a thermoacoustic refrigerator.

In most cases the length of the plate is larger than the displacement of given fluid parcel. Thus, the heat from one end of the plate to the other is transported by a series of fluid parcels (Fig. 2). During the first part of refrigeration cycle each parcel moves towards pressure antinodes and leaves at its maximum displacement an amount of heat. During the second half

of the same cycle, the parcels moves backs to their starting position and pick up from the plate the same amount of heat, which was deposited there a half cycle earlier by the adjacent parcel. In effect, the heat is transferred from one end to the other by gas parcels as bucket bridge and the plate is used only for the temporary storage of heat [6].

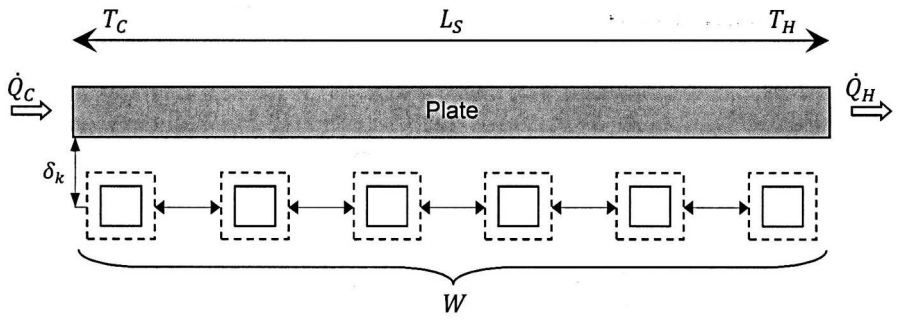

Figure 2: Heat transfer by the gas parcels along the stack plate, $\dot{Q}_c$, $\dot{Q}_H$ – cold-side and hot-side heat flux.

2.2 Mathematical model

The heat flux transported along the single plate under ordinary circumstances is small. However, in typical devices the entire cross section of the standing wave is filled by the parallel plates, and thus high heat fluxes can be easily achieved. The simplified model of the stack is considered with the following assumptions [5,7,11]:

- theory is linear, second-order effects other than energy transport, such as acoustic streaming are neglected;
- plate is perfectly rigid and stationary;
- plates have the thicknesses $2l$ and spacing $2y_0$ (Fig. 3);
- temperature spanned along the stack is much smaller than the absolute temperature and thus the thermophysical properties of the fluid can be assumed independent of coordinate longitudinal to the acoustic wave propagation direction (x);
- length of the stack plates is much shorter than wavelength (short stack approximation) and hence the pressure and parcel velocities can be

considered constant along the stack and the stack does not affect the acoustic standing wave;

- ratio between half the plate spacing y_0 and the thermal penetration depth δ_k is much greater than one (boundary layer approximation), which causes that the complex hyperbolic tangents, which arise in the solution of the short boundary layer approximation can be set to unity;
- mean fluid velocities are zero;
- acoustic amplitudes are assumed low enough to avoid turbulence;
- all variables oscillate at angular frequency ω:

$$p = p_m + p_1(x)e^{i\omega t} \,, \tag{2}$$

$$\rho = \rho_m\,(x) + \rho_1\,(x,y)\,e^{i\omega t} \,, \tag{3}$$

$$\overrightarrow{\mathrm{v}}_1 = \overrightarrow{x}\,u_1\,(x,y)\,e^{i\omega t} + \overrightarrow{y}\,w_1\,(x,y)\,e^{i\omega t} \,, \tag{4}$$

$$T = T_m\,(x) + T_1\,(x,y)\,e^{i\omega t} \,, \tag{5}$$

$$T_s = T_m\,(x) + T_{s1}\,(x,y)\,e^{i\omega t} \,, \tag{6}$$

$$s = s_m\,(x) + s_1(x,y)e^{i\omega t} \,, \tag{7}$$

where the terms with the subscript m denote the mean value and with the subscript '1' the fluctuating part of the individual variables. With these approximations, the standing wave acoustic pressure and velocity can be written as [5]:

$$p_1 = p_A \sin\,(kx) \,, \tag{8}$$

$$u_1 = i\left(1 + \frac{l}{y_0}\right)\left(\frac{p_A}{\rho_m a}\right)\cos\,(kx) = iu_1^s \,. \tag{9}$$

The expressions for energy flux and acoustic power in the stack of thermoacoustic devices, derived from the time average equations of continuity, motion and energy, are described as [5]:

$$\begin{aligned}\dot{H} = &-\frac{1}{4}\pi\delta_k \frac{T_m\beta p_1\,\langle u_1^s\rangle}{(1+\epsilon_s)\,(1+\mathrm{Pr})\left(1-\frac{\delta_v}{y_0}+\frac{\delta_v^2}{2y_0^2}\right)} \\ &\times\left[\Gamma\frac{1+\sqrt{\mathrm{Pr}}+\mathrm{Pr}+\mathrm{Pr}\epsilon_s}{1+\sqrt{\mathrm{Pr}}}-\left(1+\sqrt{\mathrm{Pr}}-\frac{\delta_v}{y_0}\right)\right] \\ &-\Pi\,(y_0K + lK_s)\,\frac{dT_m}{dx} \,,\end{aligned} \tag{10}$$

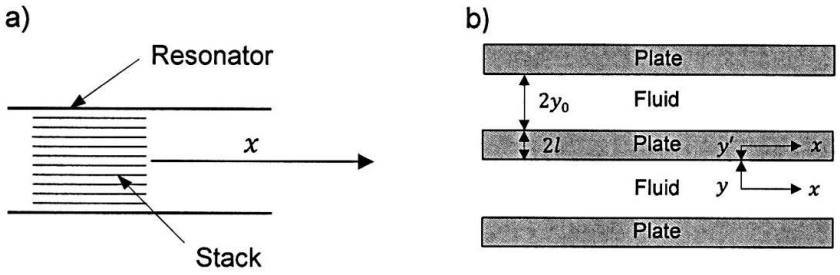

Figure 3: Stack geometry: a) overall view, b) expanded view.

$$\dot{W} = \frac{1}{4}\Pi_k \triangle x \frac{(\kappa-1)\,\omega p_1^2}{\rho_m a^2\,(1+\epsilon_s)} \times \left(\frac{\Gamma}{\left(1+\sqrt{\mathrm{Pr}}\right)\left(1-\frac{\delta_v}{y_0}+\frac{\delta_v^2}{2y_0^2}\right)} - 1 \right)$$

$$-\frac{1}{4}\Pi_v \triangle x \frac{\delta_m \langle u_1^s \rangle^2}{1-\frac{\delta_v}{y_0}+\frac{\delta_v^2}{2y_0^2}}\,, \tag{11}$$

where $\langle u_1^s \rangle$ is the mean velocity in x direction defined as $\langle u_1 \rangle = \frac{1}{y_0}\int_0^{y_0} u_1 dy = i\,\langle u_1^s \rangle$, Γ is the normalized temperature gradient described as $\Gamma = \nabla T_m / \nabla T_{crit}$ and ϵ_s is the plate heat capacity ratio expressed as $\epsilon_s = \sqrt{K\rho_m c_p / (K_s \rho_s c_s)}$. The first term in energy flux (10) describes the heat flux transported due to the thermoacoustic effect, the second term is just the ordinary conduction of heat down the temperature gradient by the fluid and solid [5].

The Eqs. (10) and (11) indicate that there are 18 independent parameters, which influence the performance of the thermoacoustic devices. These parameters can be divided into three groups [7]:

- Design and operational requirements of thermoacoustic device, such as desired cooling or acoustic power, acoustic frequency, mean pressure and mean temperature, pressure amplitude and temperature gradient imposed on the stack.
- Material related variables, which describe the thermophysical properties of the working fluid and the stack plates.

- Geometry design parameters like plate thickness or spacing.

The number of independent parameters from Eqs. (10)–(11) can be reduced through normalization. The normalized energy flux with neglected heat conduction, both in the plate and fluid, and normalized acoustic power are given as [12]:

$$\dot{H}_n = -\frac{1}{8\kappa}\delta_{kn}(\mathrm{DR})^2\frac{\sin(2x_{cn})}{(1+\mathrm{Pr})\,\Lambda}\left[\Gamma\frac{1+\sqrt{\mathrm{Pr}}+\mathrm{Pr}}{1+\sqrt{\mathrm{Pr}}}-(1+\sqrt{\mathrm{Pr}}-\sqrt{\mathrm{Pr}}\delta_{kn})\right] \tag{12}$$

$$\dot{W}_n = \frac{1}{4\kappa}\delta_{kn}(\mathrm{DR})^2 L_{sn} \times\left[\mathrm{BR}\,(\kappa-1)\cos^2(x_{cn})\left(\frac{\Gamma}{1+\sqrt{\mathrm{Pr}}}-1\right)-\frac{\sin^2(x_{cn})\sqrt{\mathrm{Pr}}}{\mathrm{BR}\Lambda}\right], \tag{13}$$

where

$$\Lambda = 1-\delta_{kn}\sqrt{\mathrm{Pr}}+\frac{1}{2}\mathrm{Pr}\delta_{kn}^2\,. \tag{14}$$

The normalized parameters are equal:

$$\Gamma=\frac{\nabla T}{\nabla T_{crit}}=\frac{\Delta T_{mn}\tan(x_{cn})}{\mathrm{BR}(\kappa-1)L_{sn}}, \qquad \delta_{kn}=\frac{\delta_k}{y_0},$$
$$\mathrm{DR}=\frac{p_1}{p_m}, \qquad \delta_{vn}=\frac{\delta_v}{y_0},$$
$$\dot{H}_n=\frac{\dot{H}}{p_m a A}, \qquad L_{sn}=k\triangle x,$$
$$\dot{W}_n=\frac{\dot{W}}{p_m a A}, \qquad x_{cn}=kx,$$
$$\Delta T_{mn}=\frac{\Delta T_m}{T_m}, \qquad \mathrm{BR}=\frac{y_o}{(y_0+l)}.$$

3 Thermoacoustic refrigerators

3.1 Classification

Thermoacoustic refrigerators can be categorized depending on the phase shift between the pressure and velocity oscillations in acoustic wave [13]. For a pure standing-wave the pressure and velocity oscillations are $\pi/2$

out of phase, while for a travelling wave are in phase. Therefore, the simple straight-line resonator such as closed-closed $\lambda/2$ or a closed-open $\lambda/4$ tube is needed to provide necessary acoustic environment for standing wave (Fig. 4a), and looped tube for travelling wave (Fig. 4b).

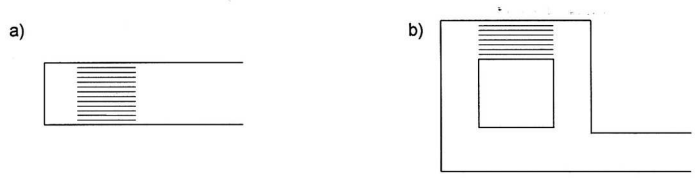

Figure 4: Schematic illustrations of resonator configurations: a) for standing wave, b) for travelling wave.

Another classification of the thermoacoustic refrigerators can be based on the source of acoustic wave. If the acoustic energy is delivered from the thermoacoustic engines, the devices are called thermoacoustically-driven thermoacoustic refrigerators. While, if the acoustic energy is provided by an acoustic driver, for example a loudspeaker, the devices are called acoustically-driven thermoacoustic refrigerators [6].

3.2 Construction

A schematic illustration of the acoustically-driven thermoacoustic refrigerator with standing wave is shown in Fig. 5. The device consists of parts such as an acoustic driver, a stack, a resonator, the heat exchangers and a working fluid.

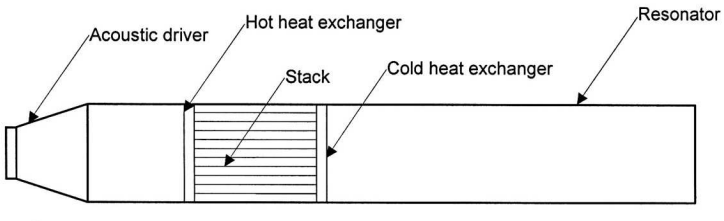

Figure 5: Schematic illustration of the standing wave thermoacoustic refrigerator with an acoustic driver.

3.2.1 Acoustic driver

The acoustic driver generates an acoustic wave with determined frequency and pressure amplitude. Commercial, moving-coil loudspeakers with wide range of frequencies are widely used. They are cheap, compact and can be easily adapted to the thermoacoustic refrigerators. But they have also one important disadvantage – low efficiency, which decreases the overall efficiency of the device. Thus, many drivers are modified to reduce the losses [12,14,15].

3.2.2 Heat exchangers

The heat exchangers in the thermoacoustic refrigerator are needed to supply heat from a low-temperature reservoir to cold end of the stack and extract heat from the hot end of the stack to a high-temperature reservoir. They should provide high heat transfer coefficients and low dissipation of acoustic power. Three types of heat exchangers are suitable for thermoacoustic refrigerators: parallel-strips, finned-tubes, and flat-tube-banks [16]. The maximum length of heat exchanger should be roughly two times the fluid parcel displacement [5].

3.2.3 Stack

The stack is the most important part of the thermoacoustic refrigerator, in which the heat-pumping process takes place. There are many different stack geometries: parallel plates, circular pores, pin arrays, triangular pores [12]. The main objective for stack geometry selection is to increase the thermal boundary layer surrounding the solid wall where the thermoacoustic effect could occur [17]. The optimal stack spacing for the parallel plates is between $2\delta_k$ to $4\delta_k$, where δ_k is the thermal penetration depth [14,15]. The stack length must meet the short stack approximation. For given operation parameters the maximum length exists, above which performance starts to decrease [7]. The stack material should minimize the losses caused by the ordinary heat conduction along the temperature gradient [5]. The most commonly used material for the stack is Mylar [12,14,15]. Typically, the stack is located closer to the pressure antinode than the pressure node. The optimal location depends on the viscous and thermal relaxation losses [17]. The optimal stack centre position proposed by Swift is $\lambda/20$ measured away from the pressure antinode [18], whereas the value postulated by Tijani it is

$\lambda/8$ [12]. In most of other experiments the optimum position falls between these two quantities [17].

3.2.4 Resonator

The resonance tube encloses heat exchangers, the stack, acoustic driver and the working fluid. The length of resonator is determined by resonance frequencies, in most cases the tubes are the quarter wave length or half wave length. The simplest and most appropriate geometry of the resonance tube is cylinder [7], but rectangular geometries are also used [19,20]. The resonator material should have large acoustic impedance to minimize the losses in acoustic wave [20].

3.2.5 Working fluid

The working fluid properties play an important role in determining cooling power and efficiency. The best working fluids for the thermoacoustic refrigerators have high ratios of specific heat and low Prandtl number [21]. These properties are sometimes optimized by using a binary mixture of helium and other noble gases [22]. In experiments related with the thermoacoustic devices air is widely used because of its availability [17].

4 Experimental setup

The schematic illustration of experimental apparatus, which let only measure the temperature across the stack, is shown in Fig. 6. It consists of the loudspeaker, the resonator, the stack, the amplifier, sound generator and measuring devices. The refrigerator has no heat exchanger at the ends of the stack, because the main aim of the experiment is to examine temperature difference across the stack ends under various operating conditions – stack positions and acoustic frequencies.

The loudspeaker constitutes the acoustic wave source. It has a frequency in the range of 40–500 Hz, 200 W RMS continuous power and 4 Ω nominal impedance. The loudspeaker is excited by the amplifier fed with a sinusoidal signal, provided by the software installed on the computer. The amplifier has a frequency response in the range of 20–20000 Hz and distortion less than 0.01%. The resonance tube is rectangular with the inner dimensions 0.045 m x 0.045 m, length of 2 m and is filled with air at atmospheric pressure. One end of the resonator is connected to the loudspeaker, second

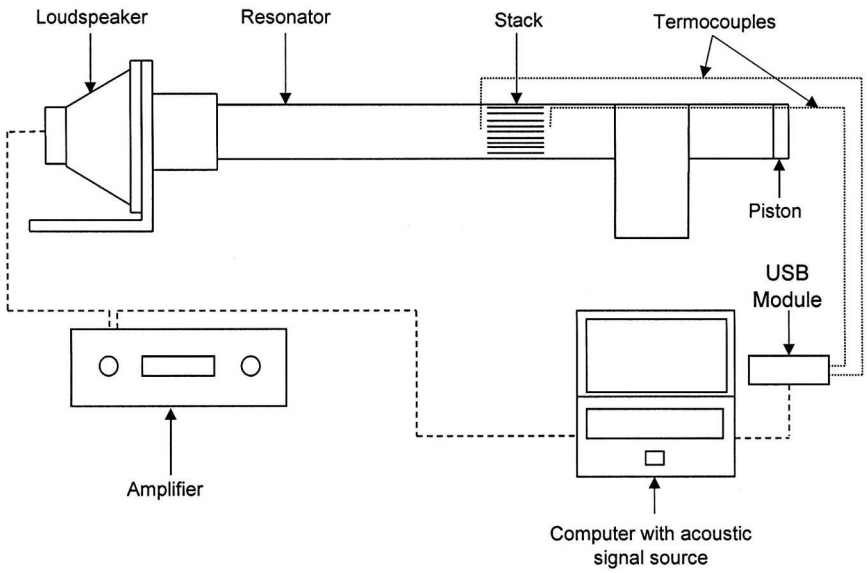

Figure 6: Schematic illustration of experimental apparatus.

is closed with the cork piston. The resonator length can be adjusted to the operating frequency by the change of piston position. The stack consists of parallel plates with dimensions 0.00178 m x 0.045 m x 0.05 m, which are spaced by the fishing line with 0.003 m thickness (Fig. 7). The plates are made from PET. The temperature difference across the stack is measured by the type-T thermocouples, which are connected to the USB module – data acquisition card. The value of the temperature for each end of the stack is then displayed by the special program installed on the computer, with the accuracy 0.1 K and is saved in the *.xlsx file.

The experiments were done at four different acoustic frequencies: 100, 200, 300 and 400 Hz, and nine different positions of the stack centre: $L_s/2$, $\lambda/16$, $\lambda/8$, $3\lambda/16$, $\lambda/4$, $5\lambda/16$, $3\lambda/8$, $7\lambda/16$, $\lambda/2$- $L_s/2$, where L_s is the stack length (50 mm) and λ is the acoustic wave length, for given frequency calculated based on equation:

$$\lambda = \frac{a}{f} \,. \tag{15}$$

The first and the last stack positions were limited by the resonator length, which in these measurements was equalled to the half-length of acoustic wave. The temperature difference was read, when the steady state was

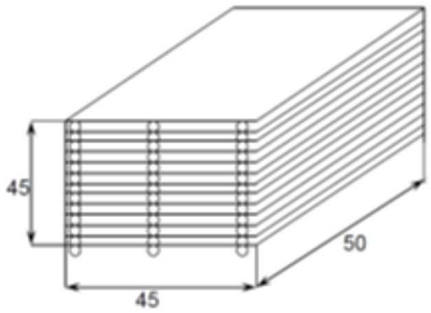

Figure 7: Schematic illustration of parallel plate stack.

achieved. Additionally, for determined resonator length, the influence of other frequencies than resonance – remaining three, was investigated (e.g., for resonator length corresponding to 100 Hz also for 200, 300, and 400 Hz).

5 Experimental results and discussion

The temperature differences between the stack ends as functions of stack position in the resonance tube at four resonance frequencies are shown in Fig. 8, where λ is the wave length for given frequency (100, 200, 300 or 400 Hz) and L_s is the stack length. For all frequencies, the dependence is close to the sinusoid, with the maximum values shifted toward the pressure antinode, which follow from the product DR$= p_1/p_m$ in Eq. (12). The maximum temperature difference for each frequency was achieved for the stack centre position at $\lambda/16$, while zero for $\lambda/4$, where λ is the pressure node at which heat flow vanishes (Eq. (12)). The temperature difference changes sign as the pressure gradient changes sign, however, for stack positions located further from the loudspeaker, behind the pressure node, the temperature differences are smaller than for the positions closer to the loudspeaker, for example $7\lambda/16$ versus $\lambda/16$, which is a consequence of acoustic power dissipation in the resonance tube.

Figure 8 indicates also that the temperature difference for the stack with determined length and plate spacing depends on acoustic frequency. The highest temperature difference is almost the same for 200 and 300 Hz, and is nearly equal to 16 K. The optimal frequency for investigated stack with 0.3 mm plate spacing should be between these two frequencies. The tem-

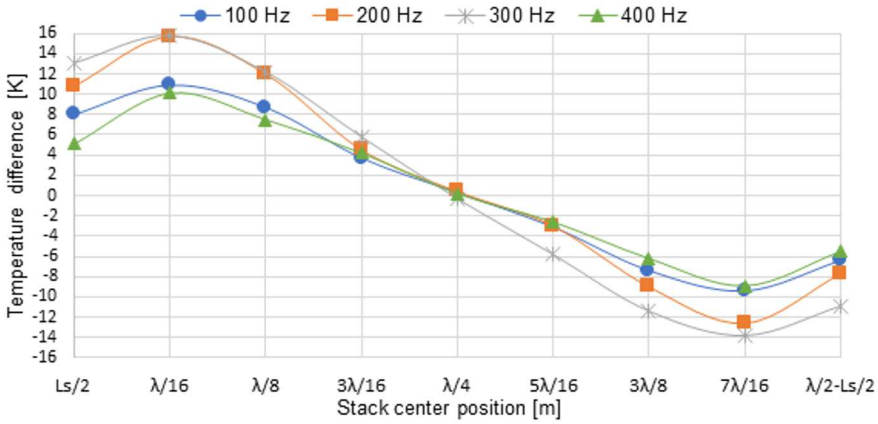

Figure 8: Temperature difference between stack ends versus stack position for resonance frequencies.

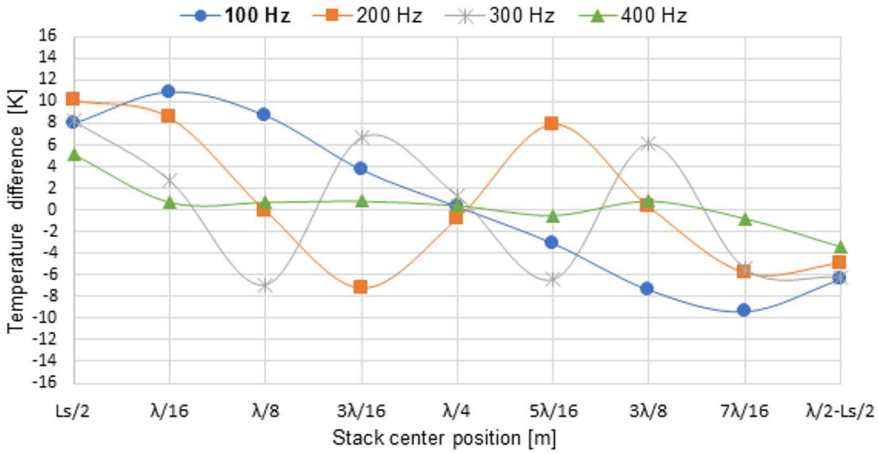

Figure 9: Temperature difference between stack ends versus stack position with main resonance frequency 100 Hz (λ is the wave length for 100 Hz).

perature differences for 100 and 400 Hz are lower than for 200 and 300 Hz. For 100 Hz, the thermoacoustic effect is reduced by the viscous losses. The plate spacing $2y_o$ is then around $1.6\delta_k$, where δ_k is the thermal penetration depth. This means also that for 100 Hz and plate spacing 0.3 mm the boundary layer approximation is not met (Sec. 2.2). For 400 Hz, the temperature distribution might be affected by the stack length.

The temperature differences across the stack for frequencies other than the resonance and resonator length other than the half-length of acoustic wave are shown in Figs. 9–12, where λ is the wave length of frequency bolded in given figure. In every case the highest temperature difference was achieved for resonator length corresponding to the half-length of acoustic wave.

Figure 9 presents the results for resonator length equal to: $\lambda/2$ for 100 Hz, λ for 200 Hz, 1.5λ for 300 Hz, and 2λ for 400 Hz. Every investigated frequency in this case is the resonance frequency. The temperature dependence of stack position is close to a sinusoid again, with zeros at both pressure and velocity nodes (or antinodes). For 400 Hz the positions, beyond first and last, are in the pressure or velocity node and thus the relation in Fig. 9 is partly linear. The maximum temperature differences obtained for 200 Hz and 300 Hz are close to the maximum temperature difference obtained for 100 Hz, but are much smaller than this presented in Fig. 8. The differences between the results depicted in Fig. 9 for 200 Hz and 300 Hz are caused partly by the increase in energy dissipation in the resonance tube, which is respectively two and three times longer, and partly by the change of the stack position relative to the position in the half-wave length resonator.

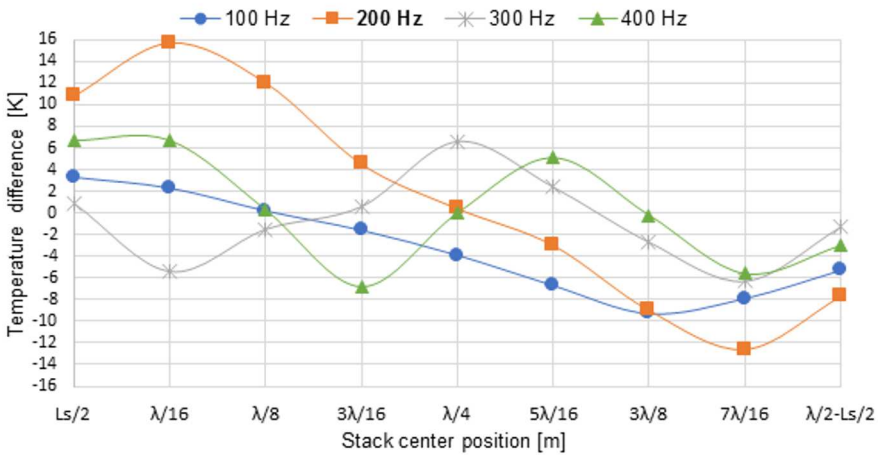

Figure 10: Temperature difference between stack ends versus stack position with main resonance frequency 200 Hz (λ is the wave length for 200 Hz).

The relations between the temperature difference and the stack position in the quarter-wave length resonator with two closed ends for 100 Hz and

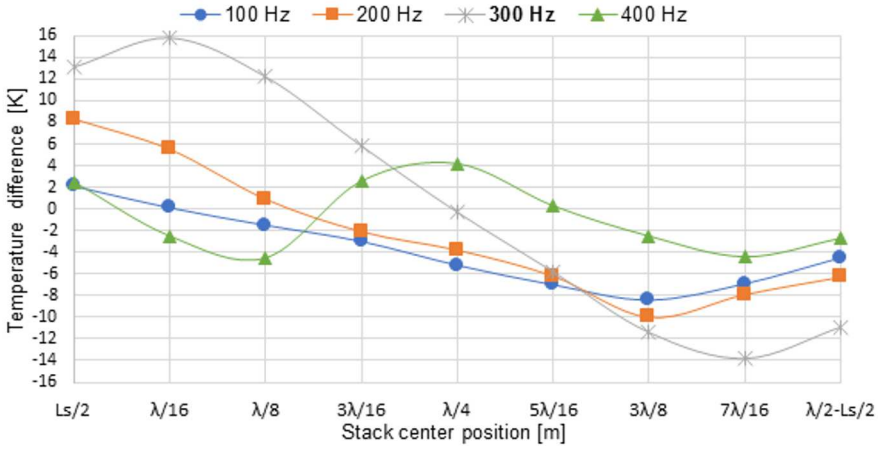

Figure 11: Temperature difference between stack ends versus stack position with resonance frequency 300 Hz (λ is the wave length for 300 Hz).

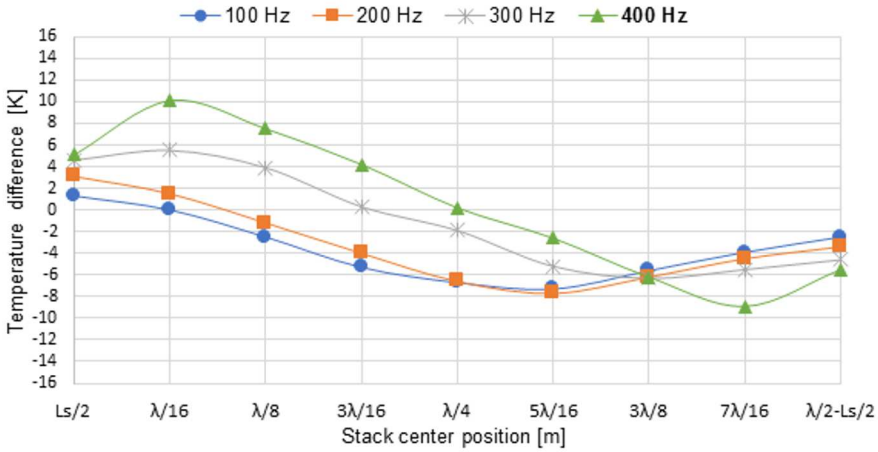

Figure 12: Temperature difference between stack ends versus stack position with resonance frequency 400 Hz (λ is the wave length for 400 Hz).

200 Hz are shown in Figs. 10 and 12. The temperature differences across the stack are lower than the results obtained for the half-wave length resonator. The acoustic wave in the quarter-length resonator with two closed ends is the combination of the incident wave and the wave reflected at the cork piston surface and thus the point at which heat transfer direction change

occurred. For the quarter-length resonator with one open end heat is always transferred in the same direction because the pressure node is located at the open end of the resonator. The temperature difference distributions for the resonator length other than quarter-wave length presented in Figs. 10–12 are also resulted from the mutual modification of the incident and reflected wave.

6 Conclusion

Theoretical and experimental investigations are carried out to examine the influence of stack position in the resonance tube and acoustic frequency on the performance of standing wave thermoacoustic refrigerator, which is measured in terms of the temperature difference produced at the ends of the stack. Nine different stack positions for four resonance frequencies with the half-wave length resonator were investigated. Additionally, the impact of other frequencies than resonance and the resonator length other than the half-wave was also checked.

The experimental results are in good agreement with the theory and confirm that stack position and acoustic frequency have significant effect on the operation of the thermoacoustic refrigerator. The highest temperature differences were obtained for resonance frequencies, resonator length corresponding to the half-length of acoustic wave, and the stack location at 1/16 of acoustic wave. The change in heat transfer direction always occurred at the pressure or velocity nodes. It was proved that the temperature difference across the stack is created also for other frequencies than resonance, but due to combination of the incident reflected wave the thermoacoustic effect is reduced.

Received 10 October 2017

References

[1] Herman C., Travnicek Z.: *Cool sound: the future of refrigeration technology? Thermodynamic and heat transfer issues in thermoacoustic refrigeration*. Heat Mass Transfer **42**(2006), 492–500.

[2] Grzebielec A., Rusowicz A., Laskowski A.: *Experimental study on thermal wave type adsorption refrigeration system working on a pair of activated carbon and methanol*. Chem. Process Eng-Inz **36**(2015), 4, 395–404, DOI: 10.1515/cpe-2015-0028

[3] Grzebielec A., Szelągowski A.: *Use of the water-silicagel sorption set in a refrigeration unit*. Przemysł Chemiczny **96**(2017), 2, 321–23, DOI:10.15199/62.2017.2.7.

[4] Xiao J. H.: *Thermoacosutic heat transportation and energy transformation. Part 1: Formulation of the problem*. Cryogenics **35**(1995), 1, 15–19.

[5] Swift G. W.: *Thermoacoustic engines*. J. Acoust. Soc. Am. **84**(1988), 4, 1145–1179.

[6] Babei H., Siddiqui K.: *Design and optimization of thermoacoustic devices*. Energ. Convers. Manage. **49**(2008), 3585–3598.

[7] Wetzel M., Herman C.: *Design optimization of thermoacoustic refrigerators*. Int. J. Refrig. **20**(1997), 1, 3–21.

[8] Tominga A.: *Thermodynamic aspects of thermoacoustic theory*. Cryogenics. 35(1995), 7, 427–440.

[9] Tijani M.E.H.: *Loudspeaker-Driven Thermoacoustic Refrigeration*. PhD thesis, Netherland University, Eindhoven 2001.

[10] Santillán A.O., Boullosa R.R.: *Space dependence of acoustic power and heat flux in the thermoacoustic effect*. Int. Commun. Heat Mass **22**(1995), 4, 539–548.

[11] Rulik S., Remiorz L., Dykas S.: *Application of CFD technique for modelling of the thermoacoustic engine*. Arch. Thermodyn. **32**(2011), 3, 175–190.

[12] Tijani M.E.H., Zeegers J.C.H., de Waele A.T.A.M.: *Design of thermoacoustic refrigerators*. Cryogenics **42**(2002), 49–57.

[13] Backhaus S., Swift G.: *New varieties of thermoacoustioc engines*. In: Proc. 9th Int. Con. on Sound and Vibration, 2002.

[14] Tijani M.E.H., Zeegers J.C.H., de Waele A.T.A.M.: *The optimal stack spacing for thermoacoustic refrigeration*. J. Acoust. Soc. Am. **112**(2002), 1, 128–133.

[15] Tijani M.E.H., Zeegers J.C.H., de Waele A.T.A.M.: *Construction and performance of a thermoacoustic refrigerator*. Cryogenics **42**(2002), 59–66.

[16] Herman C, Chen Y.: *A simplified model of heat transfer in heat exchangers and stack plates of thermoacoustic refrigerators*. Heat Mass Transfer **42**(2006), 901–917.

[17] Zolpakar N.A., Mohf-Ghazil N., El-Fawal M.H.:*Performance analysis of standing wave thermoascoustic refrigerator: A review*. Renew. Sust. Energ. Rev. **54**(20016), 626–634.

[18] Swift G.W.: *Thermoacoustic: a unifying perspective for some engines and refrigerator*. J. Acoust. Soc. Am. **113**(2003), 5, 2379–2381.

[19] Wetzel M., Herman C.: *Experimental study of acoustic effects on a single plate. Part I: Temperature fields*. Heat Mass Transfer **36**(2000), 7–20.

[20] Marx D., Mao H., Jaworski A.J.: *Acoustic coupling between the loudspeaker and the resonator in a standing-wave thermoacoustic device*. App. Acoust. **67**(2006), 402–419.

[21] Slaton W.V., Raspet R., Bass H.E., Lightfoot J.: *Working gases in thermoacoustic engines*. J. Acoust. Soc. Am. **105**(1999), 5. 2677–2684

[22] Tijani M.E.H., Zeegers J.C.H., de Waele A.T.A.M.: *Prandtl number and thermoacoustic refrigerators*. J. Acoust. Soc. Am. **112**(2002), 1, 134–143.

archives
of thermodynamics
Vol. **38**(2017), No. 4, 109–125
DOI: 10.1515/aoter-2017-0027

Online monitoring system of air distribution in pulverized coal-fired boiler based on numerical modeling

PIOTR ŻYMEŁKA*
DANIEL NABAGŁO
TOMASZ JANDA
PAWEŁ MADEJSKI

Research and Development Department, EDF Polska S.A. Ciepłownicza 1, 31-357 Kraków, Poland

Abstract Balanced distribution of air in coal-fired boiler is one of the most important factors in the combustion process and is strongly connected to the overall system efficiency. Reliable and continuous information about combustion airflow and fuel rate is essential for achieving optimal stoichiometric ratio as well as efficient and safe operation of a boiler. Imbalances in air distribution result in reduced boiler efficiency, increased gas pollutant emission and operating problems, such as corrosion, slagging or fouling. Monitoring of air flow trends in boiler is an effective method for further analysis and can help to appoint important dependences and start optimization actions. Accurate real-time monitoring of the air distribution in boiler can bring economical, environmental and operational benefits. The paper presents a novel concept for online monitoring system of air distribution in coal-fired boiler based on real-time numerical calculations. The proposed mathematical model allows for identification of mass flow rates of secondary air to individual burners and to overfire air (OFA) nozzles. Numerical models of air and flue gas system were developed using software for power plant simulation. The correctness of the developed model was verified and validated with the reference measurement values. The presented numerical model for real-time monitoring of air distribution is capable of giving continuous determination of the complete air flows based on available digital communication system (DCS) data.

*Corresponding Author. Email: piotr.zymelka@edf.pl

Keywords: Pulverized coal-fired boiler; Air distribution; Online monitoring system; Coal combustion; Combustion airflow neasurement; Numerical modeling

1 Introduction

Nowadays, the worldwide energy sector is under transformation as a consequence of the increasing deployment of renewable energy sources (RES), mostly wind and solar, combined with smart grids in the electricity generation system. For this reason, the conventional thermal power plants are required to stabilize and balance power grids by compensating for the variable electricity supply from RES. The current structure of power generation requires from fossil-fuel plants the ability to adapt to dynamic conditions and high flexibility to provide support for grid reliability. However, to meet these requirements it is necessary to keep the performance of thermal systems at the highest possible level due to economic and ecological aspects. The demand of lowering pollutant emissions and increasing power plant efficiency leads to upgrading the quality of combustion process and steam production in large-scale pulverized coal (PC) boilers. Performance optimization at different load conditions allows us to evaluate the capabilities and limitations of the combustion process [1–3].

One of the main objectives in the operation of modern combustion systems is to provide the low-pollution process with primary and secondary measures. Achieving the required emission levels can be obtained by the proper selection of combustion process parameters (e.g., the amount of excess air) and modification in firing system, such as burner redesign or air staging. The efficiency of combustion process strictly relates to the optimum balance of air to fuel. The optimal air-to-fuel ratio is one of the most important parameter affecting the boiler efficiency [4–7]. Information about the flow rate of combustion air is a fundamental parameter in control of boiler performance. Unreliable information about the airflow distribution in coal-fired boilers can result in the abnormal combustion process, overheating in the back-pass as well as slagging and fouling. However, measuring the combustion airflow can be difficult because of high flow rates at low pressures through irregular and large ducts. The online monitoring system of secondary air distribution in pulverized coal-fired boilers can provide additional information needed to reach optimal process efficiency and reduce pollutant emissions [8–14].

Study presented in this paper was performed in order to analyze the air

distribution in the front-fired pulverized coal boiler of 225 MWe power unit, operating in extended load range (from 90–225 MWe). Currently, the mass flow rate of secondary air flow supplying the OFA nozzles and burners is not measured in the unit control system. The proposed numerical model allows the identification of mass flow rates of secondary air to individual burners and to OFA nozzles. Numerical models of air and flue gas system were developed with the commercial program for power plant simulation EBSILON§Professional. Obtained results provide detailed information on the secondary air flow propagation in the wind-box, hot and cold ducts. The simulation results were compared and validated with the reference measurement values. The presented numerical model for real-time monitoring of air distribution can provide information about the current air mass flow rates (primary air (PA), secondary air (SA) and overfire air (OFA)) based on available digital communication system (DCS) data.

2 Characteristic of air and fuel supply system in pulverized coal boiler OP-650

The OP-650 boiler is a pulverized fuel front wall fired boiler with steam drum, natural water circulation and steam reheaters. General scheme of arrangement of the existing firing system in on exemplary boiler OP-650 is presented in Fig. 1. The installed firing system comprises twelve main burners in two burner levels and twelve low dust burners in one burner level above the OFA-1. The boiler has a start-up installation consisting of 12 heavy oil burners placed in pulverized fuel (PF) burners. The level of OFA-1 nozzles is permanently closed. The first two levels of burners are supplied with a high concentration mixture. The diluted coal-air mixture is provided to the third level of burners. All burners are enclosed in a common secondary wind-box, which is located on the front wall of the boiler. In addition to this, two more overfired air nozzles levels are also installed in boiler – OFA-2 (above the low-dust burners) and OFA-3 (on the rear wall).

The arrangement of individual burners and OFA nozzles in the boiler is presented in Fig. 2. The boiler is fed by six ring-ball mill units MKM-33 (marked alphanumeric A–F) and each mill feeds two main burners (swirl-type) and two low-dust burners (without swirl). In Fig. 2 the distribution from each mill to the burners is described. The two lower levels of circles show the main burners. The small red circles inside the burners are the start-up oil burners. The color and description of each burner is assigned to

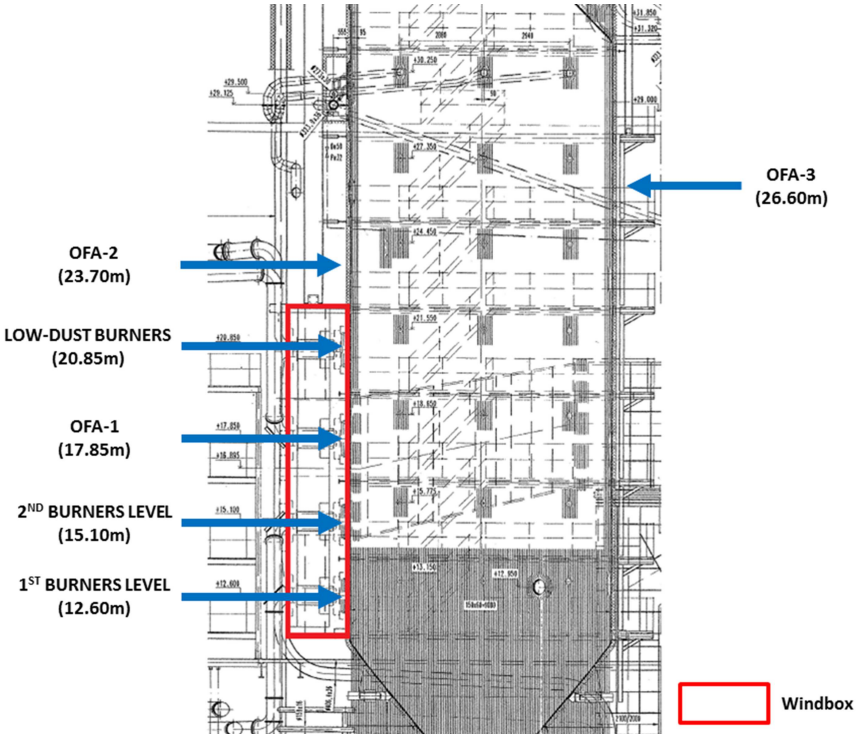

Figure 1: Arrangement of the exisiting firing system.

the proper mill, e.g., 'A1' means, the high-dust burner is supplied by mill 'A'. The combustion air of the main burners is separated into core, primary, secondary and tertiary. Above the main burners the first over fire air level is represented by blue rectangles (from 1R1 to 6R6). The OFA-1 level is out of operation. Next to the OFA-1 row the low-dust burners are located and are clustered in pairs. The burners injects the primary air with a low concentration of pulverized fuel into the furnace with certain amount of the secondary air to improve the ignition. Boiler consists of two additional level of OFA nozzles. The OFA-2 level is located above the windbox at the front wall and the nozzles operate in pairs (2R1-2R2, 2R3-2R4, 2R5-2R6). At the boiler's rear wall is OFA-3 level and the nozzles are controlled in two sections: 3R1-3R5 and 3R6-3R10. The described system of air and fuel staging in PC boiler OP-650 is an example of low-emission combustion system, which was designed to reach low-NOx conditions using primary methods.

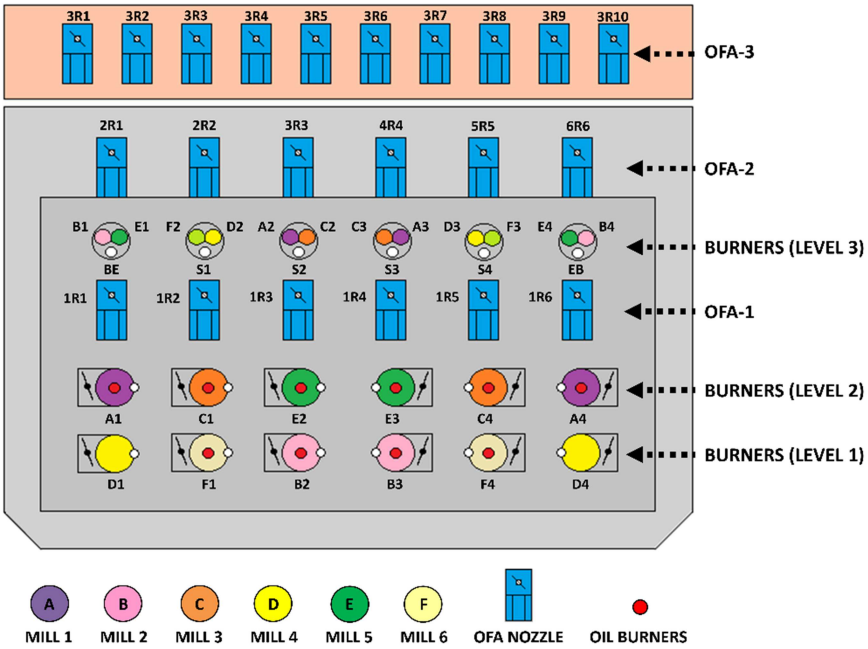

Figure 2: Arrangement of the exisiting firing system.

2.1 Combustion air distribution system

The OP-650 boiler is equipped with a three air-flue gas lines, designed to run and regulate the combustion process. Each line includes:

- RAPH – rotary air preheater (regenerative heat exchanger),
- ID fan – induced draft, exhaust fan (radial, with guiding vane on the suction side),
- FD fan – force draft, air fan (axial, variable speed rotor).

In addition, air-flue gas system contains:

- air and flue gas ducts with dampers,
- air intakes and silencers installed on the suction side of the FD fans.

The general scheme of combustion air and flue gas system is presented in Fig. 3. Three FD fans (FG1-3) supply the combustion air. Dampers in the main ducts to the windbox regulate the air volume flow to the main

burners and OFA nozzles. Three regenerative air preheaters (RAPH1-3) preheat the hot air to the boiler. The two outer RAPHs (RAPH-1 and RAPH-2) are used to heat the secondary air to a temperature of approx. 275 °C. The air preheater in the center (RAPH-2) is used to heat the hot portion of the primary air (mill air) to a temperature of approx. 315 °C. The cold portion of the primary air is bypassed around the RAPH-2 and is mixed with the hot air directly before injecting into each mills. The secondary air to OFA-2 is taken form the windbox, whereas the secondary air to OFA-3 is derived from the main air-ducts behind the RAPH-1 and RAPH-2.

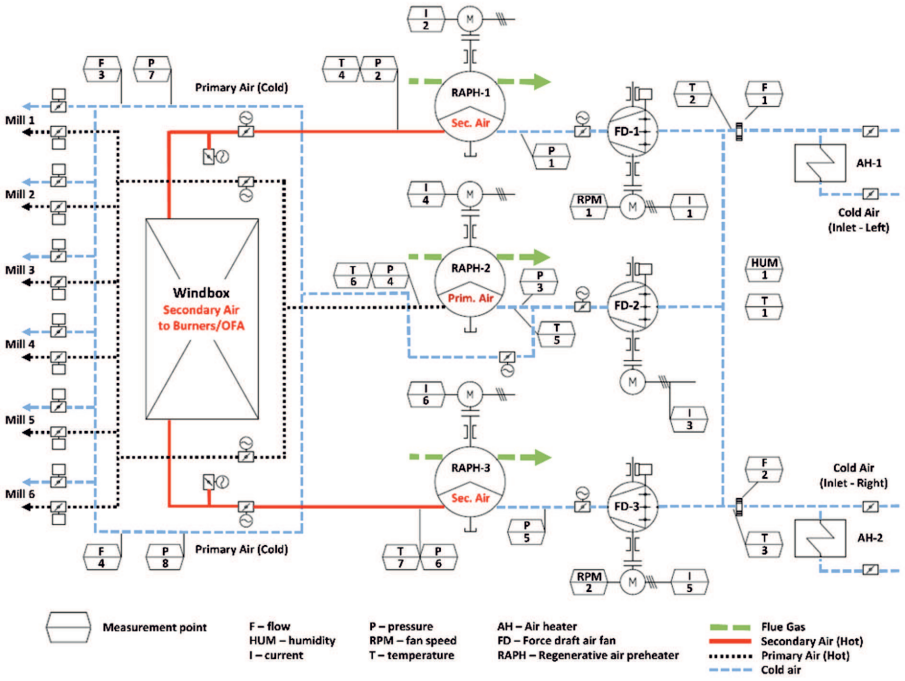

Figure 3: Arrangement of the piping and instrumentation diagram (PID) combustion air system.

3 Model of air distribution in the OP-650 boiler

Development and application of the air distribution modeling in coal-fired boiler is a complex process. Combustion air balance and the secondary air

flow propagation can be analyzed using mathematical simulation software. Modern numerical tools provide solution algorithms with a wide range of component libraries for modeling and simulation of different types of thermal and hydraulic systems [15].

The simulation model of air distribution in the OP-650 boiler system proposed in this paper has been developed in EBSILON® Professional software. The general structure of combustion air system is presented in Fig. 4. The models have been designed based on existing technical documentation and available technological diagrams. The complete model of air-fuel-flue gas system was divided into two sub-models:

- main air-flue gas distribution model (Fig.4),
- air distribution to OFA-2 and OFA-3 (Fig.5).

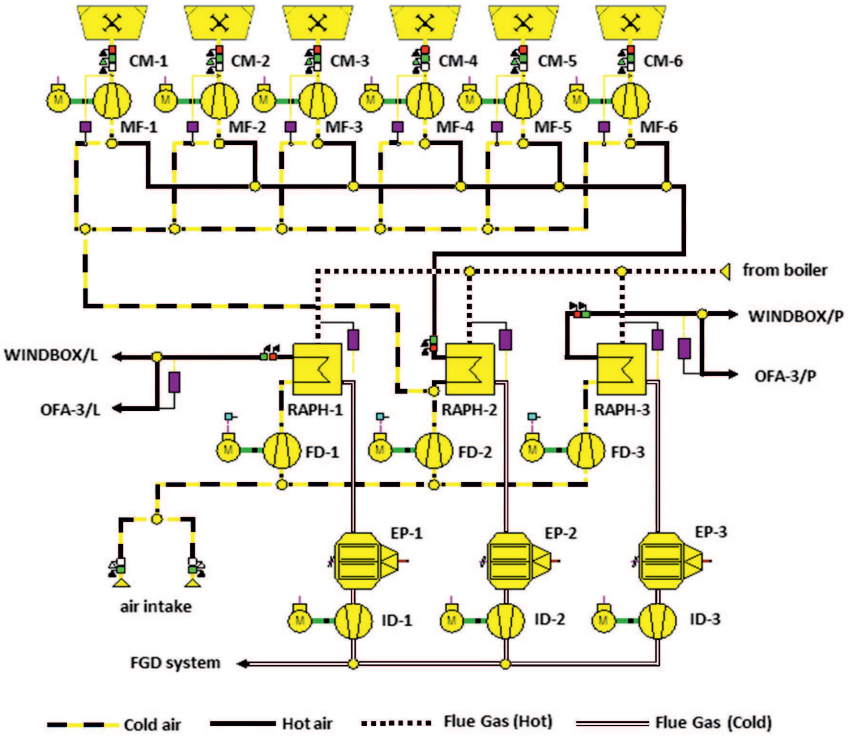

Figure 4: Model of air-flue gas distribution system.

The mathematical model of air flow in a boiler piping/duct system takes into account the variation of air temperature and pressure due to friction, as well as heat losses. The air pipe is designed phenomenologically, which means that the amount of heat losses and the extent of the pressure drop are entered in the design case. The nominal values of pressure and heat losses of air ducts were assumed in design case based on the operating data and technical specification of the OP-650 boiler. In off-design calculations the losses are scaled accordingly. However, in EBSILON® Professional software is also possible to calculate the pressure drop based on the pipe geometry (length, inner diameter, wall roughness). The phenomenological pressure drop method was used in the simulation model of air distribution.

In the off-design calculations the pressure drop results according to Bernoulli's principle with consideration of mass flow and the specific volume [15]:

$$\triangle p_{1-2} = \triangle p_{1-2N} \left(\frac{\dot{V}_1}{\dot{V}_{1N}} \right) \left(\frac{\dot{m}_1}{\dot{m}_{1N}} \right)^2 , \tag{1}$$

where: $\triangle p_{1-2}$ – pressure drop between pipe inlet and outlet (off-design mode), $\triangle p_{1-2N}$ – nominal pressure drop between pipe inlet and outlet, $\dot{V}_1$ – specific volume at pipe inlet (off-design mode), $\dot{V}_{1N}$ – nominal volume at pipe inlet, $\dot{m}_1$ – mass flow at pipe inlet (off-design mode), $\dot{m}_{1N}$ – nominal mass flow at pipe inlet.

The heat losses are specified in the design case, but in off-design calculations the temperature loss is scaled quadratically with the flow [15]

$$\triangle t_{1-2} = \triangle t_{1-2N} \left(\frac{\dot{m}_1}{\dot{m}_{1N}} \right)^2 , \tag{2}$$

where: $\triangle t_{1-2}$ – temperature drop between pipe inlet and outlet (off-design mode), $\triangle t_{1-2N}$ – nominal temperature drop between pipe inlet and outlet.

In order to determine the air flow to each OFA nozzles the control valve components (with flow coefficient) were used in off-desing simulation. This component describes the relationship between the pressure difference and the corresponding flow rate through a control valve. In desing simulation the flow coefficient K_v is calculated according to the following formula [15]:

$$K_v = \frac{\dot{V}_1}{Y} \sqrt{\frac{\triangle p_0}{\triangle p} \frac{\rho}{\rho_0}} \tag{3}$$

where: $\dot{V}_1$ – volumetric flow rate at valve inlet, Y – expansion factor, $\triangle p_0$ – reference pressure drop (for SI definition 0.1 MPa), ρ_0 – reference density

(for SI definition – 1000 kg/m^3).

Whereas in the off-design simulation the volumetric flow rate at nozzle inlet is computed depending on the nozzle position and pressure difference. The K_v factor is a relative measure of nozzle efficiency at allowing fluid flow.

The sum of secondary air flow to burners is calculated as the difference between the total air flow to three regenerative air preheaters (RAPH1-3) and sum of air flow to OFA-2 and OFA-3 nozzles. It has been assumed that the air flow to each burners is calculated in proportion to the damper position of the burners.

The structure of the simulation model presented in Fig. 4 contains following components: air fans with motors (FD), regenerative heat exchangers (RAPH), electrostatic precipitators (EP), exhaust fans with motors (ID), six coal mills (CM) with fans (MF), flue-gas desulfurization system (FGD). The description of the air and flue gas distribution was presented in Sec. 2.

3.1 Secondary air flow to OFA model

The simulation model of the secondary air flow in air ducts to the OFA-2 and OFA-3 nozzles was developed using the data contained in the available technical documentations for OP-650 boiler. The geometry of the exhaust and air duct system was included in the model based on technological schemes. The structure of the secondary air distribution model to OFA-2 and OFA-3 is presented in Fig. 5.

Simulation model of air flow to OFA nozzles takes into account following elements:

- air inlets to the nozzles OFA-2, which are controlled in pairs: OFA-2/1 – OFA-2/2 (left side), OFA-2/3-OFA-2/4 (middle), OFA-2/5-OFA-2/6 (right side), and outlet to the combustion chamber at the level of 23.7 m;
- air inlets to nozzles OFA-3, which are controlled by the five per side: OFA-3/1-5 (left side), OFA-3/6-10 (right side) and an outlet to the combustion chamber at the level of 26.6 m;
- logical lines, which allow setting value of a required opening degree of the OFA damper.

The identification process of available measuring points in the area of the windbox and burner chamber of the analyzed boiler, showed that in the

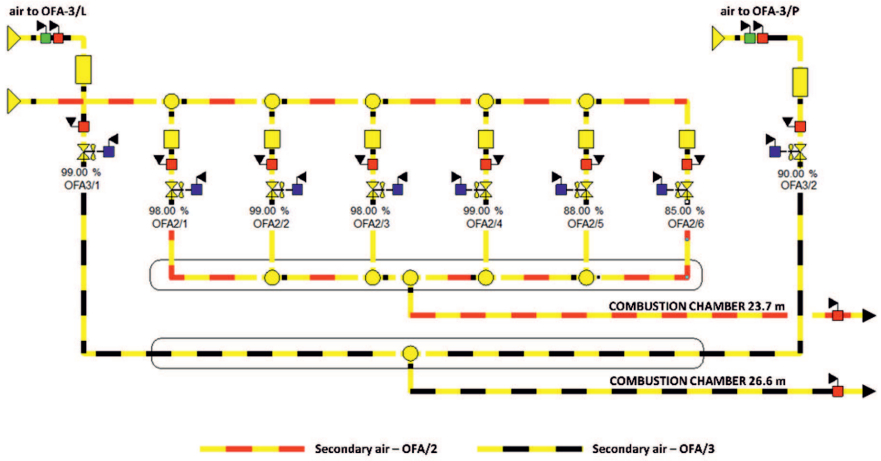

Figure 5: Model of air distribution system to OFA-2 and OFA-3.

measuring system there was no information about the pressure values in the OFA-2 and OFA-3 air ducts. The assembly of eight additional pressure measurements was proposed and installed:

- six pressure measurements in OFA-2 ducts,
- two pressure measurements in OFA-3 ducts (left and right side).

The secondary air flow to OFA nozzles can be simulated by changing: temperature and air pressure in the duct to the OFA nozzles, pressure in the windbox and combustion chamber (at level 23.6 m and 26.6 m) and the damper opening degree of the selected OFA nozzle. The main results, which can be obtained from the simulation model of secondary air distribution are the air flows to the OFA-2 and OFA-3 nozzles. These values were not measured in the boiler system.

4 Verification test of simulation models

One month measurement campaign, in order to determine the balance and air distribution in the boiler OP-650 at the real power plant was carried out. The developed simulation mathematical models of air distribution in OP-650 boiler was subjected to a verification process. The simulation results were compared with the values obtained from the reference measurements

and modeling based on 'virtual' airflow sensors (VS), which allow determining the total primary, secondary and OFA nozzles based on available DCS measurements. VS technology is based on the development of the physical model of the hydraulic network of the selected facility, including piping, manifolds, control valves and fans. So far, the system has been implemented in coal-fired power plants from 100 MWe to 1000 MWe, where it has successfully contributed to identifying and improving the distribution of air in coal boilers [16]. Based on the measurements and calculations from VS the air balance for the OP-650 boiler was determined. The data registered during the tests were analyzed in order to calculate the air flow balance of the OP-650 boiler and to compare the experimental values with the results from the simulation mathematical model.

One of the unknown of the developed model was how to determine the secondary air flow through the burners. For the purposes of the simulations, it was assumed that the amount of secondary air reaching the burners from the windbox together with the primary air should provide an excess air ratio of 0.7, at burners belt (in design mode) [5,7,8]. Additionally, it was also assumed that the pressure in the combustion chamber at level 23.7 m and 26.6 m is the arithmetic mean of the measured values available at this level. The complete list of input data needed to perform the simulation calculations is presented in Tab. 1. All listed parameters used in the calculation as input data are available in the DCS system.

4.1 Verification results

To verify the developed simulation model of air distribution in OP-650 boiler, comparisons between the simulated values and VS measurement data of a boiler operated under steady state and transient conditions were made. The verification process was carried out for a full day of boiler operation. In order to determine the correctness of the developed model, the results of the simulation calculations were compared with the results of the reference VS model and with the measurement values from the DCS system. Based on the results of the simulation calculations and measurements, the following parameters were compared:

- total air flow to boiler,
- primary air flow,
- secondary air flow to burners and secondary air flow to OFA-2 and OFA-3.

Table 1: Input parameters for simulations.

No.	Measuring point description	Unit
1	Air flow to RAPH-1–3	kNm^3/h
2	Total primary air flow to mill CM-1–6	kNm^3/h
3	Damper position burner A1, A4, B2, B3, C1, C4	%
4	Damper position burner D1, D4, E2, E3, F1, F4	%
5	Nozzle position OFA II – 1–6	%
6	Nozzle position OFA III – left and right side	%
7	Pressure in comb. chamber (level 23.7 m) – left, right and middle side	Pa
8	Pressure in comb. chamber (level 17.5 m) – left and right side	Pa
9	Pressure in comb. chamber (level 10.5 m) – left and right side	Pa
10	Pressure in windbox - left and right side	Pa
11	Air pressure in OFA-2/1–6	Pa
12	Air pressure in OFA-3 left and right side	Pa
13	Air pressure behind RAPH-1	Pa
14	Air temperature behind RAPH-1	°C
15	Air pressure behind RAPH-3	Pa
16	Air temperature behind RAPH-3	°C
17	Excess air ratio	–

The verification results of total air flow into the boiler is presented in Figs. 6 and 7. The results showed that the developed simulation model can describe the physical behavior of air distribution in OP-650 boiler with small differences from the reference values Eq. (3). In order to determine the difference between the results obtained from the simulation model and from VS modeling, the relative error was calculated according to the following formula:

$$\triangle x_i = \left(\frac{x_{i\ REF} - x_{i\ EBS}}{x_{i\ REF}} \right) \times 100\% \tag{4}$$

where: $x_{i\ EBS}$ – value of ith parameter from simulation calculation (Ebsilon), $x_{i\ REF}$ – value of ith parameter from reference measurment (EUtech).

The obtained values of relative errors are presented in Tab. 2.

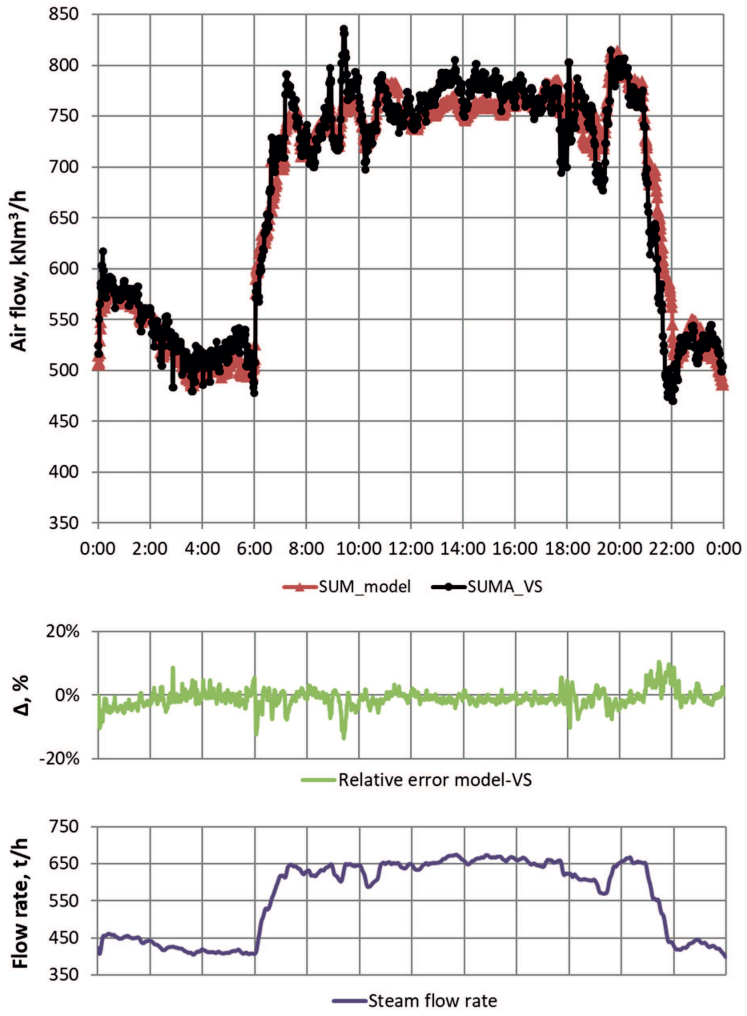

Figure 6: Verification results of total air flow into the boiler.

The average value of relative error obtained from the verification results did not exceed 6.0%. Based on the verification process, it can be confirmed that the developed simulation model of air distribution ensures high results accuracy in the whole range of boiler operation – steam flow rate in range 390–680 t/h.

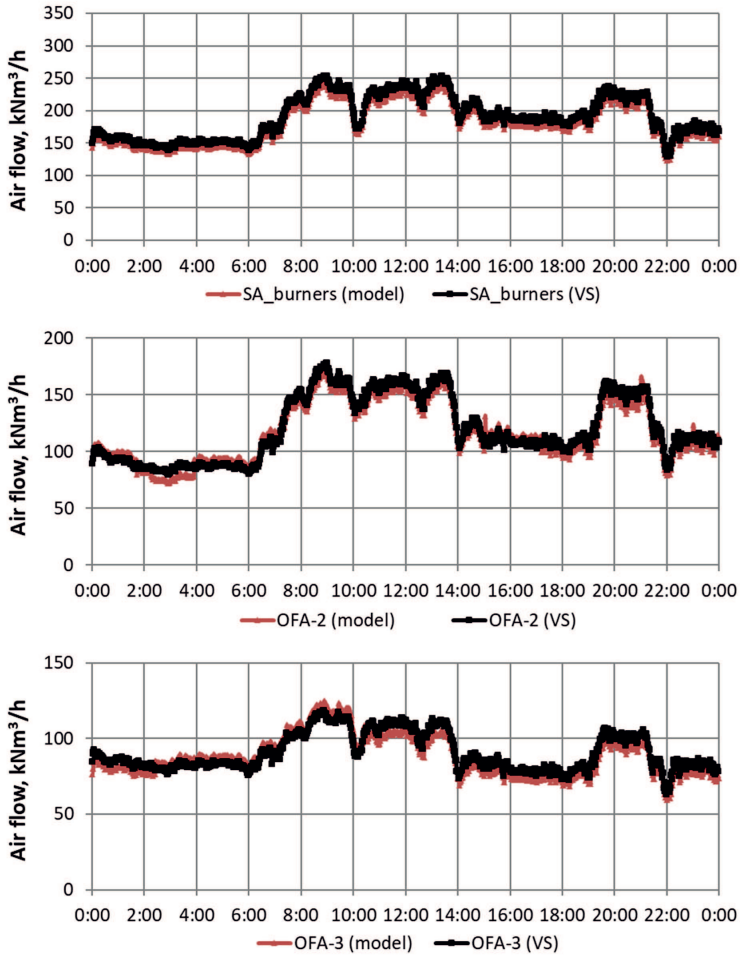

Figure 7: Verification results of secondary air (SA) flow into burners, OFA-2 and OFA-3.

The developed simulation mathematical model of air distribution has been tested and implemented in the OP-650 boiler operation system at the EDF Polska S.A. power plant in Rybnik. The values of secondary air flow to each burners and OFA nozzles have been introduced in the operating system of the analyzed boiler. Visualization graphic of existing firing system in OP-650 boiler with new air flow measurement points is presented in Fig. 8 (dashed frame).

Table 2: Relative error results

Parameter | Steam flow rate	600-680 t/h	480-600 t/h	390-480 t/h	Average
Total air flow	1.8%	2.9%	2.4%	2.1%
Secondary air flow to burners	4.3%	2.6%	2.1%	3.4%
Secondary air flow to OFA-2	4.2%	6.0%	4.5%	4.7%
Secondary air flow to OFA-3	5.5%	7.3%	5.7%	6.0%

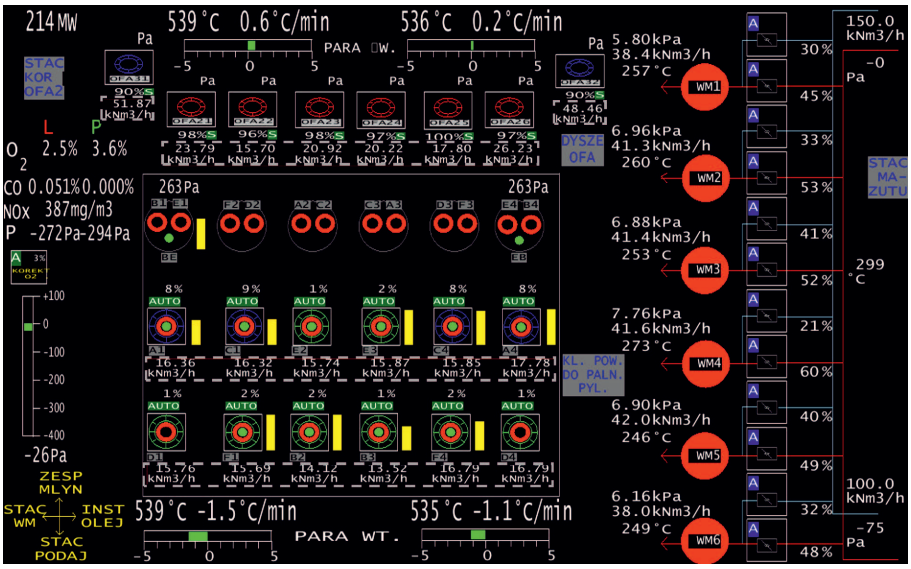

Figure 8: Firing system visualization graphic with new air flow measurement points.

5 Conclusions

Although the technology of pulverized coal-fired boiler is well known, there is still room for further improvement concerning optimization of the combustion process and proper control of combustion air distribution, which can be done using mathematical modeling. In this paper, the novel online monitoring system of air distribution in coal-fired boiler based on real-time numerical calculations has been presented. The developed simulation model allows for identification of mass flow rates of secondary air to individual burners and to OFA nozzles. The calculated results obtained from the

simulation were compared with the values from the reference measurements and VS modeling. The following parameters were used in the verification procedure: total air mass flow rate to the boiler, secondary air mass flow rate to the burners, secondary air mass flow rate to OFA-2 and to OFA-3 nozzles. Based on the results obtained from verification of the air distribution mathematical model, it can be concluded that the compatibility of results from the simulations and from the reference measurement campaign is very satisfactory. The average relative error value did not exceed 6.0%.

The presented numerical model for real-time monitoring of air distribution is capable of giving continuous determination of the total air flows (PA, SA and OFA) from available DCS data. The developed mathematical model has been successfully implemented in the real DCS control system. In the next stages of this research, there is a plan to analyze possibility to combine the developed air flow model with an advanced optimization software, to get optimal control of burners and OFA dampers [9].

Received 30 September 2017

References

[1] Modliński N., Madejski P., Janda T., Szczepanek K., Kordylewski W.: *A validation of computional fluid dynamics temperature distirbution prediction in a pulverized coal boiler with acoustic temperature measurement.* Energy **92**(2015), 77–86.

[2] Madejski P., Janda T., Modliński N., Nabagło D.: *A combustion process optimization and numerical analysis for the low emission operation of pulverized coal-fired boiler.* Chap. in *Developments in Combustion Technology.* InTechOpen, 2016, 33–76.

[3] Taler J., Trojan M., Taler D., Dzierwa P., Kaczmarski K.: *Improving flexibility characteristics of 200 MW unit.* Arch. Thermodyn. **38**(2017), 1, 75-90.

[4] Szargut J., Ziębik A.: *Fundamentals of Heat Engineering.* PWN, Warszawa 1998.

[5] Chmielniak T.: *Energy Technologies.* WNT, Warszawa 2015.

[6] Pronobis M.: *Modernisation of Power Boilers.* WNT, Warszawa 2013.

[7] Taler D., Madejski P.: *Thermomechanical CSM analysis of a superheater tube in transient state.* Arch. Thermodyn. **32**(2011), 3, 117–126.

[8] Nabagło D., Madejski P.: *Combustion process analysis in boiler OP-650k based on acoustic gas temperature measuring system.* In: Proc. 3rd Int. Conference on Contemporary Problems of Thermal Engineering, 2012.

[9] Śladewski Ł., Wojdan K., Świrski K., Janda T., Nabagło D., Chachuła J.: *Optimization of combustion process in coal-fired power plant with utilization of acous-*

tic system for in-furnace temperature measurement. Appl. Therm. Eng. **123**(2017), 717–720.

[10] Hernik B: *Numerical modeling of BP 1150 boiler by commercial numerical code.* J. Power Technologies **92**(2012), 34-47.

[11] Chen H., Liang Z.: *Damper opening optimization and performance of a co-firing boiler in a 300 MWe plant.* Appl. Therm. Eng. **123**(2017), 865–873.

[12] Purimetla A., Cui J.: *CFD studies on burner secondary airflow.* Appl. Math. Model. **33**(2009), 1126–1140.

[13] Gou X., Zhang Z.: *Real-time Model and Simulation of Combustion System in a 440t/h CFB Boiler.* In: *Challenges of Power Engineering and Environment – Proc. Int. Conf. on Power Engineering* 2007, 226–230.

[14] Vijiapurapu S., Cui J., Munukutlab S.: *CFD application for coal/air balancing in power plants.* Appl. Math. Model. **30**(2006), 854–866.

[15] *Steag Energy Services GmbH. Ebsilon Professional software, version 12.02.01.* Wetzbach Germany (2016).

[16] *Scientific EUtech Engineering GmbH.* https://www.eutech-scientific.de

archives
of thermodynamics
Vol. **38**(2017), No. 4, 127–137
DOI: 10.1515/aoter-2017-0028

Improvement of energy efficiency and environmental safety of thermal energy through the implementation of contact energy exchange processes

GENNADII BORYSOVICH VARLAMOV
KATERYNA ALEXANDROVNA ROMANOVA*
IRYNA NAZAROVA
OLGA DASCHENKO
ANDRY KAPUSTIANSKY

National Technical University of Ukraine, Igor Sikorsky Kyiv Polytechnic Institute, 03056 Kyiv, Pobedy 37, Ukraine

Abstract Energy efficiency improvement and ecological safety of heat power plants are urgent problems, which require scientifically grounded approaches and solutions. These problems can be solved partly within the presented heat-and-power cycles by including contact energy exchange equipment in the circuits of existing installations. A significant positive effect is obtained in the contact energy exchange installations, such as gas-steam installation 'Aquarius' and the contact hydrogen heat generator that also can use hydrogen as a fuel. In these plants, the efficiency increases approximately by 10–12% in comparison with traditional installations, and the concentration of toxic substances, such as nitrogen oxides and carbon monoxide in flue gas can be reduced to 30 mg/m^3 and to 5 mg/m^3, respectively. Moreover, the plants additionally 'generate' the clean water, which can be used for technical purposes.

Keywords: Thermal efficiency; Heat generator; Energy consumption; Contact hydrogen; Contact energy exchange

*Corresponding Author. Email: romanova_ko@ukr.net

Nomenclature

C	–	temperature, °C;
CHHG	–	contact hydrogen heat generator;
t_{fg}	–	flue gas temperature, °C
Q_{HHV}	–	higher heating value, J/kg
Q_{LHV}	–	lower heating value, J/kg
Q_m	–	density of irrigation, m^2/s
q_{fg}	–	loss of physical heat through the dry flue gas, J/m^3
x_{fg}	–	moisture content in flue gas, kg/kg

Greek symbols

α	–	average heat transfer coefficient
φ	–	specific coefficient of energy transformation
ω	–	gas flow rate

1 Introduction

The modern energy community faces a global problem of increasing energy efficiency and environmental safety of energy production with minimum expenses. Different methods and ways to solve this problem are aimed at obtaining the maximum effect with a minimum payback period simultaneously. In heat and power engineering, where fuel and ecological components significantly influence the payback period it is of particular importance.

This study is focused on the analysis and definition of operating conditions for existing power units and realization technology of contact energy exchange with the purpose of energy efficiency improving and ecological safety of single power objects.

A significant positive effect is obtained in the contact energy exchange installations developed in the National Technical University of Ukraine, at Igor Sikorsky Kyiv Polytechnic Institute, such as gas-steam installation 'Aquarius' and the contact hydrogen heat generator (CHHG) that also can use hydrogen as a fuel.

Scientists of National Technical University of Ukraine, at Igor Sikorsky Kyiv Polytechnic Institute have been engaged in the development of contact energy exchange facilities for more than 25 years [1–6]. These developments have both theoretical and practical implications.

2 Implementation of contact energy exchange processes

In order to solve the task, the conditions of implementing the contact energy exchange were studied in the following installations:

- boiler plants operating on natural gas and coal [7,8];
- gas-steam installation 'Aquarius' [6];
- contact heat generators operating on natural gas and hydrogen fuel [4].

Thermal calculations and the efficiency analysis, taking into account the dry and humid parameters of the outgoing flue gas, show a significant difference in its values. In boiler plants, operating on natural gas, the flue gas temperature, t_{fg}, is in range from 110 to 150 °C, and the moisture content, x_{fg}, within the limits of 0.11–0.12 kg/kg. For these conditions, the loss of physical heat through the dry flue gas, q_{fg}, is 195–220 kJ/m^3 or 7–9%, and with taking into account the moisture content in flue gas, these losses reach 315–325 kJ/m^3 or 11–12%.

Thus, the coefficient of thermal efficiency of the boiler calculated through the lower heating value, Q_{LHV}, of the fuel is 90–92% and the coefficient of thermal efficiency of the boiler calculated through the higher heating value, Q_{HHV}, of the fuel, taking into account the moisture content of the gas, is 78–81%. The difference between efficiencies corresponds to the difference between the higher and lower heating ability of the fuel, Q_{HHV}–Q_{LHV}, and equal to 10–12%. This difference is significant and opens wide opportunities for a comprehensive solution of the problem of increasing the efficiency of thermal processes in the boiler, such as:

- reducing the flue gas temperature up to 35 °C, that is less than the dew point temperature and leads to reduction of heat losses down to 4.5%;
- condensation of water vapor from the flue gas, that allows to achieve the increase in boiler efficiency rating to (78–81) + (10–12) = 88–93% (Tab. 1) [5].

An integrated solution is the implementation of contact energy exchange between the flows in a particular power unit.

To all, in the preliminary studies of the contact energy exchange processes, additional positive effects that increase the ecological purity of energy transformations and contribute to obtaining excess technical water,

Table 1: Effect of flue gas temperature and moisture content on the efficiency of the boiler.

Temperature of flue gas, °C	Moisture content, kg/kg	Physical heat loss with flue gas, kJ/m^3	Heat loss taking into account the moisture content, kJ/m^3	Physical heat loss with flue gas, %	Heat loss taking into account the moisture content (Q_{HHV}), %	Heat loss taking into account the moisture content (Q_{LHV}), %	Thermal boiler efficiency, %	
							Q_{HHV}	Q_{LHV}
110-150	0.11-0.12	195-220	315-325	7-9	11-12	18-21	90-92	78-81
35	0.11-0.12	55-60	___	4	___	5	106**	95*

* – the efficiency calculation takes into account the losses of physical heat of the flue gas without vapors condensation, Q_{HHV};
** – the efficiency calculation takes into account the losses of physical heat of the flue gas with vapors condensation, Q_{LHV}.

have been recorded in both gas-steam installation 'Aquarius' and contact heat generator. Thus, it is advisable to develop and improve the technologies for the implementation of contact energy exchange processes in individual heat supply systems as well as in cogeneration transformation systems for the chemical fuel energy with high efficiency, environmental safety and additional positive effects.

The implementation of contact energy exchange technologies into coal-fired power boilers is a particularly urgent task in connection with the acute need to save expensive organic fuels and ensure indicators of environmental cleanliness of energy production. The solution of this task in such boilers is possible with using the combustion catalysts in the furnace [7,8] and installation of the contact mixer at the boiler outlet.

In the first case, the injection of the catalyst into air and the active combustion of coal by increasing the area and volume of the contact energy exchange in the combustion zone of coal dust with oxygen molecules and the evaporated catalyst accelerate and improve the combustion process. This leads to a sizeable decrease of time of the fuel-air mixture in the combustion zone and reduction of the toxic nitrogen oxides, NO_x, concen-

tration in flue gas. In the second case, the use of a contact mixer allows us to obtain a synergistic effect. That is the energy efficiency increasing by reducing flue gas temperature and enhancing the environmental effect of cleaning of gases from toxic components due to direct contact between gas and water. The implementation of such contact energy exchange in coal and gas boilers requires additional experimental studies.

The beneficial use of the condensing heat flow any vapor produced after combustion is the thermodynamic basis for increasing the energy efficiency of such heat exchangers (Fig. 1).

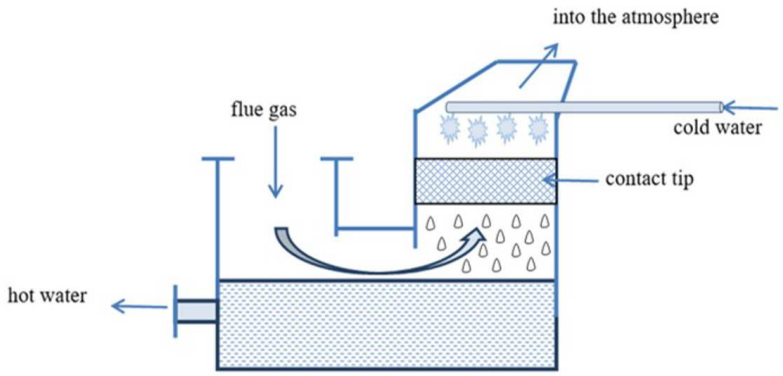

Figure 1: Principle of technological scheme of direct contact energy exchange between flue gas and water.

In the gas-steam installation 'Aquarius' contact energy exchange occurs due to the use of a contact capacitor providing isothermal condensation, and in the gas-steam installation 'Aquarius' contact implementation of energy occurs in the capacitor, wherein another important process occurs – water formation.

Active hydrogen 'liberated' during the natural gas combustion reacts chemically with air oxygen forming H_2O. For example, the gas-steam installation 'Aquarius' with a capacity of 16 MW can generate up to 30 tons of water per day under favorable conditions.

The gas-steam installation 'Aquarius' is implemented on the base of a 10 MW gas turbine with steam supply into the combustion chamber. This steam supply increases turbine power up to 16 MW. Water vapor is obtained in the cycle of installation due to the use of the flue gas heat. After the steam generator, flue gas comes into the condenser where contact

energy exchange takes place and additional technical water is generated.

The first 'Aquarius' was installed in 2003. The gas compressor station 'Stavishchenskaya' in the system of trunk gas pipelines, which were intended for transportation of natural gas from Russia to European countries was selected as the installation site.

Contact heat generators are the prominent examples of the use of contact energy exchange [4]. These heat generators provide high heat exchange characteristics of the heat exchange surface, which allows us to cool flue gas down to 35 °C. This temperature is much lower than the dew point temperature and improves the process of vapor condensation from combustion products under any thermal loads. It is useful to use the heat of condensation for heating water and to increase the indicators of ecological purity of energy transformations.

Relying on the positive effects of direct contact energy exchange, the authors developed a heat generating plant –CHHG. The main feature of CHHG is the use of hydrogen fuel for heat production in heating and hot water supply systems for consumers. The main positive features of using hydrogen in CHHG are the following:

- coefficient of thermal efficiency can reach 106% (based on the Q_{LHV} of hydrogen combustion);
- specific coefficient of energy transformation, φ, can reach up to 7–8 (for the heat pump system, the best result is $\varphi = 5$);
- high purity of heat production is characterized by the absence of carbon monoxide (CO = 0) and the concentration of nitrogen oxide emissions NO_x is at the level of 10–20 mg/m^3;
- 'generation' of additional technically clean water reaches 25 liters per hour;
- cost price of 1 Gcal/h of heat is 5–7 times less in comparison to boilers operated with natural gas.

Thus, CHHG is able to create a new heat generation platform to provide consumers with heat supply and domestic hot water heating. High indicators of energy efficiency and environmental safety of heat production in CHHG using contact energy exchange technologies are an objective basis for the commercial development of residential CHHG of various capacities and their introduction into public supply system. At the same time, objective prerequisites arise for the implementation of the principle of ecological

balance [9] and the new energy-ecological paradigm of energy production in thermal power engineering [10].

The implementation of contact heat exchange technology in existing boilers operating with natural gas is possible with various designs of direct contact devices installed in the outlet of chimney (Fig. 2).

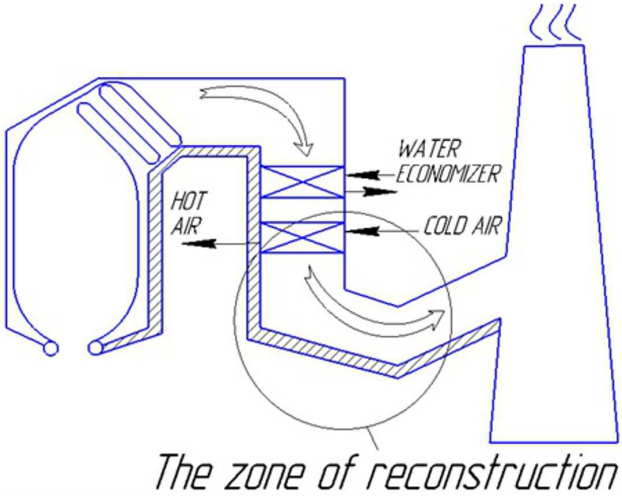

Figure 2: Scheme of a heat exchanger realising the technology of direct contact heat exchange.

The basic design of a contact heat exchanger is shown in Fig. 3.

The experimental data of dependence of the average heat transfer coefficient, α, on gas flow rate, w, and density of irrigation, Q_m, for various cases of thermal mass exchange in such equipment are presented in Figs. 4 and 5.

For coal boilers implementation of the contact energy exchange technologies is an especially urgent task in connection with exigence of economy of expensive organic fuel and supplying the ratings of ecological power production cleanliness.

The solution of the problem of increasing energy-efficiency in coal-fired boilers is possible with using a combined approach: injection of the catalyst into the furnace during the combustion process and the implementation of the contact energy exchange technology at the boiler outlet (Fig. 6).

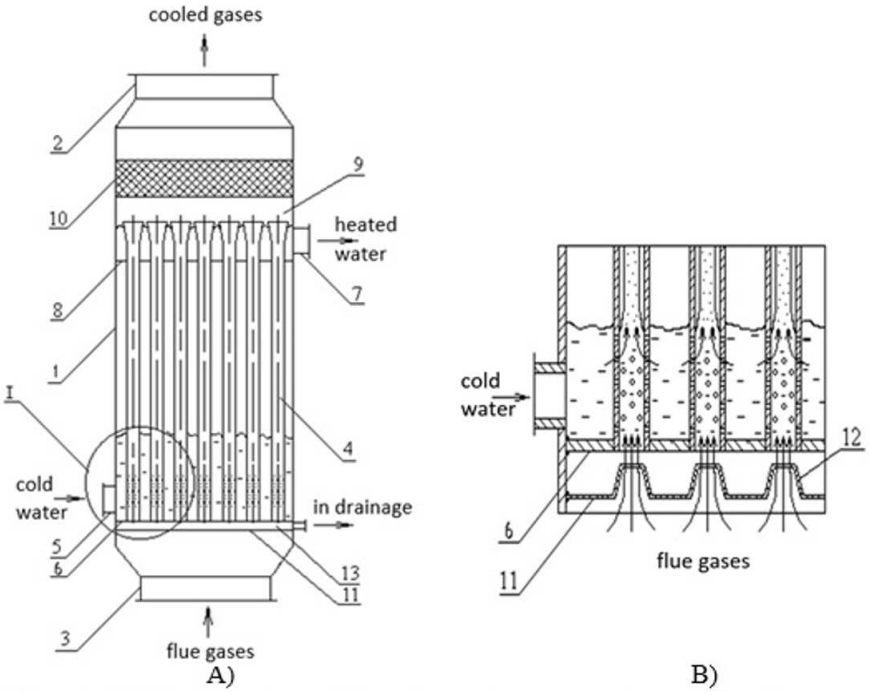

Figure 3: Outline of implementation of contact energy exchange (A) and movement of liquid and gas (B) in heating apparatus for small capacity boiler: 1 – frame, 2 – top tube, 3 – bottom tube, 4 – punched pipes, 5 – cold water supplying tube, 6 – bottom tube panel, 7 – outlet of heated water, 8 – top tube panel, 9 – chamber of water collection, 10 – separator, 11 – additional tube panel, 12 – confuses, 13 – drainage chamber with confuses.

In the first case, the injection of the catalyst into air and the active combustion through increasing the area and volume of the contact energy exchange of coal dust with oxygen molecules, and the evaporated catalyst in the combustion zone improve the combustion process. This leads to a sizeable decrease of time in which the fuel-air mixture staying in the combustion zone and reduction of the concentration of toxic nitrogen oxides NO_x in flue gas.

In the second case, the use of a contact mixer allows us to obtain a synergistic effect. That is the energy efficiency increasing by reducing flue gas temperature and enhancing the environmental effect of cleaning off gases from toxic components due to direct contact between gas and water.

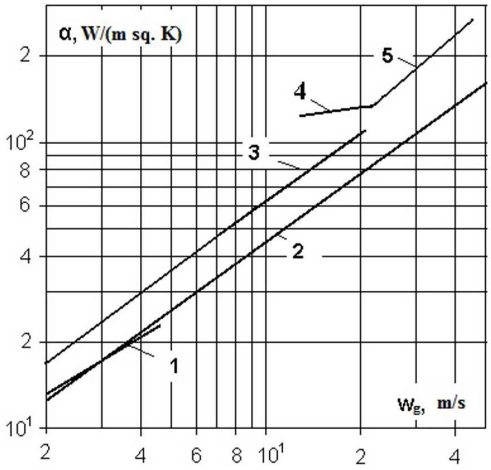

Figure 4: Dependence of the average heat transfer coefficient, α, on the gas flow rate, ω, for various cases of thermal mass exchange: 1 – Rashing's ceramic ring, 2 – dry tube, 3 – thermal mass exchange on porous nozzle (descending direct flow), 4,5 – ascending direct flow).

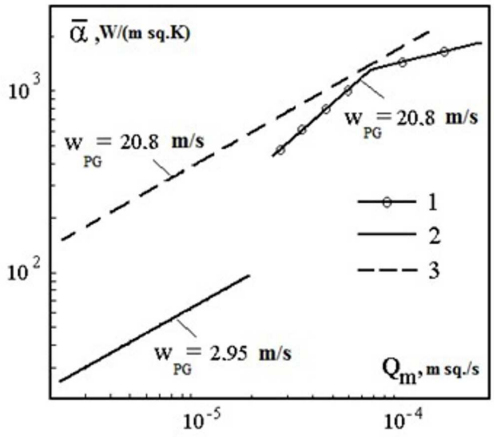

Figure 5: Dependence of the average heat transfer coefficient, α, on the density of the irrigation, Q_m, for various vases of thermal mass exchange: 1 – contact thermal mass exchange at unidirectional ascending flow of gas-steam and liquid mix, 2 – contact thermal mass exchange at countercurrent flow of gas-steam and liquid mix on porous nozzle, 3 – conventional dependence (extrapolation of the counter flow).

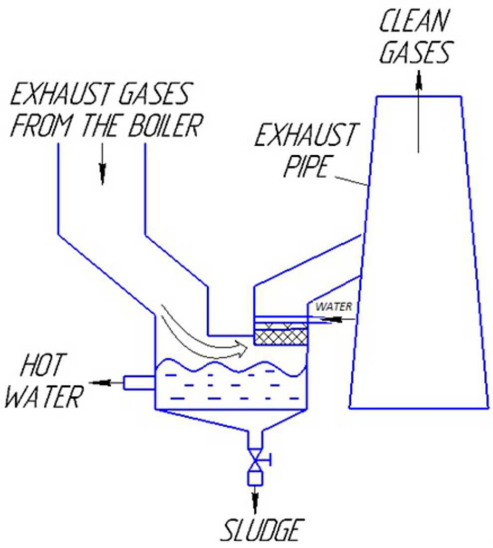

Figure 6: Scheme of implementation of direct contact energy exchangein coal-fired boilers.

3 Conclusions

1. Power plants using direct contact energy exchange can significantly improve the energy and environmental indicators of energy conversion and the generation of electrical and heat energy for individual and decentralized energy consumption. They open a wide horizon of environmentally friendly power generation.

2. Preliminary studies of contact energy exchange processes have shown us additional positive effect that increases the ecological purity of energy transformations and contribute to the production of excess technically pure water (GPU 'Aquarius', contact heat generator TWAC).

3. The feasibility of developing and implementing devices and installations with the application of contact energy exchange processes for boilers has been proved through calculations and experiments. Particularly expedient is using of contact energy exchange equipment for coal-fired boilers, since this allows us obtaining a flue gas with a high level of cleaning from both toxic CO and NO_x components, as well as from coal dust and ash.

Received 10 October 2017

References

[1] Dikiy N., Koloskova N., Shklyar V., Dubrovskaya V.: *Development and investigation of a condenser of a mixing type with a porous packing.* Prom. Heat Engineering **13**(1992), 1-3, 11–15.

[2] Dikiy N., Dubrovskaya V., Shklyar V.: *Investigation of the contact capacitor for the heat recovery circuit of the KG PTU.* Prom. Heat Engineering **23**(2001), 4-5. 81–83.

[3] Dikiy N., Uvarichev O., Solomakha A.: *The newest gas and steam turbine technology 'Aquarius' for the production of mechanical (electric) and thermal energy and its implementation in the energy complex of Ukraine.* Energetics, Economics, Technologies, Ecology **1**(2009), 16–19.

[4] Varlamov, G., Romanova K., Daschenko O., Ocheretyanko M., Kasyanchuk S.: *The use of contact heat generators of the new generation for heat production.* Eastern-European J. Enterprise Technologies **84**(2016), 52–58.

[5] Gubarev A., Kuleshov M., Pogonin A.: *Increasing the efficiency of autonomous heat supply systems when using heat-generators of condensation type.* Energy and Heat Engineering Processes and Equipment **8**(2012), 117–125.

[6] Dikiy N., Solomakha A., Suzdal E.: *Gas and steam turbine technology 'Aquarius' for joint production of electric and thermal energy.* Energy Technology and Resource Saving **3**(2012), 30–33.

[7] Kapustyansky A., Misak Y.: *Results of expert tests of the boiler TPP-210A Trypillya TPP at combustion of solid fuel with the addition of a combustion catalyst.* Power Engineering and Electrification **12**(2012), 3–8.

[8] Kapustiansky A.: *Influence of the addition of the combustion catalyst on the efficiency and economy of the operation of boilers during coal combustion.* Energy Manage. **1**(2013), 20–21.

[9] Varlamov G., Dashchenko O., Kasyanchuk S., Ocheretyanko M.: *The principle of ecological balance as a guarantee of the growth of environmental safety.* In: 'Balanced Development – 21st Century: Management, Technologies, Models' (I. Khlobystova, Ed.). WSEH, Cherkasy 2015, 153–158.

[10] Varlamov G., Dashchenko O., Romanova K., Vovchenko D., Code D.: *Realization of the new energy-ecological paradigm is the basis of sustainable development of the country in harmony with nature.* In: Proc. 13th Int. Scientific Practical Conf. 'Ecological safety: problems and solutions', Kharkiv, September 11–15, 2017.

archives
of thermodynamics
Vol. **38**(2017), No. 4, 139–163
DOI: 10.1515/aoter-2017-0029

Modeling of district heating networks for the purpose of operational optimization with thermal energy storage

MICHAŁ LEŚKO*
WOJCIECH BUJALSKI

Warsaw University of Technology Institute of Heat Engineering, Nowowiejska 21/25 00-665 Warszawa, Poland

Abstract The aim of this document is to present the topic of modeling district heating systems in order to enable optimization of their operation, with special focus on thermal energy storage in the pipelines. Two mathematical models for simulation of transient behavior of district heating networks have been described, and their results have been compared in a case study. The operational optimization in a DH system, especially if this system is supplied from a combined heat and power plant, is a difficult and complicated task. Finding a global financial optimum requires considering long periods of time and including thermal energy storage possibilities into consideration. One of the most interesting options for thermal energy storage is utilization of thermal inertia of the network itself. This approach requires no additional investment, while providing significant possibilities for heat load shifting. It is not feasible to use full topological models of the networks, comprising thousands of substations and network sections, for the purpose of operational optimization with thermal energy storage, because such models require long calculation times. In order to optimize planned thermal energy storage actions, it is necessary to model the transient behavior of the network in a very simple way – allowing for fast and reliable calculations. Two approaches to building such models have been presented. Both have been tested by comparing the results of simulation of the behavior of the same network. The characteristic features, advantages and disadvantages of both kinds of models have been identified. The results can prove useful for district heating system operators in the near future.

*Corresponding Author. Email: mlesko@itc.pw.edu.pl

Keywords: Thermal energy storage; District heating; Smart district heating; Optimization

1 Introduction

The aim of this document is to present the topic of modeling district heating systems in order to enable optimization of their operation, with special focus on thermal energy storage. The article is dedicated to energy storage in the pipelines, by shaping the supply temperature of water, rather than to utilization of hot water tanks.

Recent changes on energy markets, especially growing variations of electricity prices during the day, and the need to use combined heat and power (CHP) plants for balancing the electrical grid, make the value of heat delivered to DH systems very unstable. At the hours when the price of electricity is very high, or the CHP plant is called to production by the transmission system operator, the cogenerated heat can be considered a by-product available at zero cost. At some other hours, due to low electricity prices or the need to switch on a peak boiler, the marginal cost of heat at the CHP plant becomes much higher than the price at which it is sold to customers. This situation makes it very attractive to consider all possible ways of thermal energy storage, in order to maximize the total financial benefits from production of a CHP plant, at the same time delivering the heat to customers when they need it.

There are three basic options for thermal energy storage in DH: using hot water tanks, using thermal inertia of buildings and using the thermal inertia of pipelines. Among these three, using the thermal inertia of pipelines is the one which requires no additional investment and no remote control of substations – which makes it a very attractive solution for virtually all DH networks. In most DH systems this solution is already utilized, but the actions of overheating the network are typically done based on the experience of operators, without thorough calculation of costs and benefits. One of the reasons for this is the fact, that calculation of actual benefits at the CHP plant and of the effect on the heat losses in the network requires advanced models of the system. This article is dedicated to a part of this challenge – modeling of the network. The goal is not to make a large and precise thermo-hydraulic model, based on the real topology of actual grid. Such models, using Geographical Information System (GIS) data, are commercially available. However, their precision comes at the cost of calculation

times, which in general make them not useful for optimization of heat production with the use of thermal energy storage. Such purpose requires very simple and fast models, compatible with reliable solvers, which in turn will make it possible to choose a proper scenario among thousands of possibilities, and present it to the operators before it is too late for decisions. The two simple approaches presented in current work are aimed at answering that need.

2 Current state of research

There are many works dedicated to the topic of optimization of CHP production and modeling of DH systems. A solution to the general problem of unit commitment in power production planning under the assumption of linear models of production units has been presented by Viana and Pedroso in [1]. Badyda [2] has described the general model of a backpressure extraction turbine. Interesting methods formodeling CHP units have been presented in [3] and [4]. Fonseca and Schneider [5] have described the results of modeling a particular CHP plant with different approaches. Ziębik *et al.* [6] have performed modeling of a CHP plant based on a technological diagram, despite very limited access to operational data. Bujalski [7] has proposed a solution for optimal scheduling of a CHP plant operation, with the use of a storage tank. Fazlollahi *et al.* [8] have proposed a procedure for optimization in DH on the stage of design and operation. Ziębik and Gładysz [9] have proposed an empirical formula for determination of the optimal value of the share of cogeneration in cogeneration systems with thermal storages. There are many works about optimization and controlling seasonal storages (STES) [10,11]. The topic of utilization of demand side management in space heating for the purpose of optimization has been also discussed in several works [12,13]. Hydraulic modeling of DH networks (in steady state) has been described in [14]. Thermo-hydraulic modeling of district heating and cooling networks was the topic of numerous articles such as [15]. Basciotti *et al.* [16] have presented a model for finding an optimal profile of supply temperature in a small district heating network. Similar work has been done by Benonysson *et al.* [17]. All these works describe particular solutions and their successful implementation. None of them presents a global optimization of a large DH system, including the possibility of thermal energy storage in a hot water tank, with the use of pipelines and with the use of thermal inertia of buildings at once. The

objective of current study is to make a step towards such global optimization, by clear presentation of one part of such solution, i.e., models of the network. Rather than presenting a particular model, this article aims at a clear description and comparison of two possible approaches, in order to identify their advantages and disadvantages, which can help in choosing a proper solution for future projects dedicated to global optimization in DH.

3 Modeling a district heating network

A DH system comprises heat sources, pipelines, pumping stations, storage tanks, valves and buildings with their substations. There are already comprehensive models and commercial solutions for simulation and optimization of operation of CHP plants. The topic of modeling the inertia of buildings has been described in [13]. In this article, the focus is on district heating networks.

District heating network pipelines are insulated steel tubes of a diameter between 20 mm and 1200 mm (or even more). It is natural to subdivide network into sections, with each section representing a continuous path of tubes characterized by the same diameter, roughness, insulation parameters and water mass flow. Typically it means that sections are divided by nodes representing substations, valves, heat production plants, pumping stations, storage tanks, etc.

3.1 Hydraulic calculations

Due to the size of the networks, in case of district heating it is not feasible to use precise methods from the field of fluid dynamics (e.g., finite element method) for hydraulic simulations. Instead, the calculations are based on simple equations describing linear pressure losses and local losses, which can be found, e.g., in [18]. Based on such equations and on the mass balance in every node, it is possible to determine pressure and water flow in every point of a network, given the boundary conditions (absolute pressure at one point and pressure differences at every pump or controlling valve). In case of small networks with tree structure such calculations are very simple, in case of large grids including ring connections usually iterative approach is required.

Proper hydraulic state of the network means that:

- pressure difference between supply and return line is above the defined minimum at all the substations (it means that no regulation valve must be fully open in order to reach the desired heating power) and below the maximum which would be dangerous for the valves,
- at no point in the network the pressure drops below the global minimum limit (at which there would be a risk of underpressure resulting in air entering the pipelines through every untight connection),
- at no point in the network the pressure exceeds the global maximum limit (at which there would be a risk of damage to the pipelines).

At every moment of DH network operation, flow demands at substations and the grid configuration determine the optimal pumping scheme (power and pressure increase at particular available pumping stations) which would lead to proper hydraulic state. Finding that scheme can be done in real-time (because there are no delays) and in practice it is separated from the heat production planning. The plan of production (including supply temperature profiles) is done assuming that the pumps will allow reaching desired flows at all substations, and then the pumping control is performed in order to meet that assumption.

As the topic of current paper is strictly related to thermal energy storage, the main focus here will be on thermal models, which in fact define the delays and thermal inertia in a DH network, utilized for load shifting.

3.2 Thermal calculations

Thermal model of the network is needed for simulation of temperature propagation in the system. For given profile of the supply temperature at the heat source, outdoor temperature, heating power demands and return temperatures (or temperature drops) at all substations, assuming proper hydraulic state of the network, the thermal model should allow to simulate all the temperatures in the network and flows of DH water. As a result, total heating power at the heat source is determined (by calculation of total flow and return temperature at the heat plant), and heat losses can be calculated (based on temperature drops and flows in the pipelines).

Heat transmission is the most important phenomenon to account for. In reality, the heat is lost from both supply and return line to the ground, and also transmitted from the supply to return line. The scale of heat transfer

depends on many factors such as state of the insulation (which varies over time), type of the ground, water speed, etc. As the heat transfer coefficients are temperature dependent, a perfect model would be very complicated and non-linear, making it extremely difficult to use for optimization purposes. It is crucial for system-scale optimization to build simple, preferably linear, models, which will still be able to reflect the actual behavior of the network.

In the most general form, the heat loss from water in a pipeline is proportional to the temperature difference between inside and outside, divided by the sum of thermal resistances of pipeline and insulation layers [18]

$$\dot{Q}_{loss} = \frac{(T_{water} - T_{out})}{\sum R} = -m_{water} c_p \dot{T}_{water} \ , \tag{1}$$

where: $\dot{Q}_{loss}$ – time derivative of heat loss, T_{water} – temperature of the water in the pipeline, T_{out} – ambient temperature, $\sum R$ – sum of thermal resistances, m_{water} – mass of water inside the pipeline, c_p – specific heat of water, $\dot{T}_{water}$ – time derivative of temperature of the water in the pipeline.

Based on that, assuming constant resistances, constant amount of water (in the pipeline or in the volume of interest) and constant specific heat, the simplest (and most convenient in case of very large models) equation for the pace of temperature drop can be written:

$$\dot{T}_{water} = -x_{loss}(T_{water} - T_{out}) \ , \tag{2}$$

where: x_{loss} – the heat loss coefficient for a given pipeline or volume of interest.

Two very general approaches to thermal calculations of the network are possible:

1. Focused on particular pipeline sections, treating them as objects which experience heat losses to the surroundings, water inflow and water outflow.
2. Focused on particular volumes of water, treating them as objects which travel through the pipelines and cool down through their walls.

3.3 Modeling the network with the focus on pipeline sections

The energy balance of a pipeline section can be written as

$$\triangle E = m_{in} c_p T_{incoming} - m_{out} c_p T_{outgoing} - Q_{loss} \ , \tag{3}$$

where: $\triangle E$ – change of total energy in the pipeline section, m_{in} – mass of water which has entered the pipeline, $T_{incoming}$ – temperature of water which has entered the pipeline, m_{out} – mass of water which has left the pipeline, $T_{outgoing}$ – temperature of water which has left the pipeline, Q_{loss} – amount of heat lost to the surroundings.

As the mass of water in the pipeline does not change, Eq. (3) after differentiation can be rewritten as:

$$m_{water} c_p \dot{T}_{in\ section} = \dot{m}_{flow} c_p \left(T_{incoming} - T_{outgoing}\right) - \dot{Q}_{loss} \ , \tag{4}$$

where: $\dot{T}_{in\ section}$ – time derivative of the temperature in the pipeline section, $\dot{m}_{flow}$ – flowrate of incoming water, equal to the flowrate of the outgoing water.

In reality, a pipeline section can contain water at variable temperature, not possible to describe with a simple continuous function. It is a result of supply temperature changes at the heat source, water mixing (especially in return lines) and cooling down of the water. It is not feasible to build a model which will divide every pipeline section into elements characterized by uniform DH water temperature, and such division would have to vary in time. The most reasonable approach for simplified modeling of the whole network as an aggregation of pipeline sections is to assume uniform temperature in each section at every time step, and then calculate heat losses from each section at every time step which determines the temperature drops. The assumption is equivalent to full mixing of water within each pipeline section, which is far from reality for longer pipeline sections. However, it allows to simulate the thermal situation in the network in a simple way and without violation of energy balance principles.

Assuming uniform temperature in a pipeline section, considering Eqs. (1) and (2), Eq. (4) yields

$$\dot{T}_{in\ section} = \frac{\dot{m}_{flow}}{m_{water}} \left(T_{incoming} - T_{outgoing}\right) - x_{loss}(T_{water} - T_{out}) \ . \tag{5}$$

Based on that formula, a simple equation for fast calculation of water temperature in a pipeline section, in discrete time steps, can be written

$$T_{t+\triangle t} = T_t + \frac{\dot{m}_{flow}\triangle t}{m_{water}}\left(T_{incoming} - T_t\right) - x_{loss}(T_t - T_{out})\triangle t\ , \qquad (6)$$

where: T_t – temperature of the water in the section at time t, $\triangle t$ – time step.

Equation (6) is a base for thermal models assuming full mixing of water in every pipeline section. Their accuracy is limited, however by increasing the number of pipeline sections and adjusting the time step, they can be calibrated to bring satisfying results.

3.4 Modeling whole network as one energy buffer

A specific and probably the simplest model of the network is in fact a model with the focus on pipeline sections, but assuming that whole network is just one pipeline section (or more precisely, one energy buffer). It allows to track the state of network (in terms of charging/discharging with overheated water) and its influence on heat losses without considering the topology of the network. It can be used for preliminary calculations on any network, without preparations – it is enough to know some global coefficients (which are normally easy to compute based on historical data) and total flow. Equation (6) can be rewritten for such a model in the following form (describing the average supply temperature in whole network and the average return temperature in whole network, equal to the return temperature coming to the heat source):

$$T_{sup,t+\triangle t} = T_{sup,t} + \frac{\dot{m}_{flow}\triangle t}{m_{water}}\left(T_{\mathrm{sup}\,CHP,t\to t+\triangle t} - T_{sup,\,t}\right) - x_{loss}(T_{sup,t} - T_{out})\triangle t\ , \qquad (7)$$

$$T_{ret,\,t+\triangle t} = T_{ret,\,t} + \frac{\dot{m}_{flow}\triangle t}{m_{water}}\left(T_{ret\ SST,t\to t+\triangle t} - T_{ret,\,t}\right) - x_{loss}(T_{ret,t} - T_{out})\triangle t\ ,$$

where: $T_{sup,\,t}$, $T_{ret,\,t}$ – temperature of supply and return, at the time t, $T_{\mathrm{sup}\,CHP,t\to t+\triangle t}$, $T_{ret\ SST,t\to t+\triangle t}$ – average temperature of supply at the heat source and average temperature of return at the substations, over the time between t and $t + \Delta t$.

It can be seen especially in the formula for return temperature (which at given flow and supply temperature determines total heating power of the heat plant), that this approach can give wrong results for long networks, where the average return temperature can be far from the return temperature reaching the heat source.

3.5 Modeling the network with the focus on volumes of water

In reality the water mixing in the supply pipelines of a DH network is limited. In order to reflect this fact, an approach with the focus on volumes of water can be proposed. In this approach, pipeline sections are considered only as a frame in which volumes of water ('waves') travel. But the heat losses are calculated for each 'wave' separately. By tracing the 'waves' in the network, it is possible to determine the temperature of DH water at every point of it and at every moment. At every time step, the temperature of water in the 'wave' is decreasing, based in Eq. (2):

$$T_{water,t+\triangle t} = T_{water,t} - x_{loss}(T_{water,t} - T_{out,t})\triangle t \ . \tag{8}$$

If the water 'wave' reaches a split of pipelines (e.g., at the supply side of a substation), it must be divided in the model into two 'waves' (e.g., one flowing further in the network and one flowing through the substation to the net of return pipelines). If two waves reach a joint of pipelines (e.g., at the return side of a substation), they must be combined into one, new 'wave' at their weighted average temperature (e.g., a mixture of water returning from the substation and water flowing in the return lines at the location of the substation). The principle is illustrated in Fig. 1.

The 'wave' model seems to be the closest to reality, however it neglects the fact that there is some mass and heat exchange in the pipelines. The main drawback of that model is the fact that it is relatively complicated. Unlike in the approach focused on network sections, in the 'wave' model the number of elements on which the equations need to be applied, and their volume, are variable (as the 'waves' split and mix). This makes it more difficult to implement, and more time consuming to calculate. It is also crucial in this model, that the topology reflects the real behavior of the network, since the mechanism is based on tracing the flow of water volumes produced at different moments. On the other hand, replicating full topology of a large network would make a 'wave' model too slow for optimization calculations. A reasonable simplification is crucial, in order

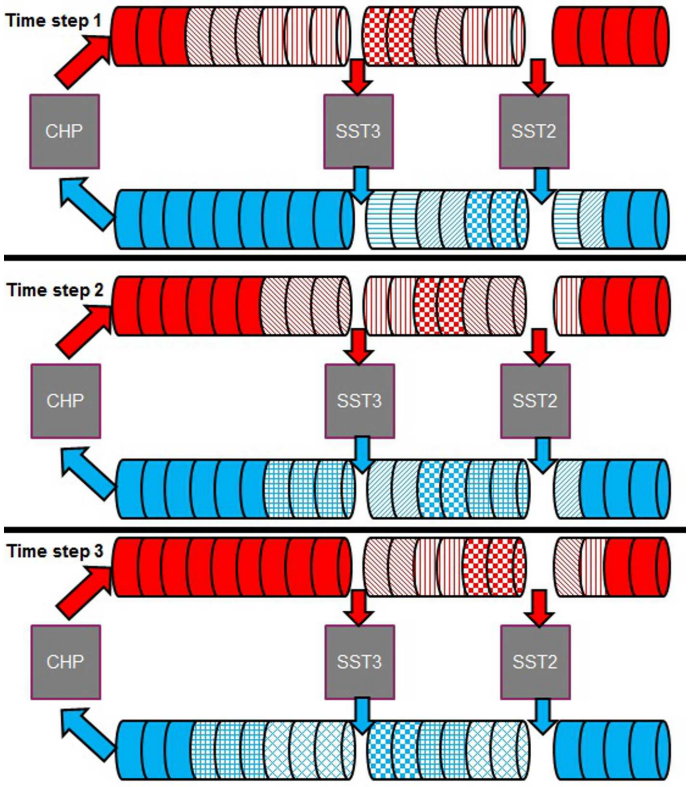

Figure 1: Principle of water wave travelling, separation and mixing.

to build an equivalent topology model which reflects the reality but omits or aggregates smaller pipelines.

3.6 Modeling the network by delays, without topology

Many DH networks are nowadays equipped with telemetry systems, providing measurements from substations and heat chambers in abundance. One of the possibilities of such systems is to trace the actual waves of supply water, by comparing the time at which a significant temperature change reaches particular points of the network. In this simple way, the time of water transportation between the heat source and each substation with measurement can be determined. The time of transportation is of course dependent on the total flow in the network, which in turn varies according

mainly to the outdoor temperature. By calculating the time of transportation under different circumstances (i.e., at different total flows), for every significant point of the network (e.g., substation) a simple function defining the time of transport can be created.

Apart from comparing the time at which a significant change of supply temperature reaches particular points of the network, also the value of the temperature in the peak of change can be monitored. By looking at the difference between peak value at the heat source and peak value at a specific point of the network, temperature drop can be described for every point of the network by a function of outdoor temperature or total water flow, or other variables.

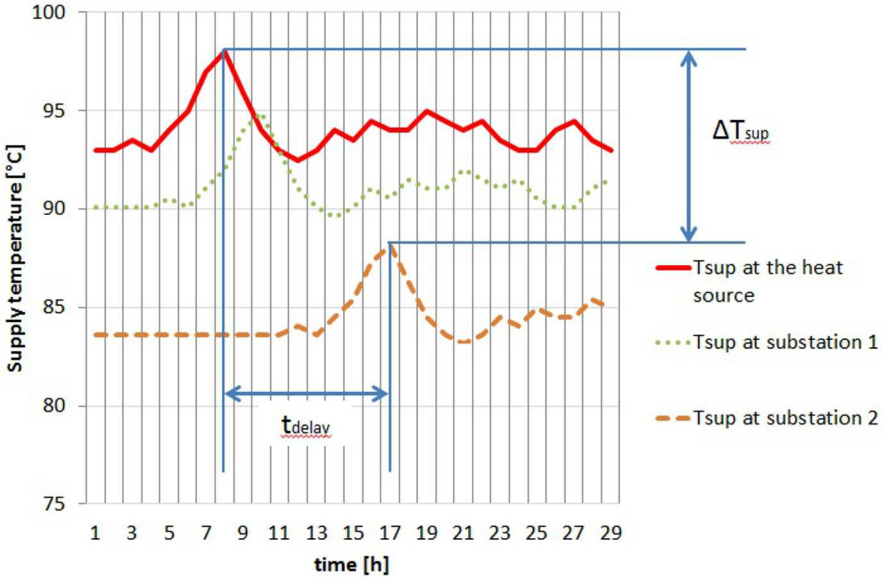

Figure 2: Illustration of finding the delay and temperature drop based on measurements of supply temperature at the heat source and at a substation.

Figure 2 illustrates the procedure of finding the delay and temperature drop for a substation. Applying this procedure many times, with measurements recorded under different circumstances, allows to build a set of equations describing transportation time and temperature drop for each significant point as a function of the circumstances which varied during tests. A set of such empirical functions can serve as a model of the network – without considering the topology of pipelines explicitly.

The approach to creation of such functions has been described with the focus on supply lines. It can be hard to trace significant changes of return temperature, because of mixing of return water at every substation outlet. A simple solution is to assume that the transportation time is the same for return lines as for supply lines (which is in general true in most grids as they are typically symmetrical and the flows are almost equal in both directions), and that the temperature drop on return side is a constant fraction of the temperature drop on the supply side (for the same reasons). Proportions between the temperature drop of supply and return will be the same as the proportions of temperature difference between outdoor temperature and respective temperatures:

$$\frac{\triangle T_{sup}}{\triangle T_{ret}} = \frac{T_{sup} - T_{out}}{T_{ret} - T_{out}} \,. \tag{9}$$

As soon as a set of formulas for all significant points of the network is ready, it can serve to model the thermal behavior of the grid without explicitly considering the topology of pipelines at all. For every substation, at every time step, the supply temperature can be calculated as

$$T_{sup}^{SST\ i}(t) = \tag{10}$$
$$T_{sup}^{heat\ source}\Big(t - t_{delay}^{SST\ i}\Big[T_{out}, \text{day type}, ...\Big]\Big) - \triangle T_{sup}^{SST\ i}\Big[T_{out}, \text{day type}, ...\Big],$$

where: $T_{sup}^{SST\ i}$ – supply temperature reaching the substation i in time t, $T_{sup}^{heat\ source}[t]$ – temperature of supply at the heat source in time t, $t_{delay}^{SST\ i}$ – time of water transport between the heat source and substation i, $\triangle T_{sup}^{SST\ i}$ – temperature drop between the heat source and substation i in supply pipelines (a function of outdoor temperature, type of the day, etc.).

Knowing the supply temperature at every important point of the network, it is possible to use the substation models and hydraulic models in order to calculate other parameters at those points. The supply temperature could be calculated more precisely with the use of total flow in the network rather than outdoor temperature; in such case the process of finding total flow and supply temperatures must be iterative. As soon as return temperatures at all substations are determined, the return temperature at the heat source can be calculated as an average of return temperatures at particular substations, weighted by their flows, and respecting the temper-

ature drops and delays:

$$T_{ret}^{source}(t) = \frac{\sum_{i=1}^{n} T_{ret}^{SST\ i}(t - t_{delay}^{SST\ i}[T_{out}, \text{day type}, ...])\dot{m}_{flow}^{SST\ i}(t)}{\sum_{i=1}^{n} \dot{m}_{flow}^{SST\ i}(t)} - \frac{\sum_{i=1}^{n} \triangle T_{ret}^{SST\ i}[T_{out}, \text{day type}, ...]\dot{m}_{flow}^{SST\ i}(t)}{\sum_{i=1}^{n} \dot{m}_{flow}^{SST\ i}(t)}, \quad (11)$$

where: $T_{ret}^{source}(t)$ – temperature of return, reaching the heat source in time t, $T_{ret}^{SST\ i}(t)$ – temperature of return at the substation i in time t, $\triangle T_{ret}^{SST\ i}$ – temperature drop between the substation i and the heat source in return pipelines (a function of outdoor temperature, type of the day, etc.), $\dot{m}_{flow}^{SST\ i}(t)$ – flowrate of DH water at substation i in time t.

Return temperature at the heat source, together with the supply temperature and total flow, allows to determine the heating power of the heat source at every time step. Thus, it is possible to fully model the thermal behavior of the network including its inertia, without building any topology model – just based on the empirically measured delays and temperature drops.

As long as the total flow in the network is constant, the model based on delays gives exactly the same results as a 'wave' model (because both assume no mixing of the water and account for delays as well as temperature drops). However, if the total flow varies in time, the results given by the model based on delays reveal its main drawback. Unfortunately, unlike the other models presented so far, the model based on delays does not by definition respect the energy balance when applied in time steps. In reality, if the total water flow at an hour X is higher than at preceding hours, then of course during the hour X the heat source will be reached by the volume of water returning from substations, which has left these substations over a period of more than an hour. For example, if the flow at substation i at hour X is 1 t/h, then on average 1 t of water from substation i will reach the heat source during that hour. Let us assume that the delay is Y, and the flow at substation i at hour $X - Y$ was 0.9 t/h. Only part of the water from substation i reaching the heat source at hour X will have the temperature determined by leaving the substation at hour $X - Y$. Other part will have a temperature resulting from leaving the substation at a later hour – which may be different. The model does not consider that. As a result, an overheat of supply during one hour of low total flow can result in an overheat of return during an hour of high total flow. And that means artificial

creation of energy in the model based on delays. This effect is significant if the flow changes are large, and may affect the results of optimizations in such cases.

4 Case study – using the inertia of the network simulated with different thermal network models

It is relatively simple to model the behavior of a DH network in steady state. All the models described above can give reasonable results for such situation. Most DH companies are used to relay on steady state calculations for the purposes of simulating the network development, designing the pipelines, sizing the heat sources, etc. However, operational optimization with load shifting is by definition connected to transient behavior of the network. In order to help in optimization of production planning utilizing the inertia of the network, a model must consider variations of supply temperature and their influence on power profile. As this is the key element, all the models described above have been compared in a case study, in order to analyze the way they handle the phenomenon of thermal energy storage in pipelines.

4.1 Model of the network

A simple model of a district heating network, comprising one heat source and three substations, has been created using different methods. The substations are connected in series. It is assumed that each of the substations consumes 10 MW of heat all the time, and that the transportation delays are:

- 10 hours between the heat source and the substation 1 (furthest from the network),
- 6 hours between the heat source and the substation 2 (in the middle),
- 3 hours between the heat source and the substation 3 (closest to the heat source).

A network that corresponds to aforementioned assumptions is presented in Fig. 3. Four Microsoft Excel sheets have been created, each of them modeling that network with one of the approaches described before. Then the

results of the same supply temperature variations, simulated with different models, have been compared.

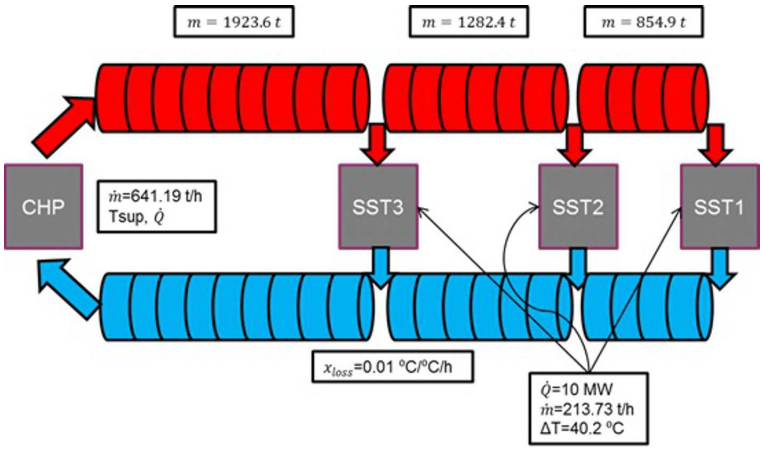

Figure 3: The simple network model built for case study.

4.2 Single overheat

A single overheat of the network, i.e., a change of supply temperature at the heat source from 93 °C to 97 °C for 4 hours and then back to 93 °C, has been simulated with all of the models described before.

Water mixing model The results of simulation with water mixing model are shown in Fig. 4. Directly after the increase of supply temperature, total heating power at the CHP plant increases sharply and remains stable for 2 time steps. Then the return temperature starts to increase, causing the heating power to slightly decrease. At the moment when the supply temperature is decreased back to initial value (end of overheat), the heating power plummets below the initial value (because return temperature is high). For some short time the power keeps decreasing, as hotter water from substations reaches the plant. Then the heating power starts to slowly increase, as the return temperature decreases, at the end of the time horizon reaching almost the initial value. The changes of both supply and return temperatures at substations are moderate and time consuming, and the borders of the wave of hotter water are disappearing over time, especially on the return side.

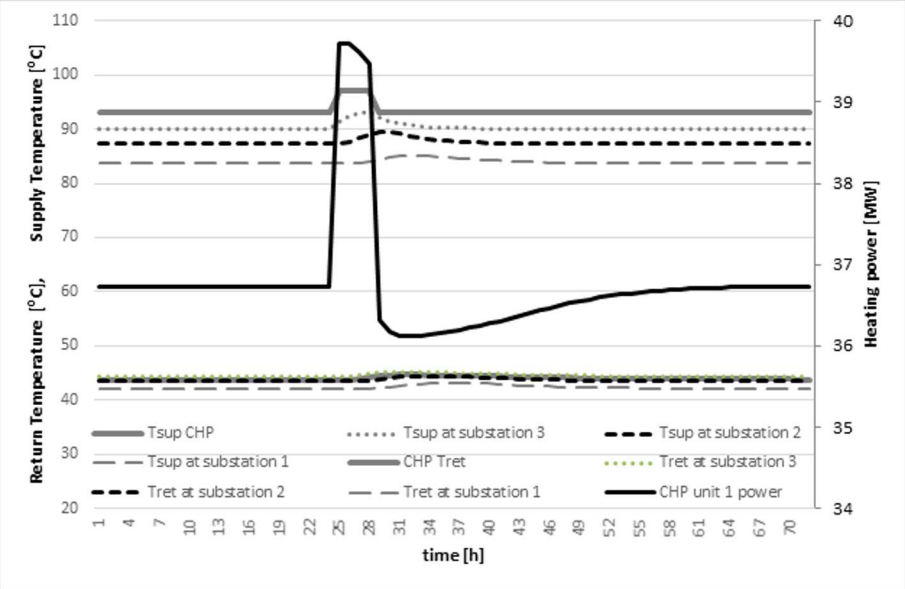

Figure 4: A single overheat of network, simulated with 'water mixing' model.

Whole network model The same case has been modelled with the approach treating whole network as one substation (with the heat demand of 30 MW, as the sum of all 3 substations) and one pipeline section (with the mass of 4060 t of water, as the sum of all 3 sections). The results are shown in Fig. 5. The supply temperature at the 'substation' which represents all substations is about the average of 3 temperatures for particular substations simulated with 'water mixing' model. The return temperature is almost the same, and most importantly, the heating power resulting from this simulation is very close to the one resulting from simulation considering 3 pipeline sections and substations. All the changes take place in the same way, and in fact the values of heating power at particular time steps differ only by up to 0.27%. It shows that as long as the purpose of modeling is to simulate the reaction of the network in order to know how much energy can be stored by a given overheat, in the 'water mixing' approach, aggregation of substations does not significantly affect the accuracy. Only if knowing the temperatures or flows at particular substations is necessary (e.g., because of constraints applied there), it is necessary to model them separately, because the supply temperatures depend to a large extent on the distance from heat source.

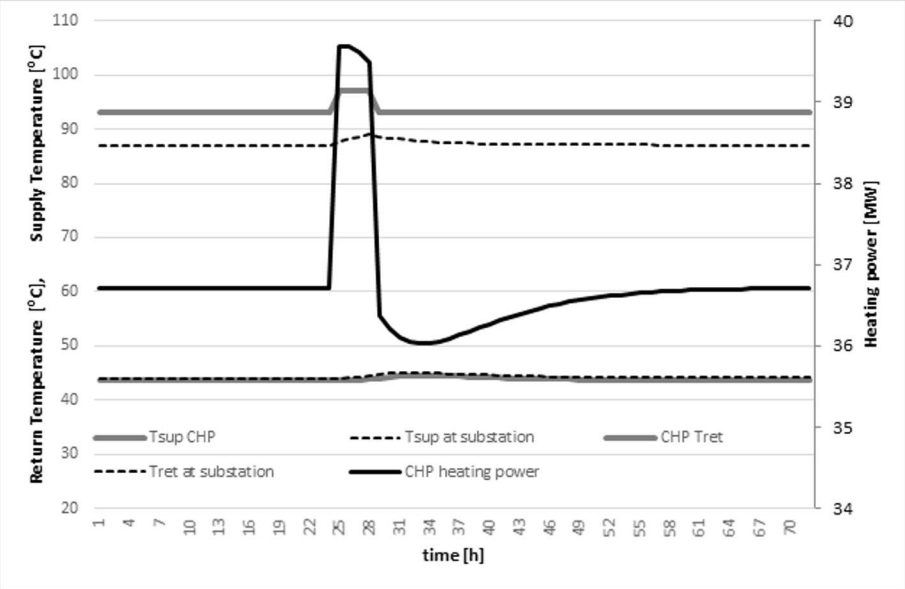

Figure 5: A single overheat of network, simulated with 'whole network' model.

Wave model Figure 6 presents the results of simulation with the 'wave' model. These results are significantly different from the results of 'water mixing' model. The hotter water propagates in the supply lines as a 'wave' with clear borders, so that the shape of supply temperature profile at every substation is the same (only the delay and the temperature drop differ). Similarly, the hotter water in the return lines propagates back to the source in the form of 'waves'. At some points of the network, multiple 'waves' can be observed – first resulting from increased temperature at the closest substation, then from increased temperature of water that left some further substation and passes by. As long as the delays between substations are longer than the duration of overheat, the waves on return side do not overlap and the first wave on the return side does not come to the heat source before the end of overheat. As a result, during the overheat the heating power of CHP plant is stable, higher than the initial heating power. After the overheat it drops back to the initial value, and then decreases further as soon as first wave of hotter water reaches the return side of CHP plant. Later the heating power goes back to the initial value, and drops again when next waves of hotter return water reach the plant. The first decrease of heating power below initial value is the biggest, because it results from

the first wave. The first wave represents the water volume from the closest substation, which spent the smallest amount of time in the network, and for this reason its additional temperature drop is smallest. So it contains hotter return water than the waves that follow, in turn resulting in smaller temperature difference at the heat source which leads to smaller heating power.

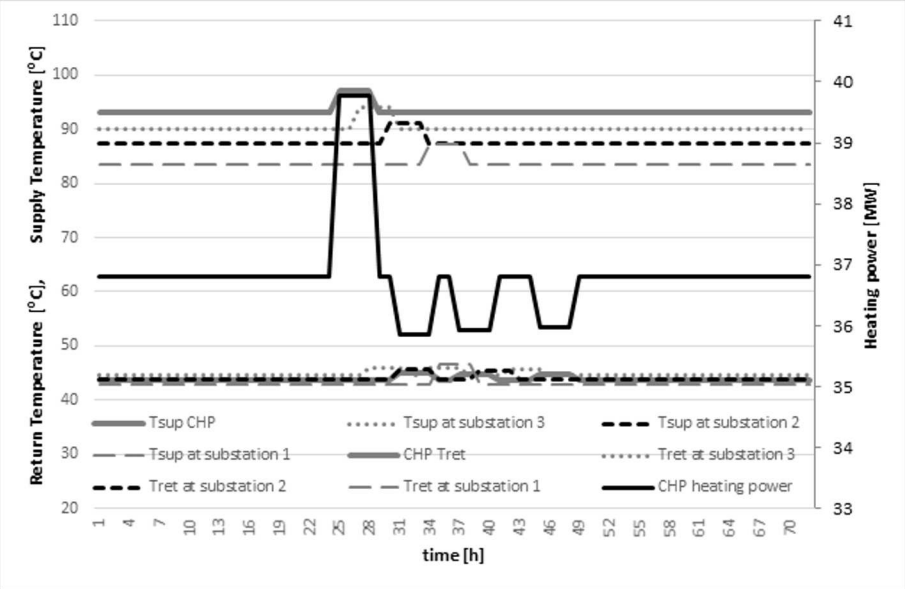

Figure 6: A single overheat of network, simulated with 'wave' model.

Delays model As it has been predicted in the theoretical part, the model based on delays has given exactly the same results as the 'wave model'. It proves that these two models are identical, as long as total flow is constant. And when it is not, the 'delays' model does not respect the energy balance. For these reasons the 'delays' model was not investigated further. It remains in fact a simpler way of defining the wave model for constant flows, and a solution which should not be used for cases where flows are significantly variable.

4.3 Long overheat

A long overheat of the network, i.e., a change of supply temperature at the heat source from 93 °C to 97 °C for 16 hours and then back to 93 °C, has been simulated with the same models as in case of the single overheat. The results given by 'water mixing' and 'whole network' model are shown in Figs. 7 and 8, respectively. The profiles of heating power and DH water temperatures are analogical to the ones simulated for a short overheat. They are also very similar to each other, with the difference between heating power in both models limited to 0.25%.

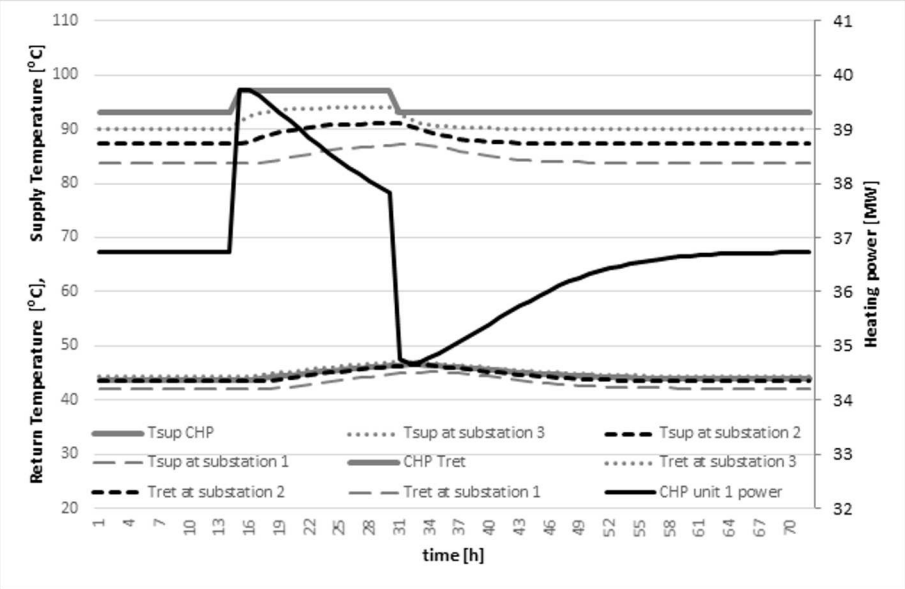

Figure 7: A long overheat of network, simulated with 'water mixing' model.

Figure 9 illustrates the results given by the 'wave' model (identical with the results from a 'delays' model). In this case, the 'waves' overlap, so the heating power during the overheat is not stable. It drops when hotter return water from the closest substation reaches the plant, and then it drops again when hotter return water from second substation reaches the plant. Then after the very large decrease due to end of overheat, the power drops for the last time when hotter return water from the third substation reaches the plant. Soon after that, the heating power increases in three steps, as three waves of hotter return water from particular substations end.

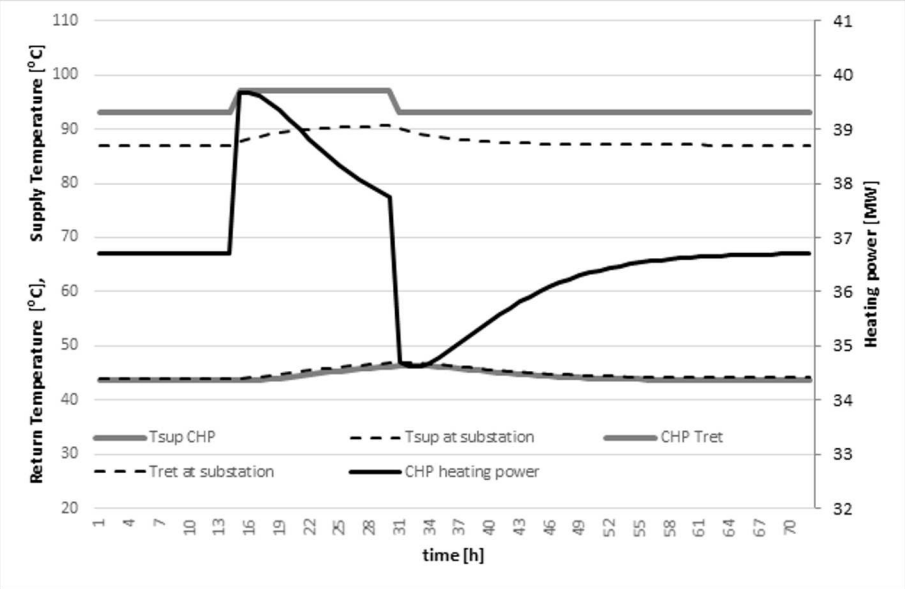

Figure 8: A long overheat of network, simulated with 'whole network' model.

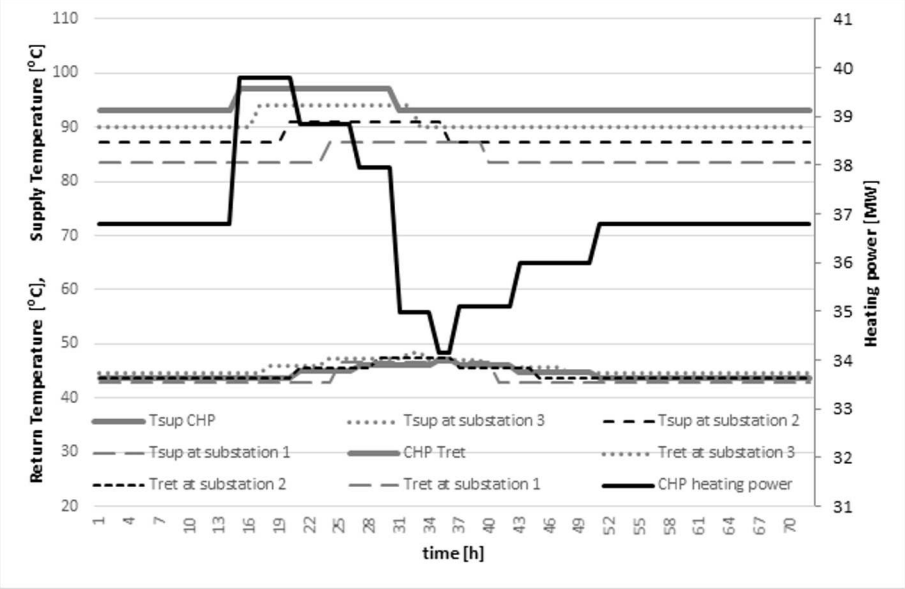

Figure 9: A long overheat of network, simulated with 'wave' model.

It is interesting, that for longer overheats, the results of 'water mixing' model and 'wave' model are less different. The steps in which heating power increases and decreases, when they are not separated by periods of heating power reaching the initial value, resemble the continuous way in which heating power changes according to the 'water mixing' model. This effect of similarity will obviously grow as the number of substations (and pipeline sections) in both models grows.

4.4 Two overheats

Two overheats of the network, i.e., a change of supply temperature at the heat source from 93 °C to 97 °C for 8 hours, then back to 93 °C for 6 hours, again to 97 °C for 8 hours and then back, have been simulated with the same models. The results given by 'water mixing' and 'whole network' model are shown in Figs. 10 and 11, respectively. Again, they are very similar to each other, with the difference between heating power in both models limited to 0.39%. Each of the overheats resembles a single overheat, and their effects add without any unexpected interaction.

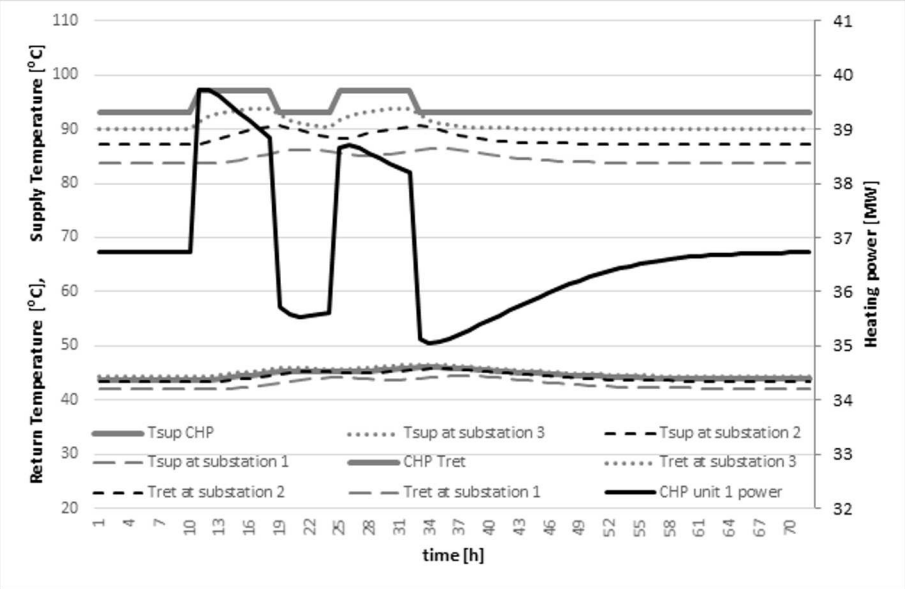

Figure 10: Two overheats of network, simulated with 'water mixing' model.

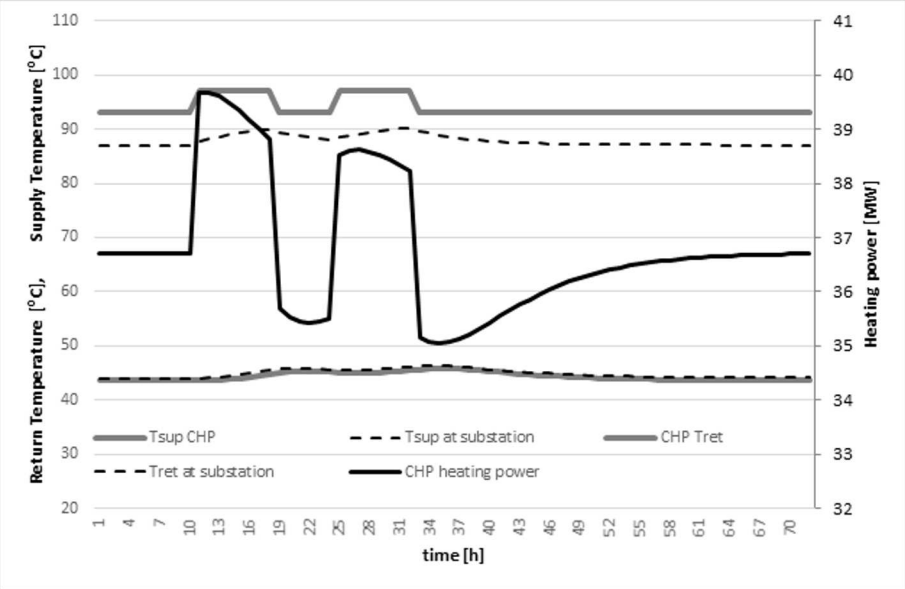

Figure 11: Two overheats of network, simulated with 'whole network' model.

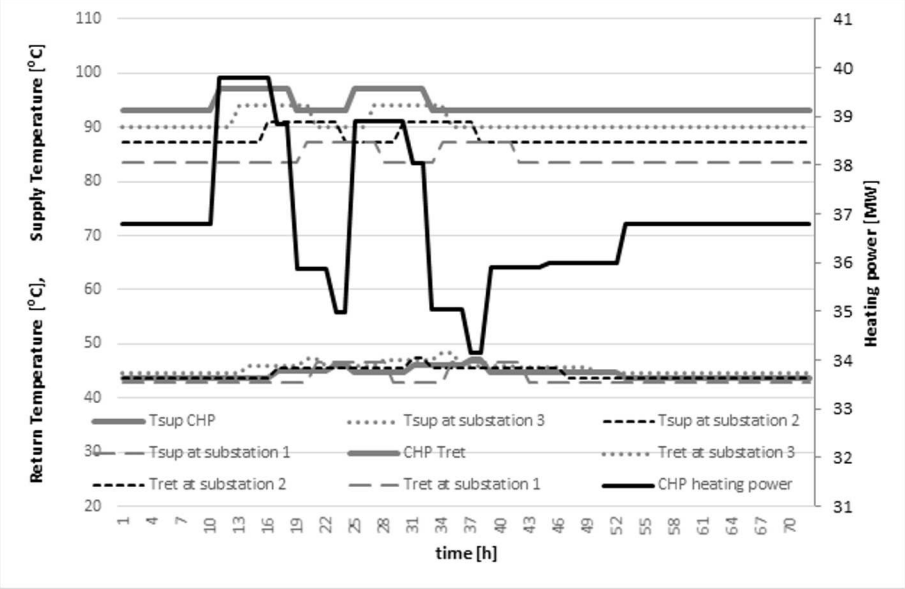

Figure 12: Two overheats of network, simulated with 'wave' model.

Figure 12 presents two overheats simulated with the 'wave' model (identical with the results from a 'delays' model). It can be seen, that in this case particular waves overlap, resulting in a complicated shape of heating power profile. However, in general this profile resembles the profiles simulated with 'water mixing' models. Both overheats have direct, significant effect on the heating power, which then weakens as the responses from substations reach the plant. In the end, the temperature of water in all network sections comes back to initial value, which of course leads to the heating power also coming back to initial value.

4.5 Conclusions from the case study

The case study has confirmed, that for constant total flow, the 'delays' model is identical with the 'wave' model, and the 'whole network' model gives almost the same results as the 'water mixing' model (from the point of view of the heat source).

The 'wave' model correctly simulates the propagation of hot water waves in the supply lines and its assumptions seem to be closer to the reality. However, its results seem to be artificial when only a few substations are modelled. The number of substations is reflected by the number of heating power drops after the overheat, which are in case of a short overheat separated by periods of heating power equal to initial value, which seems artificial. The 'wave' model is also the most complicated, difficult to create and time consuming to calculate.

The 'water mixing' model is simpler and faster than the 'wave' model. The changes simulated with it are more moderate and continuous, which in general reflects the reality well. However, it fails to simulate the way in which hot water waves propagate in the supply lines.

Both 'water mixing' and 'wave' model have a potential to be calibrated in a way which will make them reflect the reality well. What is more important, it seems that the differences between results of particular models tend to decrease as the number of substations grows and as the duration of overheat increases. For this reason, it is possible to perform optimization using any of these models, or a mixture of them. The decision, which one to use, should be taken for particular cases, based on the characteristic of the DH network, the possibilities and requirements regarding programming and time of calculations. For testing purposes, simpler and faster 'water mixing' model can be enough to perform calculations and draw conclusions. Continuity of its results also allows to make simulations with few substa-

tions in the model, without risking that some of the effects are artificial and unrealistic (like in the case of short overheat).

5 Summary

The problem of operational optimization in modern district heating networks has been outlined. Among new solutions, thermal load shifting with the use of inertia of the networks has been chosen for analysis. Two approaches to modeling of transient behavior of a network have been presented. The results of their application have been compared, advantages and disadvantages have been identified. Presented models can be used as a part of future solutions for optimization of district heating systems' operation, sometimes referred to as smart district heating.

Acknowledgement The research described in current paper has been conducted in cooperation with Veolia Energia Polska, as part of PhD program.

Received 18 October 2017

References

[1] Viana A., Pedroso J.P.: *A new MILP-based approach for Unit Commitment in power production planning*. IEEE Trans in Power Systems, 2012.

[2] Badyda K: *Mathematical model for digital simulation of steam turbine set dynamics and on-line turbine load distribution*. Transactions Inst. Fluid-Flow Mach. **126**(2014), 65–82.

[3] Szapajko G., Rusinowski H.: *Mathematicalmodeling of steam-water cycle with auxiliary empirical functions application*. Arch. Thermodyn. **31**(2010), 3, 165–183.

[4] Rusinowski H., Szapajko G.: *Energy evaluation of steam-water cycle operation with mathematicalmodeling application*. Arch.Thermodyn. **32**(2011), 4, 101–117.

[5] Fonseca J.G.S. Jr, Schneider P.S.: *Simulation of a thermal power plant with district heating: Comparative results of 5 different codes*. Energy **31**(2006), 1955–1968.

[6] Ziębik A., Szegda D., Qvale B., Elmegaard B.: *Thermodynamic simulation analysis of a multifuel CHP plant basing on the technological diagram of Avedore unit 2*. Arch. Thermodyn. **31**(2010), 1, 79–93.

[7] Bujalski W.: *Optimization of the operation of a CHP plant equipped with a heat accumulator*. Oficyna Wydawnicza Politechniki Warszawskiej, Warszawa 2013 (in Polish).

[8] Fazlollahi S., Beckera G., Maréchal F.: *Multi-objectives, multi-period optimization of district energy systems: III. Distribution networks*. Comput. Chem. Eng. **66**(2014), 82–97.

[9] Ziębik A., Gładysz P.: *Optimal coefficient of the share of cogeneration in the district heating system cooperating with thermal storage*. Arch. Thermodyn. **32**(2011), 3, 71–87.

[10] Milewski J., Wolowicz M., Bujalski W.: *Seasonal thermal energy storage – a size selection*. Appl. Mech. Mater. 467(2014), 270–276.

[11] Converse A.O.: *Seasonal Energy Storage in a Renewable Energy System*. In: Proc. of the IEEE **100**(2012), 2, 401–409.

[12] Zucker G., Palensky P., Judex F., Hettfleisch C., Schmidt R., Basciotti D.: *Energy aware building automation enables Smart Grid-friendly buildings*. Elektrotechnik & Informationstechnik **129**(2012), 4.

[13] Leśko M. Bujalski W.: *Operational optimization in district heating systems using thermal inertia of buildings*. Rynek Energii (**125**(2016), 4.

[14] Stevanovic V.D., Prica S., Maslovaric B., Zivkovic B., Nikodijevic S.: *Efficient numerical method for district heating system hydraulics*. Energ. Convers. Manage. **48**(2007), 5, 1536–1543.

[15] Oppelt T., Urbaneck T., Gross U., Platzer B.: *Dynamic thermo-hydraulic model of district cooling networks*. Appl. Therm. Eng. **102**(2016), 336–345.

[16] Basciotti D., Judex F., Pol O., Schmidt R.: *Sensible heat storage in district heating networks: a novel control strategy using the network as storage*. Austrian Institute of Technology, Energy Department, Sustainable Building Technology. https://www.researchgate.net/publication/260384884_Sensible_heat_storage_in_district_heating_networks_a_novel_control_strategy_using_the_network_as_storage, (accessed 21.11.2017).

[17] Benonysson A. *et al.*: *Operational optimization in a district heating system*. Energy Convers. Mgmt **36**(1995), 5, 297–314.

[18] Kamler W.: *Heating Technology*. PWN, Warszawa 1979 (in Polish).

archives
of thermodynamics
Vol. **38**(2017), No. 4, 165–190
DOI: 10.1515/aoter-2017-0030

Environmentally friendly replacement of mature 200 MW coal-fired power blocks with 2 boilers working on one 500 MW class Steam Turbine Generator (2on1 unit concept)

JAN GRZESZCZAK[a]*
ŁUKASZ GRELA[b]
THOMAS ACHTER[c]

[a] Rafako S.A., Łąkowa 33, 47-400 Racibórz, Poland
[b] Energoprojekt Katowice S.A., 40-159 Katowice, Jesionowa 15, Poland
[c] Siemens AG, Power and Gas Division, Freyeslebenstr. 1, 91508 Erlangen, Germany

Abstract The paper covers problems of the owners of a fleet of long-operated conventional power plants that are going to be decommissioned soon in result of failing to achieve new admissible emissions levels or exceeding pressure elements design lifetime. Energoprojekt-Katowice SA, Siemens AG and Rafako SA presents their joint concept of the solution which is a 2on1 concept – replacing two unit by two ultra-supercritical boilers feeding one turbine. Polish market has been taken as an example.

Keywords: Coal fired power plant; Flexibility increasing; Old units replacement

Abreviations

AELs	–	admissible emission levels
BAT	–	best available technology
BREF	–	BAT reference documents
CCPP	–	combined cycle power plant
COSTART	–	parallel start of boiler and steam turbine

*Corresponding Author. Email: Jan.Grzeszczak@rafako.com.pl

EPK	–	Energoprojekt-Katowice SA
ESP	–	electrostatic precipitator
FGD	–	flue gas desulfurization
GCF	–	gross capacity factor
GDP	–	gross domestic product
HI	–	high-intermediate
HP	–	high pressure
IP	–	intermediate pressure
IRR	–	internal rate of return
LCP	–	large combustion plant
LP	–	low pressure
LUVO	–	Ljungstrom rotary air heater
NPVR	–	net present value ratio
OECD	–	Organisation for Economic Co-operation and Development
PSE	–	Polskie Sieci Elektroenergetyczne S.A. (Polish Power Grid Company)
PV	–	photovoltaic
RH	–	reheated
SCR	–	selective catalytic reduction
SPC	–	set point controller
SPP	–	steam power plant (coal fired power plant)
SPPA	–	Siemens Power Plant Automation
USC	–	ultra-supercritical

1 System power demand curve in Poland

Electric power is sometimes referred to as a commodity. Yet, even as a commodity, electricity has several unique features that distinguishes it from other commodities. The first important difference is that, unlike other goods, it is very difficult to store. Energy storage is very expensive, the storage price being comparable to the original generating cost. Under grid operating conditions, production must be instantly balanced against demand because electric power must be available on demand. Hence, a portion of power-generating assets must act as a reserve, i.e., electrical generating capacity that has to be available, but is normally not used. The second major difference is the importance of electric power to the economy, standing in direct correlation with a national gross domestic product. It is crucially important to securing reliability and stability of industry. One look at the elasticity of demand versus price provides a clear picture of just how important it is. If we combine these two distinguishing features we can conclude with relative certainty that surplus supply (power reserve) has to follow demand. Hence, it is the demand curve that determines what generating capacity is required.

The Polish Power Grid Company (PSE), is the public body responsi-

ble in Poland for maintaining the grid balance. It performs analyses and publishes data related to current and predicted power demand.

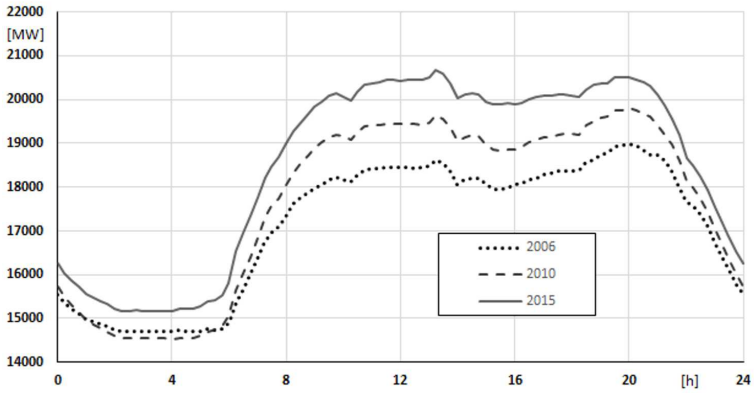

Figure 1: Poland - daily power demand profile in 2006, 2010 and 2015 [1].

As shown in Fig. 1 different unit loads (following demand) throughout the day are a consequence of the demand curve. In any economic analysis related to power generating units, the critical question arising is what will be the load percentage or, in energy industry terms, what will be the gross capacity factor (GCF). The answer to this question can be found in a monotonous curve of power demand. The curve in Fig. 2 was developed for units dispatched by PSE (centrally dispatched units).

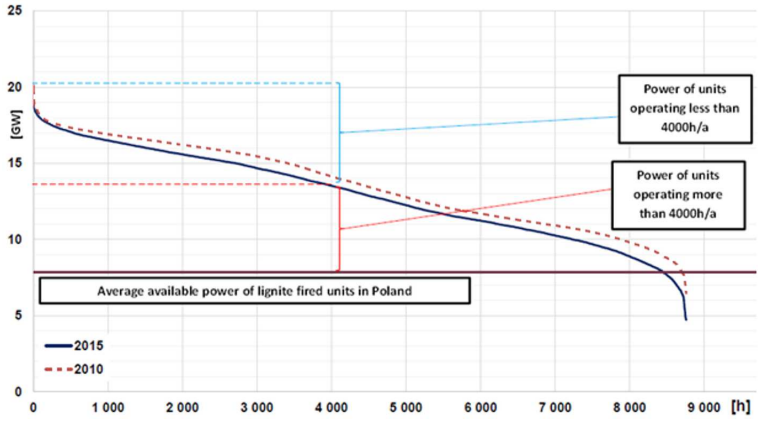

Figure 2: Poland – monotonous curve of power demand from centrally dispatched units in 2010 and 2015.

2 Future role of fossil fuel power generation and market segmentation

In electrical energy markets, a power generating unit's variable cost determines its average load and priority of operation. Thus, the lower a unit's generating costs, the more operating hours it will accumulate. By carefully analyzing the Fig. 2, three market segments can be distinguished:

- 10 GW market segment comprising base-load units, i.e., units with a generating potential exceeding 7000 h/a. This market segment should be occupied by the newest, most efficient power-generating units. However, they do not have to be particularly flexible.
- 5 GW market segment comprising units that operate at full load approximately 4000 h/a. Here, an efficiency versus flexibility tradeoff is expected.
- 5 GW market segment of peakers operating less than 2000 h/a. This market segment is occupied by flexible units whose efficiency is of secondary importance.

Additionally, cogeneration plants (approx. 10 GW) and renewable energy units (approx. 8 GW) have higher generation priority then centrally dispatched units (approx. 24 GW). It is noteworthy that grid dispatchers have limited control over cogeneration plants. It is even more important to understand that renewable energy sources, being intermittent and hardly predictable, can be a grid dispatcher's nightmare.

2.1 Power generation from renewable energy sources

In June 2016, the installed electrical generating capacity of renewable energy sources in Poland exceeded 8.2 GW. The growth of installed renewable capacity has been very rapid in recent years, as shown in Fig. 3. The authors' perspective on future growth in this sector is presented in Fig. 4. Under Polish climatic conditions, the generation capacity factors for onshore wind farms and photovoltaic (PV) plants are 2000 h/a and 1000 h/a, respectively.

2.1.1 Fossil fuel power plants – environmental protection

Fossil fuel power plants are currently under pressure to dramatically reduce their impact on the environment. In recent years, power production groups

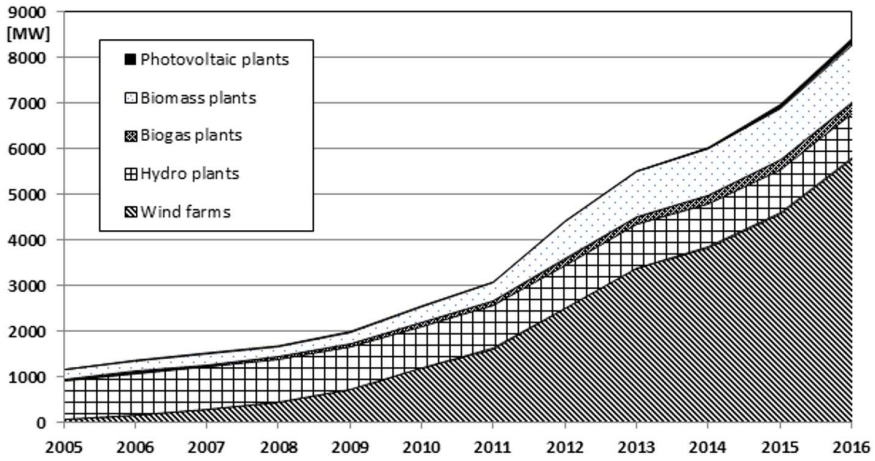

Figure 3: Diagram of installed renewable capacity growth in Poland [2].

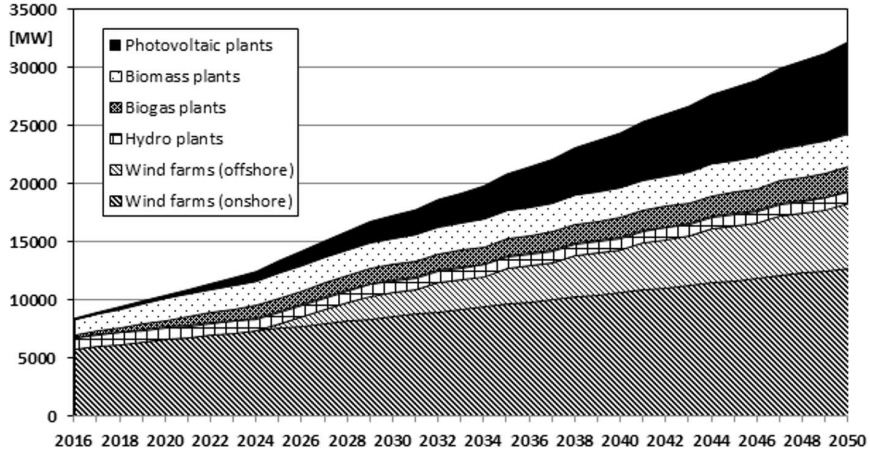

Figure 4: Diagram of projected installed renewable capacities in Poland.

have had to invest billions of euros to install dust collection, DeNO$_x$ and flue gas desulfurization (FGD) systems to meet the large combustion plant (LCP) emission limits. Nowadays, new best available technology (BAT) reference documents (BREF) must also be considered. What is more, it is predicted that prices for CO_2 emissions will rise which adds even more pressure to use only high-efficiency plants that operate at a low CO_2/kWh factor.

2.1.2 New BAT conclusions

On 31st July 2017 a resolution on the new LCP BAT was published which reduces the admissible emission levels (AELs) of existing and future power plants. The number of substances subject to emissions limits has increased: to NO_x and SO_x are now added Hg, NH_3, HCl and HF. Furthermore, a number of AELs have been stipulated for wastewater from flue gas treatment systems, and some AELs previously limited in scope have been tightened. The time allotted to adapt an installation will be four years.

2.1.3 OECD financing rules

The more stringent financing rules introduced by the Organisation for Economic Co-operation and Development (OECD) in November 2015 have strongly impacted the aforementioned methodology, requiring changes in the marketplace. The conditions of these new financing rules are summarized in Tab. 1. This implies that steam power plants built in future need to be supercritical or ultra-supercritical (USC) units in order to receive attractive financing.

Table 1: Framework conditions for OECD financing, depending on technology [3].

Maximum repayment terms

PLANT UNIT SIZE (gross installed capacity)	**Unit > 500 MW**	**Unit ≥300 to 500 MW**	**Unit < 300 MW**
Ultra-supercritical (*i.e.*, with a steam pressure >240 bar and ≥593°C steam temperature), OR Emissions < 750 g CO_2/kWh	12 years[1]	12 years[1]	12 years[1]
Supercritical (*i.e.*, with a steam pressure >221 bar and >550°C steam temperature), OR Emissions between 750 and 850 g CO_2/kWh	Ineligible	10 years, and only in IDA-eligible countries[1,2,3]	10 years, and only in IDA-eligible countries[1,2,3]
Subcritical (*i.e.*, with a steam pressure < 221 bar), OR Emissions > 850 g CO_2/kWh	Ineligible	Ineligible	10 years, and only in IDA-eligible countries[1,3]

3 Structure of current generating assets in Poland

The power generation industry in Poland is coal-based. Hard coal- and lignite-fired plants together account for 82% of the electric power generated in the country. A detailed structure is presented in the graph (Fig. 5).

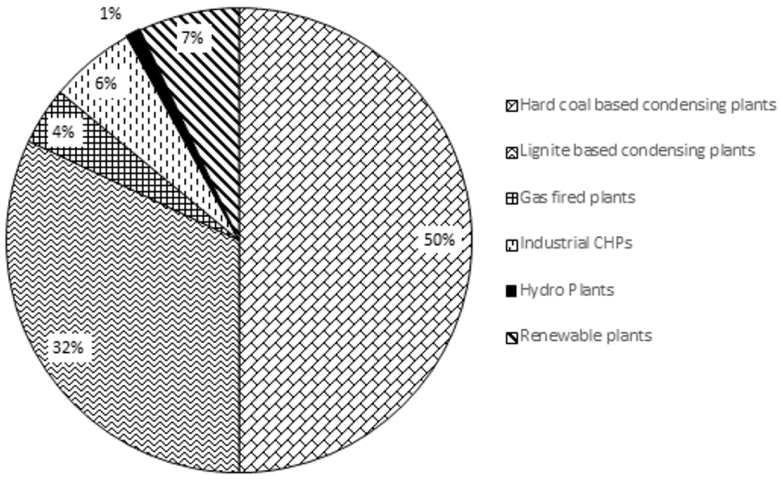

Figure 5: Poland. Structure of electric power generation by fuel in 2016.

Generating assets in Poland are aging. The average age of the centrally dispatched units is between 30 and 40 years, as presented in Fig. 6. Considering the fact that the design service life of a power plant is 40 years and for pressurized components 200 000 operating hours, it can be concluded that both construction of new units and rehabilitation projects will be necessary.

4 200 MW-class units in the Polish fleet – a weakness or opportunity?

Approximately forty percent of Polish power generating capacity is based on 200 MW-class units. The youngest units were commissioned in 1983, while the oldest have been in service 50 years. Most of these units have been modernized. In the case of Turow Power Plant, a rehabilitation project included installation of a completely new power train. Table 2 presents a detailed breakdown of the 200-MW-class units.

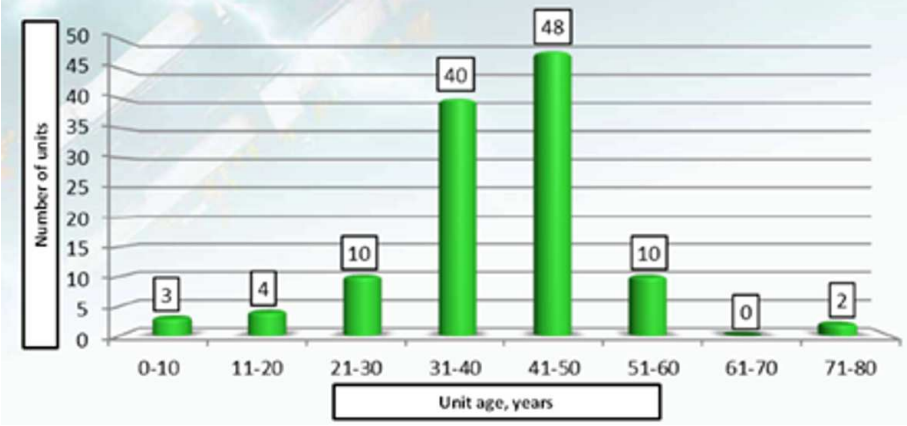

Figure 6: Centrally dispatched units in Poland – age structure.

Table 2: 200 MWe class units in Poland.

Power plant	Units and capacity	Total rated power, MW	Year of commissioning
Dolna Odra	3 x 222, 3 x 232	1362	1974–1977
Jaworzno III	5 x 225, 1 x 220	1345	1977–1979
Kozienice	3 x 228, 4 x 225, 1 x 215	1799	1972–1975
Łaziska	3 x 225, 1 x 230	905	1972
Ostrołęka	1 x 226, 1 x 221, 1 x 200	647	1972
Pątnów	5 x 200, 1 x 222	1222	1967–1969
Połaniec	2 x 225, 4 x 242, 1 x 239	1657	1979–1983
Rybnik	5 x 225, 2 x 215, 1 x 220	1775	1974–1978
Turów	3 x 235, 3 x 269	1488	1998–2005

The technical solutions applied in 200 MW units are very robust. Properly maintained units of this class can be operated much longer than their original design service life. Restrictions on operation arise either from the continually changing emissions standards or from relatively low efficiency (impacting capacity factor in the energy market).

Owners ultimately have to make decision to either decommission or modernize. If the decision is to modernize, then question is: what is the appropriate solution. It is the authors' opinion that there are two possible

solutions: either improve environmental performance to comply with the standards in force and replace critical pressurized components, or replace the power train with an arrangement of 2 boilers serving 1 steam turbine (below referred to as the 'DuoBlock' design concept). In the case of the first of the above two options, the modernized unit will be a peaker (with a capacity factor of around 2000 h/a). In the case of DuoBlock units, the 480 MW steam turbine allows application of ultra-supercritical cycle parameters. Two boilers instead of one will allow for lower minimum continuous rating at about 10 to 20% power output level. In this case, a unit will be operated in a second market segment, i.e., with a capacity factor exceeding 4000 h/a. The flexibility of the unit (with a low minimum continuous rating and good ramping ability) will be an advantage compared to a single fossil-fired boiler serving one steam turbine arrangement.

Considering the scale of the problem in the Polish generation balance (40%) and the anticipated decommissioning time (middle of next decade), it must be concluded that unanswered questions concerning 200 MW units may undermine Polish power balance. It should also be noted that the project development time starting from conceptual design phase and ending with commissioning takes 10 years for large coal-fired projects (5 years for project development and 5 years for construction). Hence, a responsible approach to energy security in Poland requires action now. Consequently, a DuoBlock solution would enable Poland to limit its CO_2 emissions level, make units more competitive, and provide a potentially attractive model for other 200 MW unit owners (for example in Turkey).

5 Technical concept of the DuoBlock

The following ideas are cornerstones of the DuoBlock design concept:

- Take advantage of the existing balance of plant systems (e.g., cooling water, coal handling, ash handling, FGD, start-up fuel installation, compressed air and water treatment systems, etc.). The decision related to those components to keep or to reconstruct is site specific. The reason behind it is obvious, i.e., limitation of investment costs.
- Increase unit output to a level at which state-of-the-art cycle parameters can be used, thereby pushing unit efficiency to the highest commercially available level. Keep sizing at a level where more economical steam turbine-generator solutions are available (high- and intermediate-pressure casing solution and air-cooled generator).

- Take advantage of the steam turbine building.
- Use two boilers to feed one turbine, allowing a lower unit minimum rating and faster startup times with two boilers (taking advantage of the steam available from first boiler while the second boiler starts up). Two boilers instead of one also enables faster power ramping because of the lesser wall thickness of critical boiler pressure components.

5.1 General

The following sections present technical details and proposed solutions for the main systems of the DuoBlock.

5.1.1 Design parameters

The parameters outlined below were selected as they are considered optimum for investment:

gross power: 480 MWe,
live steam parameters: 600 °C, 26 MPa,
live steam flow: 680 t/h, 190 kg/s,
reheated (RH) steam parameters: 600 °C, 6 MPa,
technical minimum load: $\sim 10\%$,
net plant efficiency: $> 45\%$.

Due to the limited full-load operation time (the aforementioned 4000 h/a market segment), it is not necessary to focus on achieving an exceedingly high rate of efficiency. Rather, these efforts should be put to reaching maximum flexibility at limited expense. The temperatures of both the live and reheated steam are kept at around the 600 °C level, while gross power is proposed to be 480 MWe. Net efficiency according to the best avaiable technology conclusions will exceed 45%, but the specific value for particular projects will be strongly dependent on the local coal, main cooling conditions and environmental protection installations.

Two boilers shall feed the turbine with steam in the range $\sim$ 20–100% of nominal flow. It's possible to have just one boiler in operation, which decreases power output by half. However, both boilers operation would maintain the highest control capability.

5.1.2 Flexibility

Power generation has typically consisted of units operated under steady-state conditions with low load change rates. The currently ongoing worldwide expansion of electricity production from renewable energy sources requires a wholly different operating regime for fossil fuel power plants, which are now called on to generate the residual load for the grid. According to order of merit, gas-fired power plants are the first type of power plants that have to be shut down once renewables are brought on line. Following that logic, the initial approach has been to accommodate high load change rates by bringing on line and taking off line those combined-cycle power plants that were first to adapt to achieving fast startup and shutdown times. With the increasing volume of renewable energy available, today's coal-fired power plants are facing the same requirements as gas-fired units. The know-how gained from the water-steam cycle of combined-cycle power plants is now enabling engineers to adapt steam power plants to meet these challenging requirements. The gray line in Fig. 7. shows the operation line as it was in the past. The black line shows today's requirements. The arrows indicate the necessary improvements.

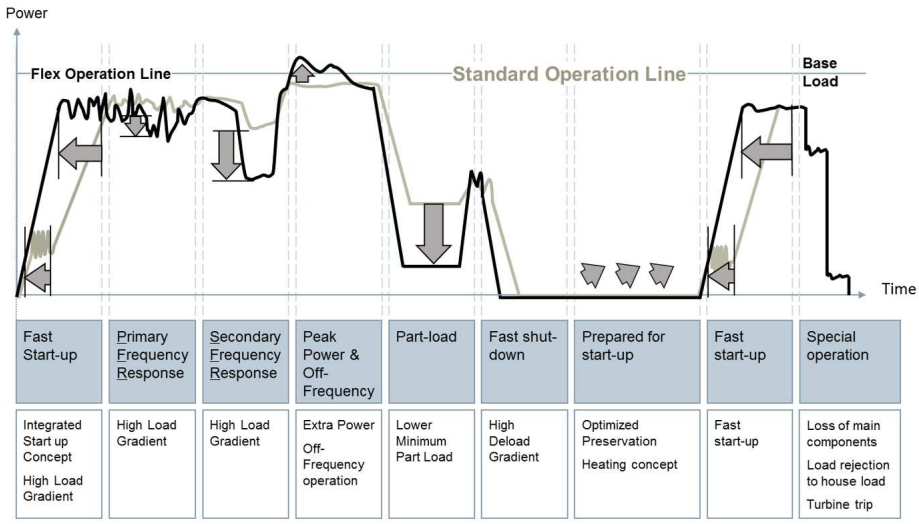

Figure 7: Power plant operation in the past and today.

To implement the functions for enhancing plant flexibility in accordance with the new operating requirements, various sets of technical measures

have been developed that can be grouped as described below.

Fast startup and shutdown In traditional steam power plants and markets, the boiler and steam turbine are started in the following basic sequence:

- Ignite the boiler.
- Increase coal-fired boiler load to the minimum turbine load.
- Stabilize pressure and temperature.
- Start the steam turbine until the bypass is closed.
- Ramp the boiler to full load with the steam turbine valve wide open.

There might be many additional steps in between, like opening of gate valves which are not mentioned.

Modern plants must attempt to heat-up the boiler and all systems as well as the steam turbine as much in parallel as possible. This will ensure for maximum load ramp rate. For this purpose, boiler operation and steam turbine operation must be decoupled with regard to temperature. For example, for a coldstart the allowed steam temperature for the steam turbine might be in a range that the boiler has to stop at a certain load until the steam turbine is warmed-up. This load hold can be avoided by using desuperheaters which will limit the temperatures. The capacity of the boiler's internal desuperheaters are normally limited because of the near-saturation conditions. Therefore, an optimum can be reached by using external desuperheaters in the main steam and reheated steam headers. They will be able to reduce the temperatures by 100 K or even up to 150 K. External desuperheaters are meanwhile standard in combined cycle power plants (CCPPs).

Startup times for coldstart as well as for warmstarts will be reduced significantly without decreasing component service life. For hotstarts it would be beneficial to keep the steam turbine under vacuum to allow the steam turbine to be started without waiting for steam purity. Furthermore, it is beneficial to start even at a certain temperature mismatch. This way of starting is also well-known from CCPPs as COSTART. This is a sort of real parallel start of boiler and steam turbine without any hold. In general, for all types of startup the steam turbine will not limit startup time, but rather directly follow the load increase of the boiler.

The market situation today requires frequent startup and shutdown of

plants. The task is therefore to get the unit on the grid in the shortest possible time without the thermal stresses impacting thick-walled boiler components violating permissible limits. Other requirements that must be met at the same time are reduced startup fuel consumption, ensuring repeatable startup and automatic differentiation between cold, warm and hot starts with bumpless transfer to coordinated power operation.

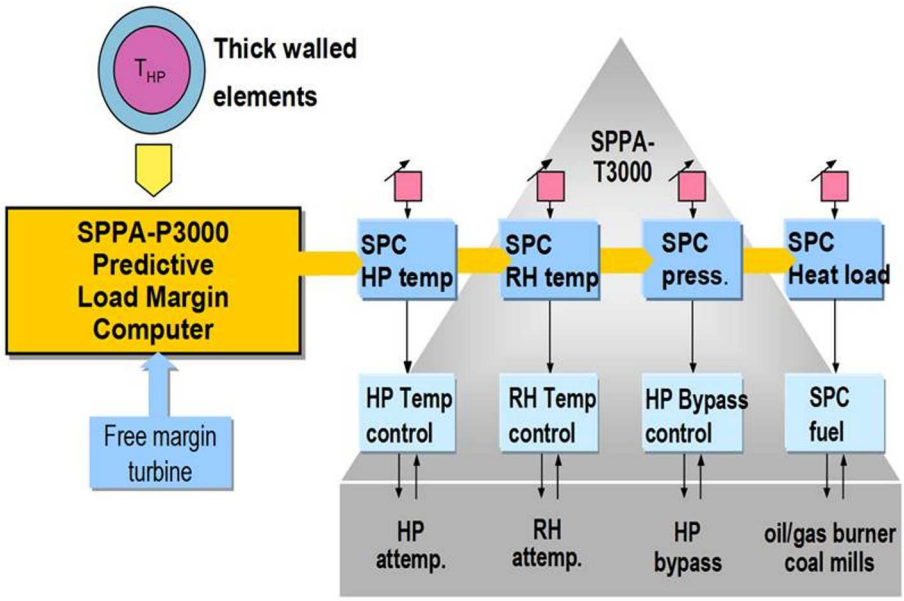

Figure 8: Siemens Power Plant Automation (SPPA) predictive load margin computer.

The predictive load margin computer calculates current thermal boiler stresses and forecasts future values for thick-walled parts from measured variables (steam temperature, pressure and mass flows). These data are used to control in Set Points Controllers (SPCs) the firing rate and the steam temperature such that material stresses do not exceed permitted limits. The process is much quicker and more reliable than pure gradient limitation as used in traditional startup circuits.

Warm standby operation Siemens has developed an electrical heating system for keeping the steam turbine warm and ready for startup while it is on the turning gear. This system heats all relevant steam turbine components to maintain the rotor shaft temperature at warm startup conditions. Compared to startup from ambient conditions, this system enables

the steam turbine to be run up to full load more than 60 min faster. In addition, the number of equivalent operating hours used per startup is significantly reduced.

Part-load efficiency/load ramps A power plant unit needs to be operated at the most profitable operating point under all operating conditions, from partial load to full-load operation. This is the task of the unit master control structure.

The model-based unit master coordinated control concept is designed for low-stress operation of the power plant. Scheduled setpoint changes by the operator or load dispatcher are performed according to a model based on the natural transmission behavior (S-shaped) of the steam generator, and do not restrict primary frequency control capability. This is achieved by coordinating the steam generator and turbine. This minimizes the amount of actuation required for load changes (overfiring) and the consequential expenditure of steam generator service lifetime.

The unit coordinated control is a coordinated pressure/load control system with a model-based feedforward control. This permits very fast, stable and targeted load changes including frequency support mode. The heat release rate in the steam generator is always kept at an equilibrium both statically and dynamically. This ensures the least possible amount of stress on the plant.

The use of an integrated prediction feature ensures that overfiring of the coal mills is extremely smooth in the case of frequency-related load changes. With scheduled load changes, the load transients can be adapted in accordance with the natural S behavior of the steam generator.

The main control variables, unit output and boiler steam pressure must be controlled using the fast-acting steam turbine control valve and the slow-acting power plant boiler. A simplified unit model comprises the dynamic boiler response and steam storage.

The model-based unit master control is also the coordinator for all subordinated additional flexibility measures like condensate throttling measures or deactivation of high pressure (HP) preheaters. Tradeoff between best cycle efficiency with full sliding pressure operation and maximum steam velocities in boiler, main and reheat steam piping shall be elaborated on a project-specific basis.

One method for increasing the final feedwater temperature is the addition of what is termed a top feedwater heater, which is used only at part

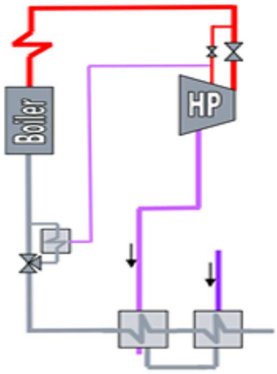

Figure 9: Top feed water heater arrangement.

load. Such a unit requires an additional extraction upstream in the HP blade path. Ideally, the steam is extracted from that point in the blading at which the additional main steam valve is connected (Fig. 9). This obviates the need for any additional nozzles on the HP turbine, and the stage valve admission point can simultaneously serve as an extraction point. Top heating steam flow is selected such that the final feedwater temperature remains constant over wide load ranges. The maximum heat rate benefit with the use of a top feedwater heater is thus approximately 0.6 percentage points at a part load of 50%.

Frequency response Figure 10 shows an overview of several options that are mainly concerned with facilitating frequency response. One common measure for frequency response is to eliminate throttling of the main steam valves (Fig. 10, item 1). While it has always been possible to do this, it bore the disadvantage of an increased heat rate during normal operation. Siemens offers the possibility of using an additional main steam valve (Fig. 10, item 2). This feature provides the advantage of optimum efficiency during normal operation with a possibility for instantaneously increasing the swallowing capacity of the steam turbine, along with the respective increase in load. The next measure is condensate throttling (Fig. 10, item 3) that enables the plant to produce at least 4% additional output by reducing the condensate flow through the low pressure (LP) preheaters and steam extraction through the respective extraction points. The surplus steam that remains within the steam turbine generates the additional power. Certain

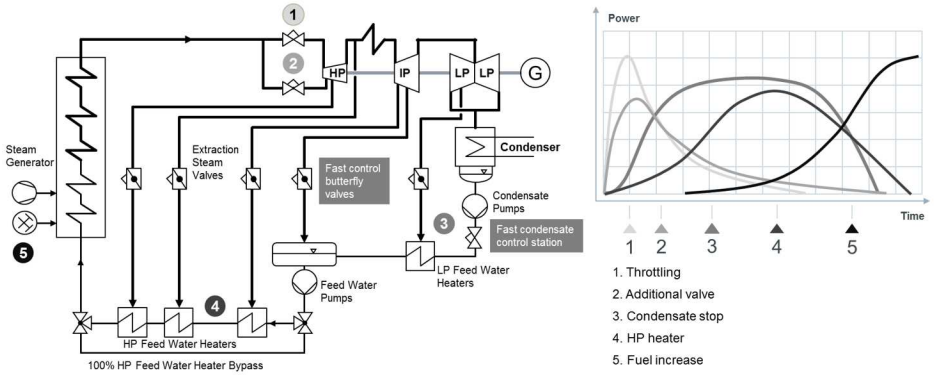

Figure 10: Measures in water-steam cycle for facilitating frequency response

features can be added to the condensate throttling system to increase response time up to 2 s. A similar approach can be used at the high pressure (HP) preheaters to increase output (Fig. 10, item 4). The response should be chosen carefully so as not to thermally stress the boiler and preheater hardware too much.

Other measures such as boiler spray and use of a bypass system with bypass spray can also be implemented to complete the set of measures chosen for project-specific needs.

Loss of main components and load rejection to house load To automatically reduce the unit load on loss of major components such as a feedwater pump or forced-draft fan, and to effect transition to a new safe operating mode by:

- Assignment of dedicated runback levels and ramps for all the major equipment units.
- Consideration of fuel-related restrictions on the load.
- Load reduction with the necessary gradient and coincident changeover of the turbine to stable inlet pressure control mode.

5.2 Steam turbine-generator package – compact, efficient and flexible

5.2.1 SST-5000 steam turbine

Siemens' proven SST-5000-Series steam turbine for USC parameters is a steam turbine consisting of at least two turbine sections: One combined high pressure/intermediater pressure (HP/IP) section (HI turbine) and either one or two LP sections, depending on cooling water temperatures. This is the best product for the lower load range of around 200 MW to 500 MW (Fig. 11). The chosen cycle parameters of 26 MPa/600°C/600°C provide a good tradeoff between product cost and product performance. Since the SST-5000 is the steam turbine module most often deployed in combined-cycle power plants, it is also Siemens' most flexible turbine. The experience gained from these power plants is excellent, especially in terms of fast load ramps.

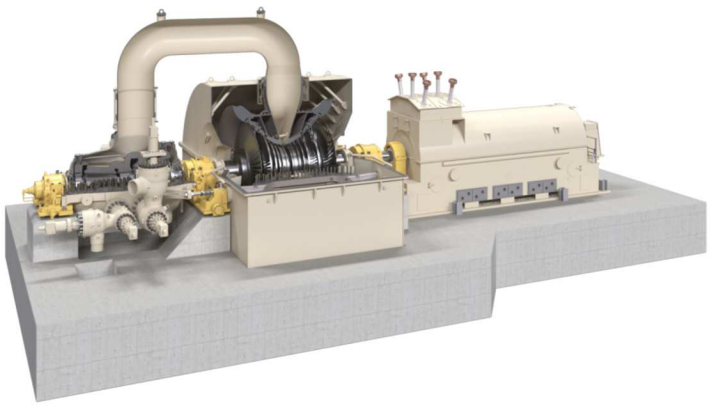

Figure 11: Steam turbine module SST-Pac 5000.

The HI turbine provides several advantages, not only in terms of maintenance but also with regard to integration into the overall power plant. Due to the fact that the main steam and reheat valves are flanged to the lower part of the HI outer casing, only the crossover pipe to the LP turbine has to be disconnected before the upper half of the turbine casing can be removed. In addition, the overall length of the turbine train is reduced to a minimum, which means the turbine foundation, too, and ultimately the entire turbine building can be as compact as possible. This is very important for incorporating a new steam turbine generator set into an available turbine

building, as in the case of a DuoBlock. The reduced number of bearings also leads to lower foundation costs. The ultra-supercritical HI module is likewise suitable for inspection intervals of 50 000 h for medium inspections and 100 000 h for major inspections. This means that first opening of the turbine casing is not necessary until after around 12 years of operation.

5.2.2 Generator for the 300 MW to 500 MW class – the SGen-2000P Series

Global increase in utilization of renewable energy has a significant impact on the operating regimes in fossil fuel power plants. Today, turbine-generator shaft train components are exposed to extremely volatile operating modes with a high number of start/stop cycles, numerous steep load ramps, and frequency and voltage fluctuations. As a consequence, thermomechanical stresses and accelerated aging of the shaft train components, including generators, must be considered in the design to avoid unexpected cost and extensive outage periods.

Siemens' answer to the increased market requirements is the new air-pressurized generator SGen-2000P featuring innovative combination of verified technologies: air and water cooling. Air-cooled generators have an excellent track record in terms of robustness, reliability and low operational cost, while water-cooled generators provide the highest output capability and efficiency in the industry. Building on the success of these air-cooled and water-cooled units, the new product line is set to replace the indirectly hydrogen-cooled SGen-2000H Series up to approximately 550 MVA, and will become a standard product in future gas turbine and steam turbine packages. Replacing hydrogen cooling with pressurized air significantly reduces plant complexity and eliminates explosion safety concerns, along with further benefits such as reduced first-time installation and commissioning scopes, lower maintenance costs, and the capability of unstaffed operation for synchronous condenser applications.

Implementation of innovative design features and load-dependent air pressure control enable SGen-2000P generators to achieve efficiency levels comparable to indirect hydrogen-cooled generators. Figure 12 provides an overview of how the auxiliary systems have been simplified.

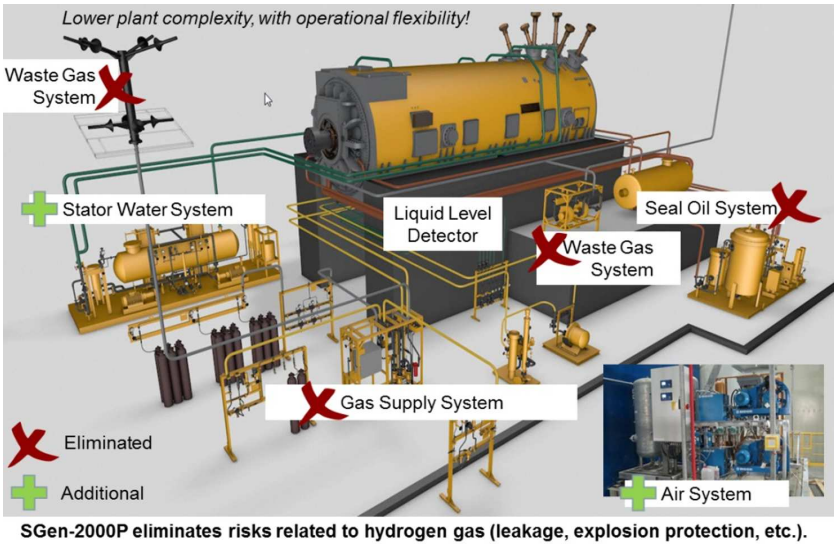

Figure 12: SGen-2000P's reduced scope of auxiliary systems compared to H_2-cooled generators.

5.3 DuoBlock boiler island

The boiler island for the DuoBlock design concept will not be characterized by any serious changes in comparison to conventional power unit configurations. Each boiler must be equipped with an independent technological line of feed and firing systems (coal feeders and mills) and flue gas selective catalytic reduction (SCR), Ljungstrom rotary air heater (LUVO) and electrostatic precipitator (ESP). Wet FGD should be used, which might possibly be configured in a common system serving both boilers.

It must be considered that individual project solutions may vary depending on the site arrangement of existing buildings and systems. What is more, some of them (like SCR and absorbers, rarely ESPs) may be used and modernized. In the feasibility study it is very important as the more existing components (installations and machinery) are used, the more cost-efficient DuoBlocks become.

5.3.1 Dedicated ultra-supercritical boiler

Boiler house layout Presented below is a boiler house at 0.00 m elevation, which is usually a shared structure in most Polish 200 MWe units.

The boiler house is designed and constructed as a conventional structure with 9 m x 12 m spacing. The boiler structure is supported on six pillars isolated from the boiler house structure. On the left side there are four coal mills on separate foundations, and in the middle a wet deslagger. Separate foundations were also used for primary and secondary air fans.

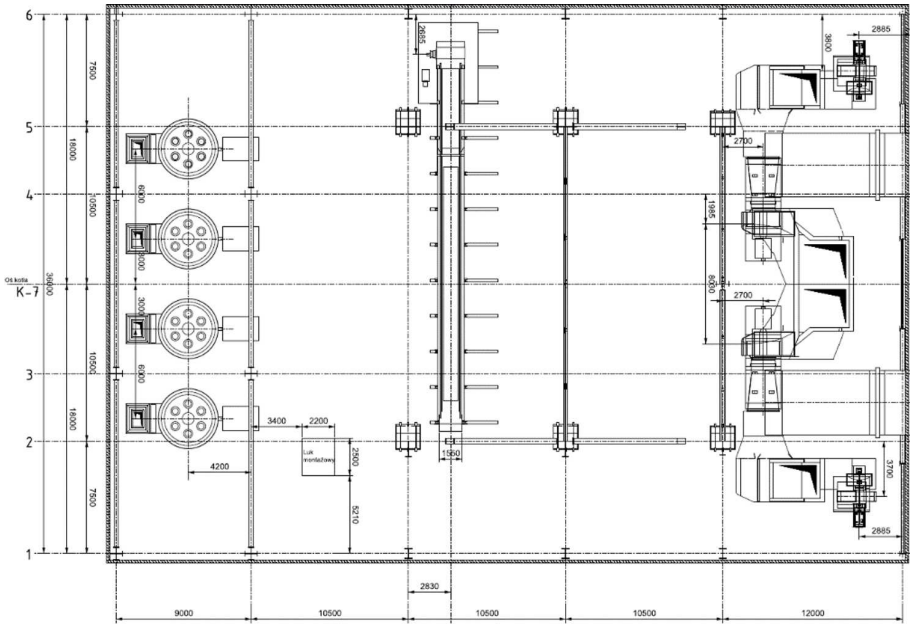

Figure 13: Typical boiler house 0.00-m elevation layout in Polish 200-MWe units.

BP-680 boiler design BP-680 boiler was designed by Rafako for an R&D project financed by the Polish National Research and Development Center in a program dedicated to working out solutions for the existing Polish fleet of 200-MWe power plant units commissioned in the 1970s.

It is assumed that the boilers serving the DuoBlock must be installed in the existing building, including in particular the foundations. This assumption leads to the following conclusions:

- To use the existing structure, a newly designed boiler combustion chamber must keep nearly the exact same dimensions of the old OP-650 unit;
- To ensure the integrity and safety of the foundations, tower-type boil-

ers cannot be used, and the existing shape of the two-pass boiler must be retained.

The resultant boilers shall have combustion chamber diameters of 15620 mm x 9020 mm, be two-pass type, and slightly taller than the OP-650. It fulfills the conditions of fitting within the existing structure.

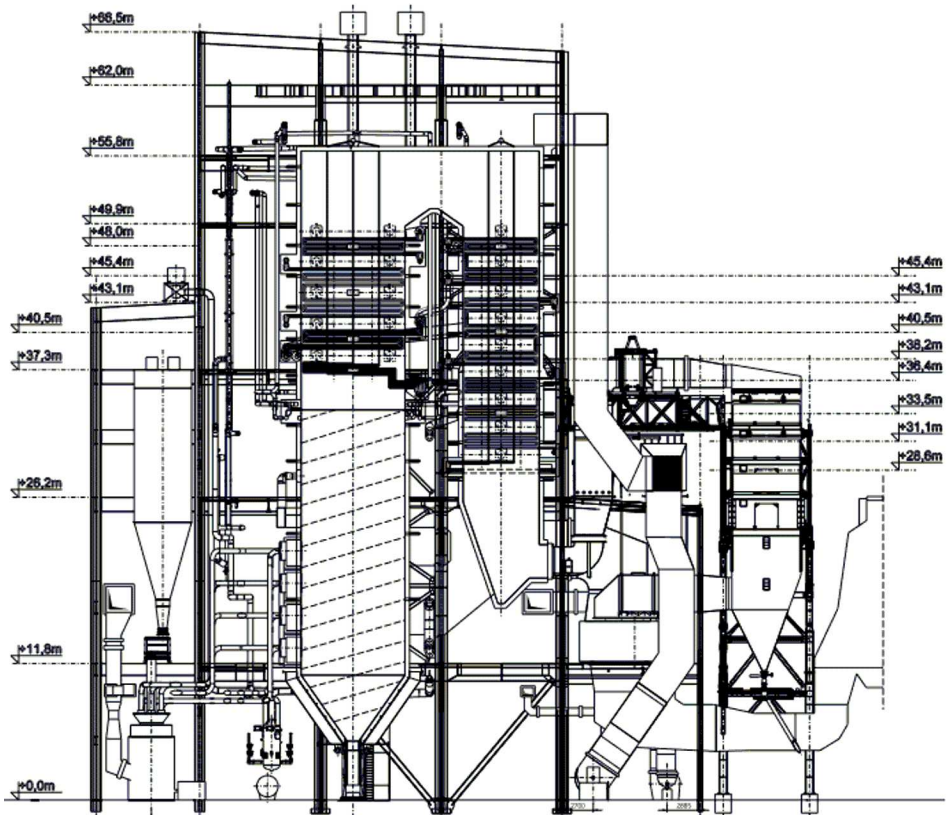

Figure 14: BP-680 boiler design concept (cross-section).

One of few changes introduced will be switching the primary air fan to the cold air duct; placing the fan behind the LUVO (on the hot side) was eliminated from engineering applications many years ago.

5.3.2 Example solution for the Kozienice project

One example of a Polish power station where the DuoBlock could be built is Kozienice Power Plant, where currently eight 200 MWe units are in op-

eration. The plant has been adjusted to meet the present AELs – a SCR reactor for each boiler and a common wet FGD plant for four boilers were built. These installations would have to be modernized and a new ESP built in order to ensure compliance with the new BAT AELs.

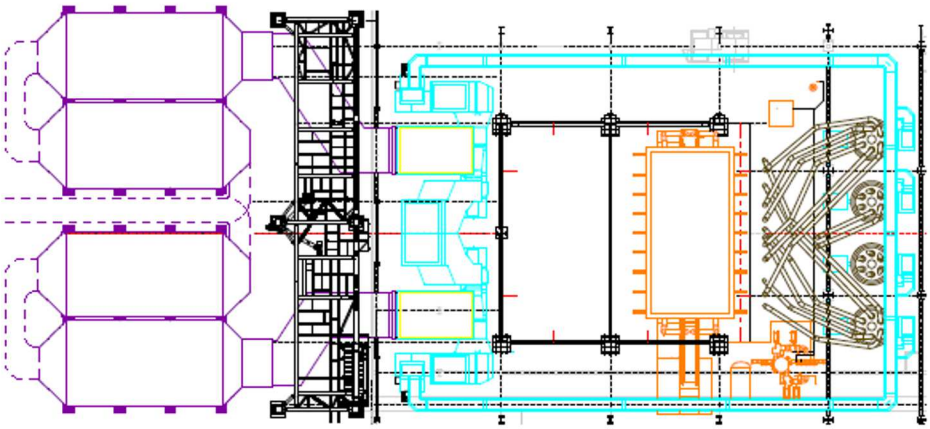

Figure 15: DuoBlock's boiler island for Kozienice.

The SCR system was already designed to be prepared for additional layers of catalyst, so the changes must focus on the choice of catalyst to ensure both NOx reduction and Hg oxidation. With limited space, it was proposed to build a complete new two-pass ESP (6 zones altogether). This avoids the high operating costs of bag filter technology and does not impact the existing layout – as the ESP fits between the existing SCR and foundation of a draught fan. As far as desulfurization is concerned, it's possible as well to modernize the absorber. The proposed investments are presented in Tab. 3.
Final selection of the way to reduce emissions must be preceded by thorough analysis, and detailed information about the existing installation must be provided.

6 Economic analysis of the DuoBlock design concept

The estimated investment cost for a DuoBlock unit has been identified at 2.3 billion PLN (roughly equivalent to EUR 550 million), which is at least EUR 200 million less than the price tag for a 500 MW-class greenfield unit.

Table 3: Ways to modernize existing absorber in the wet FGD installation.

Method	Result	Required investments
formic acid additive	increase efficiency of absorption	• complete installation of formic acid dosage
sieve tray	dynamic local flue gas – suspension mixing	• fan with higher compression • possible need of structural reinforcement
additional spray level	increase of suspension – flue gas reaction surface	• increase in absorber height • complete new pipeline with supports, valves and the circulation pomp • structural reinforcement of the absorber and pipelines

Investment costs for DuoBlock depend on the technical conditions of the existing balance of plant equipment, which must be thoroughly considered as site-specific parameters. In terms of income, the electricity market-related income has been taken into account in these calculations.

A forecast has been prepared of the capacity factors and energy price developments based on the Polish electricity market model. The electricity market model for the entire country was developed by EPK. It runs on the Plexos market simulation tool. The results are presented on the graphs in Figs. 16 and 17.

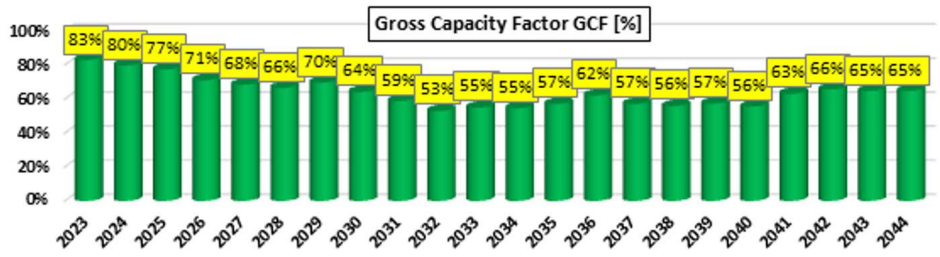

Figure 16: Capacity factors for DuoBlock units under Polish market conditions.

The net present value ratio (NPVR) achieved is 0.61, while the internal rate of return (IRR) is 9.37%. Both of these figures are acceptable from the perspective of the economy of contemporary power investments.

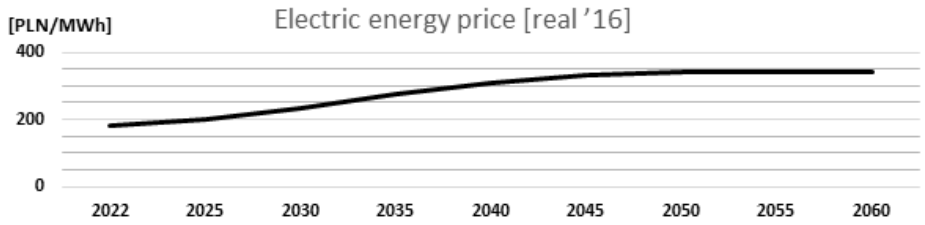

Figure 17: Electric power price forecast.

7 Conclusions and strengths of the DuoBlock idea

In a number of countries where the energy market is a cornerstone of power generation business, power plant assets are under continuous economic pressure. The consequential choice is to optimize both operation and maintenance. Yet, high investment costs for new units and relatively slow technological progress (the incremental efficiency growth of new technology over years) create a situation in which the total energy costs of new units are no lower than those of existing plants. This creates hardly any incentive for investment.

Considering the nature of demand curves, particular attention has to be given to the market segment where generating assets operate at a capacity utilization factor of approximately 4000 h/a. This particular regime requires tradeoff between efficiency and flexibility. On the other hand side, long investment cycles and aging among older generating assets are putting the energy security of a number of countries at risk. Poland is one good example. The design concept of the DuoBlock answers these challenges.

From a macroeconomic standpoint, it is a perfect fit for Poland's national demand. At lower investment costs and shorter construction times, the solution is competitive with any other solution in its market segment (GCF 4000 h/a). The optimized design enables use of state-of-the-art cycle parameters while keeping CAPEX low in comparison to 1000 MW coal-fired greenfield plants, especially for the power island.

From the plant operators' technical perspective, the design concept fits into existing power plant arrangement plans, allowing for staged rehabilitation of older units. The concept as thus presented grants a second life to aging power plants.

What transmission system operators require from plant operators is fast response to demand changes. The concept of a 2-on-1 configuration allows

unprecedented flexibility. Normally, one limit to minimum continuous rating of the unit is boiler flame stability. A low minimum continuous rating resulting from a single-boiler operating mode in a DuoBlock arrangement is of course two times lower than in a standard one-on-one concept. With a large steam source available from the first boiler in the startup process of the second boiler, it is possible to shorten startup times and cut the costs of startup below what are considered industry standards. This makes the operational difference in terms of changeover between single- and dual-boiler operation unnoticeable for the transmission system dispatcher.

Another perspective arises from environmental concerns. The fuel for the described unit is coal, which does not sound particularly 'green'. However, the design concept has been tailored specifically for DuoBlock cooperation with large numbers of wind power and PV power sources. Those latter 'volatile' sources must be backed up by predictable, reliable yet flexible power generation. Thus, from the point of view of environmentally concerned persons, application of the DuoBlock will enable renewables to assume an even larger share of the power generation system.

8 Authors diclaimer

This document contains forward-looking statements and information Ő that is, statements related to future, not past, events. Such statements are based on our current expectations and certain assumptions, and are, therefore, subject to certain risks and uncertainties. A variety of factors, affect its operations, performance, business strategy and results and could cause the actual results, performance or achievements of authors companies worldwide to be materially different from any future results, performance or achievements that may be expressed or implied by such forward-looking statements. For us, particular uncertainties arise, among others, from changes in general economic and business conditions, changes in currency exchange rates and interest rates, introduction of competing products or technologies by other companies, lack of acceptance of new products or services by customers targeted by authors companies worldwide, changes in business strategy and various other factors. Should one or more of these risks or uncertainties materialize, or should underlying assumptions prove incorrect, actual results may vary materially from those described in the relevant forward-looking statement as anticipated, believed, estimated, expected, 28 J. Grzeszczak et el. intended, planned or projected.

Received 2 October 2017

References

[1] PSE, Load of Polish System, http://www.pse.pl/index.php?dzid=78 (accessed 1 July 2017).

[2] URE, Installed Power in Renewable Sources, Enclosures https://www.ure.gov.pl/pl/rynki-energii/energia-elektryczna/odnawialne-zrodla-ener/potencjal-krajowy-oze/5753,Moc-zainstalowana-MW.html (accessed 1 November 2017).

[3] OECD, Sector Understanding on Export Credits for Coal-Fired Electricity Generation Projects, http://www.oecd.org/officialdocuments/publicdisplaydocumentpdf/?cote=TAD/PG(2015)9/FINAL&docLanguage=En (accessed 1 July 2017).

archives
of thermodynamics
Vol. **38**(2017), No. 4, 191–207
DOI: 10.1515/aoter-2017-0031

Modeling the performance of water-zeolite 13X adsorption heat pump

KINGA KOWALSKA*
BOGDAN AMBROŻEK

West Pomeranian University of Technology, Szczecin, Institute of Chemical Engineering and Environmental Protection Processes, al. Piastów 42, 71-065 Szczecin, Poland

Abstract The dynamic performance of cylindrical double-tube adsorption heat pump is numerically analysed using a non-equilibrium model, which takes into account both heat and mass transfer processes. The model includes conservation equations for: heat transfer in heating/cooling fluids, heat transfer in the metal tube, and heat and mass transfer in the adsorbent. The mathematical model is numerically solved using the method of lines. Numerical simulations are performed for the system water-zeolite 13X, chosen as the working pair. The effect of the evaporator and condenser temperatures on the adsorption and desorption kinetics is examined. The results of the numerical investigation show that both of these parameters have a significant effect on the adsorption heat pump performance. Based on computer simulation results, the values of the coefficients of performance for heating and cooling are calculated. The results show that adsorption heat pumps have relatively low efficiency compared to other heat pumps. The value of the coefficient of performance for heating is higher than for cooling

Keywords: Desorption; Adsorption; Mathematical simulation; Heat pump; Coefficient of performance

Nomenclature

A	–	adsorption potential, J/mol
E_0	–	characteristic energy of the adsorbent, J/mol
COP	–	coefficient of performance
COP_h	–	coefficient of performance for heating

*Corresponding Author. Email kingateresakowalska@gmail.com

COP_{ref} – coefficient of performance for cooling
C_{pa} – heat capacity of liquid adsorbate, J/(mol K)
C_{pf} – specific heat of fluid, J/(kg K)
C_{ps} – heat capacity of adsorbent, J/(kg K)
C_{pw} – specific heat of the wall ,J/(kg K)
D_s – surface diffusivity, m^2/s
D_1 – inner diameter of the heat transfer tube, m
D_2 – outer diameter of the heat transfer tube, m
D_3 – outer diameter of the adsorbent layer, m
h_f – heat transfer coefficient between the fluids and the tube, $W/(m^2K)$
h_s – heat transfer coefficient between the metal and the adsorbent, $W/(m^2K)$
ΔH_a – heat of adsorption, J/mol
ΔH_v – heat of vaporization, J/mol
L – length of the adsorbent layer, m
n – constant in the Dubinin-Astakhov equation
m_a – mass of adsorbent, kg
m_w – mass of metal tube, kg
p – vapor pressure of adsorbate, Pa
p_c – pressure of condensation, Pa
p_e – pressure of evaporation, Pa
p_s – saturation vapor pressure of adsorbate, Pa
q^* – equilibrium value of $\overline{q}$, mol/kg
$\overline{q}$ – adsorbate concentration in adsorbent particle, mol/kg
Q_c – heat released in the condenser, J
Q_e – heat absorbed in the evaporator, J
Q_{1-2} – heat of isosteric heating process, J
Q_{2-3} – heat of isobaric desorption process, J
Q_{3-4} – heat of isosteric cooling process, J
Q_{4-1} – heat of isobaric adsorption process, J
r_p – radius of the adsorbent particle, m
R – gas constant, J/molK
t – time, s
T – temperature ,K
T_a – temperature of adsorption, K
T_c – condenser temperature, K
T_{CO} – inlet temperature of cooling fluid, K
T_e – evaporator temperature, K
T_f – fluid temperature, K
T_H – inlet temperature of heating fluid, K
T_s – adsorbent temperature, K
T_w – wall temperature, K
T_1–T_4 – initial temperature for heating, desorption, cooling and adsorption steps, respectively, K
v_f – fluid velocity, m/s
V – volume adsorbed, m^3/kg
V_0 – limiting adsorption volume, m^3/kg
z – axial coordinate, m

Greek symbols

β	–	affinity coefficient
δ_w	–	thickness of the wall (heat transfer tube, inner tube thickness), m
δ_s	–	thickness of the adsorbent layer, m
ε	–	porosity of the adsorbent bed
$\rho(T)$	–	temperature dependent density of liquid adsorbate, mol/m^3
ρ_w	–	wall (heat transfer tube) density, kg/ m^3
ρ_f	–	fluid density, kg/m^3
ρ_s	–	adsorbent particle density, kg/m^3

1 Introduction

The recent years of civilization development have significantly influenced natural environment. Pollution generated by power plants and other industries has caused ecosystem degradation and created the need to replace conventional fuels with renewable sources. One of the technologies that delivers 'clean energy' is the adsorption heat pump. This systems has recently become an interesting field of research. The advantage of such a solution is the ability to use working pairs, which are fully environment-friendly and are characterized by simple working principles and long life time [1–9]. Moreover, the most important reasons for the use of adsorption heat pumps are simplicity, no moving parts, low maintenance requirements, and shock resistance. Due to this fact, adsorption heating devices can be used where large amounts of waste heat are generated, e.g., in chemical plants and power plants. Another application is for domestic purpose but it is still in phase of research and development.

The design of an adsorption heat pumps requires the knowledge of the thermodynamics and principle of working of these systems. In the adsorption heat pumps, transfer of mass and heat is a cyclic process. The efficiency of the heat pump depends on the appropriate selection of adsorbate-adsorbent pair, system design and temperature conditions. The adsorbate-adsorbent pairs should be characterized by high sorption capacities and the ability to work in a wide temperature range [1–3].

In this paper, a mathematical model of the cylindrical double-tube adsorption heat pump has been developed, taking into account heat balance equations for fluid, adsorbent wall, and adsorbent. The adsorption rate was calculated using a linear driving force (LDF) model. The method of the lines (MOL) was used to solve the mathematical model. As the working pair the system water-zeolit 13X was chosen. The results of computer simulations were used for analysis of the impact of evaporator and con-

denser temperatures on adsorption and desorption kinetics. The values of the coefficients of performance for heating and cooling were calculated. The problems encountered during the study were explained in the conclusions.

2 Adsorption heat pump description

An adsorption heat pump consists of four main parts: adsorber, condenser, evaporator, and the expansion valve. Figure 1 illustrates a schematic diagram of adsorption heat pump.

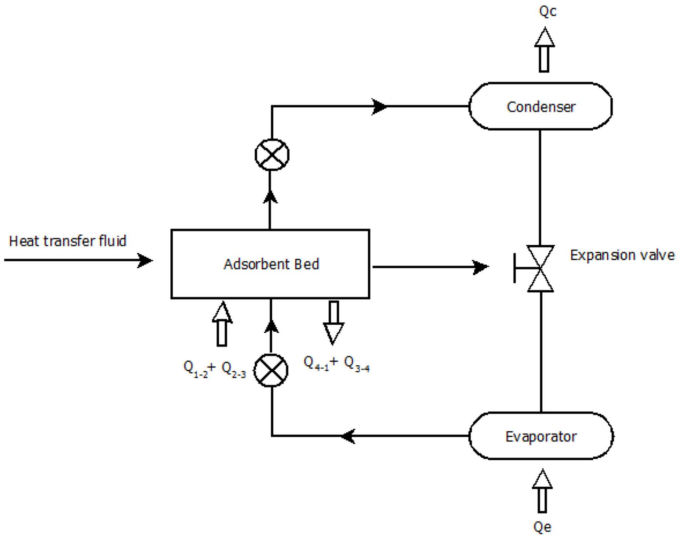

Figure 1: Schematic diagram of adsorption heat pump.

The adsorber is a cylindrical double-tube heated or cooled by an external fluid (Fig. 2). The inner tube is covered with adsorbent layer, e.g., zeolite surrounded by the outer tube to give space for working fluid vapor passage. The adsorbent may be in the form of: (1) grain or pellets (traditional adsorbent used as it is received from manufacturer), (2) powder consolidated by a binder or (3) powder consolidated by a binder and adhered on metal [2]. The first configuration is characterized by low heat transfer coefficient at metal–adsorbent interface, because of weak contact between the metal surface and adsorbent grains. Using consolidated adsorbents adhered on metal allows improvement of metal–adsorbent heat transfer due to adsorbent adhesion on metal surface.

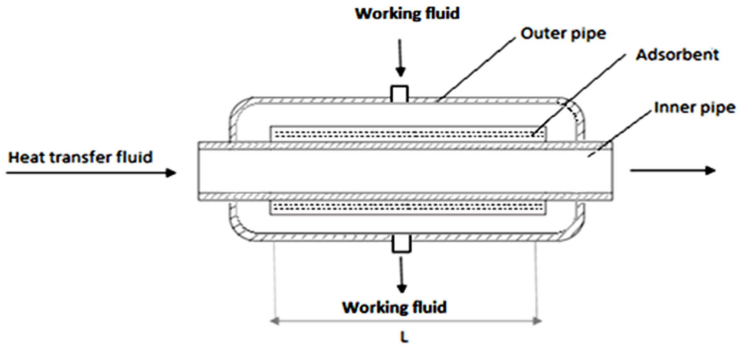

Figure 2: Schematic of the adsorber.

In adsorption heat pump adsorbate is circulated between adsorber, condenser, and evaporator. The thermodynamic cycle on an isoster of an adsorbent–adsorbate pair is presented in Fig. 3. Basically, an adsorption cycle consists of four steps: isosteric heating (1–2), isobaric desorption (2-3), and isosteric cooling (3-4), isobaric adsorption (4-1) [3].

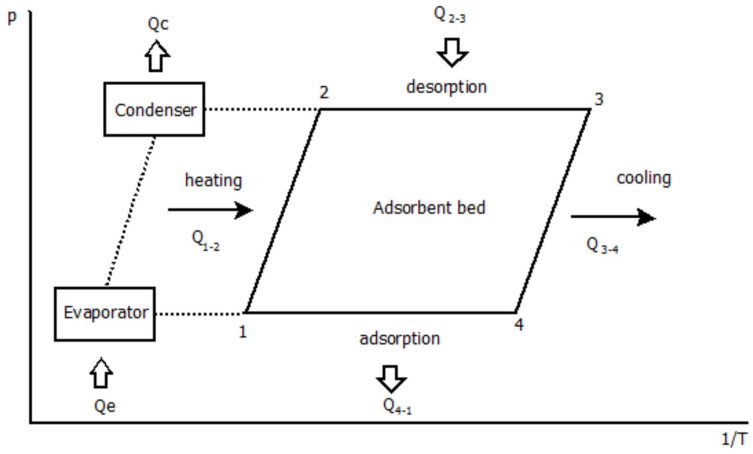

Figure 3: Adsorption heat pump cycle.

During isosteric heating (step 1-2) the adsorbent bed is heated by heat transfer fluid (HTF). The pressure increases from p_e to p_c due to working fluid vapor desorption. When the vapor pressure is equal to the condens-

ing pressure isobaric desorption begins (step 2-3). The adsorbent bed is connected to the condenser. The heat of condensation, Q_c, of the working fluid can be discharged into the environment or used for heating purposes. The liquid working fluid flowing from the condenser through the expansion valve is directed to the evaporator. At the end of desorption step adsorber is disconnected from the condenser and isosteric cooling starts (step 3-4). During this step, the bed is cooled using the heat transfer fluid. The pressure in the adsorbent bed decreases from p_c to p_e as a result of the lowering of adsorbent temperature and the adsorption of working fluid vapor. During adsorption (step 4-1) the bed is connected to the evaporator. This allows adsorption of working fluid vapors. Adsorbate is evaporated gaining heat from the environment, Q_e. In this way, the cooling effect occurs during the adsorption step. Adsorption is an exothermic process. Heat released during this process, Q_{4-1}, can be utilized for heating purposes. For this application, the heat removed from the adsorbent bed during cooling step, Q_{3-4}, can be also used [3].

Exhaust gas or oil can be used as a heat transfer fluid during heating and desorption. During cooling and adsorption, air and water are commonly used as a heat transfer fluid. For the water-zeolite system, the heat transfer fluid temperature during heating and desorption is in the range from 369 K to 633 K [3]. Evaporator and condenser temperatures for this system are included in the range from 275 K to 313 K and 293 K to 313 K, respectively.

3 Mathematical model of adsorption heat pump

The mathematical model describing the dynamic performance of adsorption heat pump consists of integrated partial differential and algebraic equations. A one-dimensional non- equilibrium model has been used. The model equations are obtained by applying differential energy and material balances to the control volume shown in Fig. 4.
The following assumptions are made:

- gas phase follows the ideal gas law,
- the pressure gradient across the bed is neglected,
- heat losses from adsorber to the ambient are negligible,
- solid and gaseous phases are in thermal equilibrium,

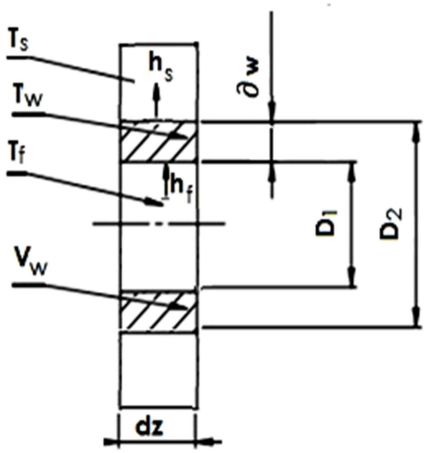

Figure 4: Control volume dz. T_s – adsorbent temperature, T_w – wall temperature, T_f – fluid temperature, V_w – volume of wall, h_s – heat transfer coefficient between the metal and the adsorbent, h_f – heat transfer coefficient between the fluids and the tube, D_1 – inner diameter of the heat transfer tube, D_2 – outer diameter of the heat transfer tube.

- radial concentration, temperature and velocity gradient within the adsorbent bed are negligible,
- intraparticle heat transfer resistance is negligible,
- adsorber bed is consolidated by a binder and adhered on a metal surface,
- axial conduction within the column wall is negligible.

Based on the above assumptions, the energy balance for the heat transfer fluid is represented by the following equation:

$$v_f \frac{\partial T_f}{\partial z} + \frac{\partial T_f}{\partial t} = \frac{4h_f}{C_{pf}\rho_f D_1}\left(T_w - T_f\right) \ . \tag{1}$$

The energy balance for the inner tube is stated as

$$\frac{\partial T_w}{\partial t} = \frac{2}{\delta_w(D_2 + D_1)\rho_w C_{pw}}\Big[h_f D_1\left(T_f - T_w\right) - h_s D_2\left(T_w - T_s\right)\Big] \ . \tag{2}$$

The heat balance for the adsorbent bed can be written as

$$\frac{\partial T_s}{\partial t} - \frac{\Delta H_a}{\left(C_{ps} + \overline{q}C_{pa}\right)}\frac{\partial \overline{q}}{\partial t} = \frac{2h_s D_2}{\delta_s\left(D_3 + D_2\right)\rho_s\left(1-\varepsilon\right)\left(C_{ps} + \overline{q}C_{pa}\right)}\left(T_w - T_s\right). \tag{3}$$

Due to the fact that in the balance equations there is a component determining the mass transfer rate, it is necessary to determine a kinetic model. The mass-transfer rate inside the adsorbent particle is explained by the linear driving-force (LDF) model:

$$\frac{\partial \overline{q}}{\partial t} = \frac{15 D_s}{r_p^2}(q^* - \overline{q}) \,. \tag{4}$$

The LDF model is a compromise between solution accuracy and calculation efficiency, and is adequate in most adsorption applications [10–15].

The boundary conditions for the HTF are:
Adsorption:

$$T_f|_{z=0} = T_{CO} \,, \tag{5}$$

$$\frac{\partial T_f}{\partial z}\Big|_{z=L} = 0 \,. \tag{6}$$

Desorption:

$$T_f|_{z=0} = T_H \,, \tag{7}$$

$$\frac{\partial T_f}{\partial z}\Big|_{z=L} = 0 \,. \tag{8}$$

The initial conditions for $0 < z < L$ and $t = 0$ are:

$$\overline{q}\,(0,z) = \overline{q}_0\,(z)\,; T_s\,(0,z) = T_{s0}\,(z)\,; T_f\,(0,z) = T_{f0}\,(z)\,; T_w\,(0,z) = T_{w0}\,(z) \,. \tag{9}$$

The solution of the model equations requires the knowledge of the state of the adsorbent bed at the beginning of each step. In this paper, it is assumed that the final concentration of working fluid in adsorbent layer and temperature profiles in the adsorber for each step define the initial conditions for the next one. For the adsorption step in the first adsorption cycle:

$$\overline{q}_0\,(z) = 0; \;\; T_{s0}\,(z) = T_{f0}\,(z) = T_{w0}\,(z) = T_a \,. \tag{10}$$

The set of partial differential equations (PDEs) representing the adsorption heat pump (1)–(4), together with the boundary and initial conditions, (5)–(10), is solved by the numerical method of lines.

The spatial discretization is performed using second-order central differences with 10 equally spaced axial nodes, and the PDEs are reduced to a set of ordinary differential equations (ODEs). The set of ODEs is solved using the Polymath ODE Solver [16].

In order to calculate the coefficient of the performance of adsorption

heat pump, the following equations are used [3,4]:
isosteric heating (1-2)

$$Q_{1-2} = \int_{T1}^{T2} \left[m_a \left(C_{p,s} + \overline{q} C_{p,a} \right) + m_w C_{p,w} \right] dT \ , \tag{11}$$

isobaric desorption (2-3)

$$Q_{2-3} = \int_{T2}^{T3} \left[m_a \left(C_{p,s} + \overline{q} C_{p,a} \right) + m_w C_{p,w} \right] dT + \int_{2}^{3} m_a \Delta H_a dq \ , \tag{12}$$

isosteric cooling (3-4)

$$Q_{3-4} = \int_{T3}^{T4} \left[m_a \left(C_{p,s} + \overline{q} C_{p,a} \right) + m_w C_{p,w} \right] dT \ , \tag{13}$$

isobaric adsorption (4-1)

$$Q_{4-1} = \int_{T4}^{T1} \left[m_a \left(C_{p,s} + \overline{q} C_{p,a} \right) + m_w C_{p,w} \right] dT + \int_{4}^{1} m_a \triangle H_a dq \ , \tag{14}$$

the heat of evaporation

$$Q_e = m_a \Delta q \triangle H_V + \int_{Tc}^{Te} m_a \Delta q C_{p,a} dT \ , \tag{15}$$

the heat of condensation

$$Q_c = m_a \triangle q \triangle H_V \ . \tag{16}$$

4 Selection of adsorbent-adsorbate pair

The performance of adsorption heat pump generally depends on the equilibrium and thermodynamic properties of the adsorbent-adsorbate working pair. For this reason the optimal working pair should be chosen individually for each configuration of heat pump. The design and dynamic simulation of these systems requires the knowledge of the adsorption equilibria for the system of interest, over a wide range of operation temperature and pressure. This information is used to calculate the heat of adsorption, which is crucial for the choice of working pair [17–23]. The results of extensive studies on the adsorption equilibrium for various adsorbate–adsorbent systems have been reported in [4]. These studies were done for the following adsorbate–adsorbent systems: water–alumina, water–silica gel, water–zeolite 13X,

ammonia–activated carbon, ammonia–charcoal, ammonia–polymer resin. Based on the information provided in this paper, water was selected as adsorbate, and zeolite 13 X as adsorbent. For the application being investigated, water has the following positive attributes: has a high latent heat of vaporization, is easily accessible, non-flammable and non-toxic. Adsorption isotherm of water on zeolite 13X has extremely non-linear pressure dependence, which is of importance in adsorption heat pump applications. The physical properties of zeolite 13X are given in article [4].

Adsorption equilibrium of water on zeolite 13X was described using the Dubinin-Astakhov (D-A) model:

$$V = V_o \exp\left[-\left(\frac{A}{\beta E_o}\right)^n\right] , \tag{17}$$

where

$$A = RT \ln\left(\frac{p_s}{p}\right) \tag{18}$$

is an adsorption potential.

Values of D-A model are [4]: $V_0 = 2.114 \times 10^{-4}$ m^3/kg, $\beta E_0 = 18445.0$ J/mol; $n = 1.806$. Equation (17) relates volume of adsorbed compound, V, partial pressure of adsorbate, p, and temperature, T. The concentration of adsorbate in adsorbent, q^*, is given by

$$q^* = V\rho\,(T) \ . \tag{19}$$

Saturation vapor pressure, p_s, and temperature dependent density of liquid adsorbate, $\rho(T)$, are calculated using the following relations:

$$\log_{10}(p_s) = D + E/T + F\log_{10}(T) + GT + HT^2 , \tag{20}$$

$$\rho\,(\mathrm{T}) = BC^{-(1-T/T_c)^m} \ . \tag{21}$$

The values of the parameters are: $B = 347.10$ kg/m^3, $C = 0.27400$, $m = 0.28571$, $T_c = 647.13$ K, $D = 29.8605$, $E = -3.1522\times10^3$, $F = -7.3037$; $G = 2.4247\times10^{-9}$, $H = 1.8090\times10^{-6}$.

The isosteric heat of adsorption, (ΔH_a), was determined from the equilibrium information using the Clausius-Clapeyron equation:

$$\Delta H_a = RT^2\left(\frac{\partial \ln p}{\partial T}\right)_{q^*} \ . \tag{22}$$

For the calculation of the pressure derivative in the above equation, the relationship between pressure and temperature was described using D-A model (Eqs. (17)–(19)).

5 Results

A series of studies was carried out and the results of numerical simulations were presented in Figs. 5–8. The input values of heat pump parameters are collected in Tab. 1.

Table 1: Model input data.

Symbol	Value	Unit
C_{pw}	478	J/(kg K)
D_1	1.0×10^{-2}	m
D_2	1.2×10^{-2}	m
D_3	2.8×10^{-2}	m
$\frac{15D_s}{r_p^2}$	1.0×10^{-2}	1/s
h_f	1000	W/(m^{2}K)
h_s	250	W/(m^{2}K)
L	0.1	m
v_f	0.1	m/s
ε	0.65	–
ρ_s	2280	kg/m^3
ρ_w	7800	kg/m^3

Figure 5 shows the variations of the cooling fluid, the wall and the adsorbent bed temperatures at two different positions during adsorption process. These results are obtained for the initially clean bed. As can be seen, adsorption is a highly exothermic process.

The effect of the evaporator temperature on the adsorption kinetics is shown in Fig. 6. As can be seen, the increase in evaporator temperature increases the amount of adsorbed working medium. This is obvious because as the evaporator temperature increases, the vapor pressure of the working medium increases as well.

Figure 7 shows the changes in temperatures of the solid phase, column walls and fluid at two different positions. It can be seen that all these temperatures are practically the same after about 250 s. The influence of the condenser temperature on the desorption kinetics and on the final concentration of the adsorbate in the adsorbent bed is shown in Fig. 8. It can be observed that as the temperature of the condenser increases, the final

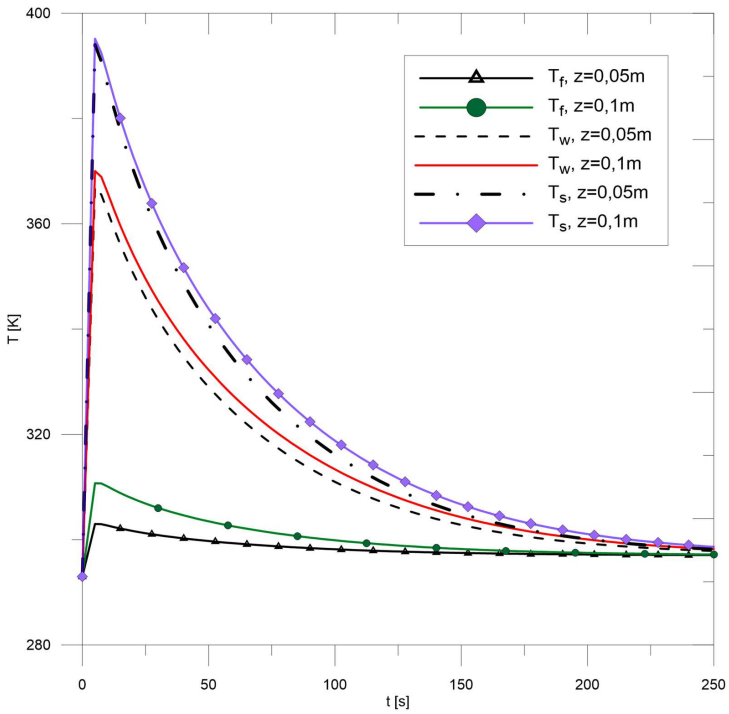

Figure 5: Time evolutions of the cooling fluid, the wall and the bed temperatures at two different positions during adsorption process (T_a = 293 K, T_e = 273.5 K, T_{CO} = 293 K).

content of the adsorbate in the bed increases as well.

The results of the computer simulations were used to calculate the coefficient of performance for heating and cooling (COP_h and COP_{ref}, respectively). These coefficients are defined as follows:

$$COP_{\mathrm{h}} = \frac{Q_c + Q_{3-4} + Q_{4-1}}{Q_{1-2} + Q_{2-3}} \,, \tag{23}$$

$$COP_{ref} = \frac{Q_e}{Q_{1-2} + Q_{2-3}} \,. \tag{24}$$

Exemplary calculation results are shown in Tab. 2. As can be seen, the value of the coefficient of performance for heating is higher than for cooling.

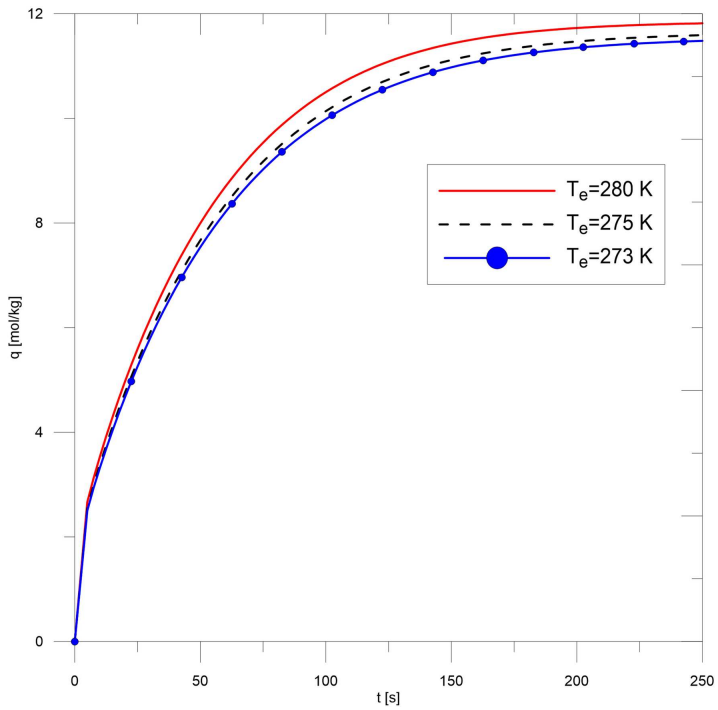

Figure 6: The effect of evaporator temperature on the adsorbate concentration in adsorbent bed during adsorption process (z =0.05 m, T_a = 293 K, T_{CO} = 293 K).

Table 2: Coefficients of performance of cylindrical double-tube adsorption heat pump for heating and cooling (T_H = 533 K, T_{CO} =293 K, T_e =273.5 K, T_c = 313 K).

COP_{ref} [%]	COP_h [%]
32	54

6 Conclusions

In this paper, a nonequilibrium model has been developed and used for predicting the dynamic performance of cylindrical double-tube adsorption heat pump. The model is based on the energy and mass conservation laws, stated in one-dimensional form and solved in time and space using the method of lines. Linear driving-force (LDF) model was used to calculate the mass transfer rate. Water was selected as adsorbate, and zeolite

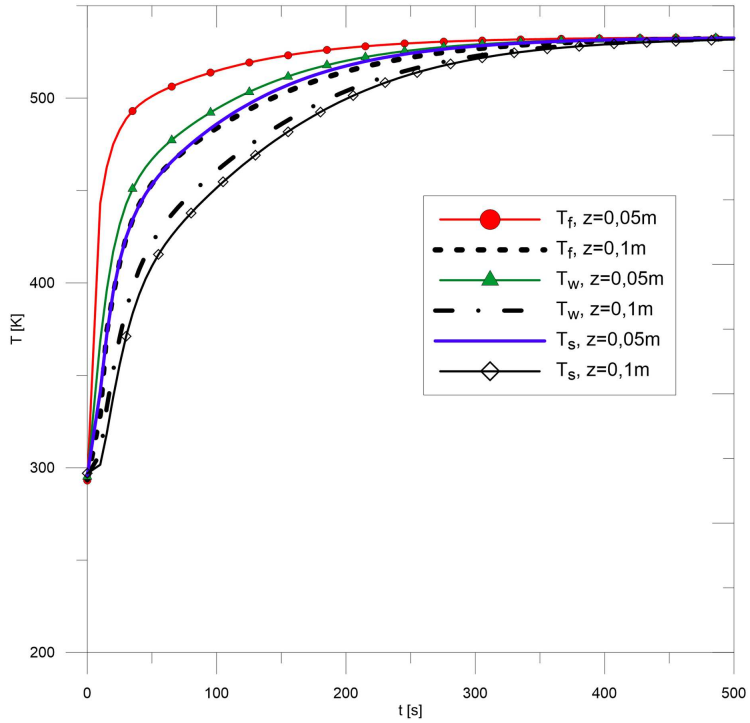

Figure 7: Time evolutions of the heating fluid, the wall and the bed temperatures at two different positions during desorption process ($\overline{q}_0(z) = 11.37 \frac{\text{mol}}{\text{kg}}$, $T_{s0}(z) = T_{f0}(z) = T_{w0}(z) = 293$ K, $T_c = 313$ K, $T_H = 533$ K).

13 X as adsorbent. Adsorption equilibrium was described using the Dubinin – Astakhov (D-A) model. The effect of the evaporator and condenser temperatures on the adsorption and desorption kinetics, respectively, was examined.

The results of the computer simulations allowed the calculation of the coefficient of performance (COP) for heating (COP_h) and cooling (COP_{ref}). Obtained value of $COP_{ref} = 32\%$ and $COP_h = 54\%$ showed that the adsorption heat pumps have relatively low efficiency compared to other heat pumps. For this reason, installations of this type are best suited for waste heat.

Received 6 October 2017

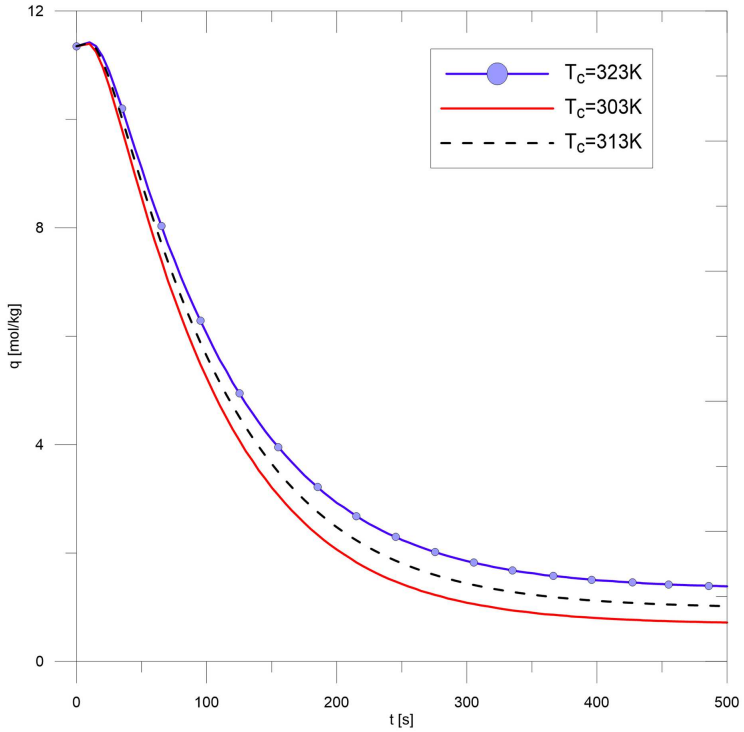

Figure 8: The effect of condensation temperature on the adsorbate concentration in adsorbent bed during desorption process (z =0.05 m, $\overline{q}_0(z) = 11.37 \frac{\text{mol}}{\text{kg}}$, $T_{s0}(z) = T_{f0}(z) = T_{w0}(z) = 293$ K, $T_H = 533$ K).

References

[1] Zhang L.Z.: *A three-dimensiona non-equilibrium model for an intermittent adsorption cooling system.* Solar Energy **69**(2000), 27–35.

[2] Marletta L., Maggio G., Freni A., Ingrasciotta M., Restuccia G.: *A non-uniform temperature non-uniform pressure dynamic model of heat and mass transfer in compact adsorbent bed.* Int. J. Heat Mass Tran. **45**(2002), 3321–3330.

[3] Demira H., Mobedib M., Ülkü S.: *A review on adsorption heat pump: Problems and solutions.* Renew. Sust. Energ. Rev. **12**(2008), 2381–2403.

[4] Ambrożek B., Zwarycz-Makles K., Szaflik W.: *Equilibrium and heat of adsorption for selected adsorbent-adsorbate pairs used in adsorption heat pumps.* Polska Energetyka Słoneczna **5**(2012), 1–4, 1-11.

[5] Chahbani M.H., Labidi J., Paris J.: *Modeling of adsorption heat pumps with heat regeneration.* Appl. Therm. Eng. **24**(2004), 431–447.

[6] Yong L., Sumathy K.: *Review of mathematical investigation on the closed adsorption heat pump and cooling system.* Renew. Sust. Energ. Rev. **6**(2002), 305–337.

[7] Pesaran A., Lee H., Hwang Y., Radermacher R., Chun H.H.: *Review article: Numerical simulation of adsorption heat pumps.* Energy **100**(2016), 310–320.

[8] Teng W.S., Leong K.C., Chakraborty A.: *Revisiting adsorption cooling cycle from mathematical modelling to system development.* Renew. Sust. Energ. Rev. **63(**2016), 315–332.

[9] Saha R.P., Choudhury B., Dasa R.K., Sur A.: *An overview of modelling techniques employed for performance simulation of low–grade heat operated adsorption cooling systems.* Renew. Sust. Energ. Rev. **74**(2017), 364–376.

[10] Schork J.M., Fair J.R.: *Parametric analysis of thermal regeneration of adsorption beds.* Ind. Eng. Chem. Res. **27**(1988), 457–469.

[11] Rusowicz A., Grzebielec A.: *Analysis of the use of adsorption processes in trigeneration systems.* Arch. Thermodyn. **34**(2013), 4, 35–49.

[12] Vasiliev L.L., Filatova O.S., Tsitovich A.P.: *Application of sorption heat pumps for increasing of new power sources efficiency.* Arch. Thermodyn. **31**(2010), 2, 21–43.

[13] Grzebielec A., Rusowicz A., Jaworski M., Laskowski R.: *Possibility of using adsorption refrigeration unit in district heating network.* Arch. Thermodyn. **36**(2015), 3, 15–24.

[14] Ko D., Kim M., Moon I., Choi D.: *Analysis of purge gas temperature in cyclic TSA process.* Chem. Eng. Sci. **57**(2002), 179–195.

[15] Ruthven D.M., Farooq S., Knaebel K.S.: *Pressure swing adsorption.* VCH, New York 1994.

[16] Schiesser W.: *The numerical method of lines: integration of partial differential equations.* Academic Press, San Diego 1991.

[17] Kane A., Giraudet S., Vilmain J.B., Le Cloirec P.: *Intensification of the temperature-swing adsorption process with a heat pump for the recovery of dichloromethane.* J. Environ. Chem. Eng. **3**(2015), 734–743.

[18] Chuaa H.T., Nga K.C., Maleka A., Kashiwagib T., Akisawab A., Sahab B.B.: *Modeling the performance of two-bed, sillica gel-water adsorption chillers.* Int. J. Refrig. **22**(1999), 194–204.

[19] Sakoda A., Suzuki M.: *Fundamental study on solar powered adsorption cooling system.* J. Chem. Eng. Jpn. **17**(1984), 52–57.

[20] Cho S.H., Kim J.N.: *Modeling of a silica gel/water adsorption cooling systems.* Energy **17**(1992), 829–839.

[21] Saha B.B, Boelman E.C., Kashiwagi T.: *Computer simulation of a silica gel-water adsorption refrigeration cycle – the influence of operating conditions on cooling output and COP.* ASHRAE Trans. Res. **101**(1995), 348–357.

[22] Boelman E.C., Saha B.B., Kashiwagi T.: *Experimental investigation of a silica gel-water adsorption refrigeration cycle – the influence of operating conditions on cooling output and COP.* ASHRAE Trans. Res. **101**(1995), 358–366.

[23] Boelman E.C., Saha B.B., Kashiwagi T.: *Parametric study of a silica gel-water adsorption refrigeration cycle – the influenceof thermal capacitance and heat exchanger UA-values on cooling capacity, power density and COP*. ASHRAE Trans. Res. **103**(1997), 139–148.

archives
of thermodynamics
Vol. **38**(2017), No. 4, 209–227
DOI: 10.1515/aoter-2017-0032

Monte Carlo analysis of the battery-type high temperature gas cooled reactor

MARCIN GRODZKI
PIOTR DARNOWSKI*
GRZEGORZ NIEWIŃSKI

Warsaw University of Technology, Institute of Heat Engineering, Nowowiejska 21/25, 00-665 Warsaw, Poland

Abstract The paper presents a neutronic analysis of the battery-type 20 MWth high-temperature gas cooled reactor. The developed reactor model is based on the publicly available data being an 'early design' variant of the U-battery. The investigated core is a battery type small modular reactor, graphite moderated, uranium fueled, prismatic, helium cooled high-temperature gas cooled reactor with graphite reflector. The two core alternative designs were investigated. The first has a central reflector and 30×4 prismatic fuel blocks and the second has no central reflector and 37×4 blocks. The SERPENT Monte Carlo reactor physics computer code, with ENDF and JEFF nuclear data libraries, was applied. Several nuclear design static criticality calculations were performed and compared with available reference results. The analysis covered the single assembly models and full core simulations for two geometry models: homogenous and heterogenous (explicit). A sensitivity analysis of the reflector graphite density was performed. An acceptable agreement between calculations and reference design was obtained. All calculations were performed for the fresh core state.

Keywords: HTGR; HTR; Monte Carlo; Serpent; U-battery; SMR; Battery type

1 Introduction

The nuclear power provides over 11% of the electricity consumed worldwide. There are about 450 operating power reactors and about 60 are

*Corresponding Author. Email piotr.darnowski@itc.pw.edu.pl

under construction [1,2]. Most of currently operating and constructed nuclear power plants (NPPs) are using high power ($\sim$ 1 GWe) light-water reactors (LWRs). The absence of carbon dioxide emissions, low-cost fuel, high capacity-factor and stable baseload power production are considered as the most important advantages of the nuclear power. In the era of a significant development of the renewable energy sources and gas sources, nuclear power loses its relative importance, especially in the European Union and the United States. However, renewables have various disadvantages, such as the unpredictability of energy production, since gas sources are characterized by problems like large fuel prices and their variations. In some cases, a stable and highly reliable source of nuclear power may be needed. Small modular reactors (SMRs) have a potential to be interesting complementation to the future power grid and those may be even alternative to today's nuclear power. Unfortunately, large-sized reactors have some disadvantages. For instance, a large unit can be built only when high power demand is present and only in proper locations, characterized by sufficient cooling and properly remote. Construction and operation of a large NPP are not always possible since it is a very capital-intensive investment and very complex engineering project. Plenty of those problems do not concern SMR designs. This type of reactor requires a much lower capital investment, potentially simpler to build, the flexible option being less capital-intensive with project management being less demanding and less problematic project size and timespan. Moreover, most of the plant and reactor assembly process can be performed in the factory conditions with simpler assurance of the high manufacturing and safety standards. In fact, the unit costs are expected to be higher but it is mainly because the economy of scale is less important. Nevertheless, it is expected that this drawback will be overwhelmed by other positive effects. The detailed discussions about different aspects of the small modular reactors technology are presented in several reports and papers [2–6,8,20].

The special type of SMRs are battery type reactors, which are characterized by very long fuel cycle length ($>$ 5 years) which can be even equal to the core lifetime. Those are usually very small units with the capability of automatic operation. Their size allows construction in places where there is no access to the national power grid, like remote locations or where the power demand is much lower. Battery type SMRs are designed in such a way that each element of the reactor can be delivered by railway, by roadway or by the sea. All those factors significantly increase possible locations

for utilization of this type of reactor [7]. Some modern SMR designs may provide not only the electricity but the process heat which may be a very interesting option for the industry.

There are many types and designs of SMRs or battery type reactors [5] and one of them are high-temperature gas-cooled reactors (HTGR) [11,14,15]. The technology is significantly different from commonly used light water reactors and HTGRs are not commonly used. However, interest in this technology has increased significantly in recent years. One of the most notable advantages of this type of reactor is high core outlet coolant temperature (above 700 °C) and it allows to reach higher thermal efficiency than in any traditional reactor. Moreover, high-temperature heat can be used in many industrial processes, e.g., hydrogen production. So far, 7 reactors of this type have been built and 2 of them are still operational today HTR-10 (China) and HTTR (Japan) [8]. At present, one HTR-PM reactor is under construction in China [8]. There are many new designs and projects being developed around the World [2].

In the open literature, there is a description of a very small prismatic battery-type high-temperature helium gas cooled reactor, which can operate up to ten years without refueling. The reactor design is called U-battery and detailed data for several alternative designs are described in the publicly available reports [7,9]. The concept has been under development since 2007 by Delft University of Technology and Manchester University and financed by URENCO, Koopman and Witteveen. Currently it is developed by the U-battery consortium in partnership with several companies. It is worth to mention that, the alternative 10 MWth core design is being considered to be built in Poland [21]. The basic aim of this study was to build a numerical model and perform neutronic calculations, data analysis and comparison with literature for the selected U-battery design variant.

2 Materials and methods

2.1 SERPENT computer code

The SERPENT is a continuous energy neutron transport Monte Carlo computer code which has been developed by Finnish VTT research center since 2004 [18,22,23]. The code was used as a state-of-the-art Monte Carlo tool for reactor physics application with fuel burnup capability. The code is a popular research tool in design and analyses of the novel reactor systems. The code and Monte Carlo method were applied as an excellent tool

to obtain the effective multiplication factor in complex geometries and its abilities to perform this task may be better than in the case of deterministic tools. All calculations were performed with recent SERPENT version 2.1.28 and two different nuclear data libraries ENDF/B-VII and JEFF-3.1.1 [18,22].

2.2 The core design and models

2.2.1 The basic design

The considered core is a prismatic-type 20 MWth HTR with TRISO type fuel. The reactor core is composed of several prismatic fuel elements (37 or 30) which are made of identical fuel blocks stacked into four axial levels (37×4 or 30×4). The reactor uses inert helium as a coolant which has a negligible impact on the neutron economy and with core inlet temperature 250 °C and outlet temperature 750 °C. The fuel blocks are made of graphite and ceramic materials with high thermal capacity and heat resistance. Thanks to that the core is accident resistant – it has a large time scale of transients and accidents. Moreover, it has low power density which allows in most cases to use only passive coolant systems to remove decay heat. The core has a negative reactivity temperature coefficient – reactor power is decreasing when the temperature in the core is increasing. Electricity generation can be produced in a direct or indirect cycle. It's working as a 'nuclear battery', which means that it can work from 5 to 10 ten years without refueling with high burnup capability ($\sim$ 70 GWd/tHM). All core design data used in this paper are based on the *Design of U-Battery* [7] report and documents related to it [9,10]. Various design alternatives of this reactor were considered in those reports.

2.2.2 TRISO particles and fuel compacts

The reactor uses TRISO-coated type fuel particles embedded in fuel compacts. Those are concentric spherical particles with the kernel made of uranium dioxide with enrichment equal to 20 wt% U-235. The kernel is coated by several protective layers. The first layer, buffer, directly covers fuel kernel and is made of low-density pyrocarbon. It is designed to accommodate gaseous fission products and to attenuate fission product recoil from a kernel with fuel. The next layer, inner pyrolytic carbon (IPyC), is made of high-density pyrocarbon and is also designed to hold fission products. The third layer is made of silicon carbide (SiC) and is the primary

containment. The last layer is made of pyrocarbon and is called outer pyrolytic carbon (OPyC) layer [11]. Table 1 shows the density of materials and thickness of each layer and fuel compact parameters.

Table 1: TRISO and fuel compact parameters [7].

TRISO Parameter	Value	Unit
Radius of fuel kernel	250	μm
Density of fuel kernel	10.5	g/cm^3
Thickness of buffer layer	100	μm
Density of buffer layer	1	g/cm^3
Thickness of IPyC layer	35	μm
Density of IPyC layer	1.9	g/cm^3
Thickness of SiC layer	35	μm
Density of SiC layer	3.2	g/cm^3
Thickness of OPyC layer	40	μm
Density of OPyC layer	1.97	g/cm^3
Compact Parameter	Value	Unit
Radius of fuel compact	0.6225	cm
Height of fuel compact	4.93	cm
Packing Fraction of TRISO	0.3	–

The TRISO particles are formed in the so-called fuel compacts and those are characteristic for prismatic type cores. They have a cylindrical shape and comprise with TRISO and graphite matrix. The fifteen compacts are stacked inside the fuel block (column). The amount of fuel is corresponding to the packing fraction equal to 30% and it is defined as a ratio of the total fuel particles volume to the fuel compact volume (Tabs. 1 and 2).

The geometry of the prismatic HTGR reactor is relatively difficult to model. The most concerning problem is the modelling of TRISO particles embedded in fuel compacts. Two types of geometry models were analyzed in this work. The first is simplified and uses homogenization of the compacts. Hence, the fuel compact is filled with the mixture of the TRISO particle materials and matrix materials. The model is created as follows: first, the exact amount of individual material that is present in the fuel compact volume is calculated. Then the density of each material in fuel compact

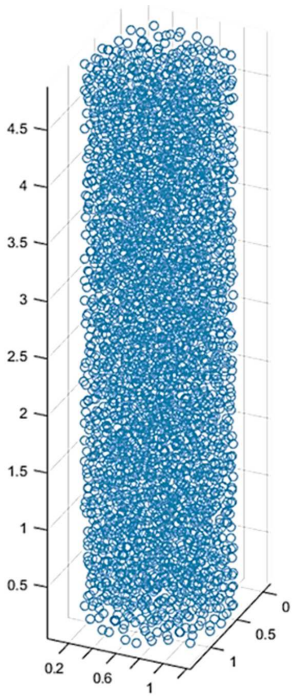

Figure 1: Visualization of the single fuel compact with TRISO particles locations for heterogenous (explicit) geometry model. Units are centimeters.

is calculated: the mass of the material is divided by the volume of fuel compact. Fuel compact is filled by the homogenous material, which is a mixture of all the materials occurring in its volume. Thanks to that, the complicated model with precise positioning of TRISO particles is avoided. As a result, the calculations are made with some degree of simplicity and it causes differences in neutron multiplication properties of the system. Otherwise, this approach was used in the reference report [7,9] and it is popular in some HTGR analyses.

The second approach is the explicit model and it is taking into account random microstructure of the fuel. The Serpent code allows the user to provide particles coordinates and to model precisely the TRISO fuel. In order to create the most accurate model that takes into consideration the positions of TRISO particles, a special dedicated code has been developed that calculates the geometry parameters and generates random particle coordinates. It was evaluated that there should be 4416 TRISO particles

in each fuel compact (30% volume fraction) and coordinate points were generated using the code (see Figs. 1 and 2). For simplicity, only one random configuration was used in the SERPENT calculations for all fuel compacts (see Fig. 1). It is the important simplification, the generation of the distinct random patterns for every single fuel compact was considered as complex task beyond the scope of this work. The maximum reactivity uncertainty due to the deviation in the geometry pattern may be estimated to be less than 150 pcm (per cent mile) [25]. This value is the maximum difference between cubic pattern and multiple realizations random pattern for infinite medium described in [25]. What is more, the reference [24] compares cubic pattern with random pattern for a full-core HTR and the deviation is less than 50 pcm. However, in this research, the fuel geometry heterogeneity effect [9] onto the neutron multiplication was intended to be shown and estimated quantitively with single random geometry realization.

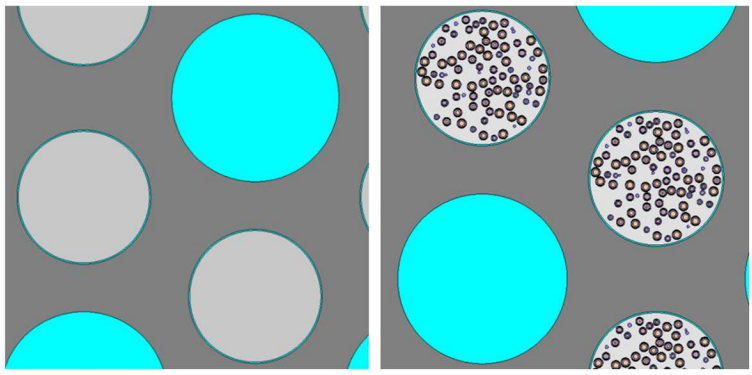

Figure 2: Magnified fuel block cross-section with visible fuel compacts, cooling channels and matrix. Homogenized geometry (left) and heterogenous explicit type geometry with TRISO particles (right).

2.2.3 Fuel-blocks

The hexagonal (prismatic) blocks made of graphite are stacked to form a fuel element (Tab. 2). Particularly, four fuel blocks are set tight side by side. Each block contains graphite matrix, fuels channels (rods) filled with fuel compacts and helium coolant channels (holes). Additionally, in the proposed fuel design, there are six fixed burnable poison (FBP) channels [9]. The calculations which are the main part of this report, as well as

reference results are taken from the literature [9], relating to fuel blocks with FBP replaced by fuel compacts. There is also a special type of block, entirely made of the graphite which works as a reflector. The basic fuel block design is based on GT-MHR fuel block as described in [12]. Figures 3 and 4 presents the vertical and horizontal cross-section for the fuel block SERPENT models.

Table 2: Basic parameters of fuel block [9].

Parameter	Value	Unit
Width flat-to-flat	36	cm
Height of the block	80	cm
Number of fuel channels	216	–
Radius of fuel channel	0.635	cm
Number of coolant channels	102/6	–
Radius of coolant channel	0.794/0.635	cm
Number of fixed burnable (FBP) holes	6	–
Radius of FBP hole	0.635	cm
Number of fuel compacts per one channel	15	–
Number of fuel blocks per fuel element	4	–

2.2.4 The core design and full core models

There are two core configurations considered, the first case has 37 (37×4) blocks per core level and the second 30 (37×4) blocks. The main difference is due to seven central fuel blocks which are replaced by reflector blocks in the second case. Figures 5 and 6 present SERPENT model's visualizations for both core configurations. Fuel blocks are surrounded by the permanent side reflector and its outer diameter is 3.1 m. The thickness of the side reflector depends on the outer diameter of the reactor vessel. There are other layers between side reflector and RPV as described in design reports but those were not modelled. Figures 5 and 6 (right) show top and bottom reflectors modelled by 0.5 m high graphite layers. Coolant channels run through reflectors in accordance with blocks channels. It should be noted that the whole geometry is modelled only until the side reflector as in reference calculations [7].

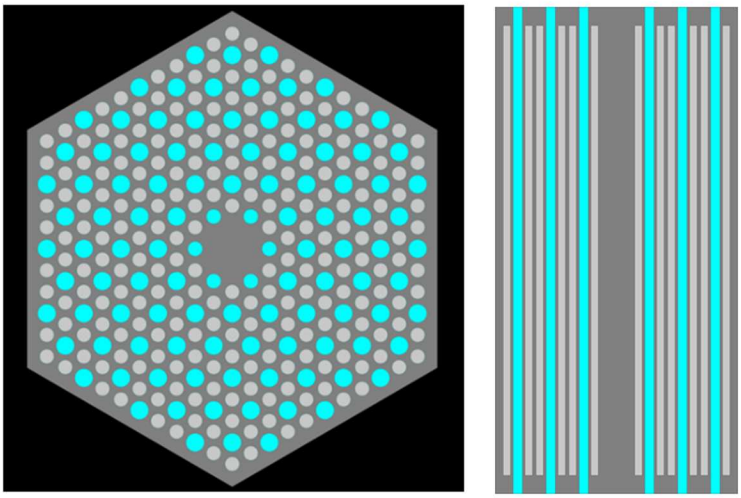

Figure 3: Fuel block homogenous type, horizontal cross-section (left) and vertical cross-section (right).

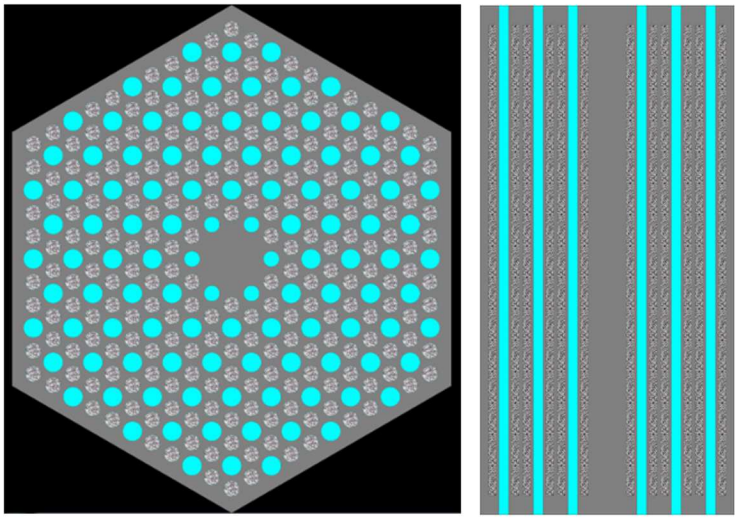

Figure 4: Fuel block horizontal cross-section, explicit type geometry (left) and vertical cross-section (right).

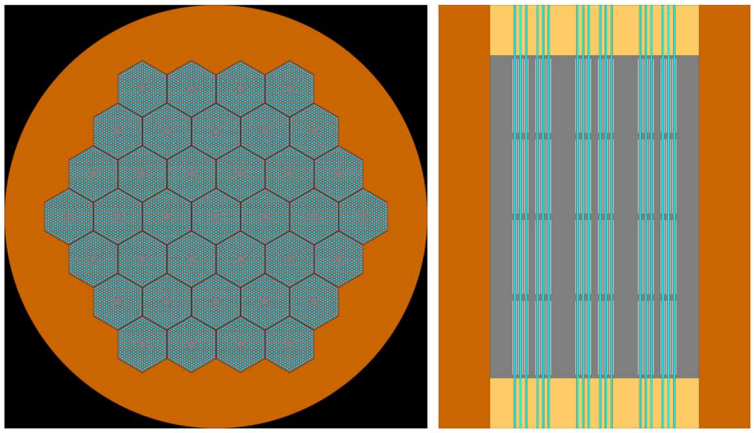

Figure 5: Full-core model horizontal cross-section for 37 × 4 reactor, explicit type geometry (left) and vertical cross-section (right).

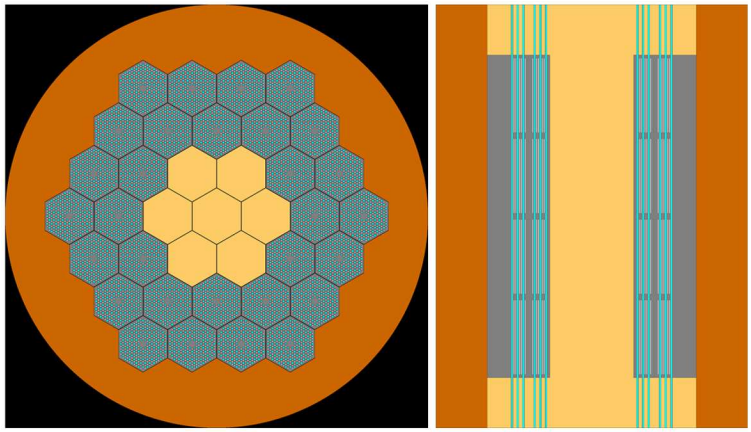

Figure 6: Full-core model horizontal cross-section for 30 × 4 reactor, explicit type geometry (left) and vertical cross-section (right).

The graphite densities applied in calculations are presented in Tab. 3. Due to the lack of precise data concerning the graphite densities for core structures, certain values were based on data available in the following references: [13,12,16,17]. It was also the motivation to perform, additional sensitivity calculations related to reflector's graphite density.

Table 3: Graphite densities for different reactor components.

Name	Value	Unit
Permanent reflector graphite	1.73	g/cm^3
Reflector block graphite	1.78	g/cm^3
Fuel block graphite	1.85	g/cm^3
Top and bottom reflector graphite	1.78	g/cm^3
Fuel compact graphite	1.2	g/cm^3
Reflector's graphite density for additional calculations	2.3	g/cm^3

2.3 Investigated cases

The first group of analyzed cases: 0A and 0B (Tab. 4), covers single fuel block calculations with the estimation of the infinite multiplication factor (see Figs. 3 and 4). Reflective boundary conditions were applied on all outer boundary surfaces. Simulations were performed with 20000 neutrons per 500 active cycles and 100 inactive cycles. The second group, (Tab. 3) covers full core cases (see Figs. 5 and 6), and for all of them black boundary conditions were applied, and simulations were performed with 200000 neutrons per cycle, 500 active and 100 inactive cycles. The selected neutron populations and cycles were based on the recommendations and typical approach in Monte Carlo criticality analysis [26].

Table 4: List of the basic cases analyzed with SERPENT.

Case	Description
0A	single fuel block, homogenous type
0B	single fuel block, explicit type
IA	37x4 full core, homogenous type
IB	37x4 full core, explicit type
IIA	30x4 full core, homogenous type
IIB	30x4 full core, explicit type

The current state-of-the-art Monte Carlo criticality simulations involve studies of the fission source convergence and it covers the multiplication

factor (eigenvalue) and Shannon Entropy investigation [19]. Those parameters were examined for all models and satisfactory convergence was achieved with 100 inactive cycles.

The single fuel block models, both homogenized and explicit cases and full core homogenized cases were compared with reference results. Those were obtained with SCALE5.1 or SCALE6 package with KENO Monte Carlo solver and were taken from reference [9] and are reproduced in Tab. 5. Worth to highlight is the fact that the explicit model reference results cover only the single fuel block case. Monte Carlo standard deviations were reported only for the full-core calculations ($\sim$ 130 pcm).

Table 5: Reference values obtained with SCALE/KENO code. Taken from [9].

Ref. case	Type	Code	$k_{eff}{}^*$	σ^*
0A	fuel block, homogenous model	Scale 6	1.3945	N/A
0B	fuel block, explicit model	Scale 6	1.4456	N/A
IA	reactor 37×4 type, homogenous model	Scale 5.1	1.2980	0.0017
IIA	reactor 30×4 type, homogenous model	Scale 5.1	1.3397	0.0017

Information about reflector's graphite density was missing in the reference documentation [7,9]. Additional sensitivity calculations were performed for the full core cases IA, IB, IIA and IIB. Hence, two variants of reflector density were calculated: the first variant assumed values consistent with the industrial grade graphite. In the second variant reflector's graphite density was assumed to be 2.3 g/cm^3, which is equal to anisotropic graphite's density. The new reflector density is the only change in comparison to other cases' parameters. The idea of performing a calculation for alternative reflector's density comes from the reference [13], the oldest document containing information about the design.

In general, the reactivity differences were calculated according to the formula (in units of pcm)

$$\Delta\rho = \frac{k_1 - k_0}{k_1\ k_0} \times 10^5 \tag{1}$$

and the relative (percent) difference between the results by the following formula:

$$\mathrm{RD} = \frac{k_1 - k_0}{k_1} \times 100\,, \tag{2}$$

where k_1 and k_0 are neutron multiplication factors (eigenvalues) for compared cases.

3 Results and discussion

3.1 Single block results

Table 6 shows the results of the infinite multiplication factor, k_{inf}, calculations for the 0A (fuel block, homogenous type) and 0B (fuel block, explicit type) cases compared with reference values. This is the only chance where comparison of the reference values for the explicit and homogenous model for the same cases was possible.

Table 6: Comparison of the SERPENT and reference results [9] for fuel single blocks calculations.

Case	Type	Lib.	k_{inf} SERPENT	σ SERPENT (pcm)	k_{inf} ref. value	$\Delta\rho$ (pcm)	RD,%
0A	Homogenous	ENDF	1.39323	0.00017 (12)	1.3945	65	0.09
0A	Homogenous	JEFF	1.39288	0.00018 (13)	1.3945	83	0.12
0B	Explicit	ENDF	1.44871	0.00028 (19)	1.4456	-149	-0.22
0B	Explicit	JEFF	1.44847	0.00016 (11)	1.4456	-137	-0.20

The results obtained using the JEFF library are slightly lower than those calculated with the ENDF library with the difference less than < 20 pcm for both explicit and homogenous geometry models. SERPENT calculations are close to the reference results for both libraries with reactivity differences being less than 150 pcm (see Tab. 6). The minor difference in k_{inf} are found for the homogenous model (Case 0A) and the slightly larger difference was found for the explicit model (Case 0B). What is more, it was observed that the infinite multiplication factors calculated for the explicit models are higher than for the homogenous models by about ~ 2800 pcm and similar differences are present for reference calculations. In consequence, it can be observed that the heterogeneity effect is strong in terms

of reactivity and the SERPENT code is able to reproduce it.

The SERPENT calculated Monte Carlo relative statistical errors (Tab. 6) are characterized by standard deviations smaller than 20 pcm. On the contrary the KENO statistical errors were not reported [9] and it is not possible to assess the effects of the Monte Carlo uncertainty. Otherwise, taking into account the nature and practice of neutronic simulations with different codes for such complex systems the results with about $\sim$ 150 pcm deviation are satisfactory and with $\sim$ 50 pcm are considered as very good. Larger differences for the explicit model are probably caused by the application of the different random geometry pattern.

3.2 Full-core results

Table 7 shows the results of the effective multiplication factor calculations for homogenous full-core models: IA (37×4) and IIA (30×4) cases compared to the homogenous full-core reference values (see Tab. 5). What is more, Tab. 7 shows a comparison of the basic cases with low (standard) reflector density and sensitivity cases (with asterisk*) with large reflector density.

Table 7: Comparison of the full-core SERPENT results with reference results for homogenous models.

Case	Lib.	k_{eff} SERPENT	σ SERPENT (pcm)	k_{eff}, ref. value	σ ref. (pcm)	$\Delta\rho$ (pcm)	RD, %
Base case: standard reflector graphite density							
IA	ENDF	1.26502	0.00010 (8)	1.2980	131	2009	2.54
IA	JEFF	1.26476	0.00010 (8)	1.2980	131	2025	2.56
IIA	ENDF	1.30756	0.00009 (7)	1.3397	127	1835	2.40
IIA	JEFF	1.30729	0.00010 (8)	1.3397	127	1851	2.42
Sensitivity case: modified reflector graphite density 2.3 g/cc							
IA*	ENDF	1.29725	0.00010 (8)	1.2980	131	45	0.06
IA*	JEFF	1.29691	0.00010 (8)	1.2980	131	65	0.08
IIA*	ENDF	1.33924	0.00013 (10)	1.3397	127	26	0.03
IIA*	JEFF	1.33898	0.00010 (8)	1.3397	127	40	0.05

The base case SERPENT results with standard reflector density are up to 2000 pcm lower than reference results obtained with SCALE/KENO. In consequence, it led us to the conclusion that there are very significant differences in modelling. Several potential sources of differences were studied but the reflector density was identified as the most probable.

Table 6 shows that sensitivity cases results are very close to the reference homogenous results. Differences in reactivity are 26–65 pcm and relative difference is less than 0.1%. This allows us to conclude that there is a high probability that the reflector's graphite density was equal to (or close) 2.3 g/cc and this value has been used in reference calculations. However available data and performed calculations cannot prove with certainty such a hypothesis over reasonable doubt. Otherwise, statistical errors of the IA* and IIA* cases (Tab. 6) are 2 to 5 times larger than differences expressed in terms of reactivity. Hence, from the Monte Carlo uncertainty point of view, those results are convergent. Nevertheless, SERPENT calculations were performed with substantially larger neutron population and the statistical errors are an order of magnitude lower than reference results.

Table 8 shows the differences between the explicit (B) and homogenous (A) geometry models for base cases and sensitivity cases (*). In general, the effective multiplication factors calculated with the explicit model are higher by about $\sim$ 3000 pcm and $\sim$ 1800 pcm in the base and sensitivity cases respectively. Hence, as expected, similarly to the single assembly calculations heterogeneity effects are strong. The differences for sensitivity cases are in general $\sim$ 100–200 pcm lower than base cases. Worth to mention that the differences between calculations of the same case and geometry model but using different nuclear libraries are small $\leq$ 20 pcm for all cases (Tabs. 7 and 8). Example fission power and thermal flux intensities distribution for homogenous cases are presented in Fig. 7 (37×4) and 8 (30×4) [18].

4 Conclusions and summary

The obtained multiplication factors for the single prismatic block and the full-core sensitivity cases are considered as being in very good agreement (Tabs. 6 and 7) with the reference data [9]. On the contrary, the full-core base cases with lower reflector density diverge significantly ($\sim$ 2000 pcm). The difference of $<$ 200 pcm may be considered as a satisfactory result. It is especially due to the fact that the models were prepared using the limited design data available in the public reports, the nature of this type

Table 8: Comparison of the full-core SERPENT results for homogenous and explicite models.

		Case A – homogenous		Case B – explicit			
Case	Lib.	$k_{eff,hom}$	σ	$k_{eff,exp}$	σ	$\Delta\rho$ (pcm)	RD, %
Base case: standard reflector density							
I	ENDF	1.26502	0.00010	1.31654	0.00010	3093	3.91
I	JEFF	1.26476	0.00010	1.31617	0.00010	3088	3.91
II	ENDF	1.30756	0.00010	1.34052	0.00010	1880	2.46
II	JEFF	1.30729	0.00010	1.34037	0.00010	1887	2.47
Sensitivity case: modified reflector density 2.3 g/cc							
I*	ENDF	1.29725	0.00010	1.34730	0.00010	2864	3.71
I*	JEFF	1.29691	0.00010	1.34716	0.00010	2876	3.73
II*	ENDF	1.33924	0.00013	1.37207	0.00010	1787	2.39
II*	JEFF	1.33898	0.00010	1.37163	0.00009	1778	2.38

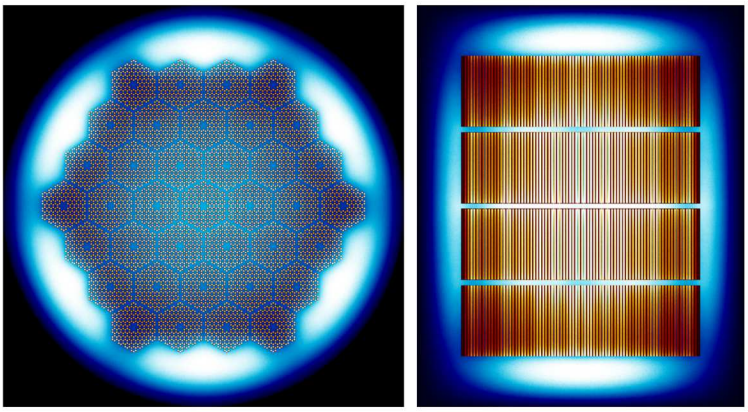

Figure 7: The thermal power and thermal flux distributions in Case IA (homogenous). Horizontal (left) and vertical (right).

of reports and fact that all nuclear number densities were calculated independently. Moreover, the reference results were calculated by different computer code (SCALE/KENO) and those were characterized by a relatively large statistical error. Worth to mention that, a smaller accuracy

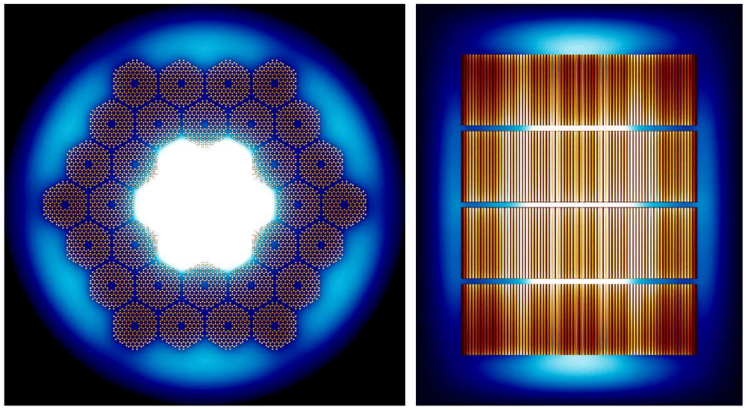

Figure 8: The thermal power and thermal flux distributions in Case IIA (homogenous). Horizontal (left) and vertical (right).

may be found in some reactor physics international benchmark exercises with detailed specifications provided.

Two types of geometrical models were analyzed, homogenous and explicit. In the homogenous model, all materials exist as a mixture in fuel compact volume. In the case of explicit model fissile material is located in clusters consisting of TRISO particles and it is random heterogenous material. Table 6 provides a basis to conclude that the single assembly models both homogenized and explicit were created properly. The larger differences in the explicit case are probably caused by the different random geometry pattern applied in reference calculations. Otherwise, single block models were appropriate to use them to create full-core models. The full-core homogenous model results were consistent with reference results. Unfortunately, explicit full-core reference results were not available.

The fuel geometry heterogeneity effects were observed and compared quantitively. In the case of full-core calculations substantially higher results came from the explicit model ($\sim$ 1800–3000 pcm). Similar effects were observed for a single block ($\sim$ 2800 pcm) and described in the literature [9]. Comparison of reference values resulting from the calculation for both explicit and homogenous models was only possible in one case – in a case of single fuel block calculations. It is because reference reports do not contain full-core explicit calculations for investigated cores. Hence, full-core explicit results presented in this report are novel for the investigated design. Nevertheless, the further study of the random explicit geometry

modelling is recommended for the future activities. The application of the single geometry realization may be questionable from the purely theoretical point of view as the selected realization may not be representative. Otherwise, the main purpose of the explicit full-core calculations was achieved, the heterogeneity effect was estimated quantitively and differences are consistent with single block heterogeneity impact.

All investigated cases were calculated using two types of libraries JEFF and ENDF as a standard approach in neutronic calculations. Results from calculations using JEFF library were in every case slightly lower than for ENDF library. The difference is due to the very complex nature of nuclear data and it occurs in any reactor analysis.

Acknowledgments We would like to deeply acknowledge Jakko Leppänen and VTT for the creation of the excellent SERPENT computer code. We would like to state, no conflict of interest with any company, organization and institution. This research was performed as independent university research and was not financed by any organization.

Received 11 October 2017

References

[1] *World Nuclear Association:* http://www.woorld-nuclear.org/information-library/current-and-future-generation/nuclear-power-in-the-world-today.aspx (accessed 5 Oct. 2017).

[2] Nuclear Energy Institute: https://www.nei.org/Knowledge-Center/Nuclear-Statistics/World-Statistics (accessed 05 Oct. 2017).

[3] International Nuclear Energy Agency: *Advances in small modular reactor technology developments*. IAEA, Vienna 2014.

[4] International Nuclear Energy Agency*: Approaches for Assessing the Economic Competitiveness of Small and Medium Sized Reactors*. IAEA Nuclear Energy Ser. NP-T-3.7, 2013.

[5] Rowiński M.K., White T.J., Zhao J.: *Small and medium sized reactors (SMR): A review of technology.* Renewable and Sustainable Energy Rev. **44**(2015), 643–656.

[6] NNL: *Small Modular Reactors (SMR) Feasibility Study.* National Nuclear Laboratory Rep., Dec. 2014.

[7] Ding M., Kloosterman J.L., Kooijman T., Linssen R., Abram T., Marsden B., Wickham T.: *Design of U-Battery.* Delft, 2011.

[8] World Nuclear Association: http://www.world-nuclear.org/information-library/nuclear-fuel-cycle/nuclear-power-reactors/small-nuclear-power-reactors.aspx (accessed 05 Oct. 2017).

[9] Ding M., Kloosterman J.L.: *Neutronic feasibility design of a small long-life HTR.* Nucl. Eng. Des. **241**(2011), 12, 5093–5103.

[10] Ding M., Kloosterman J.L.: *Thermal-hydraulic design and transient evaluation of a small long-life HTR.* Nucl. Eng. Des. **255**(2013), 347–358.

[11] *High temperature Gas Cooled Reactor Fuels and Material.* IAEA, 2010.

[12] *Gas turbine-modular helium reactor (GT-MHR) conceptual design description report.* Tech. Rep., General Atomics, 1996.

[13] Zwaan S.J. de: *Feasibility Study of the U-Battery*, PNR-131-2007-004, 2007.

[14] *History and Evolution of the HTGR.* General Atomic, 2007.

[15] *IAEA Current status and future development of modular high temperature gas cooled reactor technology.* IAEA, 2001.

[16] *Prismatic coupled neutronic/thermal fluids transient benchmark of the MHTGR MW core design, Benchmark definition 2011.*

[17] Ortensi J., Cogliati J.J., Pope M.A., Bess J.D., Ferrer R.M., Bingham A.A., Ougouag A.M.: *Deterministic Modeling of the High Temperature Test Reactor.* INL Rep., 2010.

[18] Leppänen J.: *Serpent – A Continuous-Energy Monte Carlo Reactor Physics Burnup Calculation Code, Manual,* 2015.

[19] Kaltiaisenaho T.: *Statistical Tests and the Underestimation of Variance in Serpent 2, Res. Rep.,* 2014.

[20] Samul K., Strupczewski A., Wrochna G.: *Small Modular Reactors (SMR).* Rap. National Centre for Nuclear Research, Świerk 2013.

[21] National Centre for Nuclear Research: https://www.ncbj.gov.pl/pl/aktualnosci/ncbj-planuje-budowe-badawczego-reaktora-nowej-generacji (accessed 05 Oct. 2017).

[22] Leppänen J.: *Development of a New Monte Carlo Reactor Physics Code.* D.Sc. Thesis, VTT Publication 640, Helsinki University of Technology, 2007.

[23] SERPENT Monte Carlo Code Development Status: http://montecarlo.vtt.fi/development (accessed 30 Aug. 2017).

[24] Stanisz P., Malicki M., Kopeć M.: *Validation of VHTRC calculation benchmark of critical experiment using the MCB code.* SEED 2016 Conf., E3S Web of Conf. 10, 00123, 2016.

[25] Brown F.B., Matrin W.R., Jei W., Conlin J.L., Lee J.C.: *Stochastic Geometry and HTGR Modeling with MCNP5.* Los Alamos National Laboratory Rep. LA-UR-04-8668, 2005.

[26] Brown F.B.: *A Review of Best Practices for Monte Carlo Criticality Calculations.* Los Alamos National Laboratory Rep. LA-UR-09-03134, 2009.

Notes for Contributors

ARCHIVES OF THERMODYNAMICS publishes original papers which have not previously appeared in other journals. The journal does not have article processing charges (APCs) nor article submission charges. The language of the papers is English. The paper should not exceed the length of 25 pages. All pages should be numbered. The plan and form of the papers should be as follows:

1. The heading should specify the title (as short as possible), author, his/her complete affiliation, town, zip code, country and e-mail. Please indicate the corresponding author. The heading should be followed by *Abstract* of maximum 15 typewritten lines and *Keywords*.
2. More important symbols used in the paper can be listed in *Nomenclature*, placed below *Abstract* and arranged in a column, e.g.:
   u – velocity, m/s
   v – specific volume, m/kg
   etc.
   The list should begin with Latin symbols in alphabetical order followed by Greek symbols also in alphabetical order and with a separate heading. Subscripts and superscripts should follow Greek symbols and should be identified with separate headings. Physical quantities should be expressed in SI units (*Système International d'Unités*).
3. All abbreviations should be spelled out first time they are introduced in the text.
4. The equations should be each in a separate line. Standard mathematical notation should be used. All symbols used in equations must be clearly defined. The numbers of equations should run consecutively, irrespective of the division of the paper into sections. The numbers should be given in round brackets on the right-hand side of the page.
5. Particular attention should be paid to the differentiation between capital and small letters. If there is a risk of confusion, the symbols should be explained (for example *small c*) in the margins. Indices of more than one level (such as B_{f_a}) should be avoided wherever possible.
6. Computer-generated figures should be produced using **bold lines and characters**. No remarks should be written directly on the figures, except numerals or letter symbols only. Figures should be as small as possible while displaying clearly all the information requires, and with all lettering readable. The relevant explanations can be given in the caption.
7. The figures, including photographs, diagrams, etc., should be numbered with Arabic numerals in the same order in which they appear in the text. Each figure should have its own caption explaining the content without reference to the text.
8. Computer files on an enclosed disc or sent by e-mail to the Editorial Office are welcome. The manuscript should be written as a MS Word file – $*.doc$, $*.docx$ or LaTeX file – $*.tex$. For revised manuscripts after peer review process, figures should be submitted as separate graphic files in either vector formats (PostScript (PS),

Encapsulated PostScript (EPS), preferable, CorelDraw (CDR), etc.) or bitmap formats (Tagged Image File Format (TIFF), Joint Photographic Experts Group (JPEG), etc.), with the resolution not lower than 300 dpi, preferably 600 dpi. These resolutions refer to images sized at dimensions comparable to those of figures in the print journal. Therefore, electronic figures should be sized to fit on single printed page and can have maximum 120 mm x 170 mm. Figures created in MS World, Exel, or PowerPoint will not be accepted. The quality of images downloaded from websites and the Internet are also not acceptable, because of their low resolution (usually only 72 dpi), inadequate for print reproduction.

9. The references for the paper should be numbered in the order in which they are called in the text. Calling the references is by giving the appropriate numbers in square brackets. The references should be listed with the following information provided: the author's surname and the initials of his/her names, the complete title of the work (in English translation) and, in addition:

   (a) for books: the publishing house and the place and year of publication, for example:
   [1] Holman J.P.: *Heat Transfer*. McGraw-Hill, New York 1968.

   (b) for journals: the name of the journal, volume (Arabic numerals in bold), year of publication (in round brackets), number and, if appropriate, numbers of relevant pages, for example:
   [2] Rizzo F.I., Shippy D.I.: *A method of solution for certain problems of transient heat conduction*. AIAA J. **8**(1970), No. 11, 2004–2009.

   For works originally published in a language other than English, the language should be indicated in parentheses at the end of the reference.

   Authors are responsible for ensuring that the information in each reference is complete and accurate.

10. As the papers are published in English, the authors who are not native speakers of English are obliged to have the paper thoroughly reviewed language-wise before submitting for publication.

Manuscript submission Manuscripts to be considered for publication should be electronically submitted to the Editorial Office via the online submission and reviewing system, the Editorial System, at http://www.editorialsystem.com/aot. Submission to the journal proceeds totally on line and you will be guided stepwise throughout the process of the creation and uploading of your files. The body of the text, tables and figures, along with captions for figures and tables should be submitted separately. The system automatically converts source files to a single PDF file article, for subsequent approval by the corresponding Author, which is then used in the peer-review process. All correspondence, including notification confirming the submission of the manuscripts to the Editorial Office, notification of the Editorsñs decision and requests for revision, takes place by e-mails. Authors should designate the corresponding author, whose responsibility is to represent the Authors in contacts with the Editorial Office. Authors are requested not to submit the manuscripts by post or e-mail.

The illustrations may be submitted in color, however they will be printed in black and white in the journal, so the grayscale contributions are preferable. Therefore, the figure

caption and the entire text of the paper should not make any reference to color in the illustration. Moreover the illustration should effectively convey author's intended meaning when it is printed as a halftone. The illustrations will be reproduced in color in the online publication.

Further information All manuscripts will undergo some editorial modification. The paper proofs (as PDF file) will be sent by e-mail to the corresponding author for acceptance, and should be returned within two weeks of receipt. Within the proofs corrections of minor and typographical errors in: author names, affiliations, articles titles, abstracts and keywords, formulas, symbols, grammatical error, details in figures, etc., are only allowed, as well as necessary small additions. The changes within the text will be accepted in case of serious errors, for example with regard to scientific accuracy, or if authors reputation and that of the journal would be affected. Submitted material will not be returned to the author, unless specifically requested.
A PDF file of published paper will be supplied free of charge to the Corresponding Author.

Submission of the manuscript expresses at the same time the authors consent to its publishing in both printed and electronic versions.

Transfer of Copyright Agreement Submission of the manuscript means that the authors automatically agree to assign the copyright to the Publisher. Once a paper has been accepted for publication, as a condition of publication, the authors are asked to send by email a scanned copy of the signed original of the Transfer of Copyright Agreement, signed by the Corresponding Author on behalf of all authors to the Managing Editor of the Journal. The copyright form can be downloaded from the journal's website at http://www.imp.gda.pl/archives-of-thermodynamics/ under Notes for Contributors.

The Editorial Committee